Suppressed charmed B decays

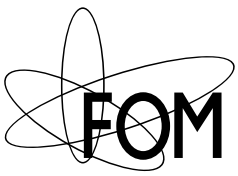

Dit werk maakt deel uit van het onderzoekprogramma van de Stichting voor Fundamenteel Onderzoek der Materie (FOM), die financieel wordt gesteund door de Nederlandse Organisatie voor Wetenschappelijk Onderzoek (NWO).

This work is part of the research programme of the 'Stichting voor Fundamenteel Onderzoek der Materie (FOM)', which is financially supported by the 'Nederlandse Organisatie voor Wetenschappelijk Onderzoek (NWO)'.

VRIJE UNIVERSITEIT

Suppressed charmed B decays

ACADEMISCH PROEFSCHRIFT

ter verkrijging van de graad Doctor aan
de Vrije Universiteit Amsterdam,
op gezag van de rector magnificus
prof.dr. L.M. Bouter,
in het openbaar te verdedigen
ten overstaan van de promotiecommissie
van de faculteit der Exacte Wetenschappen
op dinsdag 2 juni 2009 om 13.45 uur
in de aula van de universiteit,
De Boelelaan 1105

door

Hella Léonie Snoek

geboren te Voorhout

promotor:	prof.dr.ing. J.F.J. van den Brand
copromotor:	dr. H.G. Raven

Contents

Introduction **1**

1 Complex B physics **5**
1.1 Symmetries and CP violation . . . 5
1.2 CP violation in the CKM matrix . . . 6
1.3 CP violation through interference . . . 9
1.4 CP violation in B decays . . . 10
1.4.1 Mixing of neutral B mesons . . . 10
1.4.2 Time evolution of neutral B mesons . . . 12
1.4.3 Coherent $B^0\overline{B}^0$ states . . . 12
1.4.4 Three types of CP violation in B decays . . . 13
1.5 The CKM-angle γ . . . 15
1.5.1 Time dependent CP asymmetry of $B^0 \to D^{(*)+}h^-$ . . . 15
1.5.2 Large asymmetries versus large statistics . . . 17
1.5.3 Asymmetry sensitivity for different $h^\pm$ mesons . . . 17
1.5.4 $B^0 \to D^{(*)-}a_0^+$ motivation . . . 19
1.6 Electroweak a_0 coupling suppressions . . . 19
1.6.1 Conserved vector and partial-conserved axial currents . . . 20
1.6.2 G parity and second-class currents . . . 21
1.7 Factorization and $B^0 \to D^{(*)-}a_0^+$ production amplitude . . . 22
1.7.1 Matrix elements for hadronic two-body B decays . . . 23
1.7.2 QCD factorization . . . 24
1.7.3 Branching ratio of the CKM allowed decay . . . 25
1.7.4 Branching ratio of the CKM suppressed decay . . . 26
1.8 Final-state interactions . . . 27
1.9 Motivation summary . . . 30
1.10 Analysis Strategy . . . 30
1.11 Non-resonant $B^0 \to D^{(*)-}\eta\pi^+$ predictions . . . 31

2 The *BABAR* experiment **33**
2.1 The *BABAR* detector . . . 33
2.2 Silicon vertex tracker (SVT) . . . 35
2.3 Drift chamber (DCH) . . . 39
2.4 Detector of internally reflected Čerenkov light (DIRC) . . . 40

2.5 Electromagnetic calorimeter (EMC) . . . 41
2.6 Instrumented flux return (IFR) . . . 42
2.7 The online system . . . 42

3 Reconstruction of B mesons **45**
3.1 Used data samples . . . 46
3.1.1 *BABAR* data . . . 46
3.1.2 Monte Carlo simulated data production . . . 46
3.2 Particle reconstruction . . . 50
3.2.1 Reconstruction of charged particles . . . 50
3.2.2 Reconstruction of neutral particles . . . 51
3.2.3 Kaon selection . . . 53
3.3 Reconstruction of composite particles . . . 54
3.3.1 π^0 candidates . . . 55
3.3.2 η candidates . . . 56
3.3.3 K^0_S candidates . . . 56
3.3.4 D^+ candidates . . . 56
3.3.5 D^0 candidates . . . 56
3.3.6 D^{*+} candidates . . . 57
3.3.7 B^0 candidates . . . 57
3.3.8 Global decay chain fit . . . 57
3.4 Skim rates and selection efficiency . . . 58

4 Event selection **59**
4.1 Selection optimization . . . 59
4.1.1 Significance level . . . 60
4.1.2 The Monte Carlo data used for the optimization . . . 61
4.1.3 Scanning the multi-variable phase space . . . 61
4.1.4 Multiple candidates selection . . . 64
4.2 Selection variables . . . 64
4.2.1 Continuum background suppression . . . 65
4.2.2 Signal event selection variables . . . 69
4.3 Final selection . . . 76
4.4 Selected sample . . . 78
4.5 Signal selection efficiency . . . 80

5 Three dimensional likelihood fit **83**
5.1 Global fit setup . . . 83
5.2 Description of probability density functions . . . 84
5.2.1 The $m_{\rm ES}$ distribution . . . 84
5.2.2 The ΔE distribution . . . 85
5.2.3 The $\eta\pi$ invariant-mass distribution . . . 85
5.2.4 Background and signal component composition . . . 87
5.3 Summary of fixed shape parameters . . . 89

5.4 Likelihood fit performed on Monte Carlo data . . . 93
5.5 Efficiency . . . 94
5.6 Results of the likelihood fit to data . . . 94
5.7 Branching ratio determination method . . . 98

6 Validation studies **105**
6.1 Fit bias validation studies on Monte Carlo . . . 105
6.1.1 Toy Monte Carlo studies . . . 105
6.1.2 Fit bias studies on full Monte Carlo events . . . 106
6.2 Validation studies performed on data . . . 110
6.2.1 Continuum background description . . . 110
6.2.2 Validation of reconstruction and selection criteria using the D_s resonance . . . 113
6.2.3 Fit bias studies with signal enriched data samples . . . 122

7 Evaluation of systematic uncertainties **125**
7.1 Number of observed events uncertainties . . . 125
7.1.1 Bias offset . . . 125
7.1.2 Non-resonant $m_{\eta\pi}$ shape description . . . 125
7.1.3 Lineshape uncertainties . . . 126
7.1.4 Cross feed between decay modes . . . 128
7.1.5 P.d.f. shape uncertainties . . . 128
7.2 Uncertainties in the number of B events . . . 128
7.2.1 Luminosity and B counting . . . 128
7.3 Fractional branching ratio uncertainties . . . 129
7.4 Uncertainties and corrections in the selection efficiency . . . 130
7.4.1 Statistical errors on the determined selection efficiency . . . 130
7.4.2 Reconstruction and selection criteria uncertainties . . . 130
7.4.3 Track finding efficiency . . . 130
7.4.4 Neutral particle identification . . . 131
7.4.5 Summary of efficiency corrections . . . 131
7.5 Systematic errors summary tables . . . 131

8 Determination of the branching ratios **133**
8.1 Combined branching ratio fit . . . 133
8.2 Combined fit results . . . 134
8.2.1 Analysis of reconstructed $B^0 \to D^- \eta\pi^+$ events . . . 134
8.2.2 Analysis of reconstructed $B^0 \to D^{*-} \eta\pi^+$ events . . . 137
8.3 Significance of the results . . . 140
8.3.1 Significance levels . . . 140
8.3.2 Upper limit for the $B^0 \to D^- a_0^+$ signal exclusion . . . 140
8.4 Summary of obtained results . . . 142

9 Conclusions **145**
9.1 Theory recap 145
9.2 Summary of branching ratio measurements 148
9.3 Interpretation of the results 150
9.4 Outlook 151

Summary **153**

Populaire samenvatting **155**

A Selection variable tables **161**

References **169**

Acknowledgements **175**

Index **177**

Introduction

The Standard Model of particle physics describes the strong and electroweak interactions between elementary particles. The model has now survived forty years of stringent tests and has established itself firmly in the world of particle physics. However, there are clues to why the Standard Model cannot describe the Universe that we live in to full accuracy. The Standard Model is, for example, not able to explain the abundance of matter over antimatter in the Universe.

Differences between matter and antimatter could arise during the Big Bang through weak interactions. Such processes, that are called *CP* violating, were first observed in 1964 by Cronin, Fitch and collaborators[1]. The *CP* violating processes can only exist in hadronic decays if there are three or more generations of quarks. This was realized by Kobayashi and Maskawa in 1972 and led to the prediction of three new quarks[2]. The new quarks were discovered in 1974, 1977 and 1994 and are called charm, beauty and top respectively. Sakharov[3] stated that violation of *CP* is one of three conditions that need to be satisfied to explain the absence of antimatter in the Universe. Although the presence of *CP* violation in the Standard Model is now established, the predicted levels of violation are still too small to explain the data.

The relative long lifetime of the beauty quark is ideal for testing the predictions in the Standard Model towards *CP* violation. Two B factories were set up, *BABAR* (see Fig. 1) and Belle, which have now measured different aspects of *CP* violation to high accuracy. So far all measurements are in agreement with predictions from the Standard Model.

The properties of weak interactions with quarks lead to relations that can be expressed as a triangle in a complex plane, called the CKM Unitarity Triangle. The surface area of the Unitarity Triangle is directly related to the size of *CP* violation present in hadronic weak decays. The CKM triangle characteristics, side lengths and interior angles, can be measured by studying particle decays. The least restricted property of the Unitarity Triangle is the so-called CKM angle γ. Current direct measurements of this angle are performed by the study of time dependent interference in *e.g.* $B^0 \to D^{*-}\rho^+$, $B^0 \to D^{*-}\pi^+$ or $B^0 \to D^{*-}a_1(1260)^+$ decays. The sensitivity to the angle γ in these measurements is however small.

This thesis reports on the study of $B^0 \to D^{(*)-}a_0^+$ decays, which are sensitive to the

[1]Nobel Prize in Physics 1980
[2]Nobel Prize in Physics 2008
[3]Nobel Prize for Peace 1975

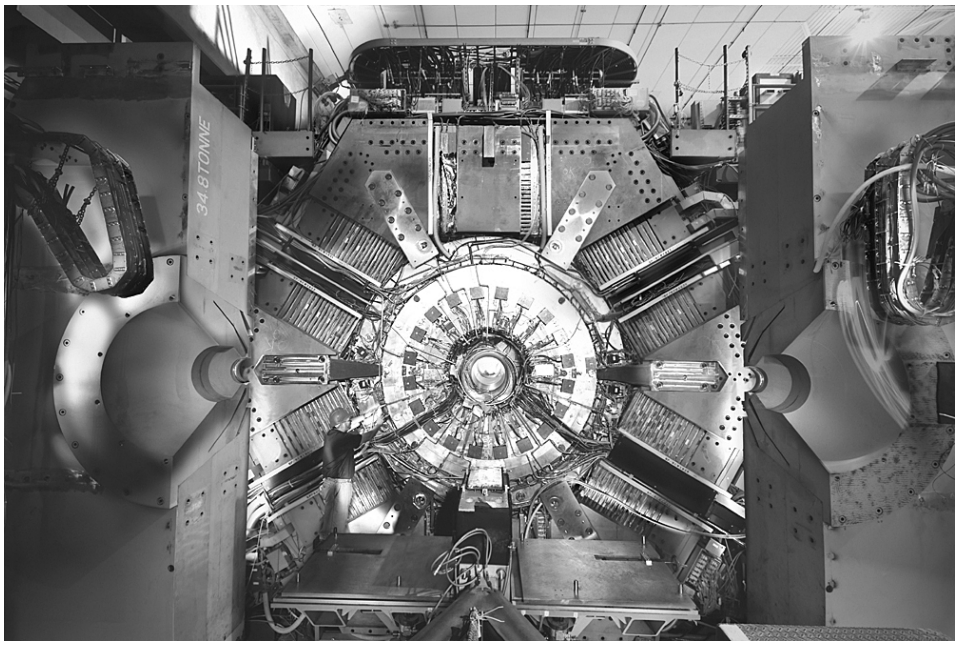

Figure 1: The *BABAR* detector during construction.

CKM angle γ. Potentially, the sensitivity to γ can be larger than that of the current measurements. The sensitivity to the *CP* phase depends on the asymmetry amplitude which in turn depends on the relative sizes of the two interfering decay amplitudes. Compared to the $B^0 \to D^{*-}h^+$ ($h = \pi, \rho$, or a_1) decays, this relative size is larger. This enhancement is caused by a suppression of one of the otherwise dominant, contributing diagrams so that the two interfering amplitudes are almost of equal size.

The two diagrams that dominate in the $B^0 \to D^{(*)-}a_0^+$ decay are presented in Fig. 2. The left diagram is suppressed by the small coupling of the a_0-meson to the W boson. The right diagram is suppressed by the small CKM element in the $b \to u$ transition.

The decay amplitude of each diagram is computed using a so-called factorization technique, which allows to express the total amplitude in terms of separate components. Non-factorizing components are related to for example final-state interactions through gluon exchange in the formed hadronic states and are very hard to calculate. Usually these non-factorizing terms have a smaller contribution to the decay amplitude compared to the factorizing terms and can be neglected. The suppression mechanism in the left diagram in Fig. 2 causes the factorizing term to become so small that non-factorizing contributions could dominate the decay amplitude. A measurement of the branching fraction of the $B^0 \to D^{(*)-}a_0^+$ decay can say something about how well the factorization technique works and is therefore valuable.

There are no previous reports on the observation of the $B^0 \to D^{(*)-}a_0^+$ decays and the low predicted decay rates (order of 10^{-6}) poses experimental challenges for the measurement of the branching fractions. Other charmed decay modes that are produced abundantly, such as $B^0 \to D^{*-}\rho^+$ and $B^0 \to D^{*-}a_1(1260)^+$, create a background that is hard to remove, especially since the width of the a_0 Breit-Wigner lineshape is not well

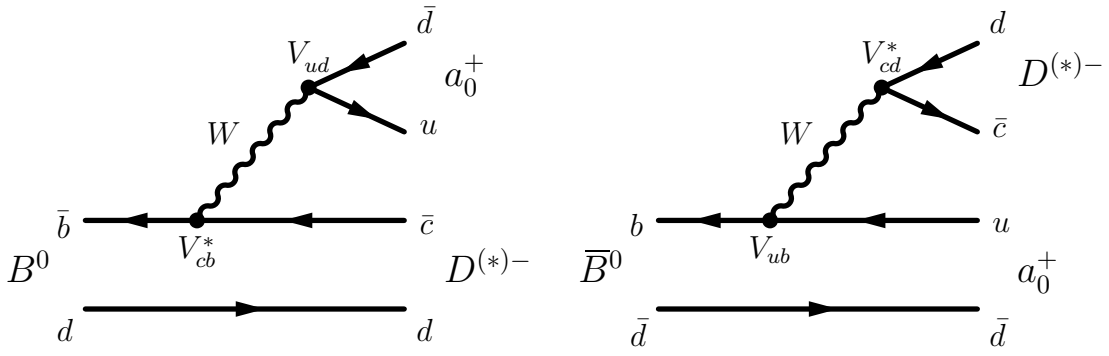

Figure 2: Feynman diagrams for the CKM favored $B^0 \to D^{(*)-}a_0^+$ decay (*left*), and the doubly-CKM-suppressed $\overline{B}^0 \to D^{(*)-}a_0^+$ decay (*right*).

known. A two-fold solution to tackle this problem is used in the analysis presented in this thesis. First an advanced data selection and subsequently a three dimensional likelihood fit is performed. The fit distinguishes the resonant $B^0 \to D^{(*)-}a_0^+$ signal, where $a_0^+ \to \eta\pi^+$, from expected non-resonant $B^0 \to D^{(*)-}\eta\pi^+$ events, resonant $B^0 \to D^{(*)-}D_s^+$, and background events. The $B^0 \to D^{(*)-}D_s^+$ events are used as a control sample to validate the analysis. The branching fraction of the non-resonant $B^0 \to D^{(*)-}\eta\pi^+$ events is measured simultaneously with the measurement of the $B^0 \to D^{(*)-}a_0^+$ branching fraction.

This thesis is organized in the following chapters. Chapter 1 gives an overview of the presence of *CP* violation in the Standard Model and how the $B^0 \to D^{(*)-}a_0^+$ decays are sensitive to the CKM angle γ. Subsequently, this chapter describes factorization with QCD corrections and how the branching fraction of the $B^0 \to D^{(*)-}a_0^+$ decay is sensitive to the kinematic terms used in factorization. Also, the possibility of rescattering contributions to the decay amplitude is discussed. Chapter 2 describes the experimental setup of the *BABAR* experiment. Chapter 3 describes the general setup of the signal selection, the data and Monte Carlo samples used, and the reconstruction of the B mesons. Chapter 4 describes the final selection of the signal. The selection variables are introduced and the procedure to optimize the cuts on these variables is described. Chapter 5 presents the setup of the three dimensional likelihood fit, the behavior of the fit on the Monte Carlo and data sample and the method that is used to extract the branching fraction from the fit results. In chapter 6 various validation tests are described that have been performed to test the fit procedure and the data selection. Chapter 7 reports on the systematic uncertainties that are present in the analysis. The results of the measurement are presented in Chapter 8, and finally Chapter 9 discusses the conclusions that can be drawn from the results.

Chapter 1

Complex B physics

This thesis presents the analysis of the search for $B^0 \to D^{(*)-}a_0^+$ decays[1]. The interest for these decays is motivated by two arguments that will be discussed at length in this chapter.

The first argument is the sensitivity of the decay modes to the CKM angle γ, which is the least accurately known angle of the Unitarity Triangle. There are many more decays sensitive to this angle, but the time-dependent analysis of the $B^0 \to D^{(*)-}a_0^+$ decay is expected to have larger sensitivity to the asymmetry than the decays that are currently deployed for the measurement of γ, such as $B^0 \to D^{*-}\rho^+$ and $B^0 \to D^{*-}\pi^+$. This will be motivated in the first five sections of this chapter.

The second argument is that the predicted decay amplitude is sensitive to differences in theoretical QCD factorization models. The usually dominant 'factorizing terms' in B decay amplitudes are suppressed by several mechanisms for the $B^0 \to D^{(*)-}a_0^+$ decay, described in Sect. 1.6. Owing to the suppression of the factorizing terms, non-factorizing terms can become visible. Different models predict different sizes for these terms. Therefore, the measurement of the branching ratio of the $B^0 \to D^{(*)-}a_0^+$ decay can possibly exclude factorization models, and as a result provide more knowledge of the strong effects that occur in the hadronization of quarks. This is discussed in Sect. 1.7.

In all weak decays that produce hadrons QCD is involved, and in almost all of these decays the hadronic physics is complex to calculate. It is the most problematic uncertainty introduced in B physics, obfuscating the extraction of 'clean' electroweak observables, forcing us to carefully choose unaffected observables. A better understanding of the hadronic processes would allow for more measurements to contribute to precision electroweak physics. The intertwinement of the complex calculations of the strong interactions and the beauty of B physics will be brought to the attention in this chapter.

1.1 Symmetries and CP violation

Three discrete transformations occur in field theory, abbreviated as C, P and T. Charge conjugation (C) interchanges particles and anti-particles; Parity (P), reverses all spatial

[1] Charge conjugation is implied throughout this thesis, unless explicitly stated otherwise.

coordinates; Time reversal (T) reverses the time flow in physical processes. In any local Lagrangian field theory, such as the electroweak theory, the combined effect of the three operators, CPT, is an exact symmetry [1, 2]. The combined CP transformation replaces a particle with its anti-particle of opposite spin-parity and reverses its momentum. For long it was assumed to be conserved in the electroweak field theory. However, after the discovery of P violation by Wu et. al. [3] in 1957 and CP violation in 1964 by Christenson et. al. [4], a revolution in the understanding of the weak interaction has taken place.

The existence of CP violation is readily accommodated in the electroweak field theory. CP violation arises whenever there are complex coupling constants that cannot be removed by any set of phase redefinitions of the fields. In the Standard Model this is only possible with three or more generations of quarks. This was first realized by Kobayashi and Maskawa [5] and led to the prediction of the third generation particles (b and t quarks and τ and ν_τ leptons) for which they received the Nobel Prize in Physics 2008.

1.2 CP violation in the CKM matrix

The interactions of charged W bosons of the weak interactions with quarks can be written as

$$\mathcal{L}_W = \frac{g}{\sqrt{2}} \sum_{i,j} (V_{CKM})_{ij} \bar{u}_i^M \gamma^\mu (1-\gamma^5) d_j^M W_\mu + h.c., \tag{1.1}$$

where u and d refer to up-type and down-type quarks, $i, j = 1, 2, 3$ denotes the three quark generations, g is the weak coupling constant, γ^μ, γ^5 are Dirac matrices and W_μ the charged weak bosons. The complex matrix elements, V_{CKM}, are introduced to relate the weak eigenstates to the mass eigenstates and define the relative strength of the quark flavor transitions. The matrix elements are physical, measurable quantities.

The three up-type quarks (u, c and t) are considered pure states by convention. Flavor mixing is induced by the 3×3 Cabibbo-Kobayashi-Maskawa mixing matrix, $\widehat{V}_{CKM}$, and operates on the three down-type quarks (d, s and b) [6, 5]. This is expressed as

$$\begin{pmatrix} d' \\ s' \\ b' \end{pmatrix} = \begin{pmatrix} V_{ud} & V_{us} & V_{ub} \\ V_{cd} & V_{cs} & V_{cb} \\ V_{td} & V_{ts} & V_{tb} \end{pmatrix} \cdot \begin{pmatrix} d \\ s \\ b \end{pmatrix} \equiv \widehat{V}_{CKM} \cdot \begin{pmatrix} d \\ s \\ b \end{pmatrix}. \tag{1.2}$$

If there are only three generations of quarks, and the quarks cannot transform into other quantum states, the CKM matrix must be a unitarity matrix. A popular parametrization of the matrix is given by Wolfenstein [7]

$$V_{CKM} = \begin{pmatrix} 1-\frac{\lambda^2}{2} & \lambda & A\lambda^3(\rho - i\eta) \\ -\lambda & 1-\frac{\lambda^2}{2} & A\lambda^2 \\ A\lambda^3[(1-\rho)-i\eta] & -A\lambda^2 & 1 \end{pmatrix} + \mathcal{O}(\lambda^4). \tag{1.3}$$

The four variables λ, ρ, η and A are called the Wolfenstein parameters. Exact definitions of the parameters can be found in [7]. The advantage of this parametrization is that the similarity between the CKM matrix and the unit matrix become particularly evident.

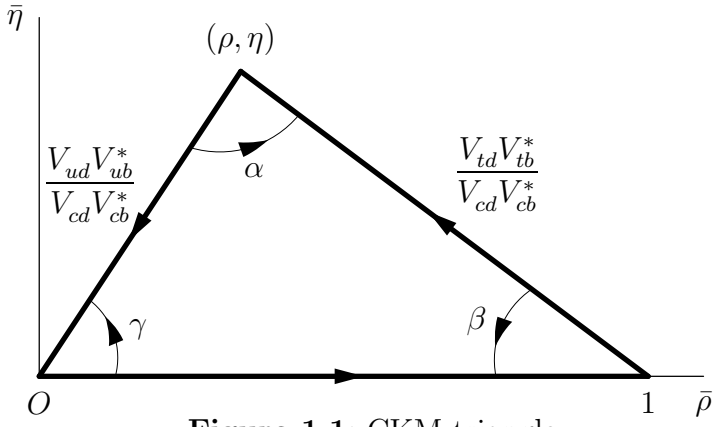

Figure 1.1: CKM triangle.

The diagonal elements are close to unity and the off-diagonal elements are increasingly small. This means that the mixing between different generations of quarks is small, also referred to as *Cabibbo*-suppressed or CKM-suppressed.

The unitarity condition of the CKM matrix leads to 9 constraining relations of which 6 are orthogonality relations. These can be represented as triangles in the complex plane. All the triangles have the same surface area, as was first pointed out by Cecilia Jarlskog [8], but only two are not squashed and have three sides that are of comparable size which makes over constraining of these triangles, by experiment, feasible. The orthogonality relations describing the two non-squashed triangles are

$$V_{ud}V_{ub}^* + V_{cd}V_{cb}^* + V_{td}V_{tb}^* = 0, \tag{1.4}$$

$$V_{ud}^*V_{td} + V_{us}^*V_{ts} + V_{ub}^*V_{tb} = 0. \tag{1.5}$$

In the Wolfenstein parametrization all entities of these two equations are the same to leading order $\mathcal{O}(\lambda^3)$. The triangle from the first relation is referred to as *the* Unitarity Triangle of the CKM matrix, see Fig. 1.1. The three angles of the Unitarity Triangle are denoted by α, β and γ and are defined as

$$\alpha \equiv \arg\left[-\frac{V_{td}V_{tb}^*}{V_{ud}V_{ub}^*}\right], \tag{1.6}$$

$$\beta \equiv \arg\left[-\frac{V_{cd}V_{cb}^*}{V_{td}V_{tb}^*}\right] \text{ and} \tag{1.7}$$

$$\gamma \equiv \arg\left[-\frac{V_{ud}V_{ub}^*}{V_{cd}V_{cb}^*}\right] \equiv \pi - \alpha - \beta. \tag{1.8}$$

While for a two-generation family situation the unitary matrix could have been chosen to be real, this is no longer possible for 3 generations. The irreducible phase introduced in the CKM matrix is the source of the *CP* violation that occurs in the hadron sector in the Standard Model. The surface area of the Unitarity Triangle is thus proportional to the size of the occurring *CP* violation in weak hadron decay [8].

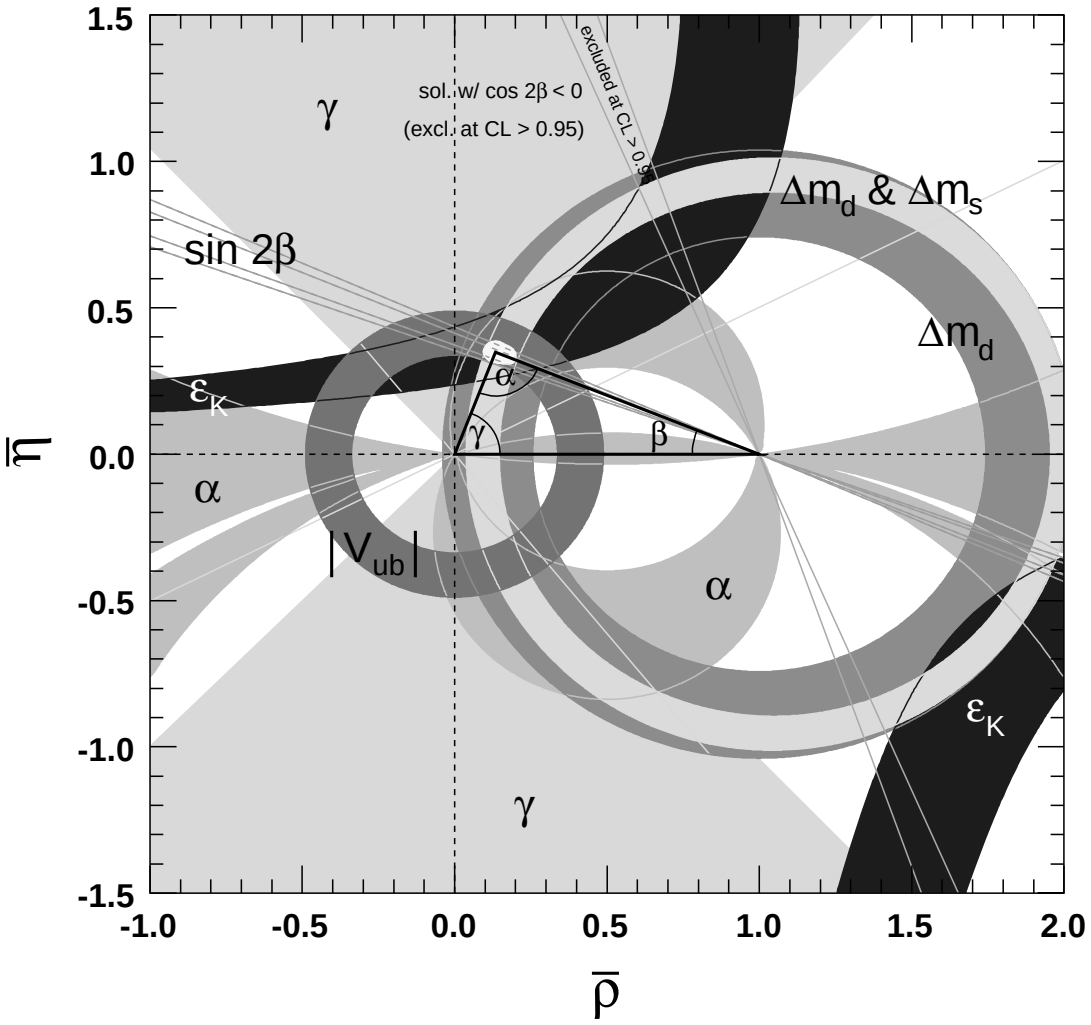

Figure 1.2: Current status of the constraints on the CKM triangle [9].

From experimental knowledge of weak hadron interactions, assuming unitarity and three generations, the current 90% confidence limits on the magnitude of the CKM matrix elements are [9]

$$|V_{CKM}| = \begin{pmatrix} 0.9739\text{–}0.9751 & 0.221\text{–}0.227 & 0.0029\text{–}0.0045 \\ 0.221\text{–}0.227 & 0.9730\text{–}0.9744 & 0.039\text{–}0.044 \\ 0.0048\text{–}0.014 & 0.037\text{–}0.043 & 0.9990\text{–}0.9992 \end{pmatrix}. \tag{1.9}$$

The current status of the constraints on the CKM triangle are shown in Fig. 1.2. It is clear from the plot that the least constrained angle, by direct measurements, is γ. A precise direct measurement of this angle will decrease the uncertainty on the apex along the $\overline{\rho}$ axis. A summary of the present constraints of the three angles is given in Table 1.1.

CKM angle	constraints
α	$(88^{+6}_{-5})^\circ$
β	$(21.5^{+1.4}_{-0.5})^\circ$
γ	$(77^{+30}_{-32})^\circ$

Table 1.1: Current constraints on the CKM angles α, β and γ [9].

The decays of B mesons are well-suited to study flavor physics and *CP* violation. Large *CP* violating effects and large mixing, explained in Sect. 1.4.1, are possible in the neutral B_d and B_s systems. The advantage over exploiting neutral K and D mesons is that the large mass of the B meson makes it possible to have a better understanding of the hadronic physics involved in decays, because $m_b \gg \Lambda_{QCD}$, which is needed to extract the size of the electroweak physics involved in the decay. Another advantage is the large number of B meson decay modes that makes it possible to measure the CKM angles in various ways reducing the theoretical and experimental uncertainties.

1.3 *CP* violation through interference

A direct measurement of *CP* violation necessarily has to be performed by the study of interference of amplitudes. Only then it is possible to study the complex phases in the CKM matrix.

In general an amplitude can contain a *CP* even part, which is invariant under the *CP* operation, and a *CP* odd part, which changes sign under the *CP* operation. Let us now introduce an amplitude, A, to a final state f, with two independent contributions,

$$A_f = A_1 e^{i(\delta_1+\phi_1)} + A_2 e^{i(\delta_2+\phi_2)}, \tag{1.10}$$

where δ_1 and δ_2 are the *CP* even phases and ϕ_1 and ϕ_2 are the *CP* odd phases. The total decay rate can now be expressed as

$$\begin{aligned}
|A_f|^2 &= A_f A_f^* && (1.11)\\
&= (A_1 e^{i(\delta_1+\phi_1)} + A_2 e^{i(\delta_2+\phi_2)}) \cdot (A_1 e^{-i(\delta_1+\phi_1)} + A_2 e^{-i(\delta_2+\phi_2)}) && (1.12)\\
&= |A_1|^2 + |A_2|^2 + |A_1 A_2| e^{i(\Delta\delta+\Delta\phi)} + |A_1 A_2| e^{-i(\Delta\delta+\Delta\phi)} && (1.13)\\
&= |A_1|^2 + |A_2|^2 + 2|A_1 A_2| \cos(\Delta\delta + \Delta\phi), && (1.14)
\end{aligned}$$

where we have used the convention $\Delta\delta \equiv \delta_1 - \delta_2$ and $\Delta\phi \equiv \phi_1 - \phi_2$. The *CP* conjugated process $\overline{A}_{\overline{f}}$ is then

$$\begin{aligned}
|\overline{A}_{\overline{f}}|^2 &= \overline{A}_{\overline{f}} \overline{A}^*_{\overline{f}} && (1.15)\\
&= (A_1 e^{i(\delta_1-\phi_1)} + A_2 e^{i(\delta_2-\phi_2)}) \cdot (A_1 e^{-i(\delta_1-\phi_1)} + A_2 e^{-i(\delta_2-\phi_2)}) && (1.16)\\
&= |A_1|^2 + |A_2|^2 + |A_1 A_2| e^{i(\Delta\delta-\Delta\phi)} + |A_1 A_2| e^{-i(\Delta\delta-\Delta\phi)} && (1.17)\\
&= |A_1|^2 + |A_2|^2 + 2|A_1 A_2| \cos(\Delta\delta - \Delta\phi). && (1.18)
\end{aligned}$$

The unnormalized asymmetry is then defined as

$$|A_f|^2 - |\overline{A}_{\overline{f}}|^2 = 2|A_1 A_2|\{\cos(\Delta\delta + \Delta\phi) - \cos(\Delta\delta - \Delta\phi)\} \quad (1.19)$$

$$= 4|A_1 A_2| \sin(\Delta\delta)\sin(\Delta\phi). \quad (1.20)$$

From this it can be seen that both *CP* even and *CP* odd phases are necessary to observe *CP* violation; if there is no *CP* even phase, the asymmetry collapses. The magnitude of the observable effect is related to the ratio of the amplitudes

$$\left|\frac{A_f}{\overline{A}_{\overline{f}}}\right|^2 = \left|\frac{|A_1|^2 + |A_2|^2 + 2|A_1 A_2|\cos(\Delta\delta + \Delta\phi)}{|A_1|^2 + |A_2|^2 + 2|A_1 A_2|\cos(\Delta\delta - \Delta\phi)}\right|^2. \quad (1.21)$$

If both $|A_1|$ and $|A_2|$ are of almost equal magnitude and with a different phase, the asymmetry is large, while a large difference in magnitude gives, at most, a small observable asymmetry.

The measurable *CP* odd phases occur only in the CKM matrix in the hadron sector of the Standard Model [10] and are called *weak phases*. The *CP* even phases can occur in scattering or the decay amplitudes. Usually dominant rescattering phases are owing to the strong interaction, thus the *CP* even phases are referred to as *strong phases*.

1.4 *CP* violation in B decays

1.4.1 Mixing of neutral B mesons

Neutral B-mesons have mass eigenstates that are not flavor eigenstates. The flavor eigenstates are useful to understand particle production and decay processes. The states of definite mass and lifetime are, by definition, eigenstates of the Hamiltonian describing the system. If *CP* was a good symmetry the mass eigenstates would also be *CP* eigenstates. This is not the case and will be discussed later on. The mass eigenstates are, in general, not the same as the flavor eigenstates and so the flavor eigenstates are mixed with one another as they evolve.

The flavor mixing occurs through second-order weak interactions that are illustrated in Fig. 1.3. This process was first observed in 1987 by both the ARGUS experiment [11] and the UA1 experiment [12].

An arbitrary linear combination of the neutral B-meson flavor eigenstates is given by

$$|\psi(t)\rangle \equiv a|B^0\rangle + b|\overline{B}^0\rangle. \quad (1.22)$$

The Schrödinger equation for the time evolution and decay can be written as

$$i\frac{d}{dt}\begin{Bmatrix} a \\ b \end{Bmatrix} = \{\mathbf{M} - \frac{i}{2}\mathbf{\Gamma}\}\begin{Bmatrix} a \\ b \end{Bmatrix}, \quad (1.23)$$

where $\mathbf{M}$ and $\mathbf{\Gamma}$ represent the mass and decay-width, 2×2 Hermitian, matrices. The off-diagonal terms, M_{12} and Γ_{12}, arise from the box diagram illustrated in Fig. 1.3. The light $|B_L\rangle$ and heavy $|B_H\rangle$ mass eigenstates are given by

$$|B_L\rangle = p|B^0\rangle + q|\overline{B}^0\rangle, \quad |B_H\rangle = p|B^0\rangle - q|\overline{B}^0\rangle. \quad (1.24)$$

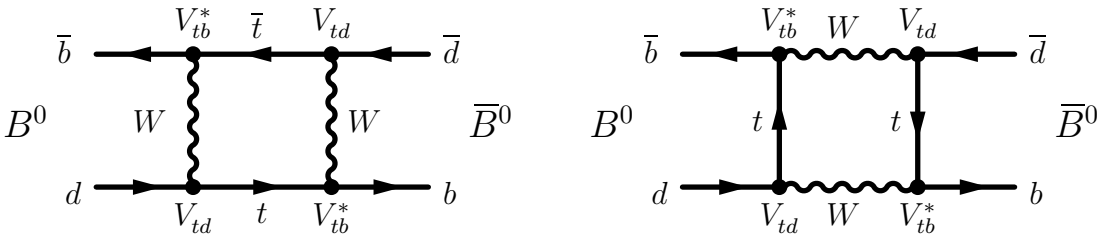

Figure 1.3: Leading box diagrams for the $B^0 - \overline{B}^0$ transitions.

The complex coefficients p and q obey the normalization condition

$$|q|^2 + |p|^2 = 1. \tag{1.25}$$

The mass difference Δm_d and the decay width difference $\Delta\Gamma_d$ are defined as

$$\Delta m_d \equiv M_H - M_L, \tag{1.26}$$
$$\Delta\Gamma_d \equiv \Gamma_H - \Gamma_L, \tag{1.27}$$

where H and L refer to the heavy and light B mass eigenstates. The lifetime difference $\Delta\Gamma_d$ is sensitive to Γ_{12}, which is produced by decay channels common to both the B^0 and $\overline{B}^0$, *e.g.* $B \to D\overline{D}$. The branching ratios for such channels are at or below the level of 10^{-3}. The eigenvalues of Eq. (1.23) can now be expressed as

$$(\Delta m_d)^2 - \frac{1}{4}(\Delta\Gamma_d)^2 = 4(|M_{12}|^2 - \frac{1}{4}|\Gamma_{12}|^2), \tag{1.28}$$
$$\Delta m_d \Delta\Gamma_d = 4\mathcal{R}e(M_{12}\Gamma_{12}^*). \tag{1.29}$$

The ratio q/p is given by

$$\frac{q}{p} = \sqrt{\frac{M_{12}^* - \frac{i}{2}\Gamma_{12}^*}{M_{12} - \frac{i}{2}\Gamma_{12}}}. \tag{1.30}$$

The Standard Model predicts $|q/p| - 1 = (2.5 - 6.5) \cdot 10^{-4}$ [9]. From this it is assumed that $\Delta\Gamma_d \ll \Gamma_d$ [13], confirmed by the measurements $|\Delta\Gamma_d/\Gamma_d| = 0.009 \pm 0.037$ [14].

The mass difference Δm_d, on the other hand, is well known

$$\Delta m_d = 0.507 \pm 0.005\,\mathrm{ps}^{-1}[14]. \tag{1.31}$$

In conclusion, the two mass eigenstates have virtually equal lifetimes but noticeably different masses. This implies that Eq. (1.28) and (1.30) can be simplified to

$$\Delta m_d = 2|M_{12}|, \quad q/p = -|M_{12}|/M_{12}. \tag{1.32}$$

1.4.2 Time evolution of neutral B mesons

Any B meson state can be written as an admixture of the states B_H and B_L whose coefficients evolve in time

$$a_H(t) = a_H(0)e^{-iM_H t}e^{-\frac{1}{2}\Gamma_H t}, \quad a_L(t) = a_L(0)e^{-iM_L t}e^{-\frac{1}{2}\Gamma_L t}. \tag{1.33}$$

A state that is created at time $t = 0$ as initially pure B^0, is denoted $|B^0_{phys}\rangle$, has $a_L(0) = a_H(0) = 1/(2p)$. Similarly an initially pure $\overline{B}^0$, $|\overline{B}^0_{phys}\rangle$, has $a_L(0) = -a_H(0) = 1/(2q)$. The time evolution of these states is thus given by

$$|B^0_{phys}(t)\rangle = g_+(t)|B^0\rangle + (q/p)g_-(t)|\overline{B}^0\rangle, \tag{1.34}$$
$$|\overline{B}^0_{phys}(t)\rangle = (p/q)g_-(t)|B^0\rangle + g_+(t)|\overline{B}^0\rangle, \tag{1.35}$$

where

$$g_+(t) = e^{-iMt}e^{-\Gamma t/2}\cos(\Delta m_d t/2), \tag{1.36}$$
$$g_-(t) = e^{-iMt}e^{-\Gamma t/2}i\sin(\Delta m_d t/2), \tag{1.37}$$

that uses $M = \frac{1}{2}(M_H + M_L)$ and $\Gamma = \frac{1}{2}(\Gamma_H + \Gamma_L)$.

1.4.3 Coherent $B^0\overline{B}^0$ states

At the *BABAR* experiment the $B^0\overline{B}^0$ meson pair is produced through the process e^+e^- $\rightarrow \Upsilon(4S) \rightarrow B^0\overline{B}^0$. Through this production mechanism the B^0 and $\overline{B}^0$ mesons are produced in a coherent $L = 1$ state. Each of the two produced B mesons evolves in time as is described above. However, owing to Bose-Einstein statistics they must evolve in phase coherently so that, until the first decay, one of each B meson flavors is present. Once the first B meson decays, the second continues to evolve.

The two particles have back-to-back momenta in the $\Upsilon(4S)$ rest frame. The forward and backward moving B mesons have the proper times t_f and t_b. Now the $B^0\overline{B}^0$ state is described as

$$|B^0_{phys}\overline{B}^0_{phys}; t_f, t_b\rangle = \{|B^0_{phys}(t_f)\rangle|\overline{B}^0_{phys}(t_b)\rangle - |\overline{B}^0_{phys}(t_f)\rangle|B^0_{phys}(t_b)\rangle\}/\sqrt{2}. \tag{1.38}$$

We now first introduce

$$A_i \equiv \langle f_i|H_W|B^0\rangle, \quad \overline{A}_i \equiv \langle f_i|H_W|\overline{B}^0\rangle. \tag{1.39}$$

From Eq. (1.38) and Eqs. (1.34-1.37) one can derive the amplitude for decays where one of the B's decays to any final state f_1 at time t_1 and the other decays to f_2 at time t_2

$$\begin{aligned} A(t_1, t_2) = &\{\langle f_1|H_W|B^0_{phys}(t_1)\rangle\langle f_2|H_W|\overline{B}^0_{phys}(t_2)\rangle \\ &-\langle f_1|H_W|\overline{B}^0_{phys}(t_1)\rangle\langle f_2|H_W|B^0_{phys}(t_2)\rangle\}/\sqrt{2} \\ = &\frac{1}{\sqrt{2}}e^{-(\Gamma/2+iM)(t_1+t_2)}\{\cos(\Delta m_d(t_1 - t_2))(A_1\overline{A}_2 - \overline{A}_1A_2) \\ &-i\sin(\Delta m_d(t_1 - t_2))(\frac{p}{q}A_1A_2 - \frac{q}{p}\overline{A}_1\overline{A}_2)\}. \end{aligned} \tag{1.40}$$

The time dependent rate for producing the combined final states f_1, f_2 is then

$$\begin{aligned} R(T,\Delta t) = Ce^{-\Gamma T}\{&(|A_1|^2+|\overline{A}_1|^2)(|A_2|^2+|\overline{A}_2|^2) - 4\mathcal{R}e(\frac{q}{p}A_1^*\overline{A}_1)\mathcal{R}e(\frac{q}{p}A_2^*\overline{A}_2) \\ &-\cos(\Delta m_d\Delta t)[(|A_1|^2-|\overline{A}_1|^2)(|A_2|^2-|\overline{A}_2|^2) + 4\mathcal{I}m(\frac{q}{p}A_1^*\overline{A}_1)\mathcal{I}m(\frac{q}{p}A_2^*\overline{A}_2)] \\ &+\sin(\Delta m_d\Delta t)[\mathcal{I}m(\frac{q}{p}A_1^*\overline{A}_1)(|A_2|^2-|\overline{A}_2|^2) - (|A_1|^2-|\overline{A}_1|^2)\mathcal{I}m(\frac{q}{p}A_2^*\overline{A}_2)]\}, \end{aligned} \tag{1.41}$$

where C is a normalization constant, and substitutions have been made for $T = t_1 + t_2$ and $\Delta t = t_1 - t_2$. This expression can be integrated over the experimentally unobservable variable T that has the range $(|\Delta t|, \infty)$. This changes $Ce^{-\Gamma T}$ to $C'e^{-\Gamma\Delta t}$ in Eq. (1.41). As a consequence only the decay-time difference, Δt, has to be measured, which is achieved by measuring the distance between the two B decays. As a consequence, no information is needed on the $\Upsilon(4S)$ decay vertex (which would introduce large errors!). This is the premise of the B factories.

Another advantage of the coherent production of the two B mesons is that by employing special B decays, so called *tagging decays*, knowledge on the flavor of the other B can be derived. An example of such a tagging decay is $B^0 \to D^{*-}l^+\nu$. In this decay the charge of the lepton is directly connected to charge of the b quark contained in the B meson. If one B decays through one of the tagging decays, not only do we know the flavor of the decaying B meson at time $\Delta t = 0$, we also know that at the same time the other B is of the opposite flavor.

1.4.4 Three types of CP violation in B decays

In the neutral B system we have two different ingredients in the amplitude that can cause interference: mixing and decay. The two ingredients give three different combinations: mixing, decay and the combination of mixing and decay. All three types are based on the interference mechanism explained in Sect. 1.3.

Direct CP violation

Direct CP violation is also known as CP violation in decay. Given the process $B \to f$ and $\overline{B} \to \overline{f}$ with decay amplitudes A_f and $\overline{A}_{\overline{f}}$, direct CP violation occurs when

$$\left|\frac{\overline{A}_{\overline{f}}}{A_f}\right| \neq 1. \tag{1.42}$$

In this type of CP violation no $B^0\overline{B}^0$ mixing is involved and it can occur in both neutral and charged B meson decays. The CP asymmetry

$$\mathcal{A}_{CP} \propto \frac{1-|\overline{A}_{\overline{f}}/A_f|^2}{1+|\overline{A}_{\overline{f}}/A_f|^2}, \tag{1.43}$$

from which then follows

$$\mathcal{A}_{CP} \neq 0. \tag{1.44}$$

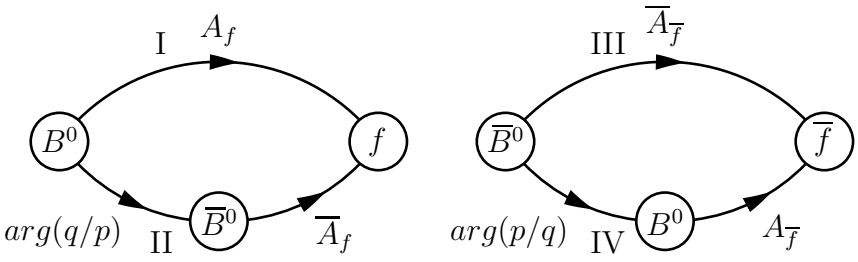

Figure 1.4: Four decay paths are illustrated. The B^0 meson can (I) directly decay to final state f, or (II) first oscillate to a $\overline{B}^0$ and then decay to the same final state. For $\overline{B}^0$ the analog paths are shown in (III) and (IV).

An example of direct *CP* violation is the decay $B^0 \to K^+\pi^-$, which has a measured asymmetry of -0.133 ± 0.030 (stat) ± 0.009 (sys) [15].

The interpretation of the experimental results in terms of CKM matrix elements is not straightforward. The asymmetry also depends on the strong phases and the uncertainty that follows from the calculation of these phases is dominant. One should note that the uncertainties do not apply to the observation of direct *CP* violation itself as the strong interactions are invariant under *CP* transformations.

CP violation in mixing

CP violation in mixing is also referred to as indirect *CP* violation. In Eq. (1.26) and (1.27), m_H, m_L, Γ_H and Γ_L are in principal all complex numbers. If the interference between the heavy and light mass states give rise to an overall phase difference ($|q/p| \neq 1$), the probabilities of the oscillations of $B^0 \to \overline{B}^0$ are different from $\overline{B}^0 \to B^0$.

CP violation in mixing is studied in semi-leptonic decays by measuring

$$\mathcal{A}_{CP} = \frac{\Gamma(B^0_{phys}(t) \to l^-\overline{\nu}_l X) - \Gamma(\overline{B}^0_{phys}(t) \to l^+\nu_l X)}{\Gamma(B^0_{phys}(t) \to l^-\overline{\nu}_l X) + \Gamma(\overline{B}^0_{phys}(t) \to l^+\nu_l X)} = \frac{1 - |q/p|^4}{1 + |q/p|^4}. \tag{1.45}$$

The *CP* asymmetry is expected to be small, at the order of $\mathcal{O}(10^{-2})$, and to date has not been observed.

CP violation in interference between mixing and decay

The third type of *CP* violation, relevant to the $B^0 \to D^{(*)-}a_0^+$ decay, occurs via quantum-mechanical interference between two possible amplitudes for the same physical process. Consider the final state f accessible to both B^0 and $\overline{B}^0$. Mixing now occurs between the decay paths $B^0 \to f$ and $B^0 \to \overline{B}^0 \to f$. This is illustrated in Fig. 1.4.

The final state f can be a *CP* eigenstate, $f = \pm\overline{f}$ (*e.g.* $B_d \to J/\psi K^0_S$). In this case the difference between the decay paths I and II in Fig. 1.4 comes solely from q/p that comes from the $B^0\overline{B}^0$ oscillations.

The case of a non-*CP* final state is worked out in Sect. 1.5.

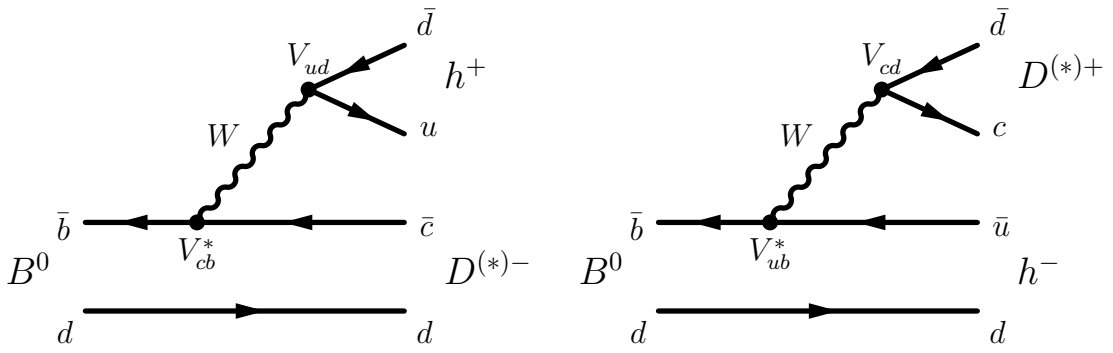

Figure 1.5: The CKM favored (*left*) and doubly CKM suppressed amplitude (*right*) for the decays $B^0 \to D^{(*)\pm}h^{\mp}$.

1.5 The CKM-angle γ

One way of measuring the angle γ is through the decay of $B^0 \to D^{(*)+}h^-$, where h^- is a meson containing a u and d quark, such as π^-, ρ^- or a_0^-[2].

The final states $D^{(*)+}h^-$ and $D^{(*)-}h^+$ are accessible for both B^0 and $\overline{B}^0$ states. The leading Feynman diagrams for the B^0 decay are shown in Fig. 1.5.

1.5.1 Time dependent *CP* asymmetry of $B^0 \to D^{(*)+}h^-$

From Eq. (1.41) we write the proper-time distributions for $\overset{(-)}{B}{}^0 \to D^{(*)\pm}h^{\mp}$

$$\begin{aligned}
R(B^0(\Delta t) \to D^{(*)-}h^+) &= Ne^{-|\Delta t|/\tau_{B^0}}\left(1 + C\cos(\Delta m_d \Delta t) + (-1)^L S_+ \sin(\Delta m_d \Delta t)\right), \\
R(\overline{B}^0(\Delta t) \to D^{(*)-}h^+) &= Ne^{-|\Delta t|/\tau_{B^0}}\left(1 - C\cos(\Delta m_d \Delta t) - (-1)^L S_+ \sin(\Delta m_d \Delta t)\right), \\
R(\overline{B}^0(\Delta t) \to D^{(*)+}h^-) &= Ne^{-|\Delta t|/\tau_{B^0}}\left(1 + C\cos(\Delta m_d \Delta t) - (-1)^L S_- \sin(\Delta m_d \Delta t)\right), \\
R(B^0(\Delta t) \to D^{(*)+}h^-) &= Ne^{-|\Delta t|/\tau_{B^0}}\left(1 - C\cos(\Delta m_d \Delta t) + (-1)^L S_- \sin(\Delta m_d \Delta t)\right),
\end{aligned} \tag{1.46}$$

where we neglect the decay width difference, τ_B^0 is the B^0 lifetime, and L is the angular momentum of the decay. The cosine terms come from interference between an even number (or direct decay) and odd number of $B^0\overline{B}^0$ oscillations. The S and C terms are

$$S_\pm = -\frac{2\mathcal{I}m(\lambda_\pm)}{1 + |\lambda_\pm|}^2, \quad \text{and } C = \frac{1 - r_\pm^2}{1 + r_\pm^2}, \tag{1.47}$$

with

$$r_+ \equiv |\lambda_+|, \qquad r_- \equiv |\lambda_-|, \tag{1.48}$$

and

$$\lambda_\pm \equiv \lambda[D^{(*)\pm}h^{\mp}] \equiv \frac{q}{p}\frac{A(\overline{B}^0 \to D^{(*)\mp}h^{\pm})}{A(B^0 \to D^{(*)\mp}h^{\pm})}. \tag{1.49}$$

[2]Throughout this thesis a_0 will refer to the $a_0^{\pm}$ (980) meson.

Assuming no CP violation in mixing ($|q/p| = 1$), as is expected in the Standard Model, a good approximation is given by

$$\frac{q}{p} = \frac{V_{tb}^* V_{td}}{V_{tb} V_{td}^*} = e^{-i2\beta}, \tag{1.50}$$

using phase convention defined by the Wolfenstein parametrization. For the final state $D^{(*)+}h^-$ the amplitude decay ratio is given by

$$\frac{A(\overline{B}^0 \to D^{(*)+}h^-)}{A(B^0 \to D^{(*)+}h^-)} = \frac{V_{cb}V_{ud}^*}{V_{cd}V_{ub}^*} \frac{\overline{M}(\overline{B}^0 \to D^{(*)+}h^-)}{M(B^0 \to D^{(*)+}h^-)}, \tag{1.51}$$

where $\overline{M}(\overline{B}^0 \to D^{(*)+}h^-)$ and $M(B^0 \to D^{(*)+}h^-)$ are hadronic decay amplitudes induced by strong interactions.

The combination of Eq. (1.50) and (1.51) and the angle definitions in Eq. (1.8) gives

$$\lambda_- = \lambda[D^+h^-] = e^{-i(2\beta+\gamma)} \left|\frac{V_{cb}V_{ud}^*}{V_{cd}V_{ub}^*}\right| \frac{\overline{M}(\overline{B}^0 \to D^{(*)+}h^-)}{M(B^0 \to D^{(*)+}h^-)}, \tag{1.52}$$

$$= e^{-i(2\beta+\gamma-\delta_{Dh})} \left|\frac{V_{cb}V_{ud}^*}{V_{cd}V_{ub}^*}\right| \left|\frac{\overline{M}(\overline{B}^0 \to D^{(*)+}h^-)}{M(B^0 \to D^{(*)+}h^-)}\right|, \tag{1.53}$$

where δ_{Dh} is the strong phase difference between $\overline{M}(\overline{B}^0 \to D^{(*)+}h^-)$ and $M(B^0 \to D^{(*)+}h^-)$. The case of the final state $D^{(*)-}h^+$ gives the ratio

$$\frac{A(\overline{B}^0 \to D^{(*)-}h^+)}{A(B^0 \to D^{(*)-}h^+)} = \frac{V_{ub}V_{cd}^*}{V_{ud}V_{cb}^*} \frac{\overline{M}(\overline{B}^0 \to D^{(*)-}h^+)}{M(B^0 \to D^{(*)-}h^+)}. \tag{1.54}$$

Conservation of CP in the strong interactions guarantees $\overline{M}_f = M_{\overline{f}}$ and $\overline{M}_{\overline{f}} = M_f$ so we can write

$$\lambda_+ = \lambda[D^-h^+] = e^{-i(2\beta+\gamma+\delta_{Dh})} \left|\frac{V_{ub}V_{cd}^*}{V_{ud}V_{cb}^*}\right| \left|\frac{M(B^0 \to D^{(*)+}h^-)}{\overline{M}(\overline{B}^0 \to D^{(*)+}h^-)}\right|. \tag{1.55}$$

From this we can see that $|\lambda_+| = |1/\lambda_-|$ and $r_+ = r_- \equiv r$. The difference between $D^{*\pm}h^\mp$ and $D^\pm h^\mp$ final states is only found in the hadronic matrix elements.

We can now rewrite Eq. (1.47)

$$S_\pm = \frac{2r}{1+r^2}\sin(2\beta+\gamma\pm\delta), \text{ and } C = \frac{1-r^2}{1+r^2}, \tag{1.56}$$

and use this in Eq. (1.46) to get the CP asymmetry

$$\mathcal{A}_{CP}(\Delta t) = \frac{F_{B_{tag}=B^0} - F_{B_{tag}=\overline{B}^0}}{F_{B_{tag}=B^0} + F_{B_{tag}=\overline{B}^0}} \tag{1.57}$$

$$= \frac{2r}{1+r^2}\sin(2\beta+\gamma)\cos(\delta)\sin(\Delta m_d \Delta t). \tag{1.58}$$

Here we have absorbed the factor $(-1)^L$ in Eq. (1.46) in the strong phase by changing $\delta \to \delta + \pi$ as was first suggested by [16].

From this we conclude that the time evolution of $B^0 \to D^{(*)\pm}h^{\mp}$ is sensitive to the *CP* angle γ. The asymmetry amplitude scales with the dominating CKM terms $|V_{ub}V_{cd}^*/V_{ud}V_{cb}^*|$ and the hadronic matrix element term $|M(B^0 \to D^{(*)+}h^-)/\overline{M}(\overline{B}^0 \to D^{(*)+}h^-)|$, as can be seen from Eq. (1.55). The hadronic term depends on the light unflavored charged meson that is substituted for $h^{\pm}$, while the CKM term does not depend on this.

1.5.2 Large asymmetries versus large statistics

From Eqs. (1.48) and (1.55) we write the asymmetry amplitude for the decay

$$r = \underbrace{\left|\frac{V_{ub}V_{cd}^*}{V_{ud}V_{cb}^*}\right|}_{r_{CKM}} \cdot \underbrace{\left|\frac{M(B^0 \to D^{(*)+}h^-)}{\overline{M}(\overline{B}^0 \to D^{(*)+}h^-)}\right|}_{r_M}. \tag{1.59}$$

From Eq. (1.9) we find that r_{CKM} is in the order of $2.0 \cdot 10^{-2}$. If now r_M is large, this compensates the r_{CKM} term and the sensitivity to the asymmetry would still be large. However, this implies that the CKM-allowed diagram in Fig. 1.5 is just as *small* as the CKM-suppressed diagram. Hence, there will be less events in the sample but with a larger asymmetry amplitude.

To understand the cost versus the benefit, we investigate the statistical error on the asymmetry $\mathcal{A}$. By using the standard error propagation

$$\sigma_{\mathcal{A}}^2 = \left(\frac{\partial \mathcal{A}}{\partial F_{B_{tag=B^0}}}\sigma_{F_{B_{tag=B^0}}}\right)^2 + \left(\frac{\partial \mathcal{A}}{\partial F_{B_{tag=\overline{B}^0}}}\sigma_{F_{B_{tag=\overline{B}^0}}}\right)^2 \tag{1.60}$$

on Eq. (1.57) and $F_{B_{tag=B^0}} + F_{B_{tag=\overline{B}^0}} \equiv N$, we find

$$\frac{\sigma_{\mathcal{A}}}{\mathcal{A}} = \sqrt{\frac{1-\mathcal{A}^2}{\mathcal{A}^2 N}} \tag{1.61}$$

where N is the number of B events in the analysis sample. We can see however that the quadratic sensitivity of the asymmetry measurement depends linearly on the decay rate but quadratically on the asymmetry amplitude, which makes the latter a more important contribution.

1.5.3 Asymmetry sensitivity for different $h^{\pm}$ mesons

Now that we understand the importance of a large asymmetry amplitude we have a look on what to expect from the hadronic contribution r_M.

In a naive approach we can calculate $M(B \to D^{(*)\pm}h^{\mp})$ by simply assuming that the CKM favored diagrams, see Fig. 1.5, can be expressed as [13]

$$M(B^0 \to D^{(*)-}h^+) \sim \langle h^+|\mathcal{H}_W|0\rangle\langle D^{(*)-}|\mathcal{H}_W|B^0\rangle, \tag{1.62}$$

$$\overline{M}(\overline{B}^0 \to D^{(*)+}h^-) \sim \langle h^-|\mathcal{H}_W|0\rangle\langle D^{(*)+}|\mathcal{H}_W|\overline{B}^0\rangle, \tag{1.63}$$

meson X:	$D^{(*)}$	D_s	π	ρ	$a_0(980)$	$a_1(1260)$
f_X [MeV]	200-230	294	131	210	~ 1.6	238

Table 1.2: Weak decay constants for different mesons taken from [9, 20, 21, 17, 22].

decay	value	decay	value
$F_0^{B\to\pi}(m_D^2)$	0.28	$A_0^{B\to D^*}(m_\pi^2)$	0.68
$F_1^{B\to\pi}(m_{D^*}^2)$	0.33	$A_0^{B\to\rho}(m_D^2)$	0.33
$F_0^{B\to D}(m_\pi^2)$	0.67	$A_1^{B\to\rho}(m_{D^*}^2)$	0.25

Table 1.3: Form factors for different B decays taken from [20].

and the CKM suppressed diagrams

$$M(B^0 \to D^{(*)+}h^-) \sim \langle D^{(*)+}|\mathcal{H}_W|0\rangle\langle h^-|\mathcal{H}_W|B^0\rangle, \quad (1.64)$$
$$\overline{M}(\overline{B}^0 \to D^{(*)-}h^+) \sim \langle D^{(*)-}|\mathcal{H}_W|0\rangle\langle h^+|\mathcal{H}_W|\overline{B}^0\rangle. \quad (1.65)$$

This approach is called conventional, or naive, factorization because it divides the Feynman diagram in two parts that are separated by the weak current. (The principles of factorization will be introduced in Sect. 1.7.) The hadronization part in the upper vertex $\langle X|\mathcal{H}_W|0\rangle$ is related to the weak decay constant, f_X, that can be calculated or measured in lepton decays where $l \to X\nu$. The B decay $\langle Y|\mathcal{H}_W|B^0\rangle$ depends on the form factor $F(q^2)^{B\to Y}$ and can be extracted from semi-leptonic decays or other B decays where the Y meson cannot be produced in the upper vertex.

Table 1.2 presents the decay constants for different mesons. The decay constant for the a_0 meson, f_{a_0} has been calculated using finite energy sum rules by Maltman [17] and Narrison [18]. All other decay constants have been confirmed by experiments. In general theoretical predictions of the decay constants have agreed well with the measurements, see for example Ref. [19].

Table 1.3 summarizes the different form factors that contribute to $\langle Y|\mathcal{H}_W|B\rangle$. Very little is known about the form factors $F_1(0)^{B\to a_0(980)}$. An estimate has been made by Chernyak [23] $F_1(0)^{B\to a_0(1450)} \simeq 0.46$ using light-cone sum rules. This result is only slightly larger then $F_0^{B\to\pi} \simeq 0.3$. A qualitative argument by Diehl and Hiller [24], based on the work of Wirbel, Stech and Bauer [25], explains that the ratio of $F^{B\to a_0(980)}/F^{B\to\pi}$ should be larger than one.

If we now look at both the decay constants and the form factors we conclude that the form factors are all of the same order of magnitude while the decay constant of the a_0 is about 2 orders of magnitude smaller compared to the other mesons in Table 1.2. The coupling of the a_0 to the weak current is heavily suppressed by two mechanisms, G parity and CVC suppression, which will be explained in Sect. 1.6.

First we focus on Eq. (1.59). We concluded earlier that $r_{CKM} \approx 2 \cdot 10^{-2}$. To increase the amplitude asymmetry r, r_M needs to be large. The hadronic asymmetry amplitude

scales as

$$r_M = \left|\frac{M(B^0 \to D^{(*)+}h^-)}{\overline{M}(\overline{B}^0 \to D^{(*)+}h^-)}\right| \approx \frac{\langle D^{(*)+}|\mathcal{H}_W|0\rangle\langle h^-|\mathcal{H}_W|B^0\rangle}{\langle h^-|\mathcal{H}_W|0\rangle\langle D^{(*)+}|\mathcal{H}_W|\overline{B}^0\rangle} \approx \frac{f_{D^{(*)}}}{f_h}\frac{F_{0/1}^{B\to h}(m^2_{D/D^*})}{F_{0/1}^{B\to D}(m_h^2)}. \tag{1.66}$$

Now assuming that

$$\frac{F_{0/1}^{B\to h}(m^2_{D/D^*})}{F_{0/1}^{B\to D}(m_h^2)} \approx \mathcal{O}(1), \tag{1.67}$$

which we conclude from the earlier discussion, we see that

$$r_M \propto \frac{f_{D^{(*)}}}{f_h}. \tag{1.68}$$

If we compare the decay constants of the different options for $h^\pm$ to that of the $D^{(*)\pm}$ meson we see that for the π and ρ mesons r_M is in the order of one while for the a_0 meson r_M is about 10^2. The large hadronic amplitude asymmetry for the a_0 compensates the small r_{CKM} and leads to an asymmetry amplitude $\mathcal{A}$ close to the maximum of one.

1.5.4 $B^0 \to D^{(*)-}a_0^+$ motivation

We conclude that the $B^0 \to D^{(*)-}a_0^+$ decay has an advantage over the $B^0 \to D^{(*)-}\pi$ or $B^0 \to D^{(*)-}\rho$ decays for the measurement of the angle γ because the asymmetry amplitude is enhanced by a factor of $\mathcal{O}(100)$. At the same time the production of the $B^0 \to D^{(*)-}a_0^+$ decay will be at a lower rate as both the contributing diagrams are suppressed. From Eq. (1.61) we can see however that the quadratic sensitivity of the asymmetry measurement depends linearly on the decay rate but quadratically on the asymmetry amplitude. As is already concluded earlier, this makes the latter a more important contribution.

There is only one problem at the horizon. The predicted branching ratios of the $B^0 \to D^{(*)-}a_0^+$ decays are very small, since both contributing diagrams are small. A too small branching ratio makes the extraction of γ in a time-dependent analysis impossible. In section Sect. 1.7 we continue the discussion on the branching ratio predictions and their uncertainties for this channel.

1.6 Electroweak a_0 coupling suppressions

In conventional factorization the pair of quarks hadronizes independently of the rest of the B decay. This implies that there is no final-state interaction (or rescattering) between the hadrons coming from the W and the other hadrons of the final state. Under this assumption the hadron production, resulting from the coupling of the quarks to the virtual W boson, follows the production rules (the same rules as in semi-leptonic τ decays [26]) that will be discussed in this section.

The structure of the vector and axial-vector hadronic currents, consistent with Lorentz invariance, has the general form [27]

$$V_\mu = \bar{u}(p')\left[g_V(q^2)\gamma_\mu + g_M(q^2)\sigma_{\mu\nu}q_\nu + ig_S(q^2)q_\mu\right]v(p), \tag{1.69}$$
$$A_\mu = \bar{u}(p')\left[g_A(q^2)\gamma_\mu\gamma_5 + g_T(q^2)\sigma_{\mu\nu}\gamma_5 q_\nu + ig_P(q^2)q_\mu\gamma_5\right]v(p), \tag{1.70}$$

where $q_\mu = (p + p')_\mu$ is the four-momentum transfer. The form factors g_i ($i = V$, A, M, S, T, P) are functions of the Lorentz scalar q^2. The values of these form factors in the limit of zero momentum transfer, $q^2 \to 0$, are called the vector, axial vector, weak magnetism, induced scalar, induced tensor, and induced pseudo-scalar couplings respectively. In particular $g_V = g_V(0)$ and $g_A = g_A(0)$ are the leading terms in V and A whereas the other terms are the induced weak currents.

Light unflavored charged mesons couple to either the vector term or the axial-vector term as is dictated by their spin-parity state. 'Natural' spin-parity $(0^+, 1^-, ...)$ states couple to the vector term, Eq. (1.69), and 'unnatural' spin-parity $(0^-, 1^+, ...)$ states to the axial term, Eq. (1.70).

Now we first investigate the differences between a vector and an axial-vector weak coupling.

1.6.1 Conserved vector and partial-conserved axial currents

The vector part of the Lagrangian Eq. (1.69) has many similarities with the electromagnetic current. In analogy to the electromagnetic interactions we can show that the vector current is (almost) conserved. Taking the divergence of the leading term (any term that contains only γ_μ would do) in Eq. (1.69)

$$\begin{aligned}
\partial^\mu V_\mu &= \partial^\mu(\psi_{\bar{u}}\, g_V\, \gamma_\mu\, \psi_v{}') && (1.71)\\
&= (\partial^\mu\psi_{\bar{u}})\, g_V\, \gamma_\mu\, \psi_v{}' + \psi_{\bar{u}}\, g_V\, \gamma_\mu(\partial^\mu\psi_v{}') && (1.72)\\
&= -i\, m_{\bar{u}}\, \psi_{\bar{u}}\, g_V\, \psi_v{}' + i\, \psi_{\bar{u}}\, g_V\, m_v\, \psi_v{}' && (1.73)\\
&= i\, g_V\, \psi_{\bar{u}}(m_v - m_{\bar{u}})\, \psi_v{}'. && (1.74)
\end{aligned}$$

The Dirac equation, $(i\gamma_\mu\partial^\mu - m)\psi_v = 0$, has been used to deduce Eq. (1.73) from Eq. (1.72). Now we see that the conserved vector current (CVC) is broken by the mass difference of the quarks that are involved. In the case of the a_0 coupling the CVC is only broken by the (small!) mass difference of the u and d quarks. In other words, the vector current is conserved up to isospin corrections.

Similarly we investigate the axial-vector current in Eq. (1.70)

$$\begin{aligned}
\partial^\mu A_\mu &= \partial^\mu(\psi_{\bar{u}}\, g_A\, \gamma_\mu\, \gamma^5\, \psi_v{}') && (1.75)\\
&= (\partial^\mu\psi_{\bar{u}})\, g_A\, \gamma_\mu\, \gamma^5\, \psi_v{}' + \psi_{\bar{u}}\, g_A\, \gamma_\mu\, \gamma^5(\partial^\mu\psi_v{}') && (1.76)\\
&= -i\, m_{\bar{u}}\, \psi_{\bar{u}}\, g_A\, \gamma^5\, \psi_v{}' - i\, \psi_{\bar{u}}\, g_A\, m_u\, \gamma^5\, \psi_v{}', \qquad (\gamma_\mu\gamma^5 = -\gamma^5\gamma_\mu) && (1.77)\\
&= -i\, g_A\, (m_v + m_{\bar{u}})\, \psi_{\bar{u}}\, \gamma^5\, \psi_v{}'. && (1.78)
\end{aligned}$$

This current is called the partially conserved axial current ($PCAC$) since it is only broken by the masses of the involved quarks but still very small for interactions with u and d quarks due to their small masses.

Due to the CVC and PCAC mechanisms, light unflavored charged mesons that couple to the vector current, natural states such as the a_0 meson, are suppressed compared with the mesons that couple to the axial current, unnatural states.

1.6.2 G parity and second-class currents

Further suppression of the a_0 weak coupling arise from G parity.

The study of the symmetries of the induced weak interaction currents has introduced the concept of G parity. The G parity operator is defined as the combination of a charge conjugation transformation and a rotation through an angle π in isospin space [28]

$$G \equiv Ce^{i\pi I_2}. \tag{1.79}$$

This transformation is a symmetry of the strong interaction [28]. It is interesting to study the properties of the terms in the vector current, Eq. (1.69), and the axial current, Eq. (1.70), under G to determine, at least at the phenomenological level, whether all terms are allowed under G parity conservation. Already fifty years ago Weinberg [29] classified the currents in two parts: vector currents with G parity $+1$ and axial currents with G parity -1 are called first-class currents (FCC) and the opposite combinations are called second-class currents (SCC). The first-class currents contains the vector, g_V, and weak-magnetism, g_M, form-factors in Eq. (1.69) and the axial, g_A, and induced pseudo-scalar, g_P, form factors in Eq. (1.70). The induced scalar, g_S, in Eq. (1.69) and induced tensor, g_T, in Eq. (1.70) belong to the second-class currents.

The requirement that V and A currents have definite G parity appears in the elaboration of a unified electroweak theory by Feynman and Gell-Mann [30] that was based on the work of Sudarshan and Marshak [31]. This requirement implies that either FCC or SCC can exist. The existence of FCC is ensured by the measurement of the large vector, g_V, and axial-vector, g_A, form vectors. Hence it follows that the SCC should not exist and $g_S(q^2) = 0$ and $g_T(q^2) = 0$.

According to this theory a virtual W boson that produces a $u\overline{d}$ state can produce even G parity natural spin-parity states or odd G parity unnatural spin-parity states.

In Table 1.4 a summary of the quantum numbers and weak decay constants are given for several mesons. The combination of G parity and spin-state gives the classification for first or second-class current. It is apparent from the table that indeed the second-class W decay constants for the b_1 and the a_1 mesons are suppressed. The effect of G parity suppression is most apparent in the large difference between the W coupling strength of the $a_1^{\pm}$ and $b_1^{\pm}$ mesons.

In summary the coupling strength of the a_0 meson to the weak current is doubly suppressed. The first suppression mechanism is via G-parity, or second-class current suppression, and the second mechanism is due to the conserved vector current in the weak interaction.

Experimental limits on second-class currents

A limit on the existence of second-class currents, or breaking of G parity, has been set by different experiments in both lepton decays and nuclear decays.

X	$\pi^{\pm}$	$a_1^{\pm}(1260)$	$b_1^{\pm}(1235)$	$a_0^{\pm}$ (980)	$\rho^{\pm}$	η
m_X[MeV]	139.6	1230	1229.5	984.7	775.5	547.5
G	$-$	$-$	$+$	$-$	$+$	$+$
J^P	0^-	1^+	1^+	0^+	1^-	0^-
weak coupling	A	A	A	V	V	n.a.
FCC or SCC	FCC	FCC	SCC	SCC	FCC	n.a.
f_X[MeV]	131	238[22]	∼0.6[22]	∼1.6	210	

Table 1.4: Summary of quantum numbers and decay constants for different mesons. For the charged mesons it is indicated to which part of the weak interaction the meson couples (natural states to the vector term and unnatural states to the axial term). From the combination with the G parity and the weak coupling it follows that the meson decays via a *first-class current* (FCC) or *second-class current* (SCC).

For example the leptonic decay, $\tau \to \nu_\tau \pi\eta$ is used for this purpose. The $\eta\pi$ system has parity [32]

$$P(\eta\pi) = P(\eta)P(\pi)(-1)^J = (-1)(-1)(-1)^J = (-1)^J, \tag{1.80}$$

and thus has the natural spin-parity $J^P = 0^+$ or 1^-. The G parity of the system is given by

$$G(\eta\pi) = G(\eta)G(\pi) = (+1)(-1) = -1. \tag{1.81}$$

The combination of the spin parity and the G parity makes it a second-class current. In 1987 a positive signal on the G-parity non-conserving [33] decay $\tau \to \nu_\tau \pi\eta$ was set by Derrick et. al. [32]. The anxiety that followed after the apparent observation of the existence of this second-class current lead to many other searches for this decay by other experiments, for example [34, 35], but the measurement could not be repeated. Later it was concluded that the signal found by [33] was more likely a statistical fluctuation or background feature [36]. The current limit on this decay is $1.4 \cdot 10^{-4}$ at 90% confidence limit (CL). The limit on $\tau \to \eta'(958)\pi\nu_\tau$ was recently set at $7.2 \cdot 10^{-6}$ at 90% CL by *BABAR* [37].

Excellent reviews of the second-class current searches can be found in Refs. [38, 39].

1.7 Factorization and $B^0 \to D^{(*)-} a_0^+$ production amplitude

In B decays a technique called factorization is used to estimate the size of the decay amplitude. In fact we have already used this technique in Sect. 1.5.3 to estimate the asymmetry amplitude for different B decays.

The factorization principle is based on the operator product expansion (OPE) formalism proposed by Wilson [40]. A weak meson decay amplitude A for a decay process

can be expressed as [41]

$$A = \langle \mathcal{H}_{eff} \rangle = \sum_i C_i(\mu, M_W) \langle O_i(\mu) \rangle. \tag{1.82}$$

The amplitude A is then factorized into the Wilson coefficient functions C_i and the matrix elements of local operators O_i. In this process the W boson and other fields with mass bigger than a factorization scale μ are integrated out. The effect of their existence is however implicitly taken into account in the Wilson coefficients. In a more intuitive interpretation one can view the expression $\sum C_i O_i$ as an effective Hamiltonian for the process considered, with O_i as the effective vertices and C_i the corresponding coupling constants.

The calculated physical parameter, in this case A, should not depend on the chosen artificial scale μ. However, most calculations do have some scale dependence because of the approximations made. In B physics the scale is usually chosen to the mass of the b quark ($\mu = m_b$) [42]. The uncertainty in the calculation is then typically estimated from the changes in the calculated quantity as the scale is varied from $m_b/2 < \mu < 2m_b$.

We now use the factorization principles to calculate the decay amplitude for the $B^0 \to D^{(*)-}a_0^+$ decay.

1.7.1 Matrix elements for hadronic two-body B decays

We follow the work of Diehl and Hiller [24] and present the low-energy (only taking into account g_V and g_A in Eqs. (1.69) and (1.70)) effective weak Hamiltonian that describes the hadronic two-body B decay

$$\mathcal{H}_{eff} = \frac{G_F}{\sqrt{2}} \left[\sum_{j,k=u,c} V_{jb} V_{kd}^* (C_1 O_1^{jk} + C_2 O_2^{jk}) - V_{tb} V_{td}^* \sum_i C_i O_i \right] + h.c., \tag{1.83}$$

where V_{xy} are the CKM matrix elements from Eq. (1.3), and C_i and O_i are the Wilson coefficients and local operators equivalent to Eq. (1.82). The first two operators O_1 and O_2 correspond to the tree level diagrams. The remaining operators are of the so-called penguin type and have no important contributions to the $B^0 \to D^{(*)-}a_0^+$ decay. The two operators that contribute are

$$O_1^{cu} = \bar{c}_\alpha \gamma^\mu (1-\gamma_5) b_\alpha \bar{d}_\beta \gamma_\mu (1-\gamma_5) u_\beta, \tag{1.84}$$

$$O_2^{cu} = \bar{c}_\alpha \gamma^\mu (1-\gamma_5) b_\beta \bar{d}_\beta \gamma_\mu (1-\gamma_5) u_\alpha, \tag{1.85}$$

where α and β are color indexes. In conventional factorization, the matrix element $\langle YX|\mathcal{H}_{eff}|B\rangle$ is written as the product of matrix elements corresponding to the B decay to Y, and the vacuum and X. By applying a Fierz transformation and keeping only color singlet contributions [43] the effective Hamiltonian $\mathcal{H}_{eff}$ is replaced by the effective transition operator $\mathcal{T}$

$$\langle D^{(*)} a_0 | \mathcal{H}_{eff} | B \rangle = \frac{G_F}{\sqrt{2}} \langle D^{(*)} a_0 | \mathcal{T} | B \rangle, \tag{1.86}$$

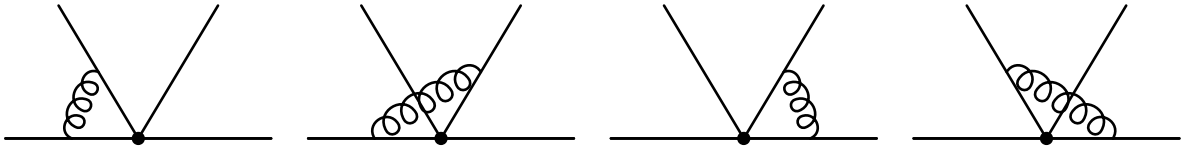

Figure 1.6: Order α_S vertex corrections. The two upward lines create the a_0 meson. The spectator quarks are not drawn.

where

$$\mathcal{T} = V_{cb}V_{ud}^* \left[a_1 \bar{c}\gamma^\mu(1-\gamma_5)b \otimes \bar{d}\gamma_\mu(1-\gamma_5)u + a_2 \bar{d}\gamma^\mu(1-\gamma_5)b \otimes \bar{c}\gamma_\mu(1-\gamma_5)u \right], \quad (1.87)$$

the $\otimes$ symbols indicate that the matrix elements are to be taken in factorized form ($\langle D^{(*)}a_0|j_1 \otimes j_2|B\rangle \equiv \langle D^{(*)}|j_1|B\rangle\langle a_0|j_2|0\rangle$). The coefficients a_1 and a_2 are related to the Wilson coefficients C_1 and C_2 at leading order by

$$a_1 = C_1 + \frac{1}{N_c}C_2 \text{ and} \quad (1.88)$$

$$a_2 = C_2 + \frac{1}{N_c}C_1, \quad (1.89)$$

where $N_c = 3$ is the number of colors[3]. The coefficient a_1 is color allowed and a_2 is color suppressed.

The Wilson coefficients C_i depend on the scale μ and on the strength of the strong coupling α_s. The coefficients at the b mass scale $\mu = m_b$ have been calculated to leading order to be $a_1 = 1.020$ and $a_2 = 0.140$ [44]. Eq. (1.86) now becomes

$$\langle D^{-(*)}a_0^+|\mathcal{H}_{eff}|B\rangle = \langle D^{-(*)}|\mathcal{H}_W|B\rangle\langle {a_0}^+|\mathcal{H}_W|0\rangle. \quad (1.90)$$

Note that the color suppressed part (term with a_2 in Eq. (1.87)) produces neutral $D^{0(*)}$ and a_0^0 mesons in the final state.

We have now derived the expression that factorizes the $B^0 \to D^{(*)-}a_0^+$ decay in two parts: the $B \to D$ decay and the a_0 produced via the weak interaction.

1.7.2 QCD factorization

Beneke, Buchalla, Neubert and Sachrajda showed [44] that for higher order in α_s the simple factorization as expressed in Eq. (1.87) is broken. Some 'non-factorizing' diagrams can be absorbed in correction terms that can be calculated. This can be expressed in the form

$$\langle D^{(*)}a_0|\mathcal{T}|B\rangle = \langle D^{(*)}|j_1|B\rangle\langle a_0|j_2|0\rangle \cdot \left[1 + \sum r_n \alpha_s^n + \mathcal{O}(\Lambda_{QCD}/m_b)\right]. \quad (1.91)$$

[3]Note that this definition of C_1 and C_2 follows the convention of [44] and differs from [43] where labels 1 and 2 have been interchanged.

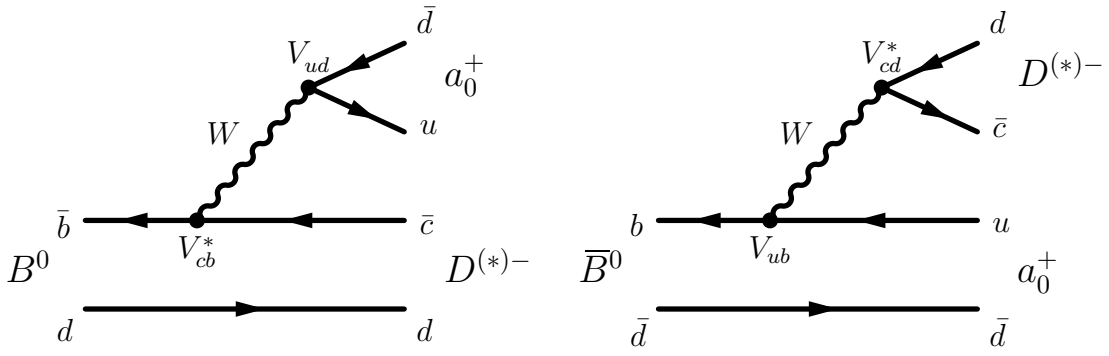

Figure 1.7: Feynman diagrams for the CKM favored B^0 decay (*left*) and doubly CKM suppressed $\overline{B}^0$ decay (*right*) to the final state $D^{(*)-}a^+$.

In this QCD factorization approach the 'non-factorizing' terms are separated into a soft part that is power suppressed and a hard part of order α_s [45]. The hard scattering diagrams relevant to the decay $B^0 \to D^{(*)-}a_0^+$ are calculable and are shown in Fig. 1.6 [46].

Following Ref. [44] a correction term is added to a_1 to include the diagrams from Fig. 1.6. The coefficient a_1 at next-to-leading order (NLO) read

$$a_1 = \underbrace{C_1 + \frac{1}{N_c} C_2}_{a_{fact}} + \underbrace{\frac{\alpha_s}{4\pi} \frac{C_F}{N} C_2 F}_{a_{cor}}, \tag{1.92}$$

where $C_F = (N_c^2 - 1)/(2N_c)$ and F is a function depending on a meson distribution amplitude $\varphi_X(u)$, where u is the momentum fraction that is carried by the quark in meson X, describing the transition from the $q\bar{q}$ pair to meson X. For details see Ref. [46]. For a non-suppressed weak decay constant the a_{cor} amounts to only a few percent of the leading order a_{fact} [24]. For suppressed decays, such as in the $B^0 \to D^{(*)-}a_0^+$ decay, the correction term can become visible. This is interesting because the dependence on the distribution amplitude $\varphi_X(u)$ and the scale factor μ, provide insight in the kinematical features of factorizing models [24].

1.7.3 Branching ratio of the CKM allowed decay

Diehl and Hiller [24] estimate the branching ratios for the decay $B^0 \to D^{(*)-}a_0^+$, using the hard-scattering correction terms, where the a_0 is produced in the upper vertex (left diagram in Fig. 1.7). The meson distribution amplitude $\varphi_{a_0}(u)$ is calculated using a so-called light-cone calculation method. Results of the calculations are summarized in Table 1.5. The prediction of the branching ratio using QCD factorization is about twice the predicted branching ratio calculated with the conventional factorization model. The prediction relies heavily on the choice of the scale factor μ.

decay mode	naive factorization	QCD factorization	
		$\mu = m_b$	$\mu = m_b/2$
$B^0 \to D^- a_0^+$	$1.1 \cdot 10^{-6}$	$2.0 \cdot 10^{-6}$	$4.0 \cdot 10^{-6}$
$B^0 \to D^{-*} a_0^+$	$1.0 \cdot 10^{-6}$	$1.8 \cdot 10^{-6}$	$3.7 \cdot 10^{-6}$

Table 1.5: Summary of predicted branching fractions for the CKM allowed decay.

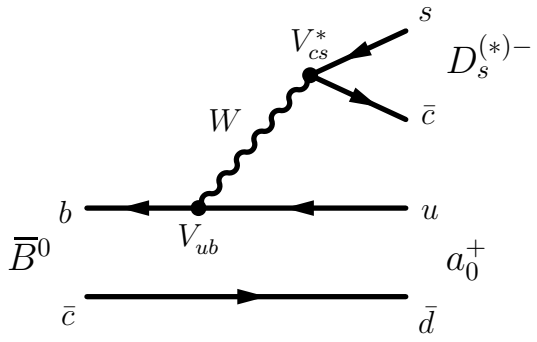

Figure 1.8: Feynman diagram for the $\overline{B}^0 \to D_s^{(*)-} a_0+$ decay.

Quark state nature of the a_0 meson

The meson distribution amplitude depends on the quark structure of the involved meson. In the calculations of Diehl and Hiller [24] the assumption was made that the a_0 meson consists of a u and a d quark. Arguments are made in the literature that the nature of the a_0 meson should be interpreted as a four-quark $q^2\bar{q}^2$ state [47]. For a discussion on this topic see Ref. [17]. We follow the arguments made by Cheng, Chua and Yang [48], and Diehl and Hiller [24], that if the observed branching ratio is much smaller than the predictions presented in Table 1.5 this could indicate the a_0 meson has a four-quark structure.

1.7.4 Branching ratio of the CKM suppressed decay

The branching ratio of the $B^0 \to D^{(*)-} a_0^+$ decay where the B meson decays directly in the a_0 meson (right diagram in Fig. 1.7) are calculated to be $\mathcal{B}(B^0 \to D^+ a_0^-) = 2.1 \cdot 10^{-6}$ and $\mathcal{B}(B^0 \to D^{*+} a_0^-) = 1.9 \cdot 10^{-6}$[24]. In this calculation only the conventional factorization contributions are calculated. QCD factorization corrections are hard to calculate for this diagram as simplifications based on the heavy-light decay structure cannot be made. However, the QCD factorization correction terms are expected to be small (in the order of a few percent) since the $D^{(*)\pm}$ decay is not suppressed and the naive weak decay constant is large, see also Table 1.2.

The form factor $F^{B \to a_0}$ has large uncertainties, see also the discussion on this in Sect. 1.5.3. If this form factor is much larger than expected, the contribution of the CKM suppressed diagram is much larger. In turn, this affects the measurement of the non-factorizing terms.

One way to verify the numerical assumptions and test the validity of the factorization approach is to measure the branching fractions for the SU(3) conjugated decay modes

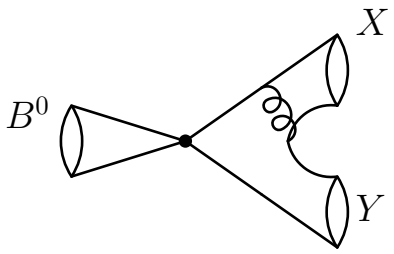

Figure 1.9: Non-factorizable annihilation diagram.

$B^0 \to D_s^{(*)+} a_0^-$. These decays can only occur via a single tree diagram presented in Fig. 1.8. We calculate the branching ratio for these decay using the predictions made by Diehl and Hiller [24] for the $B^0 \to D^{(*)-} a_0^+$ decays, and replacing the CKM elements V_{cd} by V_{sd} and form factors f_D by f_{D_s}. The predicted branching ratio is then $\sim 8 \cdot 10^{-5}$. Upper limits are set by the *BABAR* collaboration at 90% CL at $\mathcal{B}(B^0 \to D_s^+ a_0^-) < 1.9 \cdot 10^{-5}$ and $\mathcal{B}(B^0 \to D_s^{*+} a_0^-) < 3.6 \cdot 10^{-5}$[49]. The upper limit value for $B^0 \to D_s^{(*)+} a_0^-$ is lower than the theoretical expectation, indicating that the CKM suppressed contribution in the $B^0 \to D^{(*)-} a_0^+$ decay is lower than assumed.

In the $B^0 \to D^{(*)-} a_0^+$ decay, the conventional factorizing terms in both the CKM suppressed and allowed diagrams are small making it possible to measure the effects of higher-order factorizing terms. Also non-factorizing effects, that are not included in the correction term a_{cor} such as annihilation diagrams, see Fig. 1.9, can contribute to this decay mode [24].

1.8 Final-state interactions

In this section we evaluate the effects of final-state interactions (FSI) contributing to the $B^0 \to D^{(*)-} a_0^+$ decay amplitudes.

Rescattering effects are soft, long distance, strong interactions between final states. In non-leptonic two body B decays, rescattering effects occur between the weakly produced hadronic states. A schematic drawing of the decay $B \to M_1 M_2 \to M_3 M_4$, is presented in Fig. 1.10.

Rescattering can be categorized in two classes, elastic rescattering where the weakly produced mesons remain in the same isospin multiplet and inelastic rescattering where the produced mesons M_1 and M_2 exchange quantum numbers, such as spin, and rescatter to mesons M_3 and M_4.

One form of inelastic rescattering is when weakly produced vector-pseudoscalar (VP) state as for example $D^*\pi$ rescatter in the PV state $D\rho$ [50], other examples are $K^*\pi \leftrightarrow K\rho$ [25]. Note that in the rescattering processes the total angular momentum is conserved; the angular momentum J is transfered from one produced meson to the other. Under time invariance, the rescattering occurs in both directions equally. In a very similar way rescattering may occur in the process $Da_1 \leftrightarrow D^* a_0$.

Final-state interactions can modify the phase and magnitude of decay amplitudes.

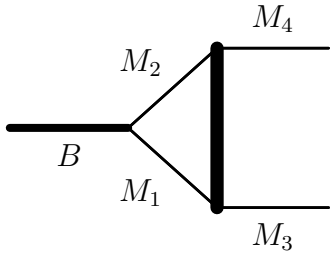

Figure 1.10: Schematic drawing of the weak decay $B \to M_1 M_2$ and the final-state rescattering of $M_1 M_2 \to M_3 M_4$.

Following Watson [51], and Nardulli and Pham [50] this is expressed as

$$A = \sqrt{S} A_b, \tag{1.93}$$

where A_b are the bare weak production amplitudes, S is the scattering matrix and A are the final amplitudes. The scattering effects are independent of the weak productions processes. Amplitudes, which are small before final-state interactions, can receive important contributions via rescattering with stronger coupled channels [25]. In the case of $Da_1 \leftrightarrow D^* a_0$ this means that although the rescattering effects of $Da_1 \to D^* a_0$ are as strong as the time reversed process $D^* a_0 \to Da_1$, the first process is expected to be larger since the bare weak production amplitude for $B^0 \to D^- a_1(1260)^+$ is about a thousand times larger than the predicted $B^0 \to D^{*-} a_0^+$ production.

A reliable way to compute soft non-perturbative effects, like inelastic rescattering, is missing at present. There are at current no theoretical predictions for the size of the inelastic rescattering effects in $Da_1 \leftrightarrow D^* a_0$. Instead we use the only quantitative calculation of inelastic rescattering performed by Nardulli and Pham [50] (for $D\rho \leftrightarrow D^*\pi$) and use this result directly with no alterations. This will by no means give a correct prediction to the size of the inelastic rescattering effects in $B^0 \to Da_1 \to D^* a_0$, but it is at present the only way to estimate the size of the rescattering effects.

We now express the decay amplitude $A_{(B \to Da_0)}$ including the final-state interaction effects as

$$A_{(B \to Da_0)} = A^{dir}(B \to D^* a_0) + A^{FSI}(B \to Da_1 \to D^* a_0), \tag{1.94}$$

where A^{dir} is the amplitude coming from the direct weak process $B^0 \to D^{*-} a_0^+$ and A^{FSI} is the rescattering amplitude. We estimate $A^{FSI}(B \to Da_1 \to D^* a_0)$ to be

$$A^{FSI}(B \to Da_1 \to D^* a_0) = \sqrt{S_{od}} \times A_b(B^0 \to Da_1), \tag{1.95}$$

where S_{od} is the off-diagonal term in the scattering matrix that is responsible for the inelastic rescattering. Using the measured branching ratio $\mathcal{B}(B^0 \to D^- a_1(1260)) = (6.0 \pm 3.3) \cdot 10^{-3}$ and the inelastic rescattering size in the order of 10^{-4} taken from [50], we derive a contribution from inelastic rescattering to the branching ratio of order 10^{-6}.

We can make a few qualitative arguments to why the inelastic rescattering effects should in fact be larger than this result. (A factor ten enhancement of the rescattering amplitude would lead to a contribution to the branching fraction of order 10^{-4}.)

The first difference between the two rescattering processes is the larger mass of the a_0 (985 MeV/c^2) and a_1 (1230 MeV/c^2) mesons compared to the π (140 MeV/c^2) and ρ (776 MeV/c^2) masses. Owing to this larger mass the mesons have more time to allow for final-state strong interactions as the momentum difference with the D-meson is smaller, see for example [52]. The chance for the final rescattering to occur will be larger.

Secondly, the mass *difference* between the a_0 and a_1 meson is much smaller than the mass difference between the π and ρ mesons. This means that less energy needs to be transfered between D^* and a_1, leading to a higher soft rescattering probability. Realize that for successful rescattering the energetically stable pion needs to be broken up to form a relatively heavy ρ meson. This requires a high energy transfer making rescattering more unlikely. The mass difference between the D^* and D meson is also relatively small $\sim 140\,\mathrm{MeV}/c^2$, so that the overlap with the ρ and π mesons is suppressed.

Third, although the same spin transfer is needed to occur between the produced mesons, the a_1 and a_0 mesons are members of the same quark spin triplet $(q\bar{q})_{(s=1,l=1)}$ whereas the spin of the $[\pi]$ ρ meson caused by the $[(q\bar{q})_{(s=0,l=0)}]$ $(q\bar{q})_{(s=1,l=0)}$ quark state. To alter the spin state of the a_1, so that it transforms into an a_0 meson state, only the projection of the internal angular momentum needs to be changed.

If we now compare the result obtained in this sections for the inelastic rescattering contribution to the predictions made by Diehl and Hiller for the bare electroweak decay amplitude, see Table 1.5, we must conclude that the contribution of final-state rescattering to the decay amplitude of $B^0 \to D^{*-} a_0^+$ is of the same order or may possibly even be larger.

The measurement of the CKM angle γ will not be compromised by the rescattering process. The channel $B^0 \to Da_1 \to D^* a_0$ contains the same weak angle, $sin(2\beta + \gamma)$ as the direct $B^0 \to D^{*-} a_0^+$ decay. However, the asymmetry amplitude r in $B^0 \to D^- a_1^+$ is different from the asymmetry amplitude in $B^0 \to D^{*-} a_0^+$. The decay constant for a a_1 meson, f_{a_1}, is of the same order as for a D^* meson, f_D^*, see Table 1.2. The CKM-allowed diagram is therefore not suppressed in the way it is suppressed for the $B^0 \to D^{*-} a_0^+$ decay. A measurement of the ratio r of the relative amplitude contributions will be needed in order to measure the CKM angle. This can be performed by measuring the cosine term in a time dependent analysis. More information about this technique can be found in [13]. The size of the inelastic rescattering, and thus of r, can also be determined by looking at the decay $B^0 \to D^* a_1 \to D a_2$. The amplitude of this channel should have the same size as the $B^0 \to Da_1 \to D^* a_0$ channel. The direct production of the CKM-allowed $B^0 \to Da_2$ is not possible since a tensor-meson cannot be produced in a weak B^0 decay, see also [24].

So far, we have discussed the possible final-state contributions to the decay $B^0 \to D^{*-} a_0^+$. Inelastic rescattering effects to the $D^+ a_0^-$ final state are even more complicated to estimate. A contributing channel could be through $B^0 \to D^* a_1 \to D a_0$, similar to rescattering in $K^*\rho \leftrightarrow K\pi$ described by Wirbel [25]. The branching ratio of the decay $B^0 \to D^* a_1$ is of the same order as $B^0 \to Da_1$, $(1.30 \pm 0.27) \cdot 10^{-2}$ versus $(6.0 \pm 3.3) \cdot 10^{-3}$. But the inelastic soft rescattering between $D^* a_1 \leftrightarrow D a_0$ is probably smaller than $Da_1 \leftrightarrow D^* a_0$. This is because only the zero angular momentum projection of the $D^* a_1$-meson pair can contribute to form a Da_0 meson pair. The contribution to the

amplitude in the $B^0 \to D^- a_0^+$ decay arising from soft inelastic rescattering is therefore expected to be smaller than the rescattering contribution in the $B^0 \to D^{*-} a_0^+$ decay amplitude.

1.9 Motivation summary

The interest in the $B^0 \to D^- a_0^+$ and $B^0 \to D^{*-} a_0^+$ decays is twofold.

We have argued that the $B^0 \to D^{(*)-} a_0^+$ decay mode has a potential high sensitivity to a measurement of the CKM angle γ in Sect. 1.5.3. In comparison to the decays $B^0 \to D^{*-}\pi^+$, $B^0 \to D^{*-} a_1(1260)^+$ and $B^0 \to D^{*-}\rho^+$ the sensitivity to γ could be enhanced by a factor hundred. The impact on the current status of the measurement on γ would be large. On the other hand the cost is that the $B^0 \to D^{(*)-} a_0^+$ decay rate is suppressed. The low statistics in the channel could severely impact the measurement, if the branching fraction of the $B^0 \to D^{(*)-} a_0^+$ decay is *too* low.

Theoretical predictions on the branching ratio of the $B^0 \to D^{(*)-} a_0^+$ decay show large QCD model dependent uncertainties. Non-factorizing terms that can be calculated by QCD factorizing models have a large impact on the branching fraction of this decay mode. Also non-factorizing inelastic soft rescattering effects can contribute to the branching ratio. A measurement or limit of the branching fraction will thus bring more insight into the theoretical models. In general a better understanding of the QCD models will be necessary to conduct weak interaction physics at the next level.

The decay amplitudes from both the CKM-allowed as the CKM suppressed diagrams are predicted in the order of 10^{-6} for the $B^0 \to D^- a_0^+$ and $B^0 \to D^{*-} a_0^+$ decay modes.

The predicted total branching ratio of the $B^0 \to D^- a_0^+$ decay mode is $3.2 \cdot 10^{-6}$ for naive factorization, and in the range $(4.1 - 6.1) \cdot 10^{-6}$ using QCD correction terms in the CKM allowed diagram.

For the $B^0 \to D^{*-} a_0^+$ decay mode this summarizes to $2.9 \cdot 10^{-6}$ for the naive factorization approach and in the range $(3.7 - 5.6) \cdot 10^{-6}$ using the QCD correction terms in the CKM allowed diagram.

A measurement of the branching ratio of the $B^0 \to D^{(*)-} a_0^+$ decay can give more insight into the factorization models and dependencies. And in addition, if the branching ratio of the decays is large enough, a very precise measurement of the CKM angle γ is possible.

1.10 Analysis Strategy

The analysis described in this thesis focuses on the measurement or exclusion of the $B^0 \to D^- a_0^+$ and $B^0 \to D^{*-} a_0^+$ decay modes where the a_0 is reconstructed in the $a_0^+ \to \eta\pi^+$ mode. Because of large uncertainties in the a_0 line width no selection restrictions can be placed on the a_0 meson mass. Instead we select the resonant $B^0 \to D^{(*)-} a_0^+$ events by a multi-dimensional fit, presented in Chapter 5, that follows the event selection. The non-resonant events are selected in the same fit and we profit from the analysis setup by performing the $B^0 \to D^{(*)-}\eta\pi^+$ branching ratio measurement at the same time.

1.11 Non-resonant $B^0 \to D^{(*)-}\eta\pi^+$ predictions

Non-resonant $B^0 \to D^{(*)-}\eta\pi^+$ events have so far not yet been observed. Theoretical predication on the branching ratio are not available either.

As for the $B^0 \to D^{(*)-}a_0^+$ decay, the diagram where the B decays into a $D^{(*)\pm}$ meson and the weak current couples to a $\eta\pi$ state is not allowed due to G-parity violation, as follows from arguments made in Sect. 1.6.2. Other diagrams can contribute. One example is a diagram where a pion is formed from the weak current and a $D^{(*)\pm}\eta$ meson is produced in the B^0 decay. Two other diagrams exist where the $D^{(*)\pm}$ meson is produced in the weak decay and creates a $\eta\pi^\pm$ meson pair in the B^0 decay. All these contributions are expected to be suppressed compared to the $B^0 \to D^{(*)-}a_0^+$ decay, because they require an additional quark pair created from the vacuum. Additionally, there are no known excited D^+ meson states that decay to a $D^{(*)+}\eta$ pair.

Experimental measurements from the similar non-resonant $B^0 \to D^{*-}\pi^+\pi^0$ decay also suggest this suppression. The branching ratio of the non-resonant $B^0 \to D^{*-}\pi^+\pi^0$ decay is suppressed compared to the resonant $B^0 \to D^{*-}\rho^+$ decay amplitude [53].

Chapter 2

The *BABAR* experiment

This analysis is performed on data collected by the *BABAR* experiment, located at the IR-2 interaction region of the PEP-II B Factory at the Stanford Linear Accelerator Center (SLAC) in Menlo Park, CA in the United States of America. The experiment has accumulated data between Oct 1999 and April 2008.

The PEP-II B Factory and the *BABAR* experiment, its detector components, the online data acquisition and trigger system, will be briefly described in this chapter. Detailed descriptions of the PEP-II B Factory and the *BABAR* detector can be found in respectively [54] and [55].

2.1 The *BABAR* detector

The *BABAR* detector is optimized to measure time-dependent *CP* violation in the B meson system. The B mesons are produced by the PEP-II B Factory, which is an e^+e^- collider. The energy of the electron (9.0 GeV) and positron (3.1 GeV) beams are tuned at the $\Upsilon(4S)$ resonance.

The $\Upsilon(4S)$ resonance lies just above the B meson pair production threshold and the operation at this resonance gives a high B meson production rate. In this production mechanism there is no room for fragmentation products and as a result the B meson pair is produced in a coherent quantum state. A measurement of time-dependent *CP* violation in the B system requires the (partial) reconstruction of both B mesons and of the lifetime difference of the B meson pair. It further uses the properties of the coherent B pair production.

A Lorentz boost of $\beta\gamma = 0.56$, that is the result of the energy difference given to the PEP-II beams, makes it possible to accurately measure the lifetime difference. The boost is optimized to the maximal separation of the B vertexes and the best vertex resolution. The average separation along the z-axis is $250\mu m$. A higher boost would give a larger vertex separation but would reduce the separation of particle trajectories, lowering opening angles, which results in a worse vertex resolution.

An asymmetric detector design maximizes the coverage in the (boosted) $\Upsilon(4S)$ frame. A longitudinal cross section of the *BABAR* detector is presented in Fig.2.1. Five sub-detectors form the *BABAR* detector and are situated in concentric cylinders around the

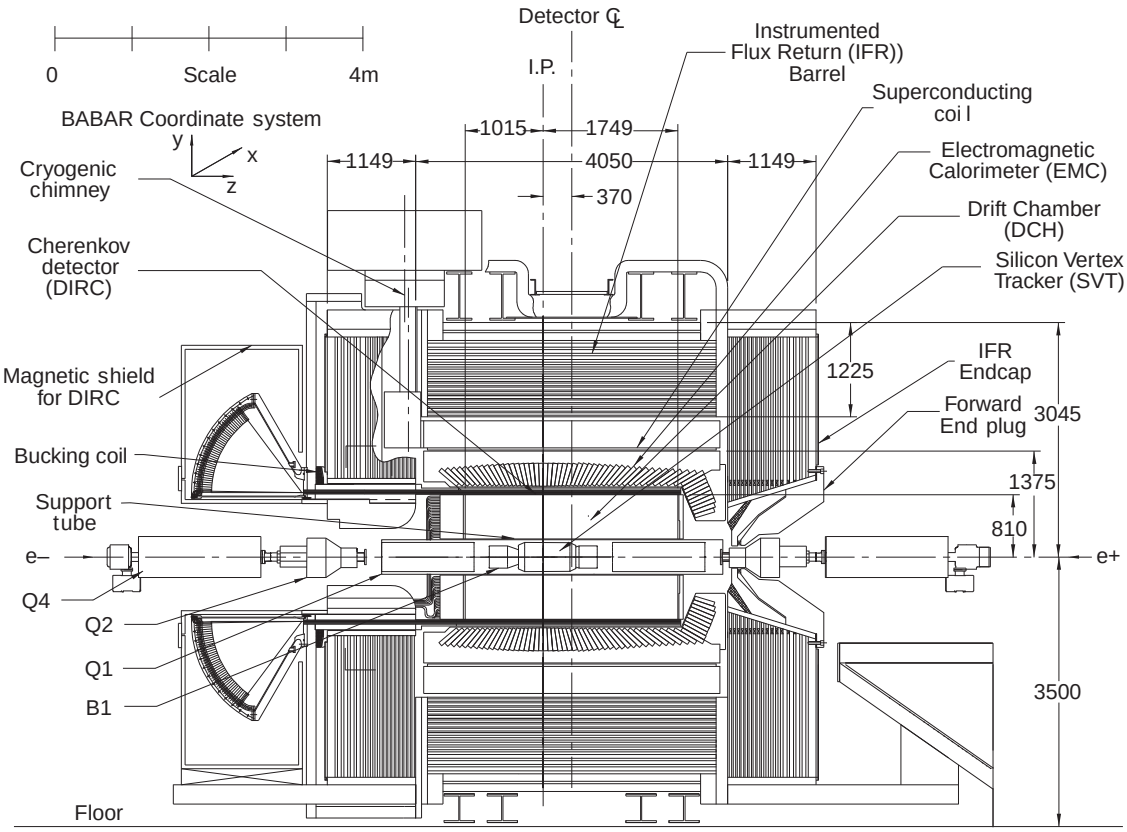

Figure 2.1: Longitudinal cross-section of the *BABAR* detector. The *BABAR* coordinate system is defined in the top of the figure.

interaction point. Inside a 1.5 Tesla superconducting solenoid sit the two tracking detectors, the silicon vertex tracker (SVT) and the drift chamber (DCH), the detector of internally reflected Čerenkov light (DIRC) specifically designed for charged hadron particle identification, and the cesium iodide electromagnetic calorimeter (EMC). The instrumented flux return (IFR) is build outside the magnetic coil and is designed to identify muons. The magnetic field in the *BABAR* detector is approximately homogeneous and aligned with the z-axis of the detector. An array of electronics provides the readout and monitoring of the detectors.

The *BABAR* detector and PEP-II interaction region layout are tightly connected. To achieve high luminosities, the beams are divided into closely spaced bunches with a 4.2 ns separation, which minimizes beam-beam interference. The beams are brought together just before the interaction point (IP) and separated immediately after, such that secondary collisions cannot occur. This is achieved by placing separation dipole magnets (B1), which horizontally displace the beams very close, at 21 cm, to the IP. The B1 magnets, as well as the Q1 quadrupole magnets are permanent magnets and are placed inside the magnetic field of the detector. Because of the close proximity to the IP the B1 magnet position limits the angular acceptance of the *BABAR* detector. The

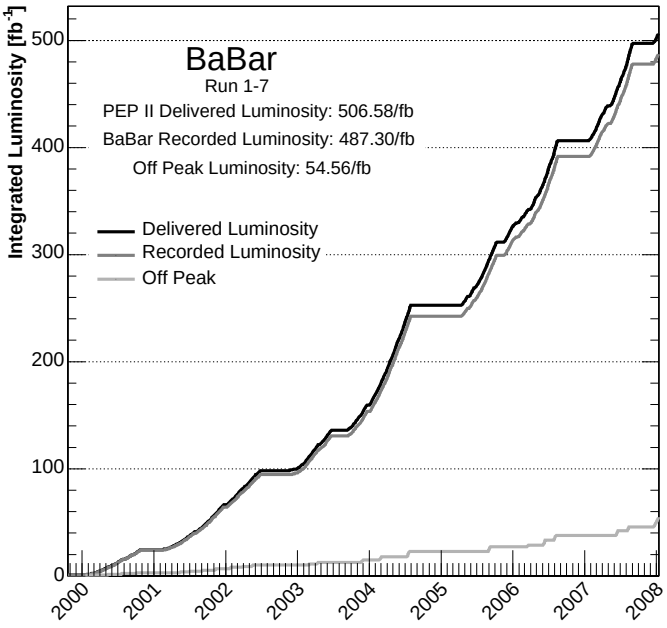

Figure 2.2: Integrated luminosity delivered by PEP-II and recorded by *BABAR* between October 1999 and December 2007.

SVT is build in between the B1 magnets and fixed to the relative movement of the B1 forward magnet.

The high luminosity produced by PEP-II and the efficient operation of both the collider and the detector makes the *BABAR* experiment also well suited to study rare B decays. The delivered and recorded luminosity are presented in Fig. 2.2.

2.2 Silicon vertex tracker (SVT)

The SVT is the inner of the two tracking detectors in *BABAR* and is crucial for the measurement of the B decay vertexes. The SVT is designed to measure both the direction and the position of charged particles close to the interaction point.

The average momentum of charged particles produced in B decays is less than 1 GeV/c, which makes multiple scattering a significant limitation on the track parameter resolution. Hence, the amount of material in the tracking system is reduced as much as possible.

The SVT consists of five layers of double sided silicon strip sensors organized in respectively 6, 6, 6, 16 and 18 modules per layer. The strips on the opposite sides of a sensor are oriented orthogonal to each other. Schematic overviews of the layers are presented in Fig. 2.3 and Fig. 2.4. The first layer is as close as 3.2 cm to the beam axis, while the outer layer is 14.0 cm away.

The first three layers are straight, positioned in a barrel geometry, and tilted by 5°

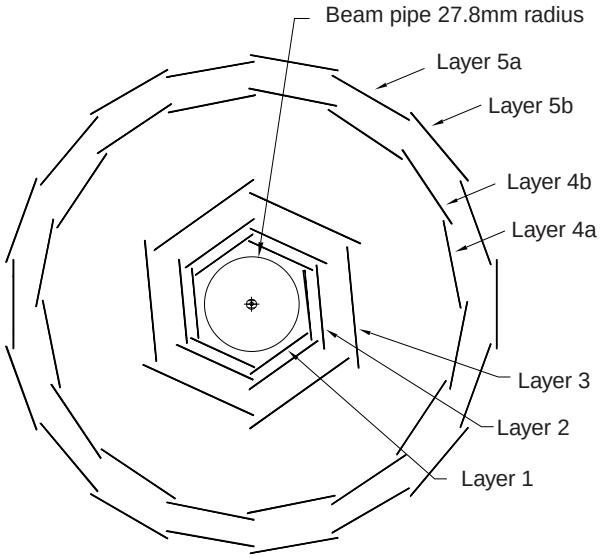

Figure 2.3: Transverse cross-section of the SVT and the beam-pipe.

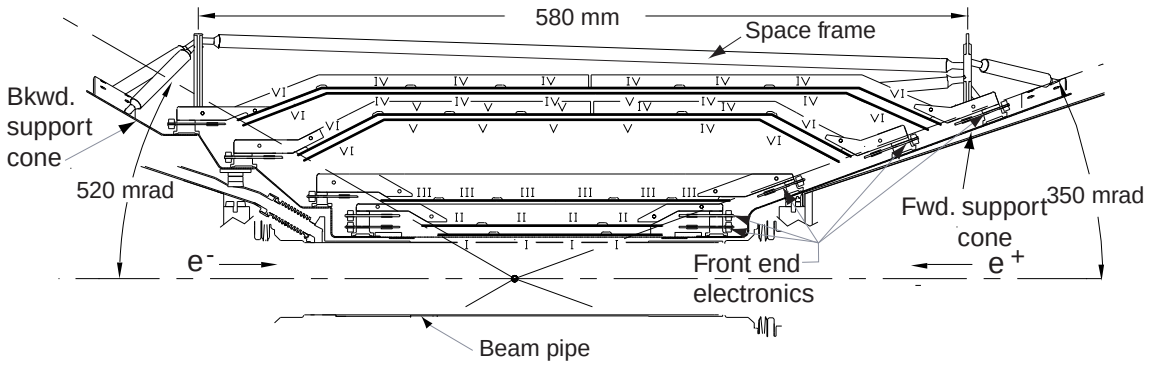

Figure 2.4: Orthogonal cross-section of the SVT and the beam-pipe.

in the transverse plane to allow an overlapping region with neighboring modules. The overlap is used for alignment of the detector. The inner three layers primarily provide position and angle information for the measurement of the vertex position. The outer two layers are arch shaped, see Fig. 2.4, and situated close to the DCH to provide the measurements needed to link the tracks reconstructed in the SVT and the DCH. This design is chosen to have the optimal measurement for particles with a large opening angle and the minimum needed silicon sensors to cover the solid angle. Because of the arch shape, the modules in the outer layers cannot be tilted to create a suitable overlap. To create an overlap region, the layers 4 and 5 are divided into two sub-layers (4a, 4b, 5a and 5b) with slightly different radii. In total about 150,000 channels are read out by front-end chips.

The SVT has a typical single-hit resolution of 10 μm and provides precise reconstruction of charged particle trajectories and decay vertexes of B and D mesons near the interaction region. It also provides stand alone tracking capability for charged parti-

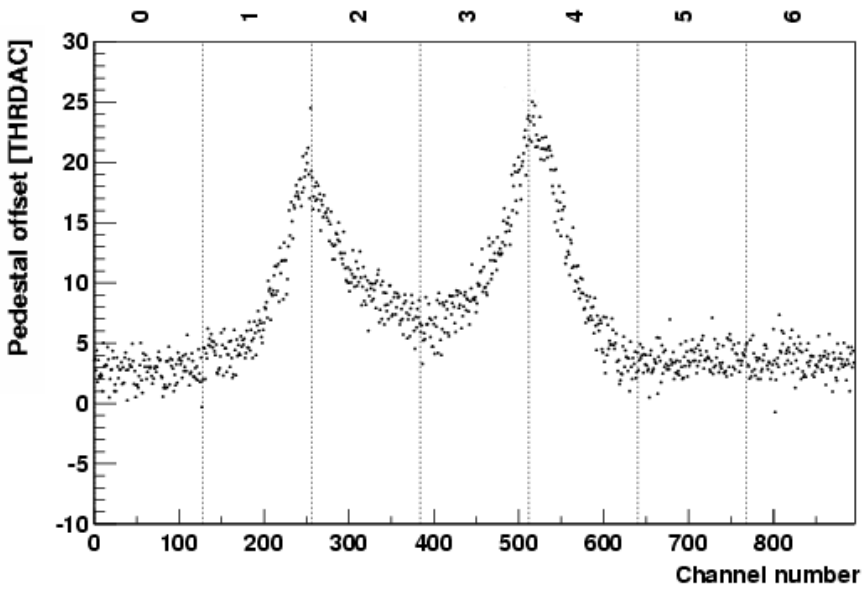

Figure 2.5: Pedestal offsets in the backward west module of the innermost layer, situated in the horizontal plane (ROS 134), measured on June 15, 2004 at an approximate integrated radiation dose of 3.3 MRad measured by the nearest PIN diode. The numbers on top of the plot indicate the chip number.

cles with a transverse momentum lower than 120 MeV/c as these particles do not reach the DCH.

The close proximity to the beam and the high luminosities delivered to the SVT cause relatively high radiation doses. The design of the AToM readout chip and of the silicon wafers was based on the expected 2 MRad radiation dose. After only 4 years of running parts of the detector already received more than that. The inner layers naturally absorb the highest dose and due to the design of the interaction region, the radiation is concentrated in a 1-cm wide band in the horizontal. The radiation in this area is caused by off beam particles which are over-bent by the permanent magnets placed at ± 20 cm from the IP to separate the two beams [56]. Away from the horizontal band, the radiation levels are up to a factor 10 lower at the same radius.

The radiation is monitored by a set of 12 reverse biased silicon pin diodes placed between the beam pipe and the innermost silicon layer, close to the AToM readout chips. Two polycrystalline chemical-vapor-deposition (pCVD) diamond sensor were placed close to PIN diodes, forward west and east in the horizontal plane, in 2003 [57] and have taken over the radiation dose measurements of the corresponding PIN diodes in 2005. The radiation is concentrated in the horizontal bending plane of the colliding beams with an average level in the range 30-50 mRad/s, this corresponds to an integrated dose of about 1.5 MRad (May 2003). The expectation for the whole life of the experiment was approximately 2 MRad.

After an accumulated dose of about 1 MRad, we measured an increase in the pedestal

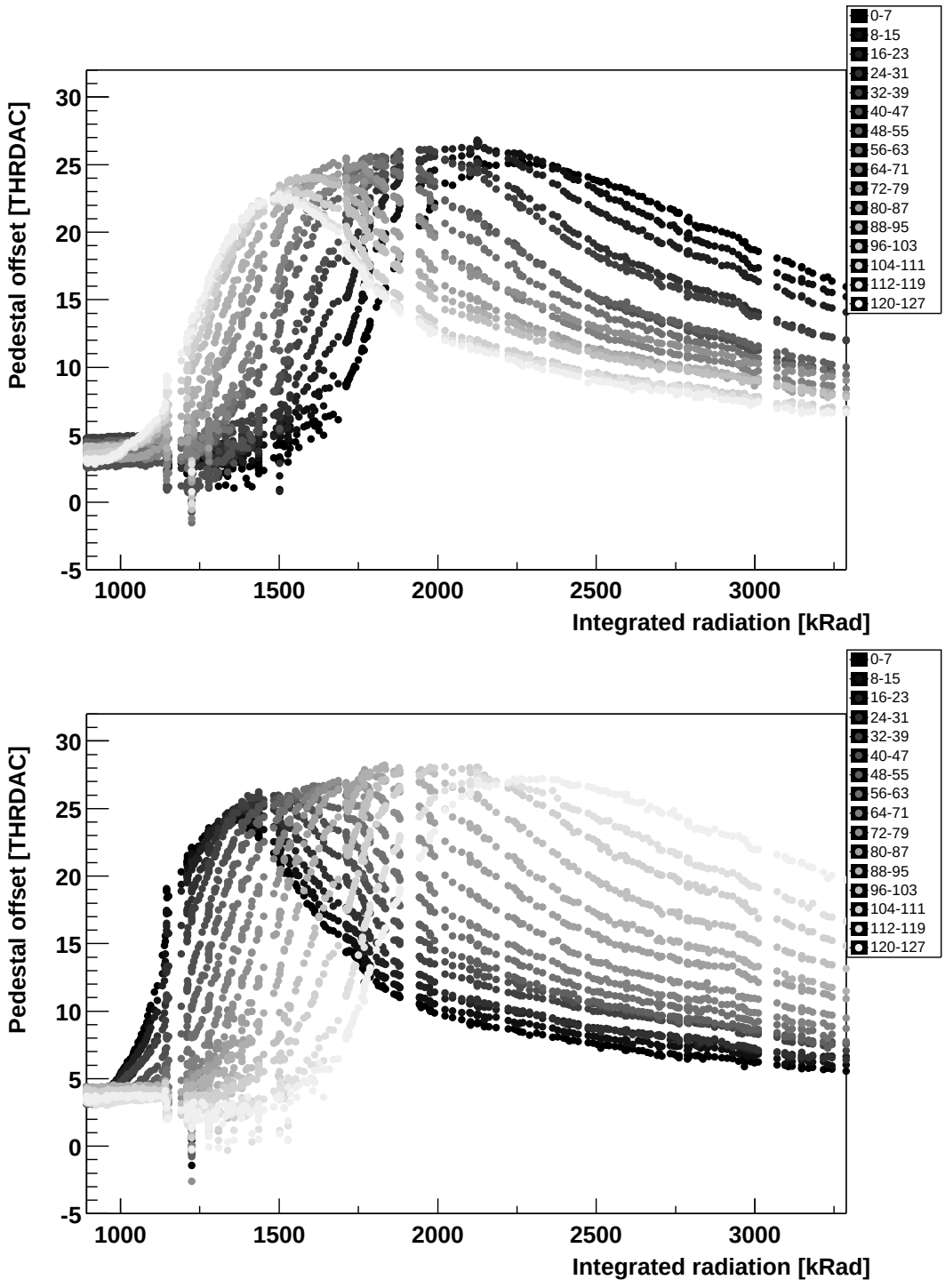

Figure 2.6: Averaged pedestal offset over groups of 8 readout channels versus the integrated radiation dose measured by the nearest PIN diode. The top (*bottom*) plot shows readout chip 2 (*3*) of the backward west module (ROS 134) of the innermost layer, situated in the horizontal plane.

of the signal into the comparator in the AToM readout chip, requiring an increased threshold level in order to keep the noise occupancy at a reasonable low level. Figure 2.5 shows the pedestal offset for a layer 1 module that is situated in the horizontal plane. The increase was first observed in the readout channels exposed to the highest amount of radiation, but other channels followed as soon as their accumulated dose reached about 1 MRad. This is illustrated in Fig. 2.6, which shows the measured pedestal offset versus the radiation dose measured with the closest PIN diode for two of the chips that are located in the backward west innermost layer in the horizontal plane. This corresponds to over-bend positrons. The readout channels in the AToM chip are geometrically offset in azimuth with respect to the silicon strips, showing that it is the most irradiated readout channel, not silicon strip which changes first. From this we conclude that the radiation damage is in the AToM chip itself. The pedestal continues to rise until an additional 400 kRad of dose has been accumulated, after which it starts to fall back toward its original value. The pedestals peak at roughly half the dynamic range of the threshold DAC, corresponding to roughly 1fC. This effect is qualitatively understood as an imbalance in the comparator circuit caused by the nonuniform irradiation [56, 58, 59, 60, 61]. After sufficient irradiation the balance slowly gets restored. This effect did not show up in the initial irradiation tests with ^{60}Co [55] as that had a uniform radiation field. Subsequent radiation tests [61] with a narrow electron beam reproduced the pedestal shift. Operationally the noise is kept under control by increasing the threshold used in the readout. However, this can only be set on a chip-by-chip basis leading to an inefficiency for small charges in channels, where the pedestal has not yet increased. A procedure has been devised which selects the optimal threshold for each chip balancing the inefficiencies from noise occupancy and minimum charge requirement.

2.3 Drift chamber (DCH)

The DCH contributes to the transverse momentum measurement and is also used for the reconstruction of vertexes outside the SVT volume that solely rely on the DCH. The DCH provides the particle identification of low momentum particles by the measurement of the ionization loss dE/dx.

The DCH is 2.8 meters long and spans the radial region $22 < r < 80$ cm. It consists of 40 layers with in total 7104 hexagonal cells. The 40 layers are divided into 10 super-layers. Twenty-four layers are given a stereo-angle to make it possible to measure longitudinal positions.

A schematic layout for the four innermost super-layers is shown in Fig. 2.7. Each cell consists of a tungsten-rhenium sense wire surrounded by six aluminum field wires. The field wires are at ground potential and the sense wires are operated at a high voltage $\sim$+1,900V. The DCH is filled with a 80:20 mixture of helium-isobutane. The material design of the DCH is optimized to minimize multiple scattering and the radiation length ($<0.2\%X_0$). The readout electronics are mounted on the backward endplate of the chamber, minimizing the amount of material in front of the calorimeter endcap.

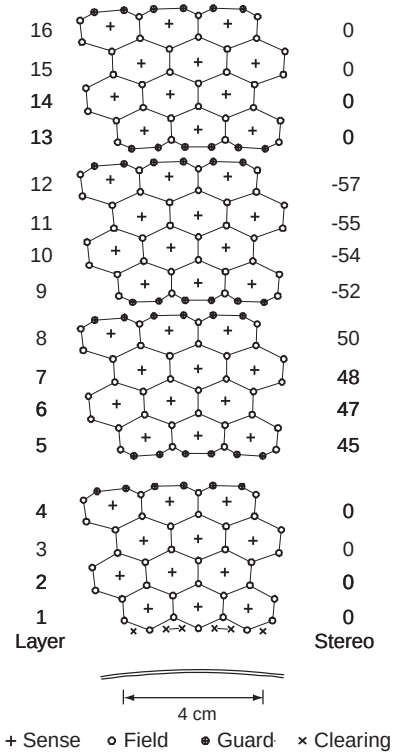

Figure 2.7: Schematic layout of drift cells for the four innermost super-layers. Lines are added between field wires to aid in visualization of the cell boundaries. The numbers on the right side give the stereo angles (mrad) of sense wires in each layer. The 1 mm-thick beryllium inner wall is shown inside of the first layer.

2.4 Detector of internally reflected Čerenkov light (DIRC)

The DIRC is a sub-detector devoted to particle identification and is specially designed to provide good pion-kaon separation for momenta between 500 MeV/c and the kinematic limit of B decays of 4.5 GeV/c. It is based on the principle that charged particles traversing a medium radiate Čerenkov light if their velocity is greater than the local phase velocity of light. The light is emitted at the Čerenkov angle, $\cos\theta_c = 1/n\beta$, which depends on the index of refraction n of the medium and the velocity of the particle $\beta = v/c$. The measurement of θ_c is then used, together with tracking information from the SVT and DCH, to identify particles.

The principle of light production, transportation and detection is illustrated in Fig. 2.8. The DIRC is positioned within the electromagnetic calorimeter and spans a small radial volume of 10 cm and is uniform to minimize the degradation of the energy measurement. It consists of 156 fused silica bars, 4.9 meter long, oriented parallel to the z axis, with a rectangular cross section of 1.7×3.5 cm^2 and a refractive index of $n = 1.743$.

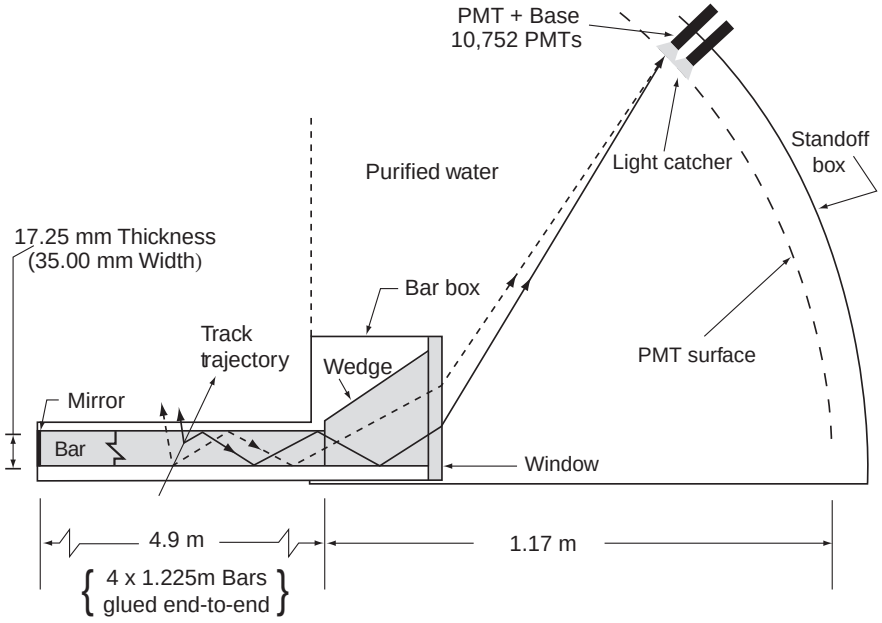

Figure 2.8: Schematics of the DIRC fused silica radiator bar and imaging region.

The Čerenkov light is transported by total internal reflection, preserving the angle of emission, to either one or both ends of the silica bar, depending on the particle incident angle. On one end a mirror is placed to avoid double instrumenting. At the other end of the bar the light enters a water tank through a silica wedge. The photons are detected by a densely packed array of photomultiplier tubes (PMTs). The PMTs are situated beyond the backward end of the magnet.

The position and arrival time of PMT signals permit the extraction of the Čerenkov angles when supplemented with track position and angle information. The timing information also assists in suppressing background photons. Covering 94% of the azimuth and 83% of the center-of-mass polar angle, the DIRC provides Čerenkov angle measurements with a resolution of ~ 3 mrad for tracks with momenta starting at the Čerenkov threshold of about 500 MeV/c and separates pions from kaons up to 4 GeV/c.

2.5 Electromagnetic calorimeter (EMC)

The electromagnetic calorimeter measures electromagnetic showers with excellent energy and angular resolution over the energy range from 20 MeV to 9 GeV. This capability allows the detection of photons from π^0 and η decays as well as from electromagnetic radiative processes. The upper bound of the energy range is set by the need to measure QED processes for calibration and luminosity determination.

The EMC is composed of a finely segmented array of in total 6580 thallium-doped cesium iodide CsI(Tl) crystals, see Fig. 2.9. The crystals, with radiation lengths between 16.0 and 17.5 X_0, are instrumented with silicon photodiodes. Two diodes are used to increase the reliability of the system.

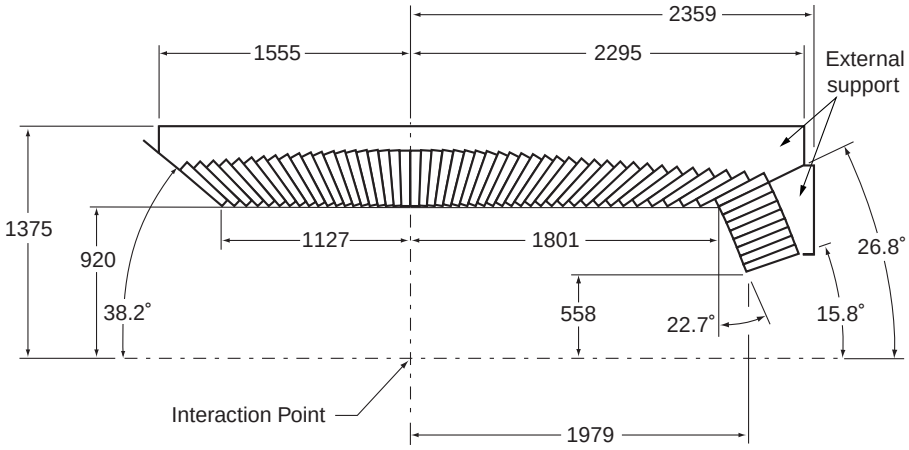

Figure 2.9: A longitudinal cross-section of the top half of the EMC indicating the arrangement of the 56 crystal rings. The detector is axially symmetric around the z-axis. All dimensions are given in mm.

The crystals are arranged in modules, which are supported individually by an external support structure, build in two sections, a barrel and a forward endcap. The barrel is arranged in 48 distinct rings with 120 identical crystals each. The end-cap holds 820 crystals arranged in eight rings. It has full coverage in the azimuthal angle and covers the polar angle range $15.8° - 141.8°$ providing a 90% solid angle coverage in the center-of-mass system. To obtain the desired resolutions, the amount of material in front of and in-between the crystals is minimized.

2.6 Instrumented flux return (IFR)

The IFR is the *BABAR* sub-system designed for muon identification and for the identification of neutral hadrons. The IFR also serves as the flux return for the 1.5 T superconducting magnet and as the support structure for the detector. The IFR consists of a hexagonal barrel with a forward and backward endcap, see Fig. 2.10. The barrel is segmented into 19 layers of resistive plate chambers (RPC) with the thickness of iron between each layer increasing from 2 cm at the inner radius to 10 cm at the outer side. The endcaps each have 18 layers of RPCs arranged in a similar way to the barrel. Single gap RPCs are inserted between the absorbers to detect streamers from ionizing particles.

2.7 The online system

The *BABAR* electronics, trigger, data acquisition (DAQ) and online computing systems are composed of tightly coupled hardware and software.

The aim of the *BABAR* trigger systems is to select interesting physics events, see Table 2.1, while rejecting background events, such that the final reconstruction event rate is under ∼370 Hz, acceptable for processing and storage. The trigger consists of a

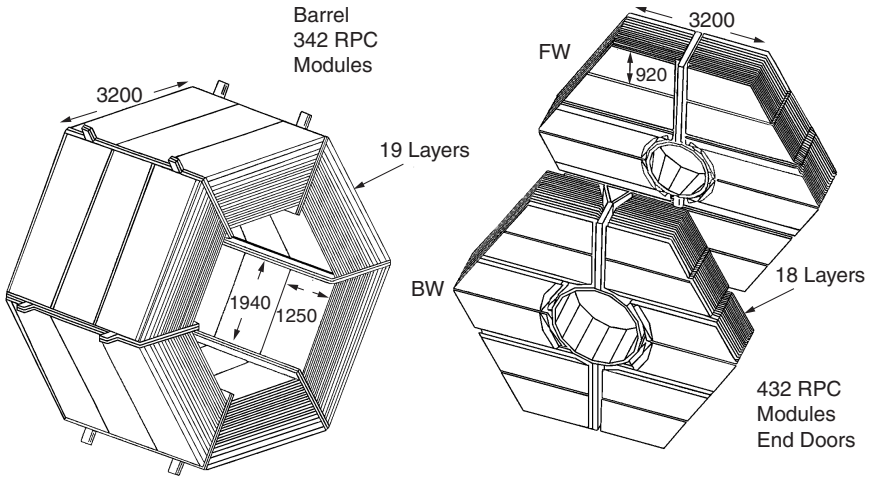

Figure 2.10: Overview of the IFR: Barrel sectors and forward (FW) and backward (BW) end doors; the shape of the RPC modules and their dimensions are indicated.

Event type	Cross section (nb)	Production rate (Hz)	L1 rate (Hz)
$B\overline{B}$	1.1	10.7	10.7
$u\overline{u} + d\overline{d} + c\overline{c} + s\overline{s}$	3.4	34.0	33.7
e^+e^-	$\sim$53	530	520
$\mu^+\mu^-$	1.2	11.7	10.3
$\tau^+\tau^-$	0.9	9.3	8.0

Table 2.1: Cross sections, production and trigger rates for the principal physics processes at 10.58 GeV/c^2 for a luminosity of $1 \times 10^{34}\text{cm}^{-2}\text{s}^{-1}$.

level 1 (L1) hardware trigger and a level 3 (L3) software trigger. The design allows for a level 2 trigger to be introduced should increasing luminosities require it, but this has never been necessary.

The L1 trigger has a maximum latency of $12\mu s$ per beam crossing. and is therefore designed to select events at a rate of up to 2.5 kHz. It consists of a drift chamber trigger (DCT), calorimeter trigger (EMT) and the global trigger (GLT). Configured to reduce background event rates, the L1 makes decisions based on the number of charged tracks above a preset transverse momentum in the DCH, showers in the EMC and tracks in the IFR. The three sub-systems triggers are considered independently, maximizing redundancy in order to measure and monitor efficiencies.

The L3 responds to the L1 output, performs a rate reduction for the main physics sources, and identifies and flags special categories of events needed for luminosity determination, diagnostic and calibrating purposes. The L3 filter acceptance for physics is about 280 Hz, while 90 Hz contain the other special event categories. The selected events are then stored for offline processing. At a luminosity of $10^{34}\text{cm}^{-2}\text{s}^{-1}$, the trigger efficiency exceeds 98% for all $B\overline{B}$ events.

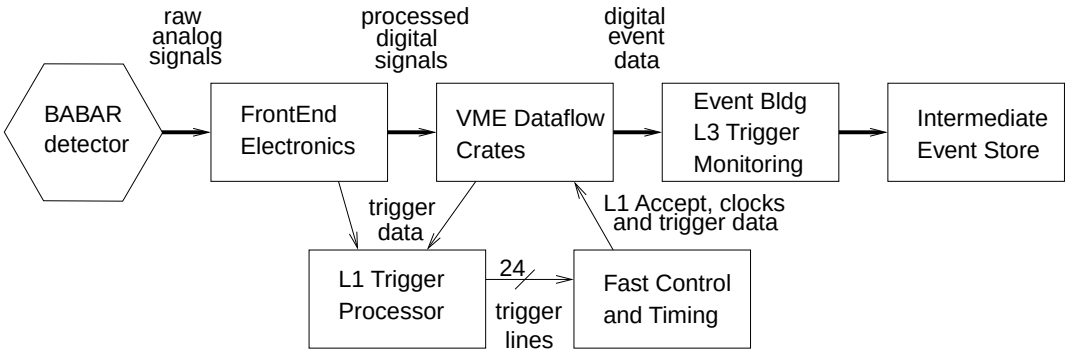

Figure 2.11: Schematic diagram of the DAQ system, from the detector to the data storage on disk for reconstruction by OPR.

A schematic drawing of the data acquisition and trigger system is shown in Fig. 2.11. The data are passed from the detectors through their front-end electronics to VME dataflow read-out modules (ROMs) through optical fibers. The ROMs carry out higher-level feature extraction with system-dependent algorithms designed to extract the signal while minimizing backgrounds and noise. The data are then passed to the L3 trigger if the L1 accept is made. Events passing the L3 trigger are written to a temporary file before online prompt reconstruction (OPR) is carried out.

Online prompt reconstruction of the collected events occurs within a few hours after logging by farms of several hundred Unix workstations running in parallel. Using the raw detector signals and the partially reconstructed events of the L3 trigger, OPR performs full reconstruction of all physics events and selects calibration events. These algorithms categorize potentially interesting events before storing the results.

Chapter 3

Reconstruction of B mesons

In the *BABAR* analysis framework the selection of signal candidates is performed in several stages, where each stage refines the sample obtained from the previous selection stage. The design of the analysis framework was mainly driven by CPU power and disk capacity efficiency.

A typical *BABAR* physics analysis selects only a tiny fraction of all events. Therefore, it is extremely inefficient for each analysis to process all available data repeatedly. Additionally, allowing many analysis jobs to access the central event store puts a large load on the system and requires a large local computing farm to provide the necessary CPU power and disk capacity. These issues are circumvented by a centrally managed pre-selection, or *skim*, of events as a first stage in the analysis chain. The skim uses basic selection criteria such as mass and momentum cuts.

Two types of skims exist, a deep-copy skim and a pointer skim. The deep-copy skim produces a complete copy of the data, the pointer skim returns only the location of the selected event in the full data sample, and is in general slower to access. The deep-copy skim is only available if the total selection rate is smaller than a few percent of the full dataset.

The skim is usually defined to have a high signal selection efficiency. The background rejection is preferably high but of less importance in this stage. It does determine how fast the second selection stage can be optimized and performed and if the skim is categorized as deep-copy or pointer skim. A single skim can be the starting sample for multiple analyses.

The second selection stage is performed under control of the user. The optimization of this stage is performed on the skimmed dataset and depends on the physics goal of the analysis, *e.g.* branching fraction measurement, time dependent analysis.

For this analysis a dedicated skim was setup. Very loose restrictions are chosen for the skim to fully exploit the more sophisticated selection criteria available in the following selection stage. This results in a high signal efficiency but unfortunately at the same time a high rate for background events. The skim was kept just small enough so that it is processed as deep-copy. The skim is chosen to select four types of decay modes, $B^0 \to D^- \eta\pi^+$, $B^0 \to D^{*-} \eta\pi^+$, $B^+ \to D^0 \eta\pi^+$ and $B^+ \to D^{*0} \eta\pi^+$. The last two modes are not discussed in this thesis, they are part of the skim to allow access for a possible

Monte Carlo sample	Type	Size (# events)	Scaling factor to full dataset
Generic $B^0\overline{B}^0$		546.5M	0.214
Generic B^+B^-		539.5M	0.213
uds		710.7M	0.644
$c\bar{c}$		417.9M	0.681
$B^0 \to D^{*-} a_0^+$	II	117k	n.a.
$B^0 \to D^{*-} a_0^+$	I	131k	n.a.
$B^0 \to D^{-} a_0^+$	II	115k	n.a.
$B^0 \to D^{-} a_0^+$	I	131k	n.a.
$B^+ \to D^{*0} a_0^+$	I	16k	n.a.
$B^+ \to D^{0}\ a_0^+$	I	16k	n.a.

Table 3.1: Sizes and scaling factors to the full Run 1-4 dataset of the Monte Carlo samples that are used for the analysis. Two types of signal Monte Carlo are used indicated with the roman indexes, please see the text for further explanation.

extension of the analysis that are needed for the measurement of γ.

This chapter describes the setup of the skim that is used in the analysis. The optimization of the selection that follows the skim is presented in Chapter 4.

3.1 Used data samples

3.1.1 *BABAR* data

This analysis uses the data acquired by the *BABAR* detector during the period October 1999 through 2004, referred to as Run 1 to Run 4; see Fig. 2.2 on page 35. This corresponds to 208 fb^{-1} collected at the $\Upsilon(4S)$ resonance (*on-peak data*). An additional 21 fb^{-1} is collected 40 MeV/c^2 below the $\Upsilon(4S)$ resonance peak (*off-peak data*), which allows the study of continuum background events, produced through the process $e^+e^- \to f\overline{f}$ where f may be any of the charged leptons or lighter quarks u, d, s or c. The total number of $B\overline{B}$ pairs analyzed is estimated to be 229.4 million.

3.1.2 Monte Carlo simulated data production

Monte Carlo simulated events are produced to understand the performance of the detector and the sources and properties of background events. In this analysis the Monte Carlo data are used to optimize the final event selection and to tune the likelihood fit, described in Chapters 4 and 5 respectively.

The production of the Monte Carlo data is performed in three stages. First, physical processes are simulated by an event generator and particle four-vectors are produced. The generator simulates the spread of energies allowed in the PEP-II beam collision to determine the energy available to the resulting particles. The beam energies are smeared

using Gaussian distributions of width 5.5 MeV and 3.1 MeV for the high- and low-energy beams, respectively. The collision point coordinates are smeared with Gaussian distributions with a width of 160 μm in $\hat{x}$ and 6 μm in $\hat{y}$. The z coordinate is modeled with a 1 cm long flat distribution.

Two different event generators are used, `Jetset` and `EvtGen`. Observed B meson decays, listed in the PDG [9], are generated with the `EvtGen` [62] generator. The unobserved part (49.75%), and the continuum $q\overline{q}$ events are produced by `Jetset`. The particles produced by the generators are propagated through a model of the material of the *BABAR* detector. Interactions between the particles and the material in the detector, and the detector response is computed using the GEANT4 [63] simulation package. The samples are presented in the same form as the raw signals within the detector and processed through the *Level 1* and *Level 3* triggers. The result is an event analogous to actual data recorded by the *BABAR* detector.

There are two kinds of produced Monte Carlo events: single mode and generic samples. The single mode Monte Carlo samples contain one or a few decay chains and are used to study the signal or specific background decays. The generic Monte Carlo samples model the complete *BABAR* dataset and all possible decays, and are grouped in four categories: $B^0\overline{B}^0$, B^+B^-, uds and $c\bar{c}$ events. The Monte Carlo samples that are in this analysis are summarized in Table 3.1.

Dedicated signal Monte Carlo is produced for this analysis in four different decay modes. The full decay chain that is produced is summarized in Table 3.2. Per event the $\Upsilon(4S)$ decay is simulated to decay in a $B^0\overline{B}^0$ pair, one of the B mesons decays generically while the other B, decays to a pre-described decay chain. The decay is modeled according to its angular distribution, based on the angular momentum and spin of the decay products. The particles are modeled taking into account their Breit-Wigner lineshape. Specific particle descriptions, such as mass and width, are predefined and use the measured values listed in the PDG [9]. The non-resonant signal $B^0 \to D^{(*)-}\eta\pi^+$ Monte Carlo events are produced as part of the generic $B^0\overline{B}^0$ Monte Carlo by `Jetset`, for these events no additional produced Monte Carlo is used.

There are four inconsistencies with the Monte Carlo generation models that are corrected for in the analysis.

First, the model used by `EvtGen` to produce the a_0 lineshape in the signal Monte Carlo lacks a kinematical factor in the Breit-Wigner lineshape function. This is discussed in Sect. 5.2.3 and is referred to as `EvtGen` *lineshape bug* . Figure 3.1 compares the lineshape with and without this bug.

Second, due to a wrong particle description, a part of the produced signal Monte Carlo has a cut-off in the lineshape, see Fig. 3.1. We have defined two different types, I and II, to label the signal Monte Carlo. Type I (II) has the cut-off (full) lineshape. The optimization of the selection makes uses of the type I, otherwise type II is used throughout the analysis.

Third, the phase-space definition that is used by `Jetset` in the $B^0 \to D^{(*)-}\eta\pi^+$ events is wrong. Figure 3.2 shows the difference in produced events in the phase-space between `Jetset` and correctly produced `EvtGen` events in the $\eta\pi$ invariant mass distribution. The impact of this error on the analysis is large but is corrected for. We refer to

Parent	Decay	Ratio
$\Upsilon(4S)$	$B^0_{spec}\overline{B}^0_{gen}$	0.5
	$\overline{B}^0_{spec}B^0_{gen}$	0.5
B^0_{spec}	$D^{*-}\ a_0^+$	1.0
a_0^+	$\eta\pi^+$	1.0
η	$\gamma\gamma$	1.0
D^{*-}	$\overline{D}^0\ \pi^-$	1.0
$\overline{D}^0$	$K^+\ \pi^-$	0.142
	$K^+\ \pi^-\ \pi^0$	0.513
	$K^0_S\ \pi^-\ \pi^+$	0.068
	$K^+\ \pi^-\ \pi^+\ \pi^-$	0.277
K^0_S	$\pi^+\ \pi^-$	1.0

(a) $B^0 \to D^{*-} a_0^+$

Parent	Decay	Ratio
$\Upsilon(4S)$	$B^+_{spec}B^-_{gen}$	0.5
	$B^-_{spec}B^+_{gen}$	0.5
B^-_{spec}	$D^*\ a_0^+$	1.0
a_0^+	$\eta\pi^+$	1.0
η	$\gamma\gamma$	1.0
D^*	$D^0\ \pi^0$	1.0
D^0	$K^-\ \pi^+$	0.142
	$K^-\ \pi^+\ \pi^0$	0.513
	$K^0_S\ \pi^+\ \pi^-$	0.068
	$K^-\ \pi^+\ \pi^-\ \pi^+$	0.277
K^0_S	$\pi^+\ \pi^-$	1.0

(b) $B^+ \to D^{*0} a_0^+$

Parent	Decay	Ratio
$\Upsilon(4S)$	$B^0_{spec}\overline{B}^0_{gen}$	0.5
	$\overline{B}^0_{spec}B^0_{gen}$	0.5
B^0_{spec}	$D^-\ a_0^+$	1.0
a_0^+	$\eta\pi^+$	1.0
η	$\gamma\gamma$	1.0
D^-	$K^+\ \pi^-\ \pi^-$	0.589
	$K^0_S\ \pi^-\ \pi^0$	0.317
	$K^0_S\ \pi^-$	0.094
K^0_S	$\pi^+\ \pi^-$	1.0

(c) $B^0 \to D^- a_0^+$

Parent	Decay	Ratio
$\Upsilon(4S)$	$B^+_{spec}B^-_{gen}$	0.5
	$B^-_{spec}B^+_{gen}$	0.5
B^+_{spec}	$\overline{D}^0\ a_0^+$	1.0
a_0^+	$\eta\pi^+$	1.0
η	$\gamma\gamma$	1.0
$\overline{D}^0$	$K^+\ \pi^-$	0.142
	$K^+\ \pi^-\ \pi^0$	0.513
	$K^0_S\ \pi^-\ \pi^+$	0.068
	$K^+\ \pi^-\ \pi^+\ \pi^-$	0.277
K^0_S	$\pi^+\ \pi^-$	1.0

(d) $B^+ \to D^0\ a_0^+$

Table 3.2: Summary of the generated signal Monte Carlo events for the four different samples with the generated decays. The B_{gen}, decays generically. The $D^0 \to K^-\ \pi^+\ \pi^-\ \pi^+$ is an incoherent sum of resonances and does not describe the interference between the underlying modes.

this bug as the `Jetset` *bug* .

Fourth, `Jetset` produces some decay modes abundantly that are not allowed or are suppressed. Most of these decays do not pass the selections. However, one specific type of events passes the selection and are removed. These events are produced by the decays: $B^0 \to D^{(*)+}K^-\eta$, $B^+ \to D^{(*)}K^+\eta$. These decays are not observed and the production amplitude is expected to be negligible. The K^+ meson must be produced by the W decay and this gives a term of V_{us} which makes it Cabibbo suppressed. In addition, to produce the additional η meson the decay is color-suppressed. Finally, no resonant states

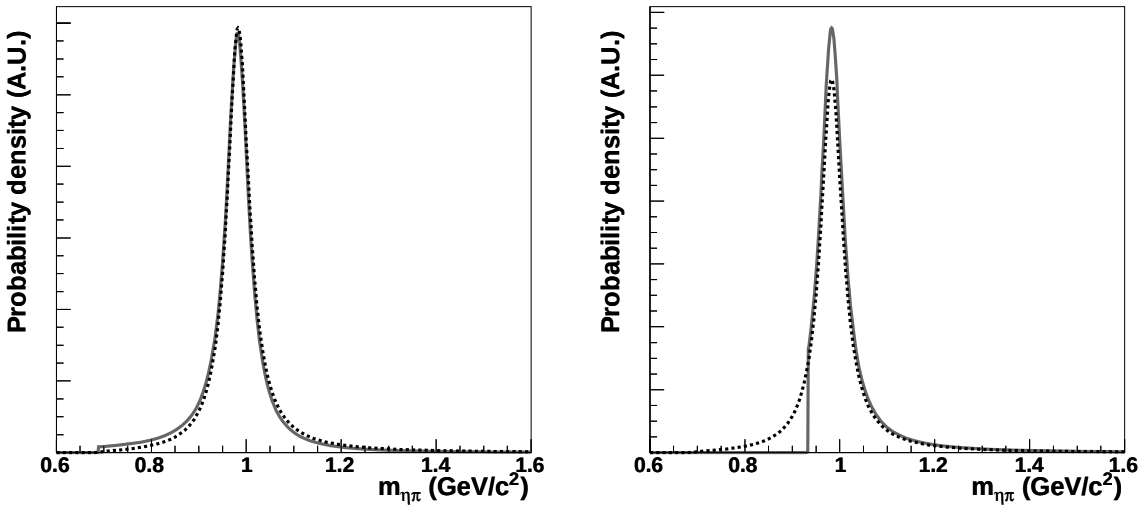

Figure 3.1: *Left:* The black dotted curve represents the correct Breit-Wigner lineshape, the solid gray curve has a missing phase-space term, which is referred to as the `EvtGen` lineshape bug. *Right:* the differences between the type I (solid gray curve) lineshape, which has a cutoff at 50 MeV/c^2 below the nominal mass and type, and type II (dotted black curve) signal Monte Carlo with the correct lineshape.

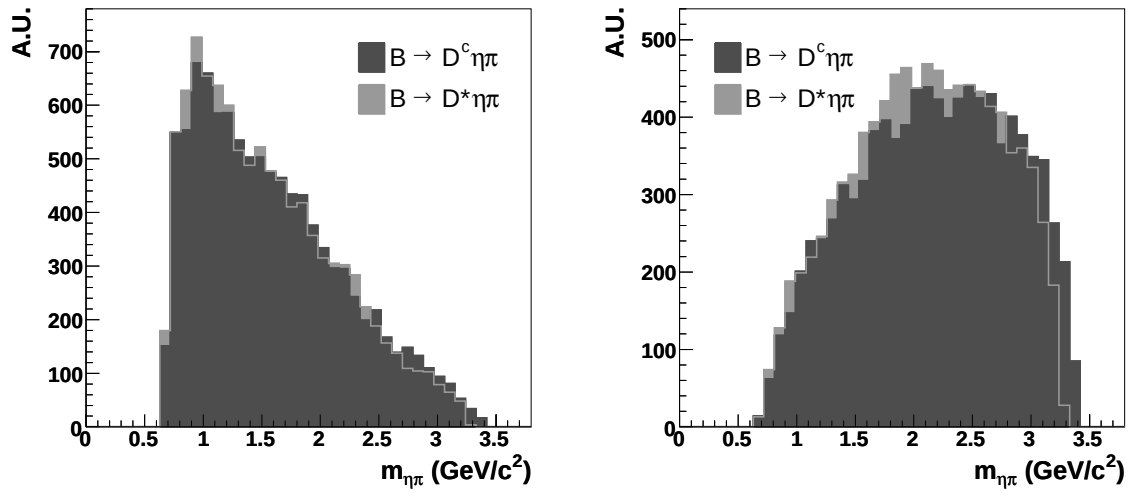

Figure 3.2: Produced $m_{\eta\pi}$ invariant-mass distribution for the $B^0 \to D^{(*)-}\eta\pi^+$ decays with `Jetset` (*left*) and `EvtGen` (*right*). There is a clear difference.

parameter	description
d_0	distance between the $PoCA$ and the origin in the $x-y$ plane
ϕ_0	azimuth angle of the track
ω	curvature of the track, $\omega = 1/p_t$
z_0	distance between the $PoCA$ and the origin along the z-axis
$\tan\lambda$	the dip angle relative to the transverse plane

Table 3.3: Parameters defining the trajectory of charged particles. The $PoCA$ is the *Point of Closest Approach* to the z-axis.

are know that can produce the $K^+\eta$ meson pair in B decays. For example, a $K_2^*(1430)$ meson cannot be produced by a W decay because it is a tensor meson.

3.2 Particle reconstruction

The reconstruction of B mesons starts with the reconstruction of charged tracks and trajectories in the detector volume. From these, composite particles such as K_S^0, η or B mesons, are formed, as described in Sect. 3.3. For a more detailed discussion on this topic we refer to Ref. [55].

In *BABAR* a set of *particle candidate lists* are defined, they categorize tracks and neutral particles using a set of selection rules. The use of these candidate lists is standardized throughout the *BABAR* analysis framework as much as possible. The skim itself is written in terms of particle candidate lists. This has the advantage that its properties (*e.g.* efficiency and purity) are well studied.

In the following sections we define the particle candidate lists that are used in this analysis.

3.2.1 Reconstruction of charged particles

The track reconstruction of charged particles uses the tracking system of the detector, the SVT and the DCH. The trajectory of a charged particle is locally defined by five parameters (d_0, ϕ_0, ω, z_0, $\tan\lambda$) that are explained in Table 3.3.

The track reconstruction begins in the drift chamber and uses the tracks found in the DCH by the L3 trigger algorithm as a starting point. A Kalman filter fitting algorithm is used that takes into account the detailed distribution of material in the detector and the full map of the magnetic field [64]. Additional drift chamber hits that are found to be consistent with the tracks are then added. Two more tracking procedures are applied to the remaining drift chamber hits that are designed to find tracks that do not pass through the entire DCH or do not originate from the interaction point.

All the tracks found in the drift chamber are extrapolated to the SVT taking into account the material and magnetic field. SVT track segments are added if they are consistent with the expected error in the extrapolation. Finally, a stand-alone SVT track finder is run on the remaining SVT hits to find low momentum tracks that do not

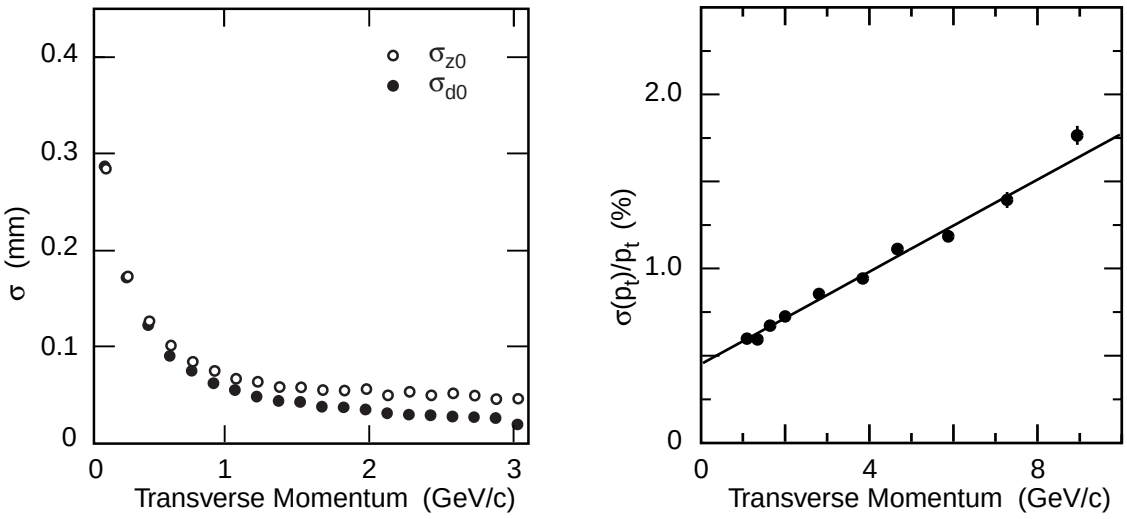

Figure 3.3: *Left:* Resolution in the parameters d_0 and z_0 for tracks in multi-hadron events as a function of the transverse momentum. *Right:* Resolution in the transverse momentum p_t determined from cosmic ray muons traversing the DCH and SVT.

reach the drift chamber.

The resolution of the five track parameters are monitored with e^+e^- and $\mu^+\mu^-$ events and checked offline in multi-hadron events and cosmic-ray muons. The measured resolutions depend on the transverse momentum p_t of the tracks. With cosmic-ray tracks with $p_t = 3\,\mathrm{GeV}/c$ the resolutions are determined to be

$$\sigma_{d_0} = 23\ \mu m, \quad \sigma_{\phi_0} = 0.43\ \mathrm{mrad},$$
$$\sigma_{z_0} = 29\ \mu m, \quad \sigma_{\tan\lambda} = 0.53 \cdot 10^{-3}.$$

The dependence of the resolution in d_0 and z_0 on the transverse momentum p_t is presented in the left plot in Fig. 3.3. The measurement is based on tracks in multi-hadron events. The right plot in Fig. 3.3 shows the resolution in the transverse momentum derived from cosmic muons. The resolution function can be parametrized by

$$\sigma_{p_T} = (0.13 \pm 0.01)\% \cdot p_T + (0.45 \pm 0.03)\%. \tag{3.1}$$

Three different particle candidate lists of charged tracks are described in Table 3.4 for later use. The categories are presented with increased quality as they pass more requirements.

3.2.2 Reconstruction of neutral particles

Neutral pion decays, η decays, electrons and photons from QED and radiative processes, produce showers in the electromagnetic calorimeter (EMC). A typical electromagnetic shower spreads over adjacent crystals forming a cluster of energy deposits. Pattern recognition algorithms have been developed to efficiently identify these clusters, and to differentiate single clusters, with one energy maximum, from merged clusters, with more

List name	Requirements
ChargedTracks	- reconstructed in SVT and/or the DCH
GoodTracksVeryLoose	- member of ChargedTracks - $p \leq 10\,\mathrm{GeV}/c$ - DoCA to beam spot $d_t \leq 1.5$ cm transverse to beam axis - DoCA to beam spot $d_l \leq 10$ cm parallel to beam axis
GoodTracksLoose	- member of GoodTracksVeryLoose - $p_T \geq 0.1\,\mathrm{GeV}/c$ - at least 12 hits in the DCH

Table 3.4: Charged track lists. DoCA is the abbreviation for *Distance of Closest Approach*.

than one local energy maximum, referred to as bumps. An example for local maximums occurrence is when photons from high-energy π^0 or η decays are unresolved, resulting in several showers in close proximity.

Clusters are formed around initial seed crystals containing at least 10 MeV of deposited energy. Neighboring crystals are added to the cluster if their energy exceeds 1 MeV. If the newly added crystal has energy greater than 3 MeV, its contiguous neighbors are also included in the cluster.

Bumps can be associated with a charged particle by projecting a track to the inner face of the calorimeter. If the distance between the track and the center of the bump is consistent with the momentum and the angle of the track, the bump is associated with the charged track. If no association is made the bump is assumed to originate from a neutral particle.

The energy resolution of the calorimeter is measured at low energies directly with a radioactive source under ideal low-background conditions. At high energies it is derived from Bhabha scattering where the energy of the detected shower can be predicted from the polar angle of the electron. Below 2 GeV, the mass resolution of π^0 and η mesons decaying into two photons of approximately equal energy is used to infer the EMC energy resolution, as shown in the left plot in Fig. 3.4. The decay $\chi_{cl} \to J/\psi\gamma$ provides a measurement at an average energy of about 500 MeV. The combination of the resolution measurements can be seen in the right plot in Fig. 3.4. At normal incidence the energy resolution for photons is described by

$$\frac{\sigma_E}{E} = \frac{2.3\%}{\sqrt[4]{E(\,\mathrm{GeV})}} + 1.9\%. \tag{3.2}$$

The measurement of the angular resolution is based on the analysis of π^0 and η decays to two photons of approximately equal energy. The resolution varies between 12 mrad at low energies and 3 mrad at high energies and is described by

$$\sigma_\theta = \sigma_\phi = \frac{3.87}{\sqrt{E(\,\mathrm{GeV})}}\mathrm{mrad}. \tag{3.3}$$

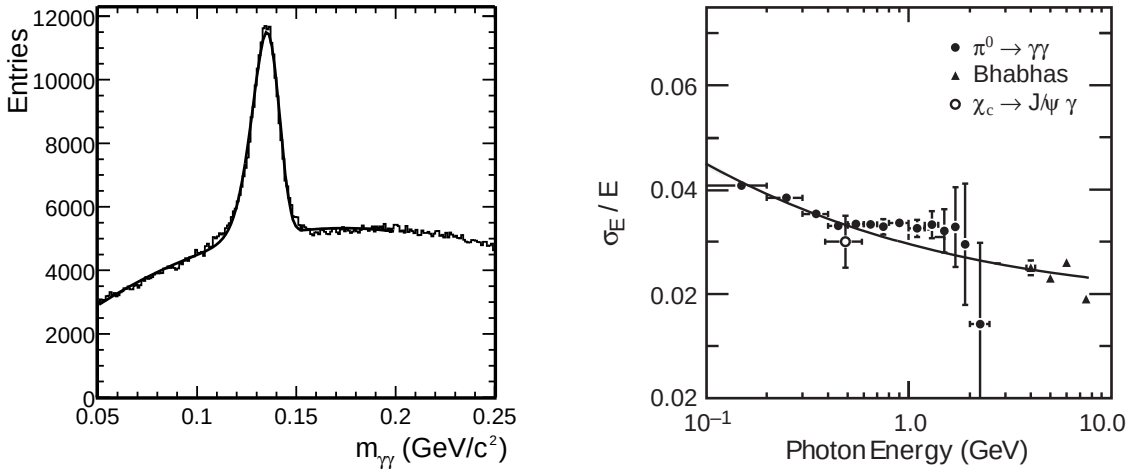

Figure 3.4: *Left:* Invariant mass of two photons in $B\overline{B}$ events. The energies of the photons and the π^0 are required to exceed 30 MeV and 300 MeV, respectively. The solid curve is a fit to the data. *Right:* The energy resolution for the EMC measured for photons and electrons from various processes. The solid curve is a fit to Eq. (3.2).

List name	Requirements
CalorNeutral	- not a member of ChargedTracks
GoodNeutralLooseAcc	- member of CalorNeutral - $E \geq 30$ MeV - lateral shape parameter[65] $\lambda_{LAT} \leq 1.1$ - polar angle $0.41 < \theta_{LAB} < 2.409$ rad
GoodPhotonLoose	- member of CalorNeutral list - lateral shape parameter $\lambda_{LAT} \leq 0.8$

Table 3.5: Neutral particle lists.

Similar to the charged tracks, the neutral candidates are organized into lists in Table 3.5.

3.2.3 Kaon selection

For a pure kaon selection a likelihood based method is developed [13] that, depending on the momentum of the particle, uses information from one or a combination of three sub-detectors: the SVT, the DCH and the DIRC [66, 67].

The distribution of the measured dE/dx in the DCH as a function of momentum is shown in Fig. 3.5. The difference between the measured dE/dx and the expected truncated mean for a given mass hypothesis, with a typical resolution of 7.5%, is used to calculate the likelihoods, $\mathcal{L}_\pi, \mathcal{L}_K$ and $\mathcal{L}_p$ assuming Gaussian distributions.

The same method is used to calculate a likelihood, based on the measured dE/dx in the SVT, using an asymmetric Gaussian distribution. For minimum ionizing particles

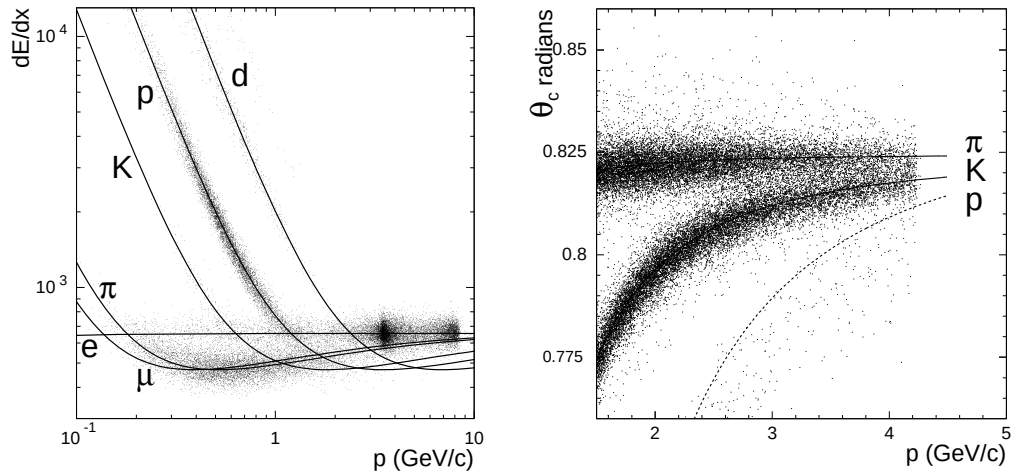

Figure 3.5: *Left:* The DCH distributions of dE/dx versus the track momenta, the Bethe-Bloch expectations for the particle types are superimposed. *Right:* The measured distribution of the Čerenkov angle θ_c of kaons, pions and protons versus the track momenta in the DIRC.

the resolution on the SVT truncated mean is about 14%. This gives a 2σ separation between pions and kaons below 500 MeV/c, and between kaons and protons for over 1 GeV/c.

For particles with a momentum between the Čerenkov threshold of 600 MeV/c up to 4.2 GeV/c, the DIRC provides a π/K separation of $\gtrsim 4\sigma$ at 3 GeV/c. The distribution of the measured Čerenkov angle versus the track momentum is shown in Fig. 3.5. A likelihood is obtained for each particle hypothesis, using two ingredients: the expected number of Čerenkov photons (assuming a Poisson distribution) and the difference between the measured and the expected angle θ_c^0, assuming a Gaussian distribution.

The NotAPion kaon selector is defined by combining the individual likelihoods from the SVT, the DCH and the DIRC. The selection criteria are summarized in Table 3.6. The NotAPion list has a nearly constant kaon-identification efficiency of about 96%, and a pion misidentification probability of not larger than 30%, for tracks in the transverse momentum range between 1 and 2.5 GeV/c. For this analysis a candidate list is used for the Kaon component where the requirement is made that the reconstructed track must satisfy both the NotAPion requirements and that of GoodTracksLoose. This particle candidate list is referred to as KMicroNotPionGTL, see also Table 3.6.

3.3 Reconstruction of composite particles

From the charged tracks and neutral particle candidate lists we reconstruct the composite particles to form the B decays that are of interest in this analysis, $B^0 \to D^- \eta \pi^+$ and $B^0 \to D^{*-} \eta \pi^+$. There are no requirements made on the a_0 meson; the selection is equivalent to a selection of non-resonant $B^0 \to D^{(*)-} \eta \pi^+$ events. This is motivated by

List name	Requirements
NotAPion	- For p < 0.5 MeV/c: $\mathcal{L}_K/\mathcal{L}_\pi < 0.1$ and $\mathcal{L}_K/\mathcal{L}_p < 0.1$ for likelihoods from both SVT and DCH - For $(0.5 \leq$ p $< 0.6)$ GeV/c: $\mathcal{L}_K/\mathcal{L}_\pi < 0.1$ and $\mathcal{L}_K/\mathcal{L}_p < 0.1$ for likelihoods from only DCH - For p > 0.6 GeV/c: $\mathcal{L}_K/\mathcal{L}_\pi < 1$ and $\mathcal{L}_K/\mathcal{L}_p < 1$ for likelihoods from only DIRC
KMicroNotPionGTL	- member of NotAPion - member of GoodTracksLoose - p > 150 MeV/c

Table 3.6: Kaon Selectors

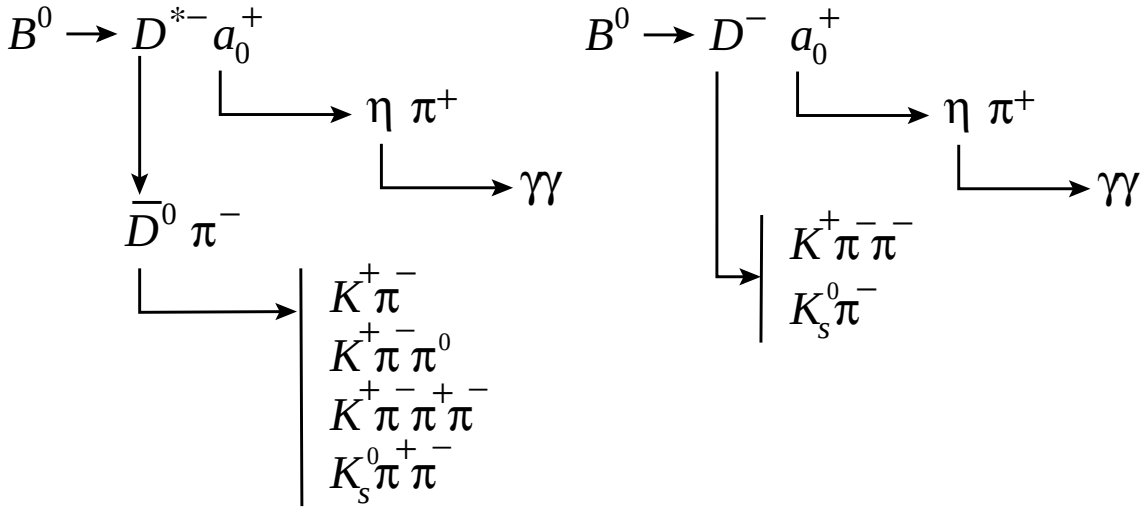

Figure 3.6: The two final reconstructed decay chains with the six different reconstructed modes. The π^0 meson is reconstructed in the $\pi^0 \to \gamma\gamma$ decay, the K^0_S in $K^0_S \to \pi^+\pi^-$.

the large uncertainties of the a_0 lineshape width. The selection allows a likelihood fit in a wide region in the invariant $\eta\pi$ mass region to search for the a_0. Figure 3.6 presents a schematic drawing of the reconstructed channels.

3.3.1 π^0 candidates

Neutral pion candidates are constructed in the most abundant decay mode, $\pi^0 \to \gamma\gamma$, with a branching ratio of $(98.798 \pm 0.032)\%$ [9]. The photons must satisfy the GoodPhotonLoose requirements and the invariant mass of the π^0 candidate is required to be in the range $(115 \leq m_{\gamma\gamma} \leq 150)\,\mathrm{MeV}/c^2$ with an energy larger than 200 MeV. The π^0 candidates are referred to as the Pi0AllDefault list.

3.3.2 η candidates

The η is reconstructed in the $\eta \to \gamma\gamma$ decay. This decay has a branching fraction of $(39.30 \pm 0.24)\%$ [9]. Two GoodPhotonLoose candidates are combined to form η candidates. The following requirements must be met: photon energies $E_\gamma \geq 50\,\mathrm{MeV}$, an invariant mass between $(470 \leq m_{\gamma\gamma} \leq 620)\,\mathrm{MeV}/c^2$, a momentum $p_\eta \geq 200\,\mathrm{MeV}/c$, maximum lateral moment $\lambda_{LAT}[65] \leq 0.8$.

3.3.3 K^0_S candidates

The K^0_S candidates are reconstructed in the decay mode $K^0_S \to \pi^+\pi^-$ which has a branching fraction of $(69.20 \pm 0.05)\%$. Another frequent decay $K^0_S \to \pi^0\pi^0$ ($\mathcal{B} \sim 31$ %) is not reconstructed in this analysis: the neutral particles are not efficiently reconstructed and would introduce background events in the analysis. The K^0_S selector pairs all possible tracks of opposite sign, using the ChargedTrack list. The mass is constrained to be in the range of $(473 \leq m_{K^0_S} \leq 523)$ MeV/c^2. These K^0_S candidates are referred to as the KsDefault list.

3.3.4 D^+ candidates

Charged $D^{(*)\pm}$ mesons The reconstructed D mesons are reconstructed in two decays.

The $D^+ \to K^-\pi^+\pi^+$mode is constructed from a KMicroNotPionGTL candidate and two GoodTracksVeryLoose tracks as pion candidates. The invariant mass for the D^+ candidate is required to be within 70 MeV/c^2 of the nominal D^+ mass.

The $D^+ \to K^0_S\pi^+$mode is constructed from a KsDefault and a GoodTracksVeryLoose candidate. The invariant mass for the D^+ candidate constrained to be within 70 MeV/c^2 of the nominal D^+ mass.

3.3.5 D^0 candidates

There are four reconstructed D^0 decay modes used in this analysis.

The $D^0 \to K^-\pi^+$mode is constructed of two GoodTracksVeryLoose candidates, for the K^+ meson and the π^+ meson. The D^0 candidate is required to have a mass within 70 MeV/c^2 of the nominal D^0 mass.

The $D^0 \to K^-\pi^+\pi^0$mode is constructed of a GoodTracksLoose candidate for the K^+, one GoodTracksVeryLoose for the π^+, and one Pi0AllDefault candidate for the π^0 meson. The mass of the reconstructed D^0 candidates is required to be within 90 MeV/c^2 of the nominal D^0 mass.

The $D^0 \to K^-\pi^+\pi^+\pi^-$ mode is constructed of one GoodTracksLoose track for the K^+ and three GoodTracksVeryLoose candidates for the three π^+ mesons. The mass of the reconstructed D^0 meson is restrained within 70 MeV/c^2 of the nominal D^0 mass.

The $D^0 \to K^0_S\pi^+\pi^-$mode is constructed of one KsDefault candidate and two GoodTracksVeryLoose candidates. The mass of the reconstructed D^0 candidate is restrained within 70 MeV/c^2 of the nominal D^0 mass.

3.3.6 D^{*+} candidates

The D^{*+} meson is reconstructed in the decay $D^{*+} \to D^0\pi^+$ which has a branching ratio of $67.7 \pm 0.5\%$ [9]. The D^{*+} decay to D^+ π^0 (branching ratio $30.7 \pm 0.5\%$) is not reconstructed. The mass difference between the D^{*+} and the D^+ is small compared to the pion mass which results in a small momentum and the reconstruction of this low momentum neutral pion creates a high background rate. In the effort to keep the analysis as a deep-copy skim this mode is not reconstructed in this analysis.

The momentum of the π^+ is small due to the small mass difference between the D^{*+} and the D^0, this pion is also referred to as *soft pion*. The D^{*+} candidates are constructed from one of the D^0 candidates discussed in Sect. 3.3.5 and one GoodTracksVeryLoose candidate that has a maximum momentum of 450 MeV/c.

The reconstructed D^{*+} candidate is required to have a mass within 500 MeV/c^2 of the nominal D^{*+} mass and a minimal momentum in the center-of-mass frame of 1.3 GeV/c.

Another requirement is placed on the mass difference between the D^{*+} and the D^0 daughter, $\Delta m = m_{D^{*+}} - m_{D^0}$. The mass of the D^0 is constrained at the nominal mass and required to be within the range of $(130 < \Delta m < 160)\,\mathrm{MeV}/c^2$.

3.3.7 B^0 candidates

B^0 meson candidates are reconstructed in two different modes, $B^0 \to D^-\eta\pi^+$ and $B^0 \to D^{*-}\eta\pi^+$. The B^0 mesons that decays via $B^0 \to D^-\eta\pi^+$ are reconstructed by combining η and D^+ candidates with a GoodTracksLoose candidate for the charged pion. The B^0 mesons reconstructed in the $B^0 \to D^{*-}\eta\pi^+$ mode, uses the D^{*+} instead of the D^+. The requirements that are placed on the reconstructed B^0 candidates are: The reconstructed B mass is within 4.5 and 5.5 GeV/c^2; No more than 550 candidates are reconstructed in a single event. (This is done to remove noisy events from the analysis.); The beam-energy-substituted mass must be in the range, $(5.18 < m_{\mathrm{ES}} < 5.35)\,\mathrm{GeV}/c^2$ (see Sect. 4.2.2 for a definition of m_{ES}); The energy difference, $|\Delta E| < 200\,\mathrm{MeV}$ (for a description of ΔE see Sect. 4.2.2).

3.3.8 Global decay chain fit

Traditionally in a *BABAR* analysis, a leaf-by-leaf fit is performed on the decay chain. For this analysis a global-decay-chain fit package is used instead. A detailed description of this vertex fit, called **TreeFitter**, is found in [68]. **TreeFitter** is a method that performs a least squares fit on the whole decay chain in one stage. This technique allows us to obtain the decay time, position and momentum parameters for all the particles in the decay chain simultaneously.

In some cases the position and momentum parameters can be improved by constraining the mass of composite particles in the decay tree to the known particle mass. In this analysis we have constrained all the masses in the reconstructed decay chain.

In addition **TreeFitter** can provide the decay lengths of the K^0_s and D^+ mesons which are used later for background suppression.

Skim line	Input sample						
	$B^0 \to D^{*-} a_0^+$ M.C. (16k)	$B^0 \to D^- a_0^+$ M.C. (16k)	$B^+ \to D^{*0} a_0^+$ M.C. (16k)	$B^+ \to D^0 a_0^+$ M.C. (16k)	Generic $B\overline{B}$ M.C. (1k)	Generic B^+B^- M.C. (1k)	Data (5k)
$B^0 \to D^{*-}\eta\pi^+$	40%	8%	37%	44%	1.9%	1.8%	0.4%
$B^0 \to D^-\eta\pi^+$	15%	30%	30%	39%	0.4%	0.9%	0.4%
$B^+ \to D^{*0}\eta\pi^+$	13%	7%	48%	46%	6.3%	7.3%	2.2%
$B^+ \to D^0\eta\pi^+$	10%	10%	10%	38%	5.0%	7.3%	2.5%
Total Skim	54%	54%	55%	57%	7.6%	7.3%	3.4%

Table 3.7: Selection fractions of the different Monte Carlo samples and measured data samples. The size of the used data samples to determine the fractions is quoted between brackets.

Events where the global-decay-chain fit has failed have an *unconverged fit* **TreeFitter** status and are removed from the analysis.

3.4 Skim rates and selection efficiency

A summary of the fractions of different data samples that are selected by the four different skims are presented in Table 3.7. (For completeness we also quote the charged B skims.)

The first four columns in Table 3.7 quote the selected fractions in the dedicated signal Monte Carlo data. Ideally, one would select 100% of the matching Monte Carlo data (row n matches to column n), and 0% in all other boxes. This would correspond to a selection efficiency of 100% with no cross-feed from other skim lines; *i.e.* the $B^0 \to D^{(*)-}\eta\pi^+$ skim would select no events that are produced via $B^0 \to D^{*-}\eta\pi^+$, $B^+ \to D^0\eta\pi^+$ or $B^+ \to D^{*0}\eta\pi^+$.

The 5^{th} and 6^{th} column of Table 3.7 represent the selected fraction of the generic B meson Monte Carlo data. Since there are no $B^0 \to D^{(*)-}a_0^+$ events produced in the Monte Carlo data and only a small fraction of $B^0 \to D^{(*)-}\eta\pi^+$ events, these numbers reflect the number of expected B meson background events.

The last column in Table 3.7 gives the selected fraction of measured data for the four different skims. Note that although these numbers might appear small, the actual number of background events in the skimmed data sample is huge ($0.4\% \times \sim 10^9$ events).

Chapter 4

Event selection

The resulting sample obtained from the skim, defined in Chapter 3 is now input to a final event selection. This stage in the data selection uses as many signal-background discriminating variables as possible to achieve the highest possible signal sensitivity. A dedicated optimization procedure is used to maximize the significance level of the selected data set. Here, the significance level reflects the sensitivity to the discovery or exclusion of $B^0 \to D^{(*)-}a_0^+$ signal, which is the primary goal of this analysis. A set of optimized rectangular box cuts is produced for each separate reconstructed decay chain[1]: two for $B^0 \to D^- a_0^+$ and four for $B^0 \to D^{*-} a_0^+$ decays.

The optimization process is described in Sect. 4.1. The discriminating variables are presented in Sect. 4.2. The optimized final selection is given in Sect. 4.3, and Sect. 4.4 gives a description of the final sample. Efficiency curves of the selected data sample are determined, for later use, in Sect. 4.5.

4.1 Selection optimization

The optimization process aims to find the highest significance level in the multi-variable phase space. We first find an appropriate definition of the significance level in Sect. 4.1.1. The method that is developed to search the variable phase-space for the optimal combination of cuts leading to the highest significance level of the final sample, is presented in Sect. 4.1.3. Finally, the best candidate selection, that deals with events where more than one B candidate survives the selection, is given in Sect. 4.1.4.

[1]Throughout this thesis the following notations are used in captions and tables for the six reconstructed decay chains. DchI for $B^0 \to D^- a_0^+$ ($D^+ \to K^-\pi^+\pi^+$), DchII for $B^0 \to D^- a_0^+$ ($D^+ \to K_S^0\pi^+$), DstI for $B^0 \to D^{*-} a_0^+$ ($D^{*+} \to D^0\pi^+$, $D^0 \to K^-\pi^+$), DstII for $B^0 \to D^{*-} a_0^+$ ($D^{*+} \to D^0\pi^+$, $D^0 \to K^-\pi^+\pi^0$), DstIII for $B^0 \to D^{*-} a_0^+$ ($D^{*+} \to D^0\pi^+$,$D^0 \to K^-\pi^+\pi^+\pi^-$) and DstIV for $B^0 \to D^{*-} a_0^+$ ($D^{*+} \to D^0\pi^+$, $D^0 \to K_S^0\pi^+\pi^-$).

4.1.1 Significance level

Two commonly used functions to define the significance level are

$$\frac{S}{\sqrt{S+B}}, \tag{4.1}$$

and

$$\frac{S}{\sqrt{B}}. \tag{4.2}$$

Here S is the number of selected signal events in a given dataset, and B is the number of selected background events expected in this sample. The number of selected signal events is connected to the selection efficiency of the signal, ϵ_S, the branching ratio of the decay, $\mathcal{B}$, and the number of $B\overline{B}$ decays in the dataset, $N_{B\overline{B}}$, by the following relation

$$S = \epsilon_S \cdot \mathcal{B} \cdot N_{B\overline{B}}, \tag{4.3}$$

Optimization of the first equation, Eq. (4.1), needs prior knowledge (or a guesstimate) of the branching ratio. This poses a problem when the branching ratio is not known and cannot be estimated. The second equation can be optimized without this knowledge. The branching ratio introduces an overall scaling factor that does not influence the optimization procedure. However, optimization based on this function becomes non-optimal for small number of selected background events as it will prefer to push the signal efficiency down to small values, see the discussion in Punzi [69].

A definition for the significance level is proposed by Punzi that needs no prior knowledge of the branching ratio and still behaves properly for small numbers of background events. The definition of the significance level SL is given by [69]

$$SL_P = \frac{\epsilon_S}{a/2 + \sqrt{B}}, \tag{4.4}$$

where a is the desired significance of the measurement and B is the number of background events. By finding the maximum of this function the minimal detectable branching ratio is found that can still be measured, or excluded, with a significance of a. By including the desired significance, a, the formula becomes more robust for small numbers of B.

We define a significance level that is used for our optimization process. It behaves exactly like Eq. (4.4) in the optimization procedure and is more practical in use

$$SL = \frac{N_{sig}}{1.5 + \sqrt{B}} \tag{4.5}$$

where N_{sig} is the number of selected signal events in the Monte Carlo sample. We have chosen to optimize for a 3σ discovery or 95% CL exclusion. The difference between Eq. (4.4) and (4.5) is a constant scaling factor and does not influence the optimization.

4.1.2 The Monte Carlo data used for the optimization

The optimization is performed using category I signal Monte Carlo and four types of background Monte Carlo data, see Table 3.1 on page 46. The number of background events obtained is scaled to match the used data sample of 208 fb^{-1}, with the use of the scaling factors summarized in Table 3.1.

A part of the signal Monte Carlo events is not correctly reconstructed and has to be considered as background. To reduce the number of mis-reconstructed events in the Monte Carlo sample we place a cut around the $a_0^{\pm}$ mass region, $(0.9 < m_{a_0} < 1.1)\,\text{GeV}/c^2$. After this cut, a selected event in the corresponding signal Monte Carlo data is assumed to be a selected signal event in the optimization procedure.

Only non-resonant $B^0 \to D^{(*)-}\eta\pi^+$, and no resonant $B^0 \to D^{(*)-}a_0^+$, events are generated in the background Monte Carlo data. For the optimization procedure the non-resonant $B^0 \to D^{(*)-}\eta\pi^+$ events are removed from the background Monte Carlo samples. After this, any selected event in the generic $B^0\overline{B}^0$ or B^+B^-, the $c\bar{c}$ or uds Monte Carlo sample is considered to be a background event.

The optimization is thus only performed for the $B^0 \to D^{(*)-}a_0^+$ signal events and not specifically for the $B^0 \to D^{(*)-}\eta\pi^+$ signal events.

During the optimization procedure the statistics of the selected background events can run into the single digit numbers and the statistical uncertainty starts to play an important role. To enhance background statistics, we loosen the selection cuts on the m_{ES} and ΔE variables and scale the area of the sidebands to the area of the signal box to make use of the fact that the background distribution is almost constant as a function of m_{ES}, and to a very good approximation linear in ΔE. In Fig. 4.1 the different areas are presented, the signal region is defined by $(5.273 \leq m_{\text{ES}} \leq 5.289)\,\text{GeV}/c^2$ and $|\Delta E| \leq 40\,\text{MeV}$, the ΔE sideband by $(5.273 \leq m_{\text{ES}} \leq 5.289)\,\text{GeV}/c^2$ and $(40 \leq |\Delta E| \leq 100)\,\text{MeV}$, and the m_{ES} sideband by $(5.200 \leq m_{\text{ES}} \leq 5.273)\,\text{GeV}/c^2$ and $|\Delta E| \leq 40\,\text{MeV}$. For the optimization of all variables, except m_{ES} and ΔE, the sideband estimation technique has been used.

For later use we define a region that is a combination of the $a_0^{\pm}$ mass region and the m_{ES}-ΔE signal region that is referred to as the a_0 box.

4.1.3 Scanning the multi-variable phase space

The optimization procedure operates in a set of cycles. In a single cycle the variables are optimized, one-by-one, in predefined search regions. If variable n is evaluated cuts are placed on all other variables. For the first cycle the set of cuts is given by the user. Each following cycle uses the optimized cuts produced by the previous cycle.

Each variable has a predefined exclusion direction, either greater or smaller than the cut position. In addition, by using absolute values and introducing offsets, intervals around for example particle masses, are defined.

The predefined search region is divided into a predefined number of bins, N_{bins}, and for every bin the significance level, SL, is calculated using Eq. (4.5). In one cycle, the significance levels are calculated for each bin, and for all variables. The search region

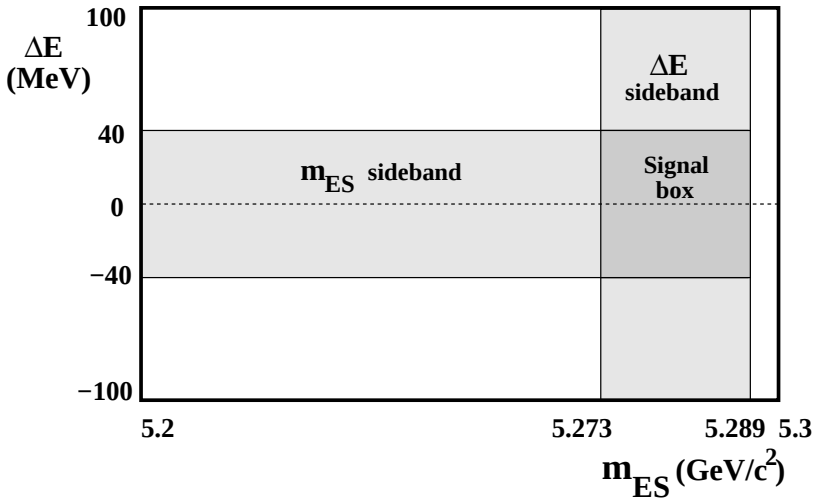

Figure 4.1: Definition of signal and sideband regions in the ($m_{\rm ES}$, ΔE) plane.

can be changed during the procedure in three different ways, zoom-in, zoom-out and displaced.

Some of the variables that are optimized are correlated and this can lead to convergence problems. Consider two positively correlated variables that are evaluated in one cycle and both lead to a looser cut. The combination of the two leading to a too loose selection. In the next cycle the same two variables are then evaluated to be tightened. If no further restrictions are made, these correlated variables may never converge. To improve the convergence of the optimization procedure, a *friction* term, F, is introduced: instead of moving the current cut to the position of the highest significance level (C_{opt}), the value is placed somewhere in between. The cut for the next cycle is calculated for variable i as

$$C_i^{j+1} = C_i^j + F \cdot (C_{i;opt}^j - C_i^j), \tag{4.6}$$

where j is the cycle number. A friction of $F = 0$ is maximal, no optimization takes place. The minimal friction of $F = 1$ gives the maximal movement of the cuts, but introduces the convergence problems. Empirically, a friction term of $F = 0.3$, leads to a stable, relatively fast, optimization procedure, with our set of variables.

The size and location of the search region is in some cases re-defined during the procedure. The region is defined between R_{min} and R_{max}, with size $R_{size} = |R_{max} - R_{min}|$. There are a two situations where the definition of the region is changed between cycles.

1. If the cut, C^{j+1}, is close to a border, R_{min} or R_{max}, the size of the region is enlarged by 20% and centered at the cut.

2. If the optimal cut position, C_{opt}^j, is within 0.1% of the new cut, C^j, the size of the region is decreased by 10% and centered at the new cut.

The requirement is made that for absolute-value variables the minimum and maximum of the probe region must be non-negative: $R_{min} \geq 0$ and $R_{max} > 0$.

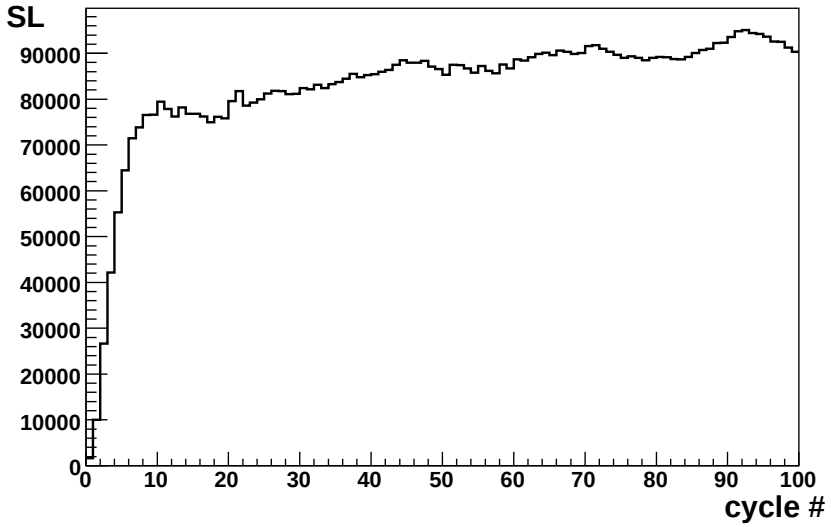

Figure 4.2: Significance level of the $B^0 \to D^- a_0^+$ ($D^+ \to K^- \pi^+ \pi^+$) decay mode for increasing cycle numbers during the optimization process.

The average time per cycle depends on the number of variables, the number of bins, and the number of Monte Carlo events for the specific decay mode. This last number varies significantly and depends on the branching ratio and pre-selection of the D^* or D^0 mode.

The procedure is monitored by calculating the significance level in each cycle. If the level converges the process is stopped and the set of cuts corresponding to the highest significance level is selected. As an example, the calculated SL for 100 cycles of the optimization of the $B^0 \to D^- a_0^+$ ($D^+ \to K^- \pi^+ \pi^+$) decay mode is shown, in Fig. 4.2.

From Fig. 4.2 it can be seen that the significance level increases on average as more optimization cycles have been performed. However, there are fluctuations; from one cycle to the next it can actually decrease. There are two mechanisms that can cause this behavior. The first is the friction term in Eq. (4.6). Because of this friction term a cut can be positioned in an area where the significance level is actually lower than at the position where it started at. The second is that the combination of optimized cut position of the individual variables does not necessarily give the optimized significance level for the combination of variables.

The fluctuating behavior cannot be compared to an overtraining effect as sometimes occurs in a neural network training. In that case, the calculated significance level is calculated on a monitoring sample, and as the neural network training becomes overtrained, the significance level of the monitoring sample starts to fluctuate where the significance level of the training sample still increases. The significance level as shown in Fig. 4.2 is however calculated on the same sample that is also used for the optimization process. The fluctuations can therefore not be the sign of overtraining of the optimization.

This of course does not exclude the possibility that our optimization might be overtrained. However, any overtraining effects that might be present in the optimization do not influence the analysis. The efficiency that is calculated is performed on an entirely different Monte Carlo sample (of type II).

The outcome of the optimization can be biased by the original set of cuts placed by the user for the first cycle, halting at a local maximum. To reduce the effects of this, the optimization procedure is repeated a couple of times using different starting sets. The most optimal set of cuts is taken as the final selection.

4.1.4 Multiple candidates selection

It is possible that, in a single event, more than one B candidate survives the final selection for a specific mode. This happens in $40-70\%$ of the events. The average multiplicity (B candidates per event) is between $3-5$ per multiplicative event, depending on the decay mode and the selection. The best candidate in the event is selected on the basis of a χ^2, computed for each candidate. For the $B^0 \to D^- a_0^+$ decay this χ^2 is defined as

$$\chi^2 = \left(\frac{m_\eta - m_\eta^{PDG}}{\sigma_{m_\eta}} \right)^2 + \left(\frac{m_{D^\pm} - m_{D^\pm}^{PDG}}{\sigma_{m_{D^\pm}}} \right)^2, \tag{4.7}$$

where m_x is the mass of meson x, m_x^{PDG} is the meson mass as listed in the PDG [9], and σ_{m_x} is the Gaussian width of its mass distribution. The χ^2 for the $B^0 \to D^{*-} a_0^+$ decay is defined by

$$\chi^2 = \left(\frac{m_\eta - m_\eta^{PDG}}{\sigma_{m_\eta}} \right)^2 + \left(\frac{\Delta m - \Delta m^{PDG}}{\sigma_{\Delta m}} \right)^2, \tag{4.8}$$

where Δm is defined as the mass difference between the reconstructed $D^{*\pm}$ meson and the nominal D^0 mass, and Δm^{PDG} is the mass difference as listed in the PDG. The candidate with the smallest χ^2 is selected.

Many more variables could be used to define the χ^2, such as ΔE or $m_{\rm ES}$, however this would create a bias in the analysis, moving background events toward the signal area.

4.2 Selection variables

This section describes the variables that are used to reduce the number of background events. Every defined variable has a power to discriminate signal from background events. Optimized selection variables that do not hold unique discriminative powers, that is if they are removed the selection does not change, are removed from the selection set and not described in this section. Roughly speaking we can separate the selection variables in two categories. The first are variables that discriminate between continuum $q\overline{q}$ events and B events; these are described in Sect. 4.2.1. The second set of variables, described in Sect. 4.2.2, are discriminatory toward signal events.

Any figure shown in this section is produced with the skimmed Monte Carlo data and shows the distribution of the selected events in the DstI decay mode or, if stated explicitly, in the DchI or DchII decay mode. Some cuts are placed to select the signal area: m_{ES} <5.27 GeV/c^2 (except for the m_{ES} plot itself), $|\Delta E| < 100\,\mathrm{MeV}$ and a converged **TreeFitter** fit. Non-resonant $B^0 \to D^{(*)-}\eta\pi^+$ and other over-abundantly produced background states, see Sect. 3.1.2, are removed from the shown generic B Monte Carlo samples.

4.2.1 Continuum background suppression

The $\Upsilon(4S)$ resonance is little over twice as heavy as the B mass. In the $\Upsilon(4S)$ frame the produced B meson pair is therefore almost at rest. The subsequent decay of the B mesons is therefore highly isotropic. The mass of the u, d, s and c quarks are much lighter than the b quark mass. Hence, the decay of continuum background events have a jet-like topology. A reconstructed B mass in such an event would require to utilize particles from more than one jet.

Variables that are sensitive to this geometrical difference are called *event shape* variables. In this section the different event shape variables are described.

The thrust of the B event

The thrust of an events is defined by [70]

$$T = \frac{\sum_i |\hat{T} \cdot \mathbf{p}^*{}_i|}{\sum_i |\mathbf{p}^*{}_i|}, \tag{4.9}$$

where $\hat{T}$ is direction to which the thrust is calculated, $\mathbf{p}_i^*$ is the momentum in the $\Upsilon(4S)$ frame, and the summation sums over all the particles in the event. Thrust is a measure of the alignment of the particles within an event and has a quantity in the range (0.5, 1.0). We calculate the thrust using the direction of the reconstructed B as $\hat{T}$. The lower the thrust, the more spherical the event is, the higher the thrust the more momenta lie collinear to the reconstructed B momentum and thus the more jet-like the event is. The distribution of the thrust is plotted in Fig. 4.3 for the different types of events.

The thrust angle

The thrust axis is the vector where the thrust, calculated by Eq. (4.9) is maximal. The thrust angle, θ_T, is defined as the angle between the thrust axis of the B candidate and the thrust axis of the rest of the event. In a perfectly isotropic event, there is no relation between the thrust axis and the B momentum. The distribution of this variable for $B\overline{B}$ events is therefore flat. If the B meson is reconstructed in a continuum background event, the thrust axis is collinear with the B meson direction and thus peaks at $|\cos\theta_T| \sim 1$, as is shown in Fig. 4.3.

In a similar way the thrust and the thrust angle can be calculated considering only the reconstructed B meson. This information is used in the Fisher discriminant that is described on page 68.

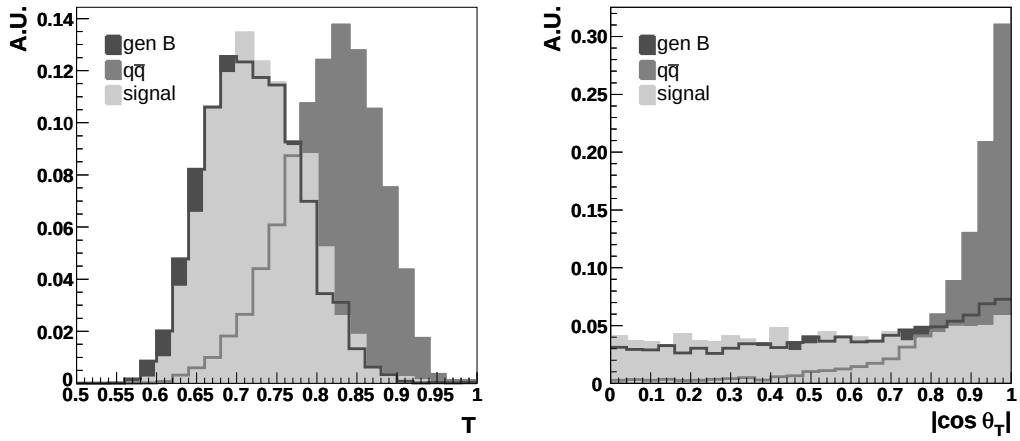

Figure 4.3: Normalized distributions of the thrust (*left*) and thrust angle (*right*) distributions for signal, generic B and $q\overline{q}$ events.

The sphericity of the event

The sphericity tensor is defined as [71],

$$S^{\alpha\beta} = \frac{\sum_i p_i^\alpha p_i^\beta}{\sum_i \mathbf{p}_i^2}, \tag{4.10}$$

where $\alpha, \beta = 1, 2, 3$ corresponds to the x, y, z components of the momentum (in the $\Upsilon(4S)$ frame) vector $\mathbf{p}_i^*$, the summation sums over all the particles in the event. By standard diagonalization of $S^{\alpha\beta}$ one finds three eigenvalues $\lambda_1 \geq \lambda_2 \geq \lambda_3$, and $\lambda_1 + \lambda_2 + \lambda_3 = 1$. The sphericity of the event is then defined as

$$S = \frac{3}{2}(\lambda_2 + \lambda_3), \tag{4.11}$$

so that $0 \leq S \leq 1$. Sphericity is a measure of the summed $p_\perp^2$ with respect to the event axis. A two-jet event corresponds to $S \sim 0$ and an isotropic B event to $S \sim 1$.

The sphericity angle

The sphericity angle θ_S, is defined as the angle between the momentum direction of the B candidate and the sphericity axis, which is the eigenvector corresponding to largest eigenvector, λ_1. The isotropic character of the B decays causes the distribution of $|\cos\theta_S|$ to be flat for correctly reconstructed B mesons and will peak at ~ 1 for continuum background events, as is shown in Fig. 4.4.

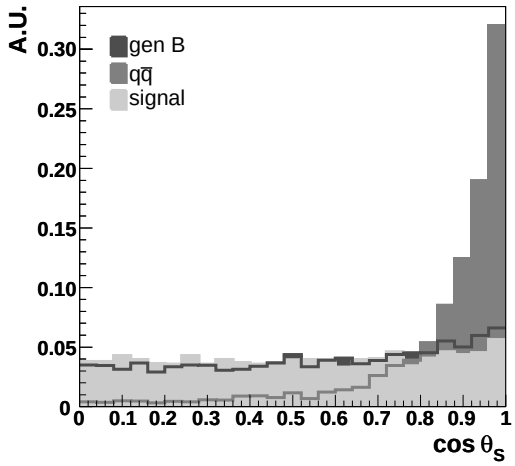

Figure 4.4: Normalized distribution of the sphericity angle for signal, generic B and $q\overline{q}$ events.

The normalized second Legendre moment

The normalized second Legendre moment is defined as

$$\frac{\mathcal{L}_2}{\mathcal{L}_0} = \frac{\sum_i |\mathbf{p}_i^*| \cos^2 \theta_i}{\sum_i \mathbf{p}_i^*}, \tag{4.12}$$

where θ_i is the angle between the momentum direction in the $\Upsilon(4S)$ frame $\mathbf{p}_i^*$ and the thrust angle. The summation sums over all the particles in the event. $\mathcal{L}_2/\mathcal{L}_0$ is defined in the range (0, 1). A perfect two-jet event has $\mathcal{L}_2/\mathcal{L}_0 = 1$, more isotropic events have values close to 0.5. The distribution for different kind of events are shown in Fig. 4.5.

The normalized second Fox-Wolfram moment

The Fox-Wolfram moments $\mathcal{H}_l$, where $l = 0, 1, 2, \ldots$, are defined as [72],

$$\mathcal{H}_l = \sum_{i,j} \frac{|\mathbf{p}_i^*||\mathbf{p}_j^*|}{E_{vis}^2} \mathcal{P}_l \left(\cos \theta_{ij}\right), \tag{4.13}$$

where θ_{ij} is the opening angle between hadrons i and j and E_{vis} the total visible energy of the event. Autocorrelations, i.e. $i = j$, are included. The $\mathcal{P}_l(x)$ are the well-known Legendre polynomials.

The normalized ratio $R2 = \mathcal{H}_2/\mathcal{H}_0$, has values in the range (0, 1). $R2$ values closer to 0 indicate a more spherical event, values closer to one a more jet-like event. The distribution of $R2$ for signal and background events are shown in Fig. 4.5.

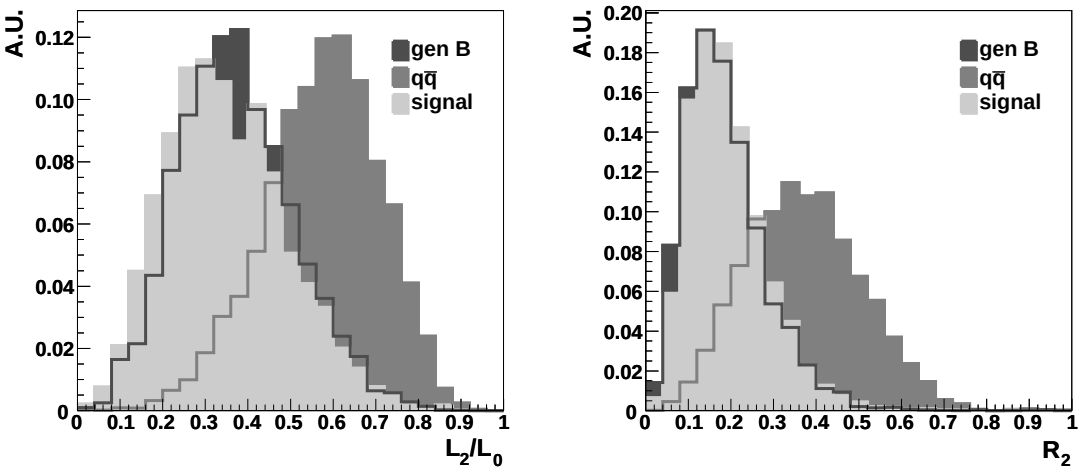

Figure 4.5: Normalized distribution of $\mathcal{L}_2/\mathcal{L}_0$ (*left*) and $R2$ (*right*) for signal, generic B and $q\overline{q}$ events.

Momentum flow

The space around the thrust axis $\mathbf{T}$, can be divided into nine cones, each of which covers an angle $\Delta\theta = \frac{\pi}{18}$. The nine cones together cover $\Delta\theta = \frac{\pi}{2}$, and the space beyond, is mirrored into this region. The momentum flow

$$p_i = \sum_j |\mathbf{p}_{ij}^*|, \tag{4.14}$$

is defined as the scalar sum of all momenta $\mathbf{p}_j^*$, in the $\Upsilon(4S)$ frame, found inside the ith cone. In general, more energy is found in the cones nearer the candidate thrust axis in jet-like continuum background events than in the more isotropic $B\overline{B}$ events. This variable is one of the variables used in the Fisher discriminant, described next.

The Fisher discriminant

A Fisher discriminant is a linear combination of a set of measurements. The coefficients of the Fisher discriminator are determined in a way that maximizes its overall ability to discriminate between signal and background events [73].

The Fisher discriminant $\mathcal{F}$ combines eleven different event shape variables, the helicity angle of the B meson ($\cos\theta_B$), defined in the next section, the thrust angle of the B meson ($\cos\theta_{T_B}$) and the nine different momentum flow cones. In equation form,

$$\mathcal{F} = \sum_{i=1}^{11} \alpha_i x_i. \tag{4.15}$$

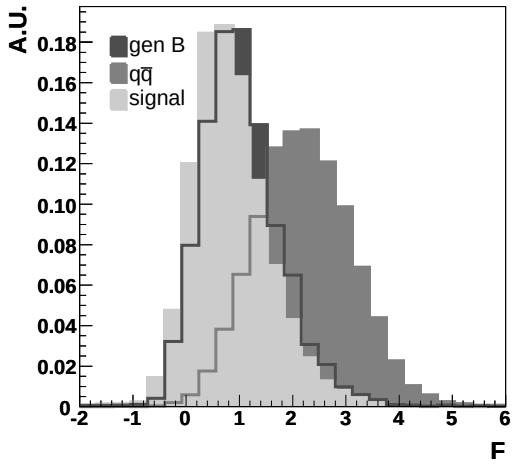

Figure 4.6: Normalized distribution of the Fisher discriminant for signal, generic B and $q\overline{q}$ events.

The coefficients α_i are optimized for the discrimination between B decays and continuum background. We have used the optimized coefficients taken from Ref. [74]. The Fisher distribution for the different types of events is given in Fig. 4.6.

4.2.2 Signal event selection variables

In the previous section we have presented variables that discriminate between B events and continuum background events. In this section the variables are presented that discriminate between the specific $B^0 \to D^{(*)-}\eta\pi^+$ and $B^0 \to D^{(*)-}a_0^+$ signal events, and all other background events.

The ΔE variable

The *energy difference* ΔE is defined as

$$\Delta E = E^* - E^*_{beam}, \tag{4.16}$$

where E^* is the energy of the reconstructed B meson in the $\Upsilon(4S)$ frame, E^*_{beam} is half the $\Upsilon(4S)$ energy. Because the $\Upsilon(4S)$ decays into exactly two B mesons with no additional particles, E^*_{beam} is the best estimate for the B energy. As E^*_{beam} is very accurately known from the accelerator center of mass energy, the resolution of ΔE is dominated by the measurement of E^* which is in turn dominated by the momentum resolution and depends on the reconstructed decay chain. Correctly reconstructed decays will spread around $\Delta E = 0$. Incorrectly identified particles, missing or additional tracks in the reconstruction lead to a shift in ΔE. For example, a reconstructed decay where one pion too many has been assigned to the reconstructed B decay, has a $\Delta E \sim \mathrm{m}_\pi$. Figure 4.7

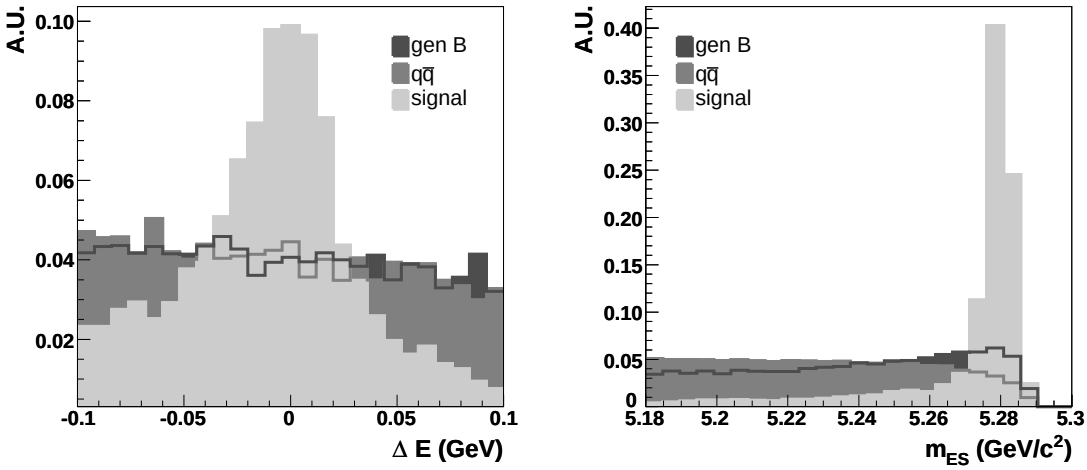

Figure 4.7: Normalized distributions for ΔE (*left*) and $m_{\rm ES}$ (*right*) for signal, generic B and $q\overline{q}$ events.

shows the distribution for the different types of events in a region of 200 MeV around zero.

The $m_{\rm ES}$ variable

The *beam energy substituted mass* is defined as

$$m_{\rm ES} = \sqrt{E^{*2}_{beam} - \mathbf{p}^{*2}_B}, \tag{4.17}$$

where $\mathbf{p}^*_B$ is the momentum of the reconstructed B candidate in the center of mass rest frame. Since $|\mathbf{p}^*_B| \ll E^{*2}_{beam}$, the experimental resolution on $m_{\rm ES}$ is dominated by beam energy fluctuations. Signal events are centered around the B meson mass. Background events can be separated in a combinatorial and a peaking component.

The combinatorial background is distributed as an Argus function described by [75]

$$\mathtt{A}(m_{\rm ES}; m_0, \xi) = m_{\rm ES} \cdot \sqrt{1 - (m_{\rm ES}/m_0)^2} \cdot e^{\xi\left(1-(m_{\rm ES}/m_0)^2\right)}, \tag{4.18}$$

where m_0 is the upper kinematic limit fixed at the beam energy, and ξ controls the slope of the function.

A peaking background event has a similar decay constitution to a signal event and therefore constructs a B mass in the B mass region and peaks around ΔE =0. An example of such a decay is $B^0 \to D^{(*)-} D^+_s$, where $D^+_s \to \eta\pi^+$: this decay produces the same final state particles as the $B^0 \to D^{(*)-} a^+_0$ or $B^0 \to D^{(*)-}\eta\pi^+$ signal decay modes.

The peaking background is not covered by the Argus function and is a Gaussian like distribution centered at the B mass. The contribution of this distribution can be determined with Monte Carlo studies. The total normalized distributions for the signal and background components are presented in Fig. 4.7.

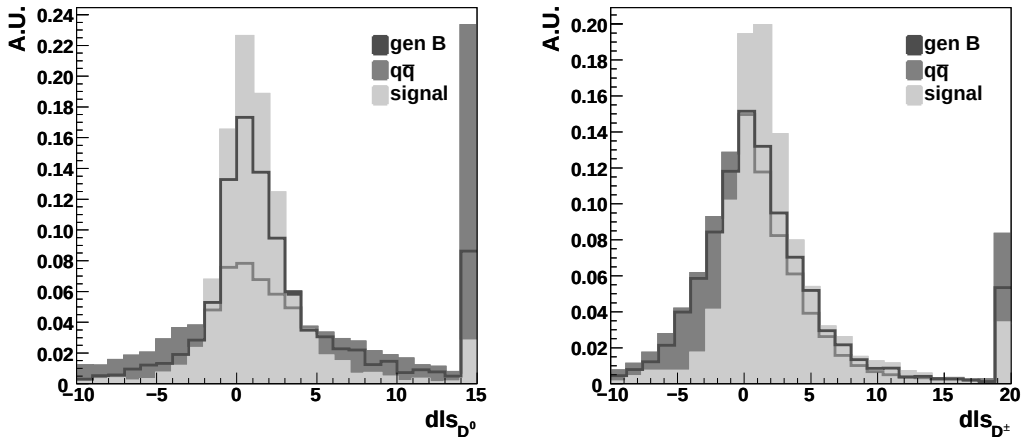

Figure 4.8: Normalized distribution for the decay length significance of the reconstructed D^0 (*left*) or $D^\pm$ (*right*) meson for signal, generic B and $q\overline{q}$ events reconstructed in the DstI (*left*) and DchII (*right*) decay mode. The last bin shows the overflow, or integral of the area on the right of the plotted region.

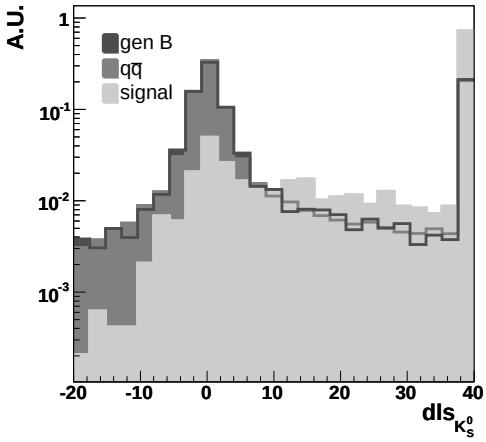

Figure 4.9: Normalized distribution for the DchII mode of the decay length significance of the K^0_S meson for signal, generic B and $q\overline{q}$ events. The last bin shows the overflow, or integral of the area on the right of the plotted region.

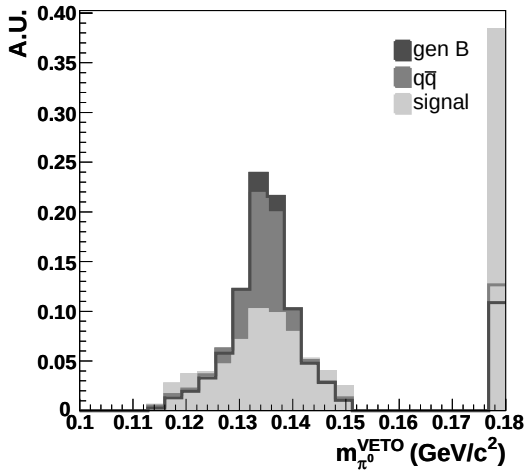

Figure 4.10: Normalized distribution of the reconstructed π^0 veto mass for signal, generic B and $q\overline{q}$ events in the DchII decay mode. The last bin shows the reconstructed π^0's that where not considered as potential π^0 candidates.

The decay length significance

For mesons with a relatively large lifetime, the K_S^0, the D^0, and the D^+ mesons, we calculate a decay length significance, *dls*. Figures 4.8 and 4.9 show the decay length significance distributions.

The overlapping photon veto

Both π^0 mesons and η mesons can decay into two photons. In a typical *BABAR* event η mesons are outnumbered by the produced π^0's, and thus most of the photons originate from a π^0 decay. A reconstructed η meson that passes all the selection criteria, can still be reconstructed from two random photons in the event. The chance that one of the random photons originates from a π^0 decay are high.

We pair each of the two selected photons with any other photon found in the event, and calculate the invariant mass of the new pair. When this is close to the π^0 mass the η meson candidate is vetoed.

Figure 4.10 shows the normalized distributions of the reconstructed π^0 mass.

Helicity angles

Another powerful method for suppressing backgrounds is to exploit the spin structure of the $e^+e^- \to \Upsilon(4S) \to B^0 \to D^{(*)-}a_0^+$ decay chain.

In the reaction, $Y \to X \to a+b$, the helicity angle of particle a, is the angle measured in the rest frame of the decaying parent particle, in this case X, between the direction of

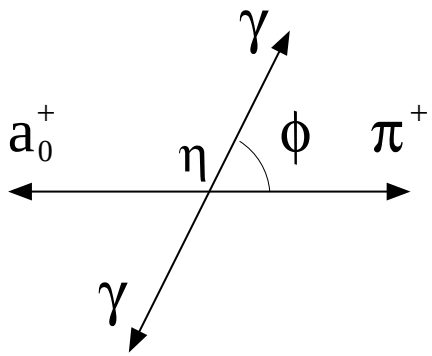

Figure 4.11: Helicity angle of the photons in the $a_0^+ \to \eta\pi^+(\eta \to \gamma\gamma)$ decay. The angle is measured between the a_0^+, or π^+, and the γ in the a_0^+ rest-frame.

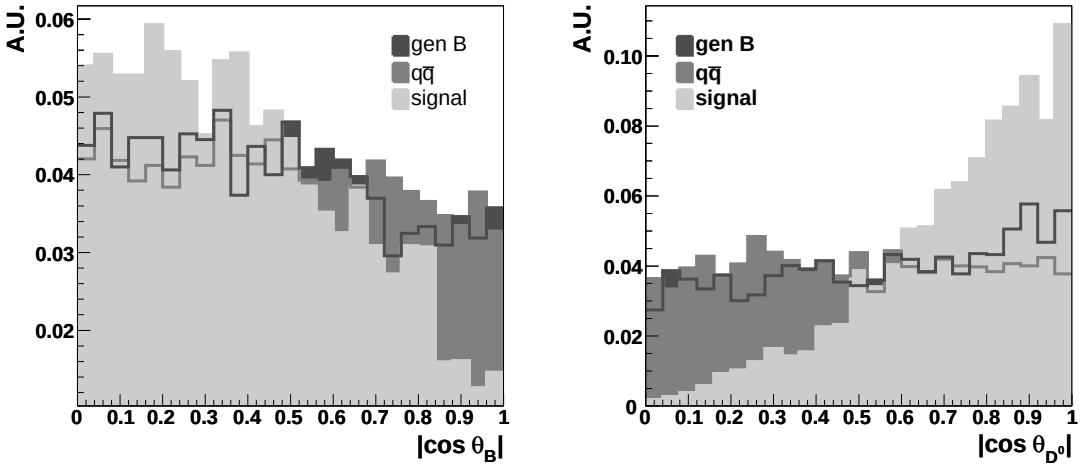

Figure 4.12: Normalized distributions of the cosine of the helicity angle of the B (*left*) and D^0 (*right*) for signal, generic B and $q\overline{q}$ events.

the decay daughter, a, and the direction of the grandparent particle, Y. As an example, the helicity angle of the photons originating from the η decay is schematically drawn in Fig. 4.11.

In the decay chain $e^+e^- \to \Upsilon(4S) \to B\overline{B}$, the $\Upsilon(4S)$ is produced with helicity $\lambda_{\Upsilon(4S)} = \pm 1$. The $\Upsilon(4S)$ decays into two (spin-zero) B mesons. The angular distribution is then given by a scaling factor multiplied with the squared Clebsch-Gordan coefficient, which is given by

$$D^{J_X}_{\lambda_X, \lambda_a - \lambda_b} = D^1_{1,0}, \tag{4.19}$$

which gives a $\sin^2\theta$ distribution. Any angular distribution that is expected in the background will be smeared because the decay will be mis-reconstructed, background events

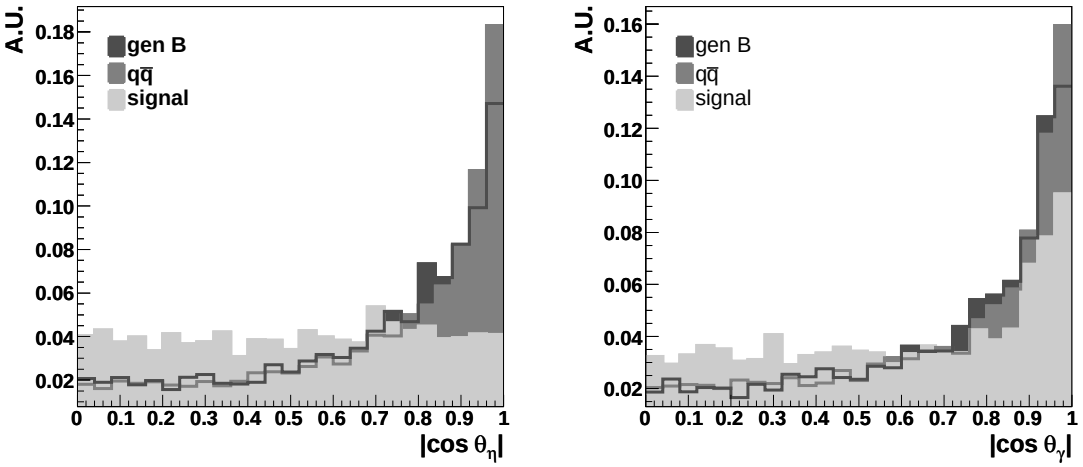

Figure 4.13: Normalized distributions of cosine of the helicity angle of the η (*left*) and the γ (*right*) for signal, generic B and $q\overline{q}$ events.

are thus expected to have a flat distribution. The normalized B helicity angle distribution for signal and background Monte Carlo samples are shown in the left plot in Fig. 4.12.

The D^0 helicity angle distribution is shown the right plot in Fig. 4.12. The decay $D^{*\pm} \to D^0\pi^\pm$, is a vector to two pseudoscalar decay. The helicity of the parent D^* must be zero, it was produced in a B decay (spin-zero) and the helicity difference of the daughters must also be zero as they are both pseudoscalars. The signal events are therefore distributed as $\cos^2\theta$. Random tracks that are assigned as the slow pion, from the D^* decay, create combinatorial background that is distributed flat, since there is no preferred angle.

The η meson is produced in the scalar to two pseudoscalars decay $a_0 \to \eta\pi$. The spin of the parent a_0 is zero so the distribution of the η helicity angle must be flat. The distribution of the η helicity angle is presented in the left plot in Fig. 4.13. The background, from B mesons and $q\overline{q}$, is not flat but peaks at $|\cos\theta| = 1$. This corresponds with a decay where the momentum of the η or the pion, from the a_0 decay, fly parallel to the D^* and B meson. In $q\overline{q}$ events this can be understood because of the jettiness of the events. The generic B background peaks at $\cos\theta = -1$. The η momentum is then aligned with the $D^{*\pm}$ momentum in the a_0 rest-frame. These are background decays that have a correctly reconstructed $D^{*\pm}$ or $D^\pm$ meson, but a mis-reconstructed η or $\pi^\pm$. Dominant background modes that peak at $|\cos\theta| \sim 1$ are $B^0 \to D^{*+}\pi^-\pi^0$, $B^0 \to D^{*+}\rho^-$, $B^0 \to D^{*+}a_1^-$ and $B^0 \to D^{*+}l^-\nu_l$. In the non-leptonic modes the photons of the neutral pion are then assigned to the η meson.

Two photons are produced by the pseudoscalar η meson, giving a flat distribution in the γ helicity angle. The right plot in Fig. 4.13 shows the helicity angle distributions of one of the photons. The signal shows a flat distribution with a small peak around 1,

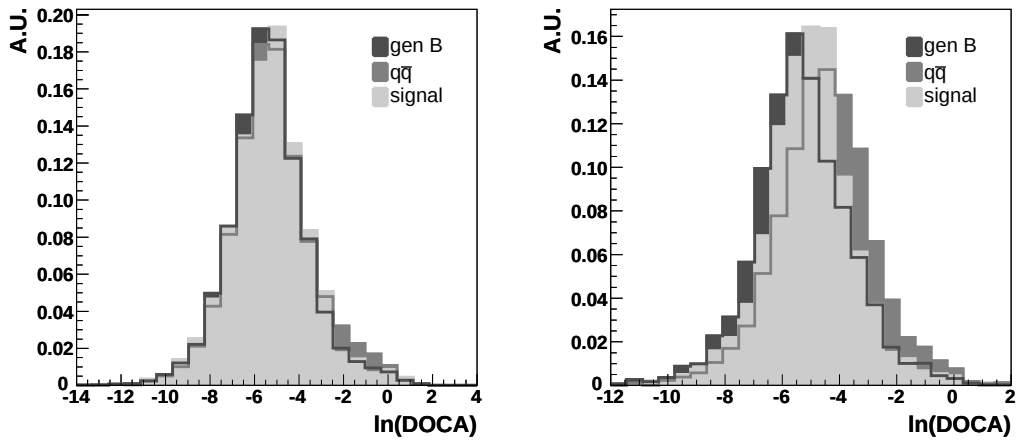

Figure 4.14: Normalized distribution of the ln($DOCA$) for signal, generic B and $q\overline{q}$ events, reconstructed in the DchII (*left*) and DstI (*right*).

due to mis-reconstruction of η mesons. The peaking behavior in the $q\overline{q}$ events can be understood in the same way as the η helicity, the photons are either parallel or anti-parallel. The peaking behavior of the generic B Monte Carlo sample is dominated by the $B^0 \to D^{*+}\pi^-\pi^0$, resonant and non-resonant decay modes.

The distance of closest approach

The distance of closest approach, or $DOCA$, is defined as the calculated distance between the bachelor pion and the $D^{\pm}$ trajectory or the reconstructed D^0 trajectory, for $B^0 \to D^- a_0^+$ and $B^0 \to D^{*-} a_0^+$ decays, respectively. Properly reconstructed events should have a DOCA consistent with zero, whereas random combinations can lead to large values. The normalized distributions for $B^0 \to D^- a_0^+$ and $B^0 \to D^{*-} a_0^+$ decays are shown in Fig. 4.14.

The χ^2 consistency of the decay chain fit

The distribution of the χ^2 consistency of the global-decay-chain fit performed by **TreeFitter** is shown in Fig. 4.15. In case the assumed signal hypothesis is correct, this is expected to be distributed uniform over the range (0, 1). If the hypothesis is wrong, small values are expected.

Particle mass, momentum and angle

Furthermore, the mass, m, momentum, p, and angles, polar angle, θ, and azimuthal angle, ϕ, are used as discriminatory variables.

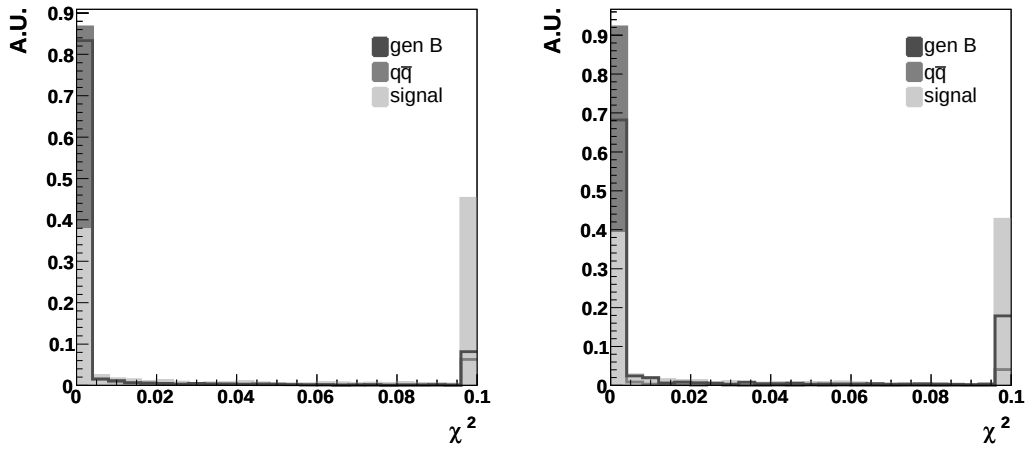

Figure 4.15: The χ^2 consistency distributions for signal, generic B and $q\overline{q}$ events. The left (*right*) plot shows the distribution for DchII (DstI) reconstructed events. Both plots show the integral of the region to the right of the plotted area.

4.3 Final selection

The results of the optimization procedure are presented in Table 4.1. Selection powers of the individual variables are summarized in App. A. Variables that do not add any selection power with respect to the other variables, *i.e.* when removal of the variable does not make a difference, have been removed from the list.

As can be seen from Table 4.1, the optimized cut positions in the variables can vary between different $D^{(*)\pm}$ meson decay modes. This is caused by a couple of reasons. First, the different various $D^{(*)\pm}$ meson decays have different fractional branching ratios. In the optimization procedure this will lead to a tighter (smaller branching ratio) or more loose selection (higher branching ratio). Second, there is the composition of particles in the reconstructed decay mode that lead to differences. For example the π^0 in the $B^0 \to D^{*-} a_0^+$ ($D^{*+} \to D^0\pi^+$, $D^0 \to K^-\pi^+\pi^0$) decay leads to the selection of more background events. Many π^0 mesons are produced in an average B decay event and as a result more B candidates will meet the selection criteria. Also some particles provide variables that are effective to reduce background, such as the decay length significance in the $dls_{K^0_S}$, this will then release the pressure on the other variables in the optimization. Third, correlations between variables and a difference in starting position in the variable phase space for the optimization cause differences in the optimization output.

The number of events in the Monte Carlo datasets, at different stages of the selection are summarized in Table 4.2. The total selection has a high background reduction power and a relatively high signal efficiency.

variable	DchI	DchII	DstI	DstII	DstIII	DstIV
$m_{\mathrm{ES}} >$	5.22	5.22	5.22	5.22	5.22	5.22
$\lvert\Delta E\rvert <$	0.1	0.1	0.1	0.1	0.1	0.1
$\chi^2 >$	0.0255	0.0499	0.01	0.01	0.01	0.01
$\lvert\cos\theta_T\rvert <$	0.905	0.959	0.996	0.738	0.972	0.98
$\lvert\cos\theta_B\rvert <$	0.953	0.964	0.89	0.775	0.891	0.81
$\lvert\cos\theta_S\rvert <$	0.872	0.851	0.931	0.868	0.901	0.889
$\lvert\mathrm{T}\rvert <$	0.919	0.847	0.853	-	0.83	-
$ln(DOCA) <$	0.95	-1.77	-1.22	-1.74	0.459	-1.11
$\mathcal{F} <$	0.923	1.4	1.55	1.79	1.02	1.83
$\lvert m_{D^\pm} - m_{D^\pm}^{PDG}\rvert <$	0.0132	0.0445	-	-	-	-
$dls_D >$	0	0	-	-	-	-
$\lvert p_K^*\rvert <$	1.9	-	-	-	-	-
$\lvert p_{\pi 2}^*\rvert >$	0.0723	-	-	0.119	-	-
$\lvert m_\eta - m_\eta^{PDG}\rvert <$	0.0235	0.0289	0.0349	0.0305	0.0278	0.0256
$\lvert p_\eta^*\rvert >$	0.64	0.679	0.68	0.7	0.628	-
$\lvert m_{\pi^0}^{VETO} - m_{\pi^0}^{PDG}\rvert >$	0.00344	9.8e$-$05	0.00533	0.00657	0.00423	0.005
$\lvert\cos\theta_\eta\rvert <$	0.822	0.852	0.787	0.812	0.768	0.86
$\lvert E_{\pi B}\rvert <$	2.2	2.29	2.37	2.21	-	-
$\lvert p_{\pi B}^*\rvert <$	1.61	1.61	1.59	1.5	1.46	1.54
$\lvert\theta_\pi\rvert <$	2.35	-	2.57	-	-	-
$\lvert E_\gamma\rvert >$	0.224	0.191	0.188	0.208	-	0.061
$\lvert\mathcal{L}_2/\mathcal{L}_0\rvert <$	0.524	0.517	0.603	0.481	0.567	0.55
$\lvert m_{K_S^0} - m_{K_S^0}^{PDG}\rvert <$	-	0.0153	-	-	-	0.0168
$\lvert dls_{K_S^0}\rvert >$	-	4.89	-	-	-	6.46
$\lvert p_{\pi 1}^*\rvert >$	-	0.391	-	-	-	-
$\lvert E_\eta\rvert >$	-	0.738	0.77	-	-	-
$\lvert\mathrm{R2}\rvert <$	-	-	0.467	0.342	-	0.431
$\lvert m_{D^{*\pm}} - m_{D^{*\pm}}^{PDG}\rvert <$	-	-	0.00295	0.00272	0.00332	0.0028
$\lvert\cos\theta_{D^*}\rvert >$	-	-	0.185	0.292	0.273	0.187
$\lvert\cos\theta_{a_0}\rvert <$	-	-	0.998	0.94	0.994	-
$\lvert m_{D^0} - m_{D^0}^{PDG}\rvert <$	-	-	0.09	0.0662	-	0.02
$\lvert\theta_{D^0}\rvert <$	-	-	1.89	-	1.81	-
$-2 < dls_D <$	-	-	6.9	5.24	4.76	5.02
$\lvert\phi_K\rvert >$	-	-	0.0128	-	-	-
$\lvert p_{\pi 1}^*\rvert <$	-	-	2.25	2.12	1.55	-
$\lvert p_{S\pi}\rvert >$	-	-	0.0784	0.08	0.0748	-
$\lvert\phi_{S\pi}\rvert >$	-	-	0.0346	-	-	-
$\lvert p_K^*\rvert >$	-	-	-	-	0.228	-
$\lvert p_{\pi 3}^*\rvert >$	-	-	-	-	0.0621	-

Table 4.1: Summarized result for the optimized variable cuts. Energies are given in GeV, momentums in GeV/c, masses and mass differences in GeV/c^2 and angles in rad. All cosined angles are helicity angles.

	DchI				DchII			
	SigMC	NonRes	$B\overline{B}$	$q\overline{q}$	SigMC	NonRes	$B\overline{B}$	$q\overline{q}$
skim	26947	99250	6265105	10459061	7143	20990	1742462	4951231
selection	3896	7710	3814	1619	1061	1373	1129	650
a_0 box	2773	1048	53	7	781	196	27	2
	DstI				DstII			
	SigMC	NonRes	$B\overline{B}$	$q\overline{q}$	SigMC	NonRes	$B\overline{B}$	$q\overline{q}$
skim	6847	20242	504851	479780	19670	100527	4100912	4355261
selection	1434	2268	1215	169	1328	1449	806	162
a_0 box	1019	365	28	0	907	212	13	0
	DstIII				DstIV			
	SigMC	NonRes	$B\overline{B}$	$q\overline{q}$	SigMC	NonRes	$B\overline{B}$	$q\overline{q}$
skim	16654	1284870	6631073	4379028	6990	41753	1800745	1162762
selection	1003	1631	953	118	359	529	340	46
a_0 box	727	272	21	2	248	84	4	1

Table 4.2: Number of events in the data sample at different stages of the selection, *skim* is the output of the skim, *selection* after the final selection and a_0 *box* is after the final selection only in the a_0 box.

4.4 Selected sample

This section describes the selected Monte Carlo data samples.

Table 4.3 presents the number of events in the different samples, the fraction of events that contain only one candidate, and the overall averaged multiplicity. As can be seen from the table, the fraction of single-candidate events ranges from 81% and 97% and the overall multiplicity lies between 1.03 and 1.23. The best-candidate-selection, described in Sect. 4.1.4, takes care of those events with multiple B candidates.

The peaking background events in the selected generic $B\overline{B}$ samples are summarized in Table 4.4. The generic B^+B^- samples show no significant peaking background modes, the highest contribution comes from $B^+ \to D^+\pi^+\pi^-\pi^0$, which has up to 5 events in the selected samples. Figure 4.16 shows the dominant background modes, in the DchI selection, distributed in the $\eta\pi$-invariant-mass spectrum.

The dominant background mode is the decay $B^0 \to D^{(*)-}D_s^+$. This mode peaks in the $\eta\pi$-invariant-mass distribution at the D_s^+ mass at 1.969 GeV/c^2, since the D_s^+ can decay via $D_s^+ \to \eta\pi^+$. This background mode poses no threat to the $B^0 \to D^{(*)-}a_0^+$ or $B^0 \to D^{(*)-}\eta\pi^+$ measurement because of its well defined narrow peak in the $\eta\pi$-invariant mass, far away from the a_0 resonance. In the fit routine, following this selection, a separate p.d.f. is setup to describe the D_s^+ peak. In fact, we will use these events as a control channel in the study of systematic uncertainties.

	DchI				DchII			
	Sig MC	NonRes	$B\overline{B}$	$q\overline{q}$	Sig MC	NonRes	$B\overline{B}$	$q\overline{q}$
events	3890	7716	3814	1619	1059	1375	1129	650
single cand	92%	93%	96%	97%	89%	91%	95%	98%
multiplicity	1.09	1.08	1.05	1.03	1.12	1.09	1.06	1.02
	DstI				DstII			
	Sig MC	NonRes	$B\overline{B}$	$q\overline{q}$	Sig MC	NonRes	$B\overline{B}$	$q\overline{q}$
events	1433	2269	1215	169	1325	1452	806	162
single cand	87%	91%	95%	97%	85%	85%	89%	90%
multiplicity	1.15	1.10	1.06	1.03	1.18	1.17	1.12	1.12
	DstIII				DstIV			
	Sig MC	NonRes	$B\overline{B}$	$q\overline{q}$	Sig MC	NonRes	$B\overline{B}$	$q\overline{q}$
events	1003	1631	953	118	359	529	340	46
single cand	84%	84%	92%	95%	89%	94%	93%	93%
multiplicity	1.17	1.19	1.09	1.05	1.12	1.07	1.08	1.07

Table 4.3: Number of events in the final selection, percentage of single candidate events and overal multiplicity of the selected data sample.

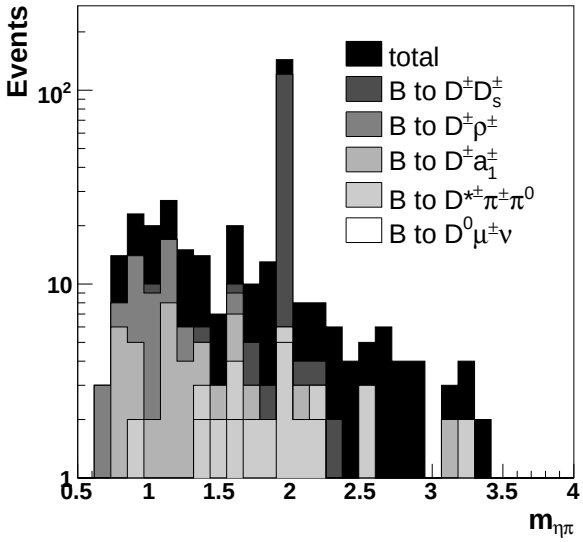

Figure 4.16: Peaking background distribution in the $\eta\pi$-invariant-mass spectrum for the DchI mode. The filled areas are incremented for the background modes quoted in the legend.

decay mode	DchI	DchII	DstI	DstII	DstIII	DstIV
generic $B\overline{B}$ backgrounds						
$B^0 \to D^+ D_s^-$	122	19	-	1	-	-
$B^0 \to D^+ \rho^-$	25	23	-	1	-	1
$B^0 \to D^+ A_1^-$	23	8	1	1	-	-
$B^0 \to D^{*+} \pi^- \pi^0$	15	3	19	6	6	5
$B^0 \to D^{*+} \mu^- \bar{\nu}$	7	-	-	-	2	2
$B^0 \to D^{*+} \rho^-$	7	4	19	5	7	4
$B^0 \to D^+ \bar{\nu}$	6	-	-	-	1	-
$B^0 \to D^{*+} A_1^-$	6	-	19	12	15	1
$B^0 \to K_S^0 X$	-	11	-	-	-	-
$B^0 \to D^+ K_S^0 \pi^-$	-	3	-	-	-	-
$B^0 \to D^{*+} D_s^-$	-	-	67	38	43	14
$B^0 \to D^+ \pi^- \pi^- \pi^+$	-	-	-	-	2	-

Table 4.4: Dominant background modes in the signal box specified as number of unscaled events per decay mode.

4.5 Signal selection efficiency

The efficiency of the resonant $B^0 \to D^{(*)-} a_0^+$ signal is defined as

$$\varepsilon \equiv \frac{N_{sel}}{N_{gen}}, \tag{4.20}$$

where N_{sel} is the number of selected events and N_{gen} the number of generated events. The efficiency is calculated per reconstructed decay mode and presented in Table 4.6. Note that the efficiency is calculated on type II Monte Carlo where the optimization is performed on type I Monte Carlo. For the calculation of the efficiency we have used only the events in the a_0 box, which places additional cuts in $m_{\rm ES}$, ΔE and $m_{\eta\pi}$, see page 61 for a definition.

The calculation of the efficiency of the $B^0 \to D^{(*)-}\eta\pi^+$ analysis is more difficult. First, we do not known how many events have been produced in the Monte Carlo datasets. The $B^0 \to D^{(*)-}\eta\pi^+$ events are generated by `Jetset` which makes it impossible to accurately find out how large the fraction of the produced $B^0 \to D^{(*)-}\eta\pi^+$ events is compared to the full Monte Carlo dataset. Secondly, the produced events are incorrectly simulated in the $m_{\eta\pi}$ phase-space due to the `Jetset` bug, see also Sect. 3.1.2. If the number of generated events would be known, still we would have to correct for the incorrect shape.

We calculate the $B^0 \to D^{(*)-}\eta\pi^+$ selection efficiency in two stages.
First, we determine the relative efficiency curve in the invariant $m_{\eta\pi}$ mass. We do this by dividing the distribution in $m_{\eta\pi}$ of the selected non-resonant events by the generated distribution. At this point we are not interested in the overall normalization but just in the shape. We subsequently fit the resulting distribution with a fifth order Chebychev polynomial of the first kind using a likelihood fit that is multiplied with two error

parameter	DchI	DchII	DstI	DstII	DstIII	DstIV
c_0	-1.25	-1.45	-8.76	-4.20	-6.56	0.46
c_1	0.29	0.29	0.64	0.58	0.73	0.57
c_2	-0.27	-0.29	-4.45	-1.74	-3.28	0.93
c_3	0.12	0.13	0.40	0.33	0.28	0.24
c_4	0.01	0.18	-1.39	-0.58	-1.00	0.12

Table 4.5: The fitted Chebychev parameters to the efficiency curves in the $m_{\eta\pi}$ mass range between 0-4 GeV/c^2.

	DchI	DchII	DstI	DstII	DstIII	DstIV
ϵ_{RS} (%)	5.75±0.09	9.8±0.3	8.6±0.02	2.21±0.06	3.09±0.10	4.51±0.23
ϵ_{NR} (%)	3.91±0.06	6.92±0.21	4.64±0.11	1.19±0.03	1.49±0.04	2.11±0.10

Table 4.6: Efficiency for the resonant (RS) and non-resonant (NR) signal selection for the different reconstructed modes.

functions, one for each kinematical limit of the phase space. The fitted Chebychev parameters are presented in Table 4.5. The resulting functions are used in the likelihood fit that follows this selection, described in Chapter 5. Subsequently, the resulting functions are multiplied with the theoretical distributions of the events defined in Eq. (5.4) resulting in the expected observed function in $m_{\eta\pi}$. This can be expressed as

$$f_{obs}(m_{\eta\pi}) = \varepsilon_{NR}(m_{\eta\pi}) \cdot f_{BW}(m_{\eta\pi}), \tag{4.21}$$

where f_{obs} is the observed distribution function, $\varepsilon_{NR}(m_{\eta\pi})$ is the calculated non-resonant efficiency curve and f_{BW} is the theoretical distribution.

Second, we compare the efficiency of the $B^0 \to D^{(*)-}a_0^+$ analysis in the area of 2 linewidths around the nominal a_0 mass, between 869 and 1097 MeV/c^2. In this area $\sim 95\%$ of the signal events are distributed. Since there are no selection criteria that distinguish the $B^0 \to D^{(*)-}a_0^+$ and the $B^0 \to D^{(*)-}\eta\pi^+$ events, we do not expect the efficiency curves to be any different from each other. The only difference is that the $B^0 \to D^{(*)-}\eta\pi^+$ events are distributed in a larger mass range compared to the $B^0 \to D^{(*)-}a_0^+$ events. Throughout this mass range the efficiency is not linear because selection variables, such as on the D^* momentum, induce kinematical constraints. Ignoring detector resolution effects, the efficiency curves in $m_{\eta\pi}$ for the $B^0 \to D^{(*)-}a_0^+$ events in the mass range $(869 < m_{\eta\pi} < 1097)\,\mathrm{MeV}/c^2$ are flat. We define

$$\varepsilon_{RS} \equiv \frac{N_{sel}^{RS}}{N_{gen}^{RS}} = \frac{N_{sel;x}^{RS}}{N_{gen;x}^{RS}} = \frac{N_{sel;x}^{NR}}{N_{gen;x}^{NR}}, \tag{4.22}$$

where $N_{state;x}$ is the number of events in the mass range x defined by $(869 < m_{\eta\pi} < 1097)\,\mathrm{MeV}/c^2$, and the RS (NR) superscription stands for the resonant (non-resonant) signal events.

We then calculate the expected efficiency of the $B^0 \to D^{(*)-}\eta\pi^+$ events distributed with the correct Breit-Wigner lineshape, using the efficiency determined on $B^0 \to$

$D^{(*)-}a_0^+$ events in the range $x = (869 < m_{\eta\pi} < 1097)\,\mathrm{MeV}/c^2$ using the following relation

$$\begin{aligned} \varepsilon_{NR} &= \frac{N_{sel}}{N_{gen}} = \varepsilon_{RS} \cdot \frac{N_{gen;x}}{N_{sel;x}} \times \frac{N_{sel}}{\cdot N_{gen}}, && (4.23) \\ &= \varepsilon_{RS} \frac{N_{sel}/N_{sel;x}}{N_{gen}/N_{gen;x}} = \varepsilon_{RS} \frac{1/f_{obs;x}}{1/f_{BW;x}}, && (4.24) \\ &= \varepsilon_{RS} \frac{f_{BW;x}}{f_{obs;x}}, && (4.25) \end{aligned}$$

where ε_{RS} is the efficiency of the resonant $B^0 \to D^{(*)-}a_0^+$ signal, N_{state} are for the non-resonant selection and $f_{state;x}$ is defined as the area of the function f_{state} in the area x relative to the full area.

The resulting calculated non-resonant signal efficiencies after the selection are presented in Table 4.6.

Chapter 5

Three dimensional likelihood fit

The two types of signal, resonant and non-resonant, and the background events that are present in the selected data sample are distinguished from each other by performing an unbinned likelihood fit.

This chapter presents the setup of the maximum likelihood fit. Sect. 5.1 describes the general setup. The different *probability density function* (p.d.f.) components of the fit are described in Sect. 5.2. The parameters, which define the various p.d.f.'s, are obtained from Monte Carlo samples and are summarized in Sect. 5.3. Section 5.4 shows the likelihood fit as fitted on Monte Carlo data. Efficiencies of the combined variable cuts and likelihood fit selections are presented in Sect. 5.5. The likelihood-fit performed on the selected data sample is presented in Sect. 5.6. The method that will be used to calculate the branching fractions from the obtained results is presented in Sect. 5.7.

5.1 Global fit setup

The aim of the fit is to distinguish between $B^0 \to D^{(*)-}a_0^+$, $B^0 \to D^{(*)-}\eta\pi^+$ and background events in the final selected data sets, making use of the different behavior in the combination of three observables.

Every reconstructed mode has its three-dimensional p.d.f. defined as the product of the p.d.f.'s of the three observables, $m_{\rm ES}$, ΔE and the $\eta\pi$ invariant mass, $m_{\eta\pi}$. This three-dimensional p.d.f. is a combination of different component p.d.f.'s that are defined for background and signal components. The components are: $B^0 \to D^{(*)-}a_0^+$ signal[1]; $B^0 \to D^{(*)-}\eta\pi^+$ signal; $B\overline{B}$ background events; specific $B^0 \to D^{(*)-}D_s^+$ background and $q\overline{q}$ ($q = u, d, s$) continuum background events. The p.d.f.'s are implemented and fitted using the `RooFit` C++ data modeling package [76].

The parameters that define the p.d.f.'s are fixed using Monte Carlo data. Only the number of events of the different components are free parameters in the final likelihood fit, the rest is fixed. The fit is defined in the following intervals: $(5.22 < m_{\rm ES} < 5.3)\,{\rm GeV}/c^2$, $(-0.1 < \Delta E < 0.1)\,{\rm GeV}$ and $(0 < m_{\eta\pi} < 4)\,{\rm GeV}/c^2$.

[1] In this chapter short notations are used in captions and tables for the following decays: $B^0 \to Da_0$ for $B^0 \to D^{(*)-}a_0^+$, $B^0 \to D\eta\pi$ for $B^0 \to D^{(*)-}\eta\pi^+$, and $B^0 \to DD_s$ for $B^0 \to D^{(*)-}D_s^+$

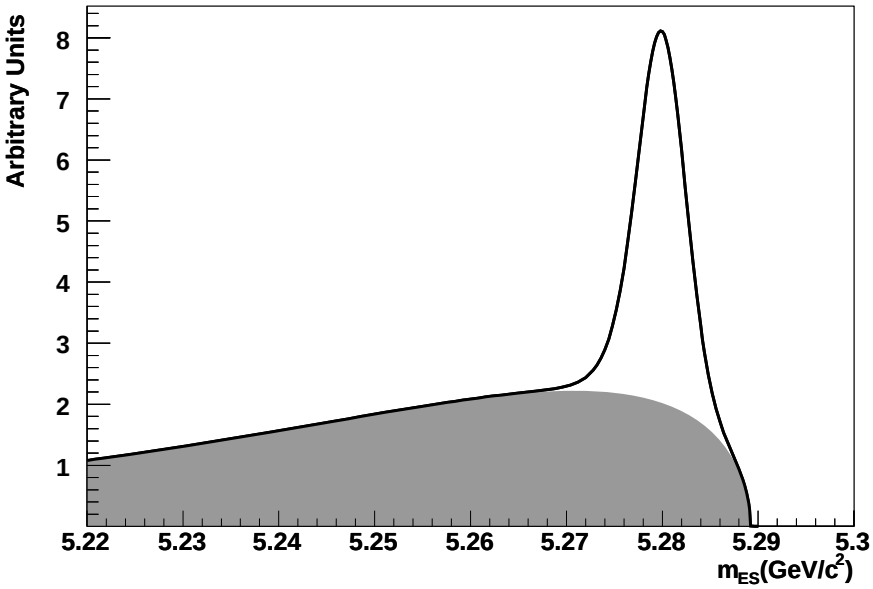

Figure 5.1: An example of the distribution in m_{ES}. The gray area shows an Argus function, the solid curve gives the stacked Cruijff distribution.

5.2 Description of probability density functions

Every component p.d.f. is defined in three dimensions, and is a product of three or more functions each defined in a single dimension. Different components of the total p.d.f. use a different set of functions. In this section the various functions used for the observables are described.

5.2.1 The m_{ES} distribution

Two different functions are defined for the m_{ES} observable described in Sect. 4.2.2.

The first is the Argus function defined in Eq. (4.18) on page 70 that describes combinatoric background events. The endpoint, m_0, of the Argus function is the upper kinematic limit and is fixed at the largest m_{ES} value found in the data set. The slope parameter, ξ, is determined on the Monte Carlo data set.

The second, is a *Cruijff* function [77] that describes signal events and the peaking background. Signal spreads around the B mass in the m_{ES} distribution. Two effects contribute to a tail on the left side of the B mass peak. First limited energy resolution in the EMC, due to energy loss in the DIRC, results in an asymmetric error on the measured energy of the reconstructed η. The second effect is the limited precision in the track reconstruction. Both effects lead to a bias toward lower m_{ES} values due to the low momentum of the B meson. The Cruijff function can describe these effects and is

defined as [77]

$$\texttt{Cr}(m_{ES};\sigma_{L,R},\alpha_{L,R},m_B) = \exp\left(\frac{-(m_{ES}-m_B)^2}{2\sigma_{L,R}^2+\alpha_{L,R}(m_{ES}-m_B)^2}\right). \tag{5.1}$$

The Cruijff function behaves as a Gaussian with separate widths, $\sigma_{L,R}$, on the left and the right side of the B mass, m_B, and a first order correction to this width, $\alpha_{L,R}$. All parameters are determined on Monte Carlo data distributions. For convergence reasons the parameters are limited to $\sigma_L = \sigma_R$, $\alpha_R = 0$ and $\alpha_L < 0.15$.

A combination of the Argus and Cruijff shapes is shown in Fig. 5.1.

5.2.2 The ΔE distribution

The ΔE observable is presented in Sect. 4.2.2. Two functions are used to describe ΔE. The first describes the background and is a first order polynomial Chebychev

$$\texttt{Ch}(\Delta E; c_0) = 1 + c_0 \cdot \Delta E. \tag{5.2}$$

The second is a Cruijff, now as a function of ΔE,

$$\texttt{Cr}(\Delta E;\sigma_{L,R},\alpha_{L,R},E_0) = \exp\left(\frac{-(\Delta E-E_0)^2}{2\sigma_{L,R}^2+\alpha_{L,R}(\Delta E-E_0)^2}\right), \tag{5.3}$$

and describes the signal, and peaking background such as the $B^0 \to D^{(*)-}D_s^+$ background events. In a perfect detector the ΔE is distributed as a perfect Gaussian around $E_0 = 0$. However, limited reconstruction precision and energy loss in reconstructed particles cause deformations. This can described by the Cruijff. Asymmetric Gaussian widths and exponential tail are allowed in the fit. All parameters are fixed on Monte Carlo samples. For fit stability the tails are limited to $\alpha_{L,R}<0.15$.

A combination of the Cruijff and the Chebychev polynomial is shown in Fig. 5.2.

5.2.3 The $\eta\pi$ invariant-mass distribution

Four different functions are used to describe the $\eta\pi$ invariant-mass distribution.

The first function is a relativistic Breit-Wigner lineshape function and is used to describe the mass resonances of the X meson (where $X \to \eta\pi$). It is described by

$$\texttt{BW}(m_{\eta\pi};M_B,M_D,m_0,\Gamma_0) = |A|^2 \cdot \underbrace{\frac{p_X}{M_B}\cdot\frac{p}{m_{\eta\pi}}\cdot m_{\eta\pi}}_{\text{phase-space factor}}, \tag{5.4}$$

and consists of the amplitude part $|A|^2$ multiplied with a phase-space factor, $m_{\eta\pi}$ is the observed mass of the X meson, M_B is the B meson mass and p (p_X) is the momentum of the π (X) in the X (B) rest frame. The amplitude is then expressed as

$$A = \frac{f_{BW}\cdot(p_X/p_{X,0})^{L_B}}{m_0^2 - m_{\eta\pi}^2 - i\cdot m_0\gamma}, \tag{5.5}$$

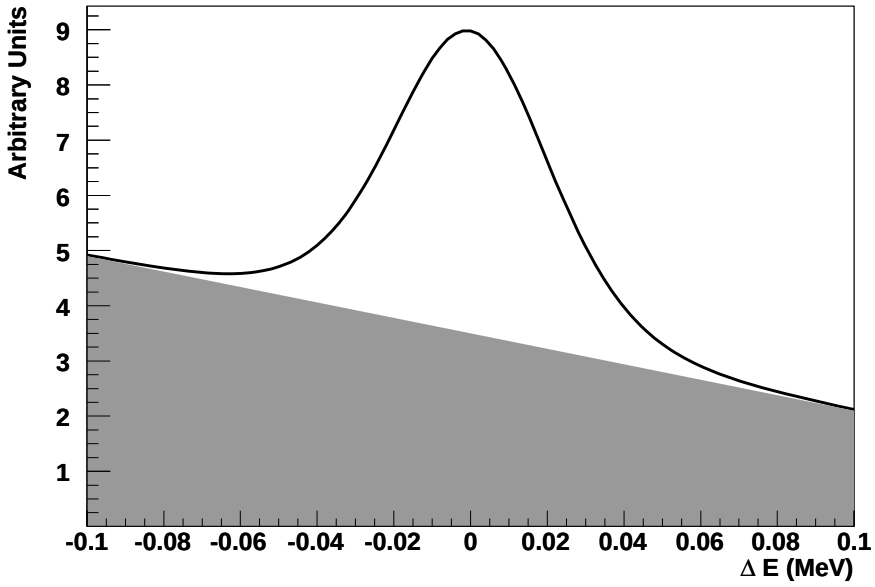

Figure 5.2: An average ΔE distribution. The gray area shows the Chebychev polynomial, the solid curve shows the stacked Cruijff distribution.

where $p_{X,0}$ is the X momentum in the B rest frame evaluated at the nominal mass m_0, L_B is the angular momentum of the B decay, and γ is the mass-dependent width given by

$$\gamma = \Gamma_0 \cdot \frac{p}{p_{X,0}} \cdot \frac{m_0}{m_{\eta\pi}} \cdot f_{BW}^2, \tag{5.6}$$

where Γ_0 is the width of the lineshape and f_{BW} is the *Blatt-Weisskopf* factor that depends on the spin of the meson X. Both the a_0 and the D_s meson have spin 0 so we write only the Blatt-Weisskopf factor

$$f_{BW} = 1, \text{ for } L_X = 0. \tag{5.7}$$

The *BABAR* event generator, `EvtGen`, that produces the $B^0 \to D^{(*)-}a_0^+$ and $B^0 \to D^{(*)-}D_s^+$ Monte Carlo simulated events, does not generate the correct lineshape. The `EvtGen` lineshape bug misses the $(p/m_{\eta\pi})$ phase-space factor in Eq. (5.4). Also, the lineshape in `EvtGen` is generated with the $L_B = 0$ component only. We correct for this bug by fitting the Monte Carlo events with a modified Breit-Wigner lineshape function that describes the generated function. The physical Breit-Wigner lineshape function is then used to fit the observed data. The masses M_B and M_D are taken from the PDG values. The a_0 lineshape parameters m_0 and γ_0 are fixed on the signal Monte Carlo data. The D_s^+ meson parameter m_0 is fixed on the generated nominal mass value for the fits to the Monte Carlo, and on the PDG value for the fits to the data samples. The D_s^+ linewidth is fixed on the fitted value to the Monte Carlo data.

The second function used, describes the non-resonant $B^0 \to D^{(*)-}\eta\pi^+$ decays, is the Breit-Wigner lineshape function as defined in Eq. (5.4) where $A = 1$. So only the phase space part of the function contributes. The non-resonant $B^0 \to D^{(*)-}\eta\pi^+$ Monte Carlo data are produced by `Jetset`. In Sect. 3.1.2 it is explained that due to a bug in `Jetset` the non-resonant Monte Carlo data are produced in a wrong way. Figure 3.2 on page 49 shows the impact of the `Jetset` bug . In order to describe the observed $B^0 \to D^{(*)-}\eta\pi^+$ events correctly we use the correct physical non-resonant Breit-Wigner lineshape function, multiplied with the efficiency as a function of the $\eta\pi$ invariant mass, as determined in Sect. 4.5.

The $B^0 \to D^{(*)-}\eta\pi^+$ Monte Carlo data are fitted with a third function and makes use of a so-called *keys* p.d.f.. This is an unbinned and non-parametric method that produces an estimation of the p.d.f. that describes the data; for a full description see Ref. [78]. The keys p.d.f. is also used to describe the $q\overline{q}$ background.

The fourth function is a fifth order Chebychev polynomial of the first kind and is used to describe the combinatoric background of mis-reconstructed B events. The fitting range in $m_{\eta\pi}$, between 0 and 4 GeV/c^2, is larger than the kinematic allowed range. In order to properly describe this, the Chebychev polynomial is multiplied with a two error functions, one mirrored to the other, both with a steep slope. This gives almost the same result as would the fit be performed in the region defined by the double error function.

A combination of the background and Breit-Wigner lineshape functions is plotted in Fig. 5.3. The lineshapes of the a_0^+ and D_s^+ mesons are well separated. The $B^0 \to D^{(*)-}D_s^+$ background does not influence the measurement of the $B^0 \to D^{(*)-}a_0^+$ branching ratio.

5.2.4 Background and signal component composition

The single dimension p.d.f.'s described in $m_{\rm ES}$, ΔE and $m_{\eta\pi}$ are now combined to form the three-dimensional component p.d.f.'s that describe the different background and signal distributions. The different combinations of functions that form the component p.d.f.'s are summarized in Table 5.1. The crosses, X, represent the one dimensional p.d.f.'s that are used to form the component p.d.f.. In three cases, (non-) resonant signal and generic $B\overline{B}$, the component p.d.f. itself is split up in two parts. The two parts are indicated with indexes I and II. This will be further explained below.

The $B^0 \to D^{(*)-}a_0^+$ signal Monte Carlo data are described by a combined p.d.f. that consists of two parts. In the reconstruction of $B^0 \to D^{(*)-}a_0^+$ signal a part is mis-reconstructed, explaining a background-like part, indicated with II, of the p.d.f.. The correctly reconstructed part is is indicated with I. A relative fraction between the two parts (correctly and mis-reconstructed) is determined on signal Monte Carlo data and is used for the determination of the signal selection efficiency. The data distribution is fitted with only part I, the mis-reconstructed events are taken care of by the generic $B\overline{B}$ p.d.f.. We define

$$S_T \equiv S + S_{MR}, \tag{5.8}$$

where S_{MR} is the number of mis-reconstructed signal events, S is the number of correctly reconstructed events and S_T is the total number of signal Monte Carlo events. The

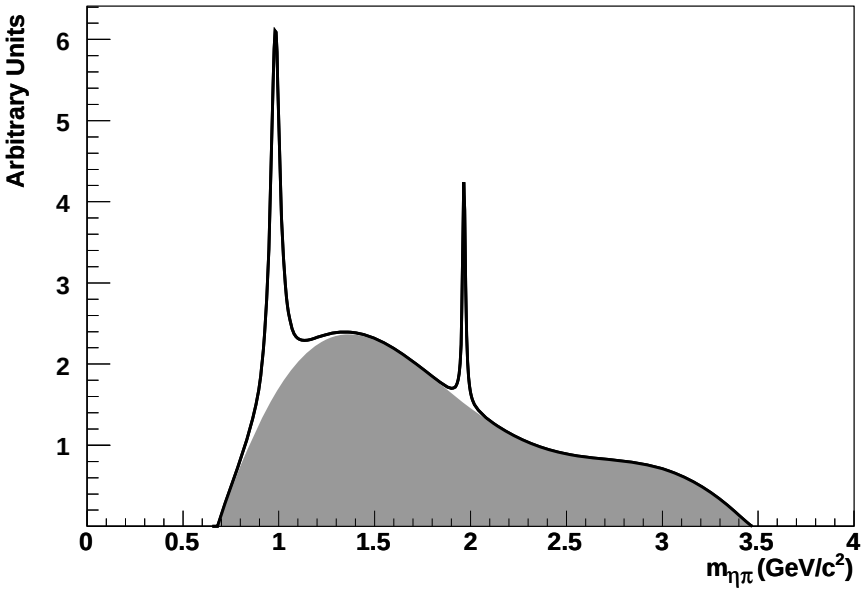

Figure 5.3: A typical $m_{\eta\pi}$ distribution. The gray area shows the Chebychev background function, the solid curve shows the stacked $B^0 \to Da_0$ and $B^0 \to DD_s$ lineshapes, with the a_0 peaking at 980 MeV/c^2 and the D_s at 1968.3 MeV/c^2.

fraction f_S, is defined as

$$f_S = \frac{I}{I + II} \equiv \frac{S}{S_T}. \tag{5.9}$$

A fraction of the $B^0 \to D^{(*)-}\eta\pi^+$ signal events can be mis-reconstructed. Like the resonant signal, the p.d.f. is split in two parts. Part I describes the signal, part II the mis-reconstructed events. The fraction between the two parts is determined on the Monte Carlo sample and used in the calculation of the efficiency. For the fit to the Monte Carlo a keys p.d.f. is used to describe the $m_{\eta\pi}$ distribution, both for part I as for part II. Similar to the signal p.d.f. we define

$$NR_T \equiv NR + NR_{MR}, \tag{5.10}$$

and the fraction f_{NR}

$$f_{NR} = \frac{I}{I + II} \equiv \frac{NR}{NR_{MR}}. \tag{5.11}$$

In the fit to the data, the mis-reconstructed events are taken care of by the general background p.d.f.'s. The $m_{\eta\pi}$ distribution is fitted with the Breit-Wigner multiplied with the efficiency function.

The generic $B\overline{B}$ component also has two parts. A fraction of the events reconstructed in the lower region in the $m_{\eta\pi}$ observable, below 1.5 GeV/c^2, has a different Argus slope

component	$m_{\rm ES}$		ΔE		$m_{\eta\pi}$			
p.d.f.	Cruijff	Argus	Cruijff	Chebychev	BW	BWnr	Chebychev	Keys
$B^0 \to Da_0$	I	II (MC)	I	II (MC)	I	-	II (MC)	-
$B^0 \to D\eta\pi$	I	II (MC)	I	II (MC)	-	I (data)	-	I, II (MC)
$q\overline{q}$	-	X	-	X	-	-	-	X
$B\overline{B}$	II	I	-	I,II	-	-	I,II	-
$B^0 \to DD_s$	X	-	X	-	X	-	-	-

Table 5.1: Summary of the component p.d.f.'s used for the different types of signal or background. Each row represents one component p.d.f., crosses, X, and roman indexes represent the used combinations. The component p.d.f.'s that are composed of two parts, explained in the text, have the parts indicated with the indexes I and II.

compared to the rest of the spectrum. This is understood to be due to the presence of $B^0 \to D^{(*)+}\rho^-$ and $B^0 \to D^{(*)+}a_1{}^-$ background events in this region. This behavior is described by using the Cruijff function in the $m_{\rm ES}$ for part II and defining this part with a different Chebychev function in $m_{\eta\pi}$. Now the Cruijff will fit any peaking behavior, or alter the Argus shape in $m_{\rm ES}$ for the lower region in $m_{\eta\pi}$. The fraction between the two parts are fixed on the Monte Carlo sample.

5.3 Summary of fixed shape parameters

The $B^0 \to D^{(*)-}a_0^+$ signal p.d.f. parameters are summarized in Table 5.2. The parameters presented, are fixed using the selected signal Monte Carlo data sample.

The non-resonant $B^0 \to D^{(*)-}\eta\pi^+$ signal p.d.f. parameters are summarized in Table 5.3. Due to the `Jetset` bug described in Chapter 2, only the $m_{\rm ES}$ and ΔE observables are described correctly. These two observables are fitted using the generic $B\overline{B}$ Monte Carlo data produced in the $B^0 \to D^{(*)-}\eta\pi^+$ mode. The $m_{\eta\pi}$ shape is fitted with two keys p.d.f.'s, subsequently defined in the $m_{\rm ES}$ signal and sideband area. Using these two keys p.d.f.'s we determine the parameters for the $m_{\rm ES}$ and ΔE shapes, and the fraction of mis-reconstructed events. When fitting the data, we do not use this defined keys p.d.f.'s and instead use the theoretical shape in the $m_{\eta\pi}$ observable, corrected for the efficiency function as is determined in Sect. 4.5.

The $q\overline{q}$ background p.d.f. parameters can be found in Table 5.4. The parameters of this p.d.f. are determined using the selected $q\overline{q}$ Monte Carlo datasets. The parameters of the p.d.f.'s describing the $B^0 \to D^{(*)-}D_s^+$ events are presented in Table 5.6. The shape parameters are fixed using the generic $B\overline{B}$ Monte Carlo dataset selecting only the region between $(1.85 < m_{\eta\pi} < 2.1)\,{\rm GeV}/c^2$. A background function defined by an Argus for $m_{\rm ES}$ and a first order Chebychev in ΔE and $m_{\eta\pi}$ is defined to fit the combinatoric background in the region. On top of that the parameters of the $B^0 \to D^{(*)-}D_s^+$ p.d.f. are fitted.

The generic $B\overline{B}$ background p.d.f. consists of two parts and is determined using

Parameter			DchI	DchII	DstI
$m_{\rm ES}$	II	A ξ	-110.0 ± 9.0	-113.0 ± 11.0	-85.0 ± 13.0
$m_{\rm ES}$	II	A m_0	5.290 fixed	5.290 fixed	5.290 fixed
$m_{\rm ES}$	I	Cr α_L	0.100 ± 0.007	0.080 ± 0.014	0.103 ± 0.012
$m_{\rm ES}$	I	Cr m_B	5.27970 ± 0.00005	5.27960 ± 0.00008	5.27980 ± 0.00008
$m_{\rm ES}$	I	Cr σ	0.00248 ± 0.00003	0.00259 ± 0.00006	0.00246 ± 0.00006
ΔE	II	Ch c_0	0.17 ± 0.10	0.0 ± 0.2	-0.2 ± 0.2
ΔE	I	Cr α_L	0.150 ± 0.002	0.150 ± 0.011	0.150 ± 0.010
ΔE	I	Cr α_R	0.15 ± 0.09	0.150 ± 0.011	0.150 ± 0.012
ΔE	I	Cr E_0	0.0010 ± 0.0007	0.0019 ± 0.0015	0.0007 ± 0.0013
ΔE	I	Cr σ_L	0.0196 ± 0.0006	0.0181 ± 0.0007	0.019 ± 0.002
ΔE	I	Cr σ_R	0.0135 ± 0.0005	0.0131 ± 0.0006	0.0146 ± 0.0009
$m_{\eta\pi}$	I	BW m_0	0.9820 ± 0.0007	0.9841 ± 0.0013	0.9827 ± 0.0012
$m_{\eta\pi}$	I	BW Γ_0	0.0600 ± 0.0015	0.056 ± 0.003	0.060 ± 0.003
$m_{\eta\pi}$	II	Ch c_0	-7.9 ± 0.2	-1.5 ± 0.3	-6.0 ± 5.0
$m_{\eta\pi}$	II	Ch c_1	-5.8 ± 0.3	-6.0 ± 2.0	5.0 ± 6.0
$m_{\eta\pi}$	II	Ch c_2	2.46 ± 0.13	8.7 ± 0.3	9.0 ± 3.0
$m_{\eta\pi}$	II	Ch c_3	7.6 ± 0.6	0.4 ± 0.6	6.0 ± 6.0
$m_{\eta\pi}$	II	Ch c_4	-7.4 ± 0.5	-10.0 ± 19.0	-10.0 ± 15.0
$m_{\eta\pi}$	II	Ch c_5	9.999 ± 0.011	8.0 ± 2.0	4.0 ± 7.0
$I/(I+II) = f_S$			0.910 ± 0.005	0.883 ± 0.011	0.896 ± 0.009

Parameter			DstII	DstIII	DstIV
$m_{\rm ES}$	II	A ξ	-91.0 ± 14.0	-69.0 ± 16.0	-68.0 ± 21.0
$m_{\rm ES}$	II	A m_0	5.290 fixed	5.290 fixed	5.290 fixed
$m_{\rm ES}$	I	Cr α_L	0.100 ± 0.003	0.09 ± 0.02	0.09 ± 0.04
$m_{\rm ES}$	I	Cr m_B	5.27980 ± 0.00009	5.27970 ± 0.00010	5.2793 ± 0.0002
$m_{\rm ES}$	I	Cr σ	0.00265 ± 0.00007	0.00248 ± 0.00008	0.0026 ± 0.0002
ΔE	II	Ch c_0	-0.1 ± 0.2	0.1 ± 0.2	0.00 ± 0.05
ΔE	I	Cr α_L	0.150 ± 0.005	0.15 ± 0.03	0.150 ± 0.013
ΔE	I	Cr α_R	0.13 ± 0.03	0.13 ± 0.08	0.09 ± 0.05
ΔE	I	Cr E_0	-0.002 ± 0.002	0.002 ± 0.014	0.003 ± 0.003
ΔE	I	Cr σ_L	0.0202 ± 0.0012	0.021 ± 0.005	0.019 ± 0.002
ΔE	I	Cr σ_R	0.018 ± 0.002	0.015 ± 0.007	0.016 ± 0.003
$m_{\eta\pi}$	I	BW m_0	0.9823 ± 0.0012	0.9823 ± 0.0012	0.981 ± 0.002
$m_{\eta\pi}$	I	BW Γ_0	0.056 ± 0.002	0.056 ± 0.002	0.055 ± 0.005
$m_{\eta\pi}$	II	Ch c_0	-8.3 ± 0.9	4.0 ± 33.0	-18.0 ± 15.0
$m_{\eta\pi}$	II	Ch c_1	-7.0 ± 5.0	-39.91 ± 0.14	-10.0 ± 16.0
$m_{\eta\pi}$	II	Ch c_2	19.9 ± 0.2	40.0 ± 6.0	20.0 ± 29.0
$m_{\eta\pi}$	II	Ch c_3	12.0 ± 5.0	5.0 ± 5.0	6.0 ± 5.0
$m_{\eta\pi}$	II	Ch c_4	3.0 ± 2.0	-9.0 ± 8.0	9.0 ± 19.0
$m_{\eta\pi}$	II	Ch c_5	17.6 ± 1.5	37.0 ± 7.0	8.0 ± 10.0
$I/(I+II) = f_S$			0.885 ± 0.010	0.894 ± 0.011	0.84 ± 0.02

Table 5.2: Fitted parameters for the $B^0 \to D^{(*)-} a_0^+$ signal p.d.f.. Part I (II) is the (mis-)reconstructed event description.

Parameter	DchI	DchII	DstI
$m_{\rm ES}$ II A ξ	-107.0 ± 7.0	-84.0 ±12.0	-105.0 ±12.0
$m_{\rm ES}$ II A m_0	5.290 fixed	5.290 fixed	5.290 fixed
$m_{\rm ES}$ I Cr α_L	0.078 ± 0.009	0.05 ± 0.02	0.06 ± 0.02
$m_{\rm ES}$ I Cr m_B	5.27970± 0.00003	5.27960± 0.00009	5.27960± 0.00007
$m_{\rm ES}$ I Cr σ	0.00247± 0.00003	0.00253± 0.00008	0.00253± 0.00006
ΔE II Ch c_0	−0.08 ± 0.07	0.07 ± 0.14	0.16 ± 0.12
ΔE I Cr α_L	0.150 ± 0.005	0.150 ± 0.009	0.15 ± 0.11
ΔE I Cr α_R	0.117 ± 0.012	0.15 ± 0.13	0.09 ± 0.03
ΔE I Cr E_0	0.0001 ± 0.0007	0.0024 ± 0.0014	−0.0004 ± 0.0015
ΔE I Cr σ_L	0.0195 ± 0.0004	0.0211 ± 0.0011	0.0201 ± 0.0010
ΔE I Cr σ_R	0.0148 ± 0.0006	0.0137 ± 0.0010	0.0170 ± 0.0004
$I/(I+II) = f_{NR}$	0.901 ± 0.004	0.868 ± 0.011	0.882 ± 0.008
Parameter	DstII	DstIII	DstIV
$m_{\rm ES}$ II A ξ	-148.0 ±12.0	-80.0 ±19.0	-113.0 ±23.0
$m_{\rm ES}$ II A m_0	5.290 fixed	5.290 fixed	5.290 fixed
$m_{\rm ES}$ I Cr α_L	0.10 ± 0.02	0.06 ± 0.06	0.0751 ± 0.0005
$m_{\rm ES}$ I Cr m_B	5.27970± 0.00009	5.2798 ± 0.0002	5.28 ± 3.0e−06
$m_{\rm ES}$ I Cr σ	0.00245± 0.00008	0.0027 ± 0.0002	0.00237± 2.6e−10
ΔE II Ch c_0	−0.26 ± 0.12	−0.06 ± 0.11	−0.3 ± 0.2
ΔE I Cr α_L	0.15 ± 0.15	0.15 ± 0.10	0.150 ± 0.015
ΔE I Cr α_R	0.14 ± 0.03	0.01 ± 0.03	0.09 ± 0.04
ΔE I Cr E_0	−0.002 ± 0.002	−0.004 ± 0.002	−0.0040 ± 0.0010
ΔE I Cr σ_L	0.021 ± 0.002	0.0181 ± 0.0012	0.0172 ± 0.0011
ΔE I Cr σ_R	0.018 ± 0.002	0.020 ± 0.002	0.0180 ± 0.0014
$I/(I+II) = f_{NR}$	0.813 ± 0.013	0.834 ± 0.011	0.89 ± 0.02

Table 5.3: Fitted parameters for the non-resonant $B^0 \to D^{(*)-}\eta\pi^+$ signal p.d.f..

Parameter		DchI	DchII	DstI
$m_{\rm ES}$	A ξ	−15.0 ± 4.0	−9.0 ± 5.0	−2.0 ± 6.0
$m_{\rm ES}$	A m_0	5.290 fixed	5.290 fixed	5.290 fixed
ΔE	Ch c_0	−0.18± 0.04	−0.20± 0.07	−0.03± 0.14
Parameter		DstII	DstIII	DstIV
$m_{\rm ES}$	A ξ	−22.0 ±11.0	−2.0 ±12.0	−7.0 ±20.0
$m_{\rm ES}$	A m_0	5.290 fixed	5.290 fixed	5.290 fixed
ΔE	Ch c_0	−0.12± 0.14	−0.1 ± 0.2	−0.2 ± 0.3

Table 5.4: Fitted parameters for the $q\overline{q}$ p.d.f..

Parameter			DchI	DchII	DstI
$m_{\rm ES}$	I	A ξ	-44.0 ± 3.0	-45.0 ± 5.0	-71.0 ± 5.0
$m_{\rm ES}$	I	A m_0	5.290 fixed	5.290 fixed	5.290 fixed
$m_{\rm ES}$	II	Cr α_L	0.150 ± 0.013	0.05 ± 0.02	0.20 ± 0.13
$m_{\rm ES}$	II	Cr m_B	5.2738 ± 0.0011	5.27960 ± 0.00009	5.2773 ± 0.0008
$m_{\rm ES}$	II	Cr σ	0.0085 ± 0.0008	0.00253 ± 0.00008	0.0052 ± 0.0006
ΔE	I	Ch c_0	-0.41 ± 0.03	-0.32 ± 0.05	-0.38 ± 0.06
ΔE	II	Ch c_0	-0.40 ± 0.14	-0.1 ± 0.2	-0.1 ± 0.2
$m_{\eta\pi}$	I	Ch c_0	3.2 ± 0.4	10.0 ± 13.0	-10.0 ± 17.0
$m_{\eta\pi}$	I	Ch c_1	-9.74 ± 0.13	-33.0 ± 3.0	-3.5 ± 1.1
$m_{\eta\pi}$	I	Ch c_2	3.1 ± 0.3	14.5 ± 1.2	2.9 ± 1.0
$m_{\eta\pi}$	I	Ch c_3	2.4 ± 0.3	-1.0 ± 2.0	7.3 ± 1.3
$m_{\eta\pi}$	I	Ch c_4	-3.0 ± 0.3	-5.0 ± 1.4	0.1 ± 0.7
$m_{\eta\pi}$	I	Ch c_5	3.0 ± 0.4	6.0 ± 2.0	3.2 ± 1.0
$m_{\eta\pi}$	II	Ch c_0	-9.26 ± 0.15	8.2 ± 0.4	9.0 ± 19.0
$m_{\eta\pi}$	II	Ch c_1	10.0 ± 4.0	7.7 ± 0.7	8.9 ± 0.4
$m_{\eta\pi}$	II	Ch c_2	0.8 ± 1.3	8.9 ± 0.3	10.0 ± 16.0
$m_{\eta\pi}$	II	Ch c_3	13.1 ± 0.2	10.0 ± 2.0	9.1 ± 0.3
$m_{\eta\pi}$	II	Ch c_4	6.0 ± 2.0	6.02 ± 0.05	4.7 ± 0.4
$m_{\eta\pi}$	II	Ch c_5	9.9 ± 0.5	10.0 ± 3.0	8.3 ± 0.4
$I/(I+II)$			0.907 ± 0.008	0.87 ± 0.02	0.84 ± 0.02

Parameter			DstII	DstIII	DstIV
$m_{\rm ES}$	I	A ξ	-54.0 ± 7.0	-41.0 ± 5.0	-77.0 ± 19.0
$m_{\rm ES}$	I	A m_0	5.290 fixed	5.290 fixed	5.290 fixed
$m_{\rm ES}$	II	Cr α_L	0.3 ± 0.2	0.3 ± 0.2	0.000 fixed
$m_{\rm ES}$	II	Cr m_B	5.274 ± 0.003	5.275 ± 0.004	5.280 fixed
$m_{\rm ES}$	II	Cr σ	0.008 ± 0.002	0.006 ± 0.002	0.006 fixed
ΔE	I	Ch c_0	-0.44 ± 0.08	-0.50 ± 0.06	-0.1 ± 0.2
ΔE	II	Ch c_0	-0.5 ± 0.3	-0.4 ± 0.3	-0.287 fixed
$m_{\eta\pi}$	I	Ch c_0	6.7 ± 0.4	3.0 ± 2.0	1.6 ± 0.3
$m_{\eta\pi}$	I	Ch c_1	-1.1 ± 0.2	-3.5 ± 0.8	2.36 ± 0.05
$m_{\eta\pi}$	I	Ch c_2	8.0 ± 2.0	9.6 ± 0.9	8.3 ± 0.2
$m_{\eta\pi}$	I	Ch c_3	5.0 ± 4.0	9.7 ± 0.3	10.0 ± 0.2
$m_{\eta\pi}$	I	Ch c_4	1.8 ± 0.8	1.1 ± 0.8	2.21 ± 0.04
$m_{\eta\pi}$	I	Ch c_5	3.0 ± 2.0	5.9 ± 0.5	5.76 ± 0.11
$m_{\eta\pi}$	II	Ch c_0	7.3 ± 1.0	6.1 ± 0.3	1.000 fixed
$m_{\eta\pi}$	II	Ch c_1	9.3 ± 1.4	6.7 ± 0.3	0.000 fixed
$m_{\eta\pi}$	II	Ch c_2	-2.3 ± 0.6	6.77 ± 0.02	0.000 fixed
$m_{\eta\pi}$	II	Ch c_3	-6.0 ± 11.0	5.2 ± 0.3	0.000 fixed
$m_{\eta\pi}$	II	Ch c_4	-4.1 ± 0.4	2.40 ± 0.08	0.000 fixed
$m_{\eta\pi}$	II	Ch c_5	8.0 ± 5.0	3.42 ± 0.09	0.000 fixed
$I/(I+II)$			0.90 ± 0.02	0.91 ± 0.02	1.000 fixed

Table 5.5: Fitted parameters for the generic B p.d.f..

Parameter		DchI	DchII	DstI
$m_{\rm ES}$	Cr α_L	0.14 ±0.09	0.17 ±0.06	0.0 ±0.2
$m_{\rm ES}$	Cr m_B	5.2802±0.0002	5.2811±0.0004	5.2798±0.0004
$m_{\rm ES}$	Cr σ	0.0023±0.0002	0.0016±0.0003	0.0030±0.0003
ΔE	Cr α_L	0.15 ±0.03	0.00 ±0.14	0.10 ±0.08
ΔE	Cr α_R	0.04 ±0.13	0.15 ±0.15	0.06 ±0.07
ΔE	Cr E_0	0.001 ±0.005	0.000 ±0.003	−0.000 ±0.006
ΔE	Cr σ_L	0.024 ±0.004	0.013 ±0.003	0.038 ±0.006
ΔE	Cr σ_R	0.019 ±0.005	0.014 ±0.004	0.016 ±0.007
$m_{\eta\pi}$	BW Γ_0	0.019 ±0.002	0.015 ±0.006	0.021 ±0.003
Parameter		DstII	DstIII	DstIV
$m_{\rm ES}$	Cr α_L	0.04 ±0.11	0.15 ±0.02	0.10 ±0.10
$m_{\rm ES}$	Cr m_B	5.2792±0.0005	5.2792±0.0004	5.2783±0.0004
$m_{\rm ES}$	Cr σ	0.0031±0.0004	0.0028±0.0003	0.0014±0.0003
ΔE	Cr α_L	0.15 ±0.02	0.15 ±0.11	0.15 ±0.09
ΔE	Cr α_R	0.13 ±0.04	0.15 ±0.10	0.00 ±0.15
ΔE	Cr E_0	−0.0109±0.0008	0.004 ±0.007	0.010 ±0.003
ΔE	Cr σ_L	0.0300±0.0012	0.036 ±0.009	0.026 ±0.010
ΔE	Cr σ_R	0.023 ±0.002	0.017 ±0.006	0.014 ±0.003
$m_{\eta\pi}$	BW Γ_0	0.014 ±0.002	0.017 ±0.003	0.020 ±0.006

Table 5.6: Fitted parameters for the $B^0 \to D^{(*)-}D_s^+$ specific background p.d.f..

the selected generic $B\overline{B}$ Monte Carlo dataset. The results are presented in Table 5.5. First, the $m_{\rm ES}$ and ΔE parameters of part I are determined selecting the area $m_{\eta\pi} > 1.5\,{\rm GeV}/c^2$. Above this limit no significant difference was found in the shape of $m_{\eta\pi}$ between the $m_{\rm ES}$ signal and sideband selections. The $B^0 \to D^{(*)-}D_s^+$ background is fitted with the already defined $B^0 \to D^{(*)-}D_s^+$ p.d.f.. After fixing the $m_{\rm ES}$ and ΔE parameters of part I, the full p.d.f. is fitted in the entire $m_{\eta\pi}$ region.

5.4 Likelihood fit performed on Monte Carlo data

The likelihood fit on the Monte Carlo data, using the p.d.f.'s described in this chapter, are presented in Fig. 5.4 through 5.9. Each figure presents the resonant signal, the non-resonant signal and the accumulated-unscaled background for the reconstructed decay mode (rows) for one of the reconstructed decay modes. The Monte Carlo data are projected in the $m_{\rm ES}$, ΔE and $m_{\eta\pi}$ observables (columns). The (non-) resonant signal Monte Carlo data sample are fitted with the corresponding (non-) resonant component p.d.f. as is defined in Table 5.1. The unscaled accumulated background is fitted with the total background p.d.f. that consists of the $B\overline{B}$, $q\overline{q}$ and $B^0 \to DD_s$ components as described in Table 5.1. For a detailed description we refer to the caption of Fig. 5.4.

The results of the likelihood fits to the unscaled (not scaled to the data sample) Monte Carlo data samples are presented in Table 5.7.

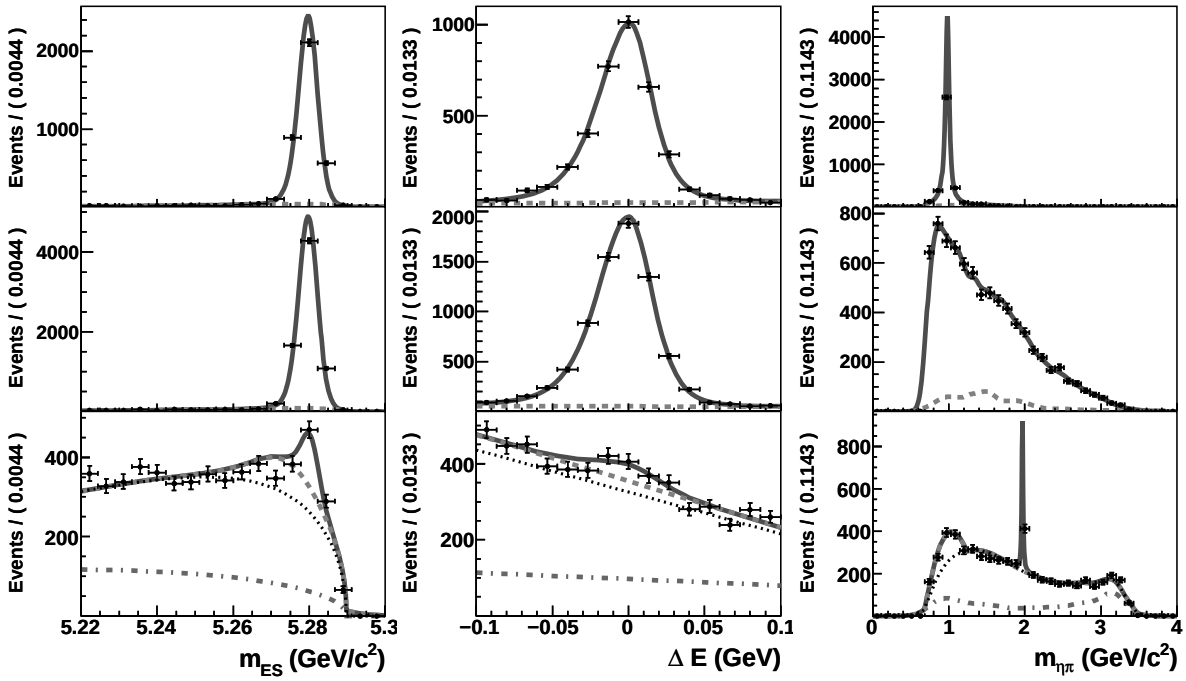

Figure 5.4: Distributions of reconstructed Monte Carlo B candidates in the DchI mode, projected on $m_{\rm ES}$, ΔE and $m_{\eta\pi}$ (from left to right) and for resonant signal, non-resonant signal and background Monte Carlo data (from top to bottom). The solid curves are the fit projections for the corresponding component p.d.f.'s. The dashed curve in the top (*middle*) row shows the projected background component in the resonant (*non-resonant*) signal p.d.f.. The bottom row shows the accumulated projections of the $q\overline{q}$ (dot-dash), the generic B part I (dotted) and generic B part II (dashed) p.d.f.'s. The total background p.d.f. also describes the reconstructed $B^0 \to DD_s$ events.

5.5 Efficiency

The efficiency of the resonant signal selection and likelihood fit is defined as the number of selected events, S, divided by the number of produced events. The results are presented in Table 5.8. The efficiency of non-resonant signal selection is calculated by multiplying the efficiency obtained in Sect. 4.5 with the fraction NR/NR_T as is determined on the Monte Carlo sample.

5.6 Results of the likelihood fit to data

The selected data and the likelihood-fit results are presented in Figs. 5.10-5.15 for each decay mode separately. Each figure shows nine projections of the same data set on the $m_{\rm ES}$, ΔE and $m_{\eta\pi}$ observables. The second and third rows show the side- and signal region in $m_{\rm ES}$ respectively as is indicated in the corresponding $m_{\rm ES}$ plot. For a full

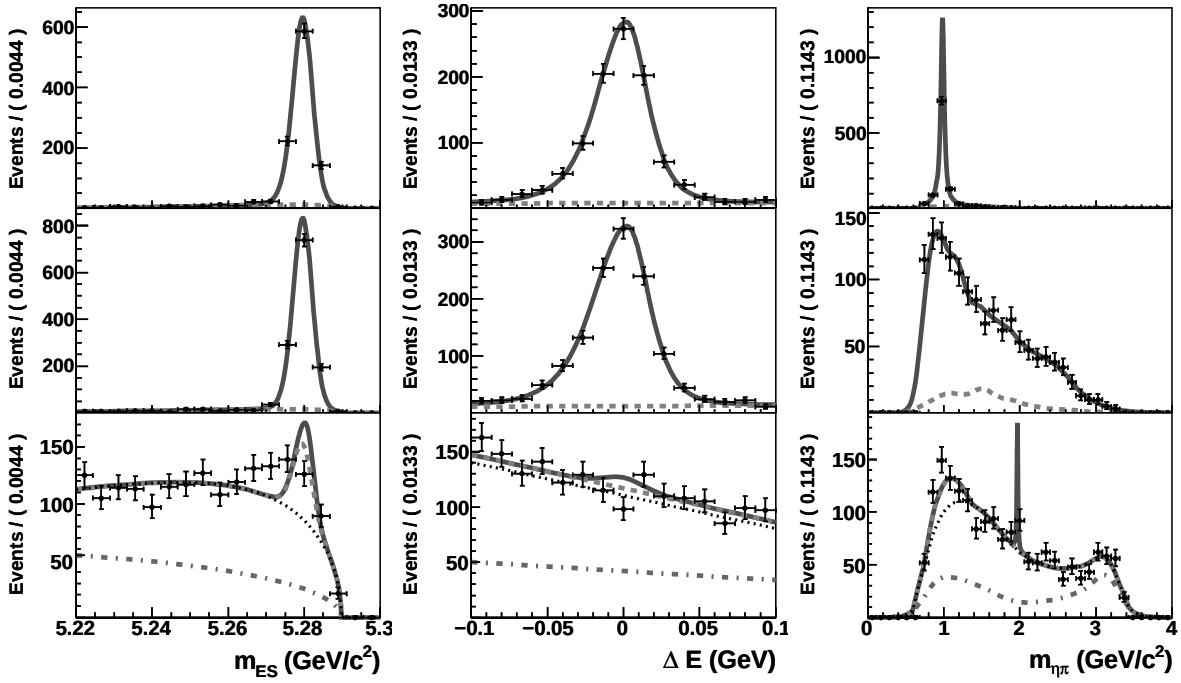

Figure 5.5: Distributions of reconstructed Monte Carlo signal candidates in the DchII mode, see the caption of Fig. 5.4 for a description.

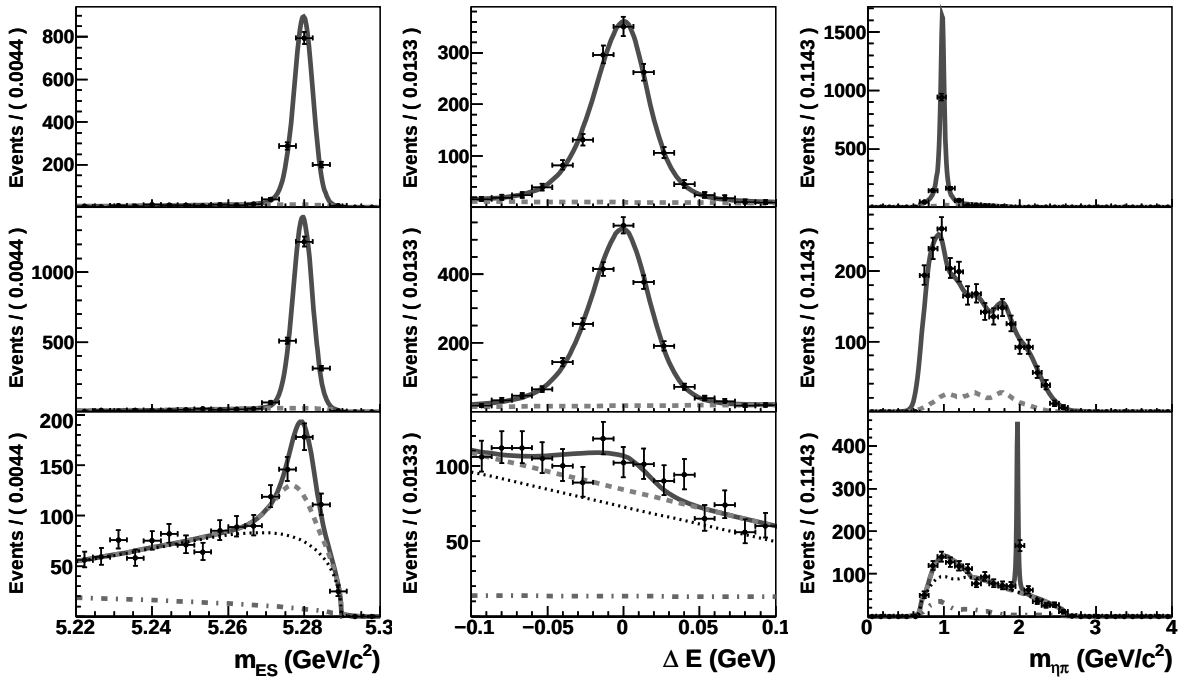

Figure 5.6: Distributions of reconstructed Monte Carlo signal candidates in the DstI mode, see the caption of Fig. 5.4 for a description.

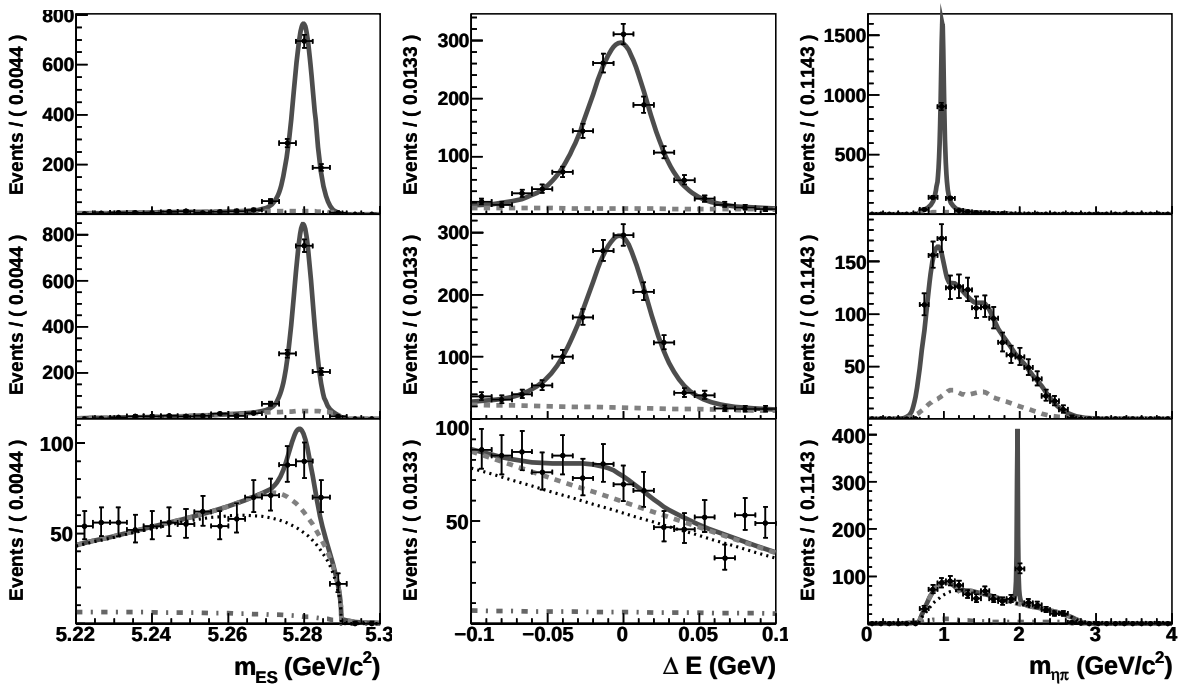

Figure 5.7: Distributions of reconstructed Monte Carlo signal candidates in the DstII mode, see the caption of Fig. 5.4 for a description.

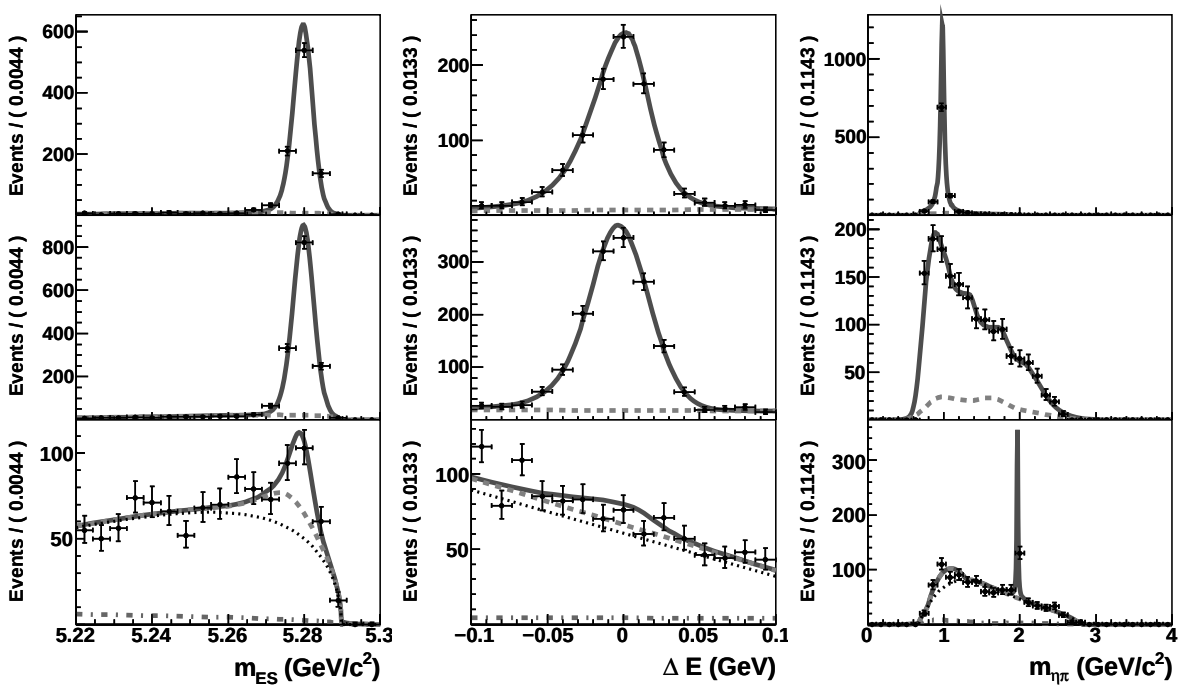

Figure 5.8: Distributions of reconstructed Monte Carlo signal candidates in the DstIII mode, see the caption of Fig. 5.4 for a description.

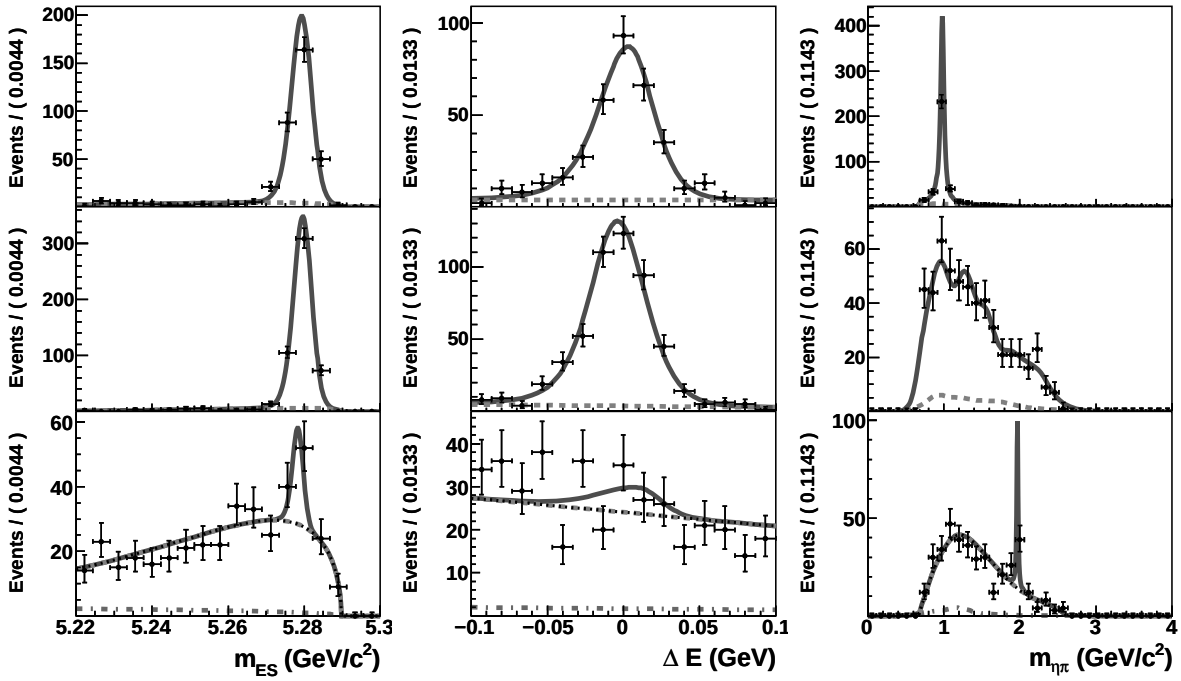

Figure 5.9: Distributions of reconstructed Monte Carlo signal candidates in the DstIV mode, see the caption of Fig. 5.4 for a description.

description see the caption of Fig. 5.10. The fitted p.d.f. is projected on the data in the plots. Note that each dataset is fitted only once and the nine plots are projections of the same data set and fit result.

The fitted p.d.f. describes the data points in the samples to a satisfying level for all reconstructed decay modes, in all three dimensions and all nine projections. The D_s^+ resonance can be clearly identified for four of the six decay modes, all but the reconstructed modes $B^0 \to D^- a_0^+$ ($D^+ \to K_S^0 \pi^+$) and $B^0 \to D^{*-} a_0^+$ ($D^{*+} \to D^0 \pi^+$, $D^0 \to K_S^0 \pi^+ \pi^-$).

The results of the likelihood fits are summarized in Table 5.9. Note that the errors given in Table 5.9 only present the statistical errors as obtained by the likelihood fit and do not reflect the error of the total measurement. The systematic error is calculated in Chapter 7, after the validation of the selection and likelihood fit are presented in Chapter 6.

From the fit results we see that a positive number of signal events is found for the four $B^0 \to D^{*-} a_0^+$ modes, but not in the two $B^0 \to D^- a_0^+$ decay modes. The significance of the fitted $B^0 \to D^{*-} a_0^+$ events, and the combined results of four decay modes, are presented in Chapter 8 after the full systematic errors are calculated.

The fitted number of non-resonant signal events is positive for all six decay modes. A combined result for the two $B^0 \to D^- \eta \pi^+$ modes and the four $B^0 \to D^{*-} \eta \pi^+$ modes are presented in Chapter 8.

	DchI		DchII		DstI	
M.C. sample	#ev	fitted value	#ev	fitted value	#ev	fitted value
resonant signal	3896		1061		1434	
$\#S_T$		$3895.7^{+63.0}_{-61.8}$		$1060.9^{+33.0}_{-32.2}$		$1434.0^{+38.2}_{-37.5}$
nonres. signal	7710		1373		2268	
$\#NR_T$		$7710.0^{+88.1}_{-87.5}$		$1373.0^{+37.4}_{-36.7}$		$2267.9^{+48.0}_{-47.2}$
background	5433		1779		1384	
$\#D_s$		$188.9^{+15.4}_{-14.7}$		$26.7^{+6.3}_{-5.6}$		$119.9^{+12.2}_{-11.5}$
#Bkg		$5244.1^{+73.0}_{-72.3}$		$1752.3^{+42.3}_{-41.6}$		$1264.1^{+36.2}_{-35.5}$
$B\overline{B}/(q\overline{q}+B\overline{B})$		$0.72^{+0.02}_{-0.02}$		$0.641^{+0.034}_{-0.034}$		$0.841^{+0.030}_{-0.031}$
	DstII		DstIII		DstIV	
M.C. sample	#ev	fitted value	#ev	fitted value	#ev	fitted value
resonant signal	1328		1003		359	
$\#S_T$		$1327.8^{+37.0}_{-35.9}$		$1003.0^{+32.0}_{-31.3}$		$358.7^{+19.6}_{-18.3}$
nonres. signal	1449		1631		529	
$\#NR_T$		$1449.0^{+38.4}_{-37.7}$		$1631.0^{+40.7}_{-40.0}$		$528.9^{+23.5}_{-22.5}$
background	968		1071		386	
$\#D_s$		$77.2^{+9.8}_{-9.1}$		$75.5^{+10.0}_{-9.2}$		$24.7^{+5.7}_{-5.0}$
#Bkg		$890.8^{+30.4}_{-29.7}$		$995.5^{+32.2}_{-31.4}$		$361.3^{+19.4}_{-18.8}$
$B\overline{B}/(q\overline{q}+B\overline{B})$		$0.907^{+0.063}_{-0.066}$		$0.935^{+0.042}_{-0.044}$		$0.93^{+0.04}_{-0.05}$

Table 5.7: Results from the likelihood fits to the selected Monte Carlo samples, corresponding to Fig. 5.4-5.9, and the number of entries of the samples input to the fits.

mode	DchI	DchII	DstI	DstII	DstIII	DstIV
ε_{RS} (%)	5.23 ± 0.09	8.7 ± 0.3	7.7 ± 0.2	1.96 ± 0.05	2.76 ± 0.09	3.80 ± 0.23
ε_{NR} (%)	3.50 ± 0.06	6.0 ± 0.2	4.10 ± 0.09	0.97 ± 0.03	1.24 ± 0.04	1.88 ± 0.10

Table 5.8: The efficiency of the resonant signal modes after the likelihood fit for the resonant (RS) and non-resonant (NR) signal.

5.7 Branching ratio determination method

The observed number of signal events as presented in the previous section can be used to calculate a branching ratio using the formula

$$\mathcal{B}(B^0 \to D^{(*)-}a_0^+)_i \times \mathcal{B}(a_0^+ \to \eta\pi^+) = \frac{N_{obs}}{N_B \times \mathcal{B}(D^{(*)\pm})_i \times \varepsilon_i}, \tag{5.12}$$

where i is one of the six $D^{(*)\pm}$ decay modes, N_{obs} is the number of signal events (S), N_B is the total number of B events in the data sample, $\mathcal{B}(D^{(*)\pm})$ is the fractional branching ratio of the $D^{(*)\pm}$ decay and ε is the efficiency of the selection.

To find the non-resonant signal branching ratio, the combination $\mathcal{B}(B^0 \to D^{(*)-}a_0^+) \times \mathcal{B}(a_0^+ \to \eta\pi^+)$ can be substituted by $\mathcal{B}(B^0 \to D^{(*)-}\eta\pi^+)$ and the number of observed

	DchI		DchII		DstI	
parameter	#ev	fitted value	#ev	fitted value	#ev	fitted value
selected	1567		490		326	
#S		$-3.3^{+4.4}_{-3.0}$		$-2.2^{+2.6}_{-1.7}$		$16.8^{+6.1}_{-5.2}$
#NR		$36.1^{+11.3}_{-10.4}$		$5.0^{+5.2}_{-4.3}$		$15.1^{+6.9}_{-5.9}$
$\#D_s$		$49.6^{+8.4}_{-7.6}$		$2.2^{+2.0}_{-1.2}$		$20.6^{+5.5}_{-4.8}$
#Bkg		$1484.5^{+39.9}_{-39.2}$		$485.0^{+23.0}_{-22.1}$		$273.4^{+17.8}_{-17.0}$
$B\overline{B}/(B\overline{B}+q\overline{q})$		$0.50^{+0.04}_{-0.04}$		$0.39^{+0.07}_{-0.07}$		$0.57^{+0.08}_{-0.08}$
	DstII		DstIII		DstIV	
parameter	#ev	fitted value	#ev	fitted value	#ev	fitted value
selected	256		300		123	
#S		$8.3^{+4.4}_{-3.5}$		$1.2^{+3.4}_{-2.4}$		$3.7^{+3.4}_{-2.5}$
#NR		$12.3^{+6.6}_{-5.6}$		$40.7^{+8.9}_{-8.1}$		$8.4^{+4.6}_{-3.7}$
$\#D_s$		$15.4^{+4.7}_{-3.9}$		$13.0^{+5.0}_{-4.2}$		$0.0^{+0.5}_{-0.0}$
#Bkg		$220.1^{+16.0}_{-15.3}$		$245.0^{+16.9}_{-16.0}$		$110.9^{+11.2}_{-10.6}$
$B\overline{B}/(B\overline{B}+q\overline{q})$		$0.64^{+0.13}_{-0.13}$		$0.77^{+0.09}_{-0.10}$		$0.72^{+0.11}_{-0.12}$

Table 5.9: Results from the likelihood fits to the observed distributions and the number of the selected B candidates, corresponding to Fig. 5.10-5.15.

events, N_{obs}, with NR.

Using formula Eq. (5.12) we can combine the results from the different decay modes to four main results; the branching fraction from the resonant and non-resonant signal both in the D^+ and the D^{*+} decay modes. Before we do this in Chapter 8, we first validate the setup of the analysis and investigate possible biases in the fit in Chapter 6 and determine correction terms and systematic uncertainties in Chapter 7.

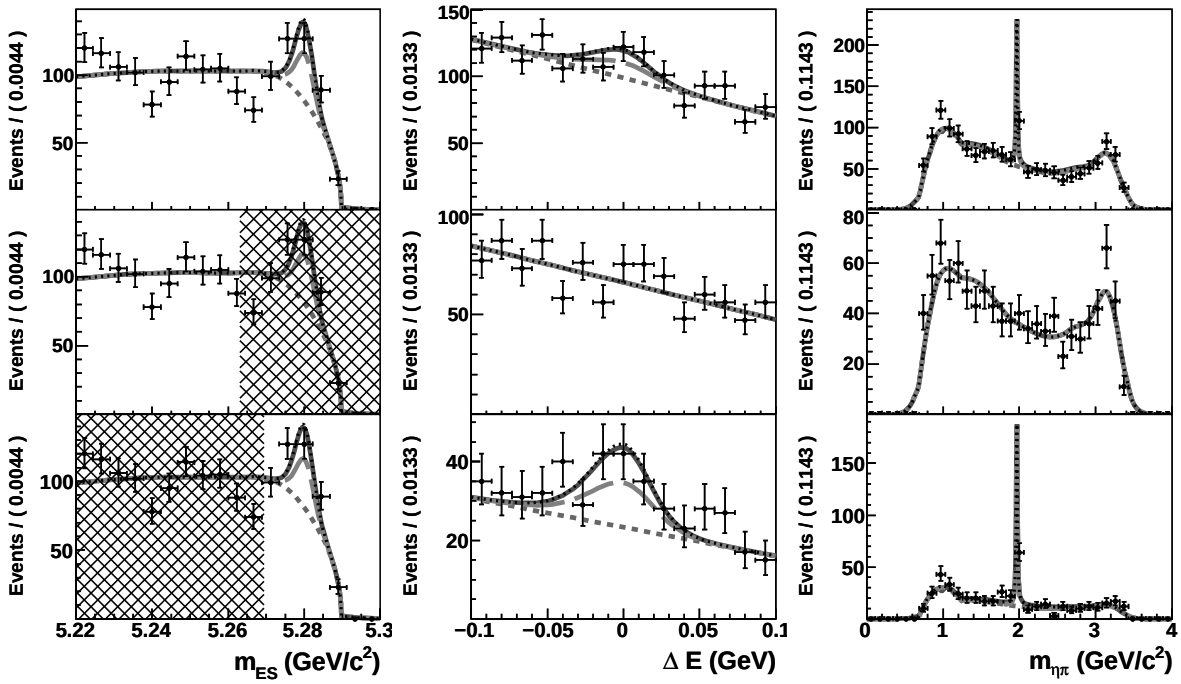

Figure 5.10: Observed distribution of the reconstructed B candidates in the DchI mode projected in, from left to right, $m_{\rm ES}$, ΔE and $m_{\eta\pi}$. The top (middle, *bottom*) row shows the full (sideband, *signal* selected) region. The exclusion region per row is indicated by the hatched area in the $m_{\rm ES}$ projection of the data sample. The component background p.d.f.'s are accumulated in the following order: background (short dashed), $B^0 \to D^{(*)-} D_s^+$ (long dashed), non-resonant $B^0 \to D^{(*)-} \eta\pi^+$ signal (dotted), $B^0 \to D^{(*)-} a_0^+$ signal (solid) curve.

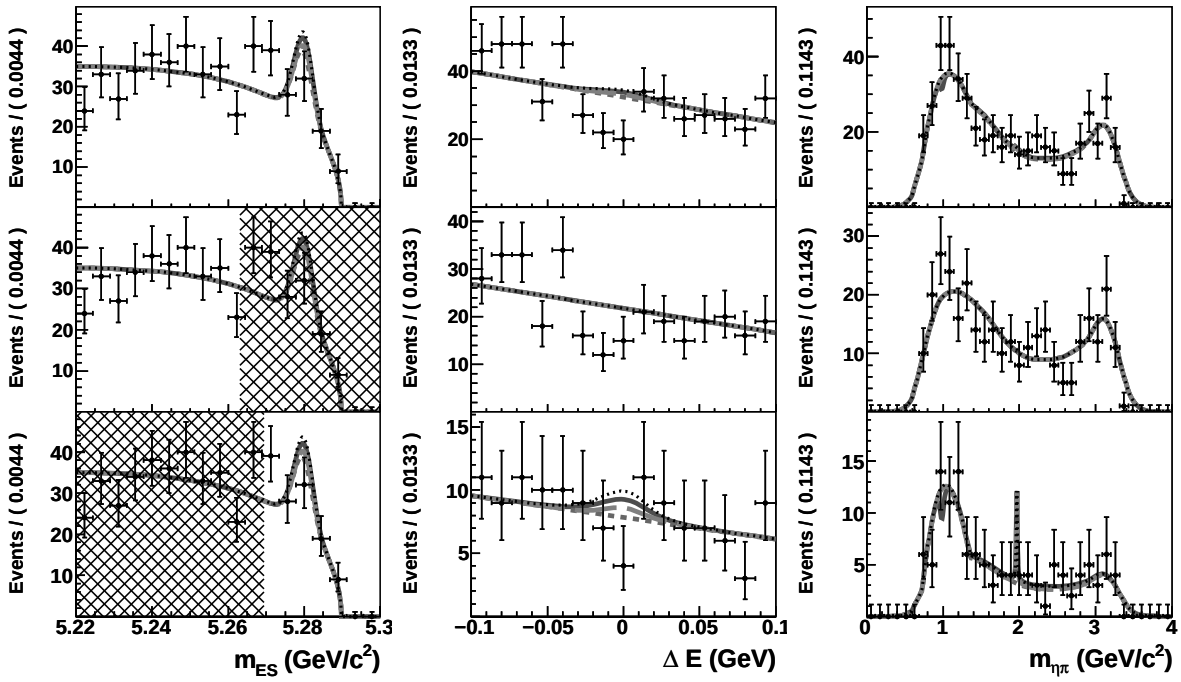

Figure 5.11: Observed distributions of reconstructed B candidates in the DchII mode, see Fig. 5.10 for a description.

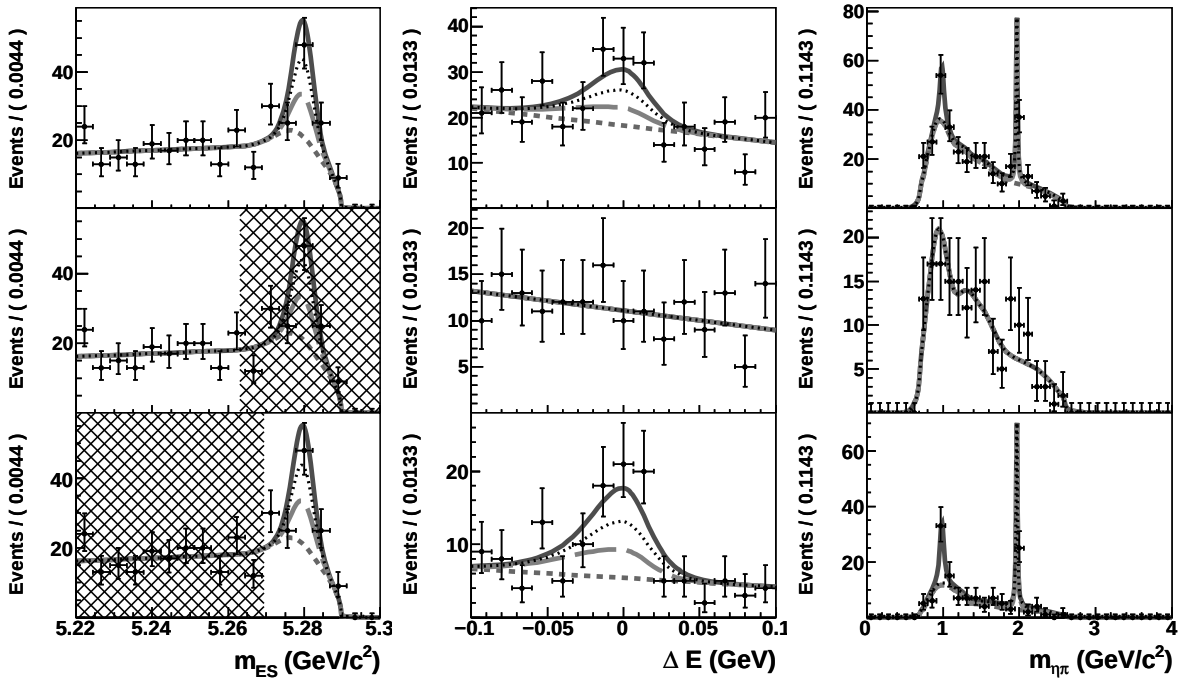

Figure 5.12: Observed distributions of reconstructed B candidates in the DstI mode, see Fig. 5.10 for a description.

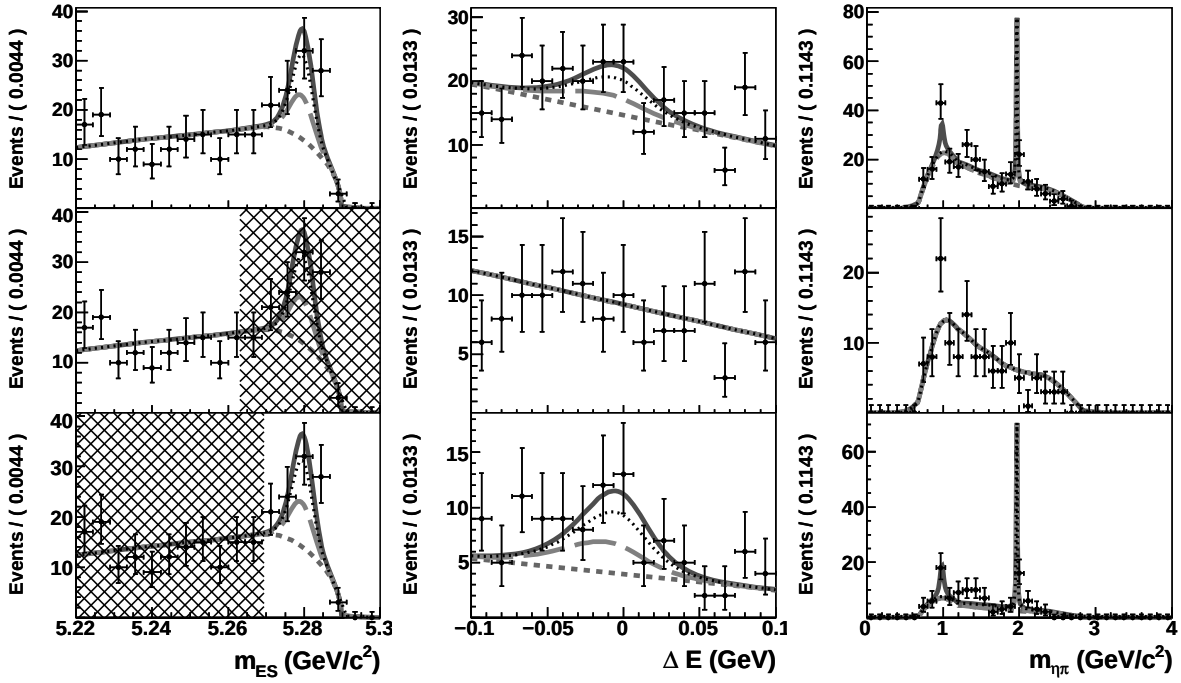

Figure 5.13: Observed distributions of reconstructed B candidates in the DstII mode, see Fig. 5.10 for a description.

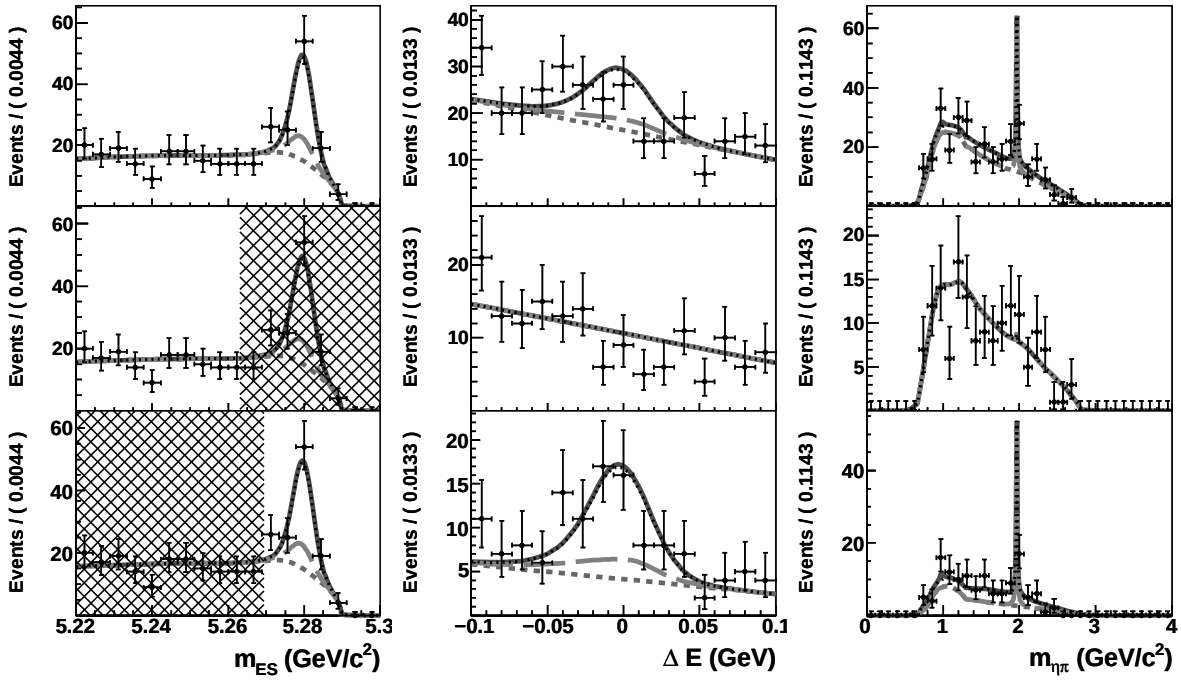

Figure 5.14: Observed distributions of reconstructed B candidates in the DstIII mode, see Fig. 5.10 for a description.

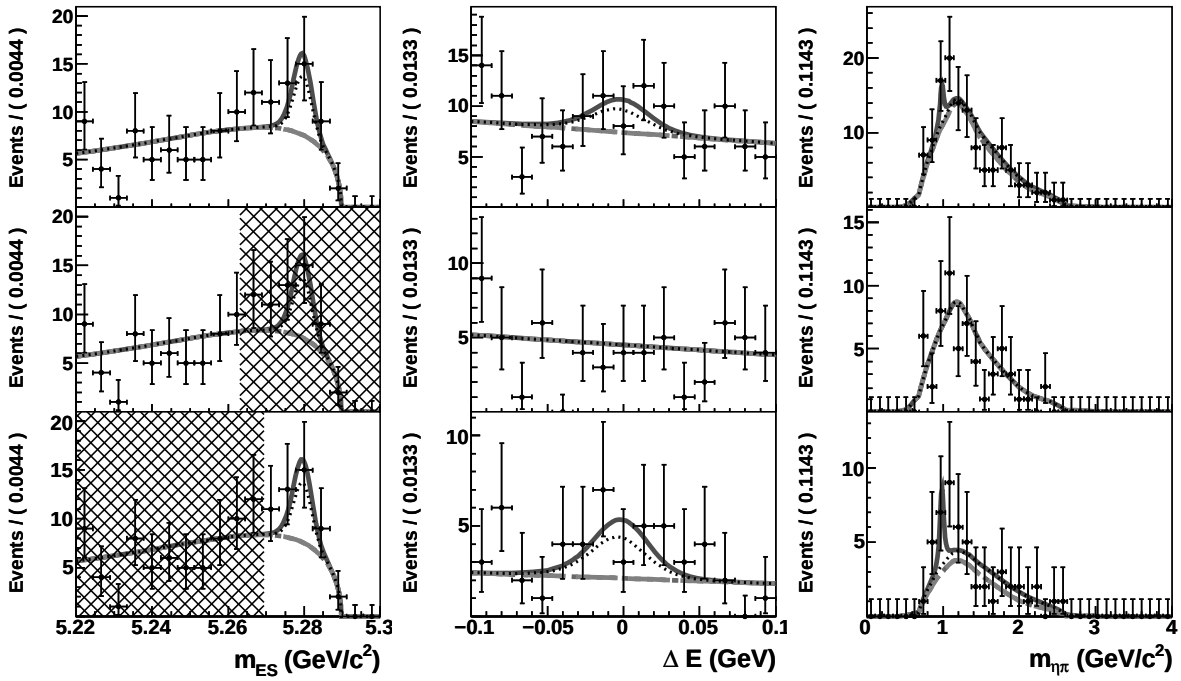

Figure 5.15: Observed distributions of reconstructed B candidates in the DstIV mode, see Fig. 5.10 for a description.

Chapter 6

Validation studies

Various validation tests have been performed to verify the quality of the fit procedure, the selection criteria and the decay chain reconstruction. The test methods and results will be described in this chapter.

First the performance of the likelihood fit algorithm is tested on Monte Carlo samples. Second we perform various tests on data.

6.1 Fit bias validation studies on Monte Carlo

To validate the fit procedure and determine possible biases introduced by the algorithms, a study has been performed on fast parametrized simulated data, or 'toy', Monte Carlo events and on fully simulated, or 'full', Monte Carlo events, described in Sect. 3.1.2.

6.1.1 Toy Monte Carlo studies

In total 18000 toy Monte Carlo sample sets have been produced, 3000 for each $D^{(*)\pm}$ decay mode. The samples are generated using the p.d.f. shapes that are also used to fit the data. The same constitution and number of background events are produced as found in the fit to the data, as summarized in Table 5.9. A third of the sets are produced without signal events, a third with 10 resonant signal events added and third with 10 non-resonant signal events added to the background sample. The parameters determined by the likelihood fits are compared with the input values, so-called 'true' values, by calculating the pull. The pull on a parameter x is defined by

$$pull_x = \frac{x_{fit} - x_{true}}{\sigma_x}, \tag{6.1}$$

where x_{fit} is the fitted parameter, σ_x the associated fit error and x_{true} is the true value of the parameter. The pull distributions are fitted with a Gaussian function. The mean and widths of the fitted Gaussians are presented in Table 6.1.

The fit algorithm gives consistent, unambiguous results. No artificial biases are introduced in the fitted parameters by the algorithm. The errors are neither over- nor

pull	background only		+10 signal events		+10 non-resonant events	
	mean	width	mean	width	mean	width
DchI *decay*						
#S	−0.07±0.05	1.00±0.04	−0.03±0.05	1.01±0.03	−0.12±0.05	1.06±0.04
#NR	0.08±0.04	0.96±0.03	−0.04±0.04	0.99±0.03	−0.02±0.05	0.99±0.03
DchII *decay*						
#S	−0.09±0.05	1.12±0.04	0.01±0.05	0.98±0.03	−0.07±0.05	1.05±0.04
#NR	−0.14±0.05	1.05±0.04	0.02±0.05	0.95±0.03	−0.05±0.05	1.04±0.03
DstI *decay*						
#S	−0.13±0.06	1.11±0.04	0.02±0.05	0.99±0.03	−0.03±0.05	1.04±0.04
#NR	0.01±0.05	1.06±0.04	−0.01±0.05	1.00±0.03	0.01±0.04	0.99±0.03
DstII *decay*						
#S	−0.19±0.06	1.13±0.04	−0.06±0.04	0.97±0.03	−0.08±0.06	1.12±0.04
#NR	0.05±0.05	1.13±0.04	−0.07±0.04	0.97±0.03	0.06±0.05	1.05±0.03
DstIII *decay*						
#S	−0.20±0.06	1.15±0.04	−0.00±0.05	0.98±0.03	−0.08±0.06	1.13±0.04
#NR	0.06±0.05	1.07±0.04	0.00±0.04	0.99±0.03	0.04±0.05	1.02±0.03
DstIV *decay*						
#S	−0.06±0.07	1.26±0.06	0.10±0.05	1.02±0.03	−0.09±0.06	1.15±0.05
#NR	0.01±0.06	1.24±0.05	−0.25±0.05	1.07±0.04	0.09±0.05	1.05±0.04

Table 6.1: The mean and width of a Gaussian fitted to the pull distributions of the fitted number of resonant (#S) and non-resonant (#NR) events of 1000 fits on a toy Monte Carlo sample. Three types of samples are fitted, the left (*middle*, right) two rows present the result on background only (*with 10 resonant signal events added*, with 10 non-resonant signal events added) samples.

underestimated. In conclusion, the fit model and its implementation performs as desired.

The fitted background fraction $B\overline{B}/(B\overline{B}+q\overline{q})$ is not very sensitive. As an example one of the distributions of this parameter is shown in Fig. 6.1. The distribution is representative for all the decay mode fits and is very broad. The two background p.d.f.'s are very similar and do not hold much discriminative power against each others shape. We do not expect any errors introduced from this insensitivity to the other fitted parameters. The correlations between the other parameters and the background fraction parameter are not significant.

6.1.2 Fit bias studies on full Monte Carlo events

To further study possible biases introduced by the fit model, we perform a test on full Monte Carlo simulations. *BABAR* does not have enough generated full Monte Carlo $B\overline{B}$ and $q\overline{q}$ background events to create more than one independent data-like Monte Carlo sample. The generic $B\overline{B}$ sample is almost five time larger then the expected $B\overline{B}$

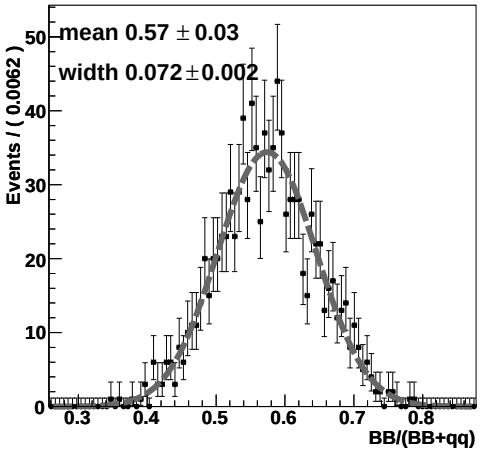

Figure 6.1: Distribution of the fitted background fraction $B\overline{B}/(B\overline{B} + q\overline{q})$ of the DstI decay mode fit. The fraction is produced around ~ 0.57. A Gaussian function is fitted to the distribution and imposed on the plot in a gray dashed line.

background in the data, while the $q\overline{q}$ Monte Carlo sample is less then twice the size. The scaling factors can be found in Table 3.1.

We randomly form (highly-correlated) samples with the expected size and composition as the data sample, by pulling random events from the background samples. Resonant events are added by pulling events from the signal Monte Carlo. Added non-resonant events are taken from produced toy Monte Carlo since we have no correct full Monte Carlo description for these events due to the `Jetset` bug, see Sect. 3.1.2. Samples are produced with no signal events added and with 2, 5, 10, 15 and 20 resonant signal full Monte Carlo events or 2, 5, 10, 15, 20 and 40 non-resonant signal toy Monte Carlo events. For each kind 100 samples are produced, in each decay mode separately, and subsequently fit. The distribution of the fit results, central values and errors, are fitted with a Gaussian. The means of these Gaussians, central values and errors, are presented in Fig. 6.2 for the resonant signal sets and in Fig. 6.3 for the non-resonant signal sets. We correct for the fraction of mis-reconstructed events in the signal Monte Carlo using the fitted ratio, f_S, presented in Table 5.2. A line is fitted to the points and the resulting parameters are presented in the plots.

From the bias test, for both the resonant signal and non-resonant signal, we conclude that no major deviations from the nominal response line (a line through the origin with slope equal to one) are found. All slopes are consistent with the nominal response line and no major offsets are found. The results of the fitted slopes are used to determine a systematic error and to correct the fitted number of resonant and non-resonant events. Both will be discussed in Sect. 7.1.1.

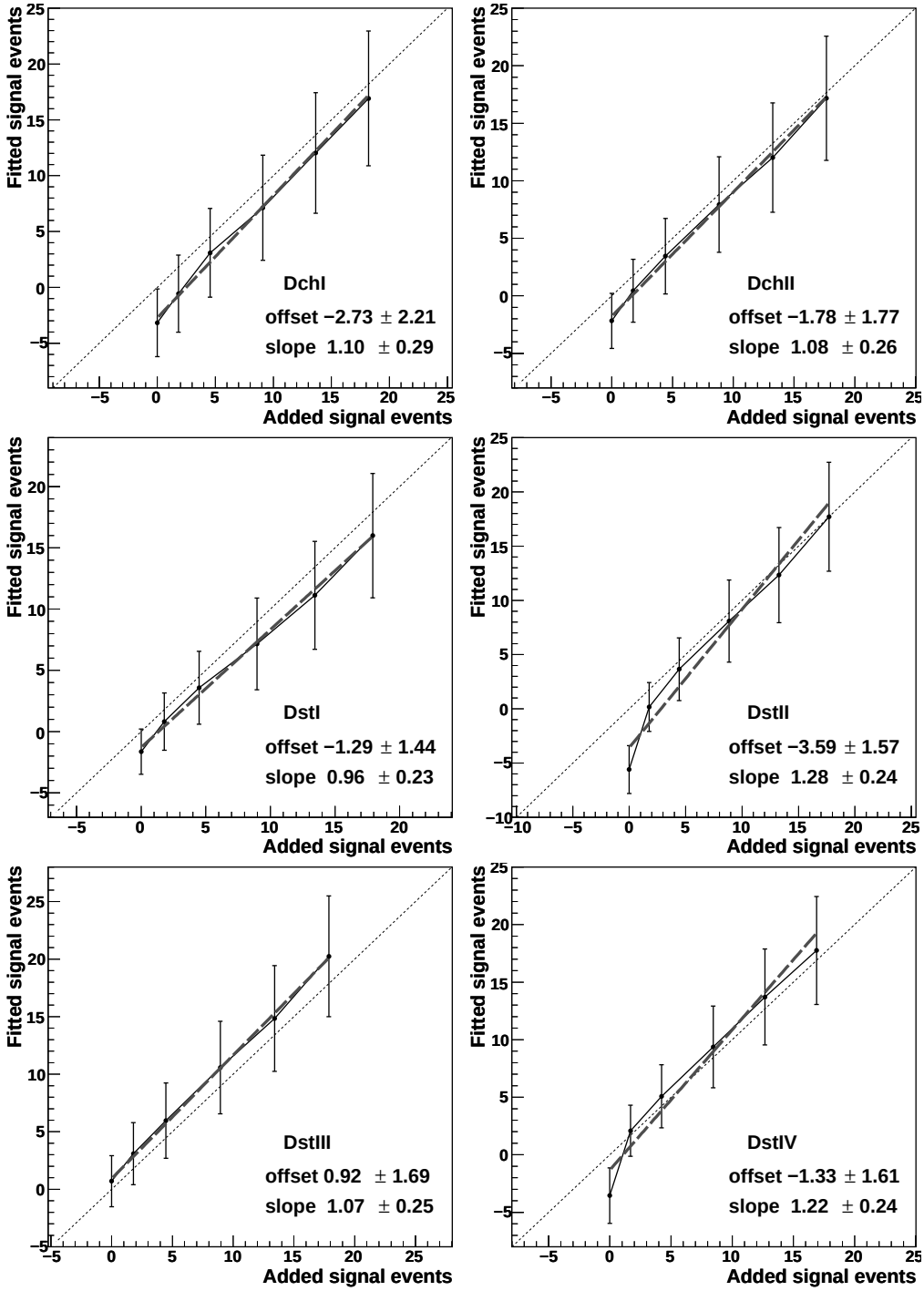

Figure 6.2: Results of bias test on full Monte Carlo samples with added signal events. Each point represents the mean of the central values for 100 fits, the error represents the mean of the fit errors. The points are fitted with a line (dashed), the resulting parameters are presented in the plots. The dotted line indicates the nominal response ($y = x$) line.

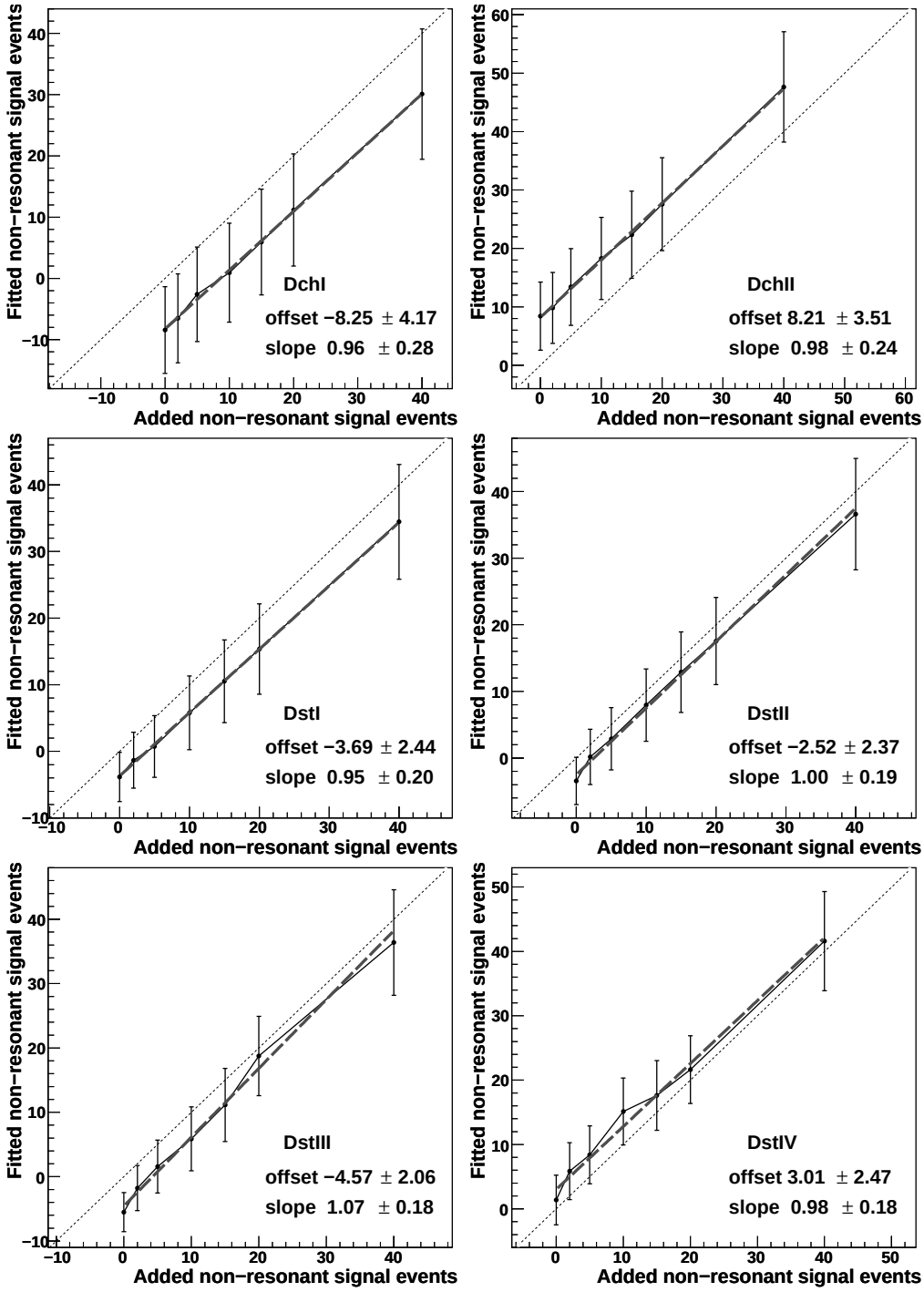

Figure 6.3: Results of bias test on full Monte Carlo samples with added toy Monte Carlo non-resonant signal events. Each point represents the mean of the central values for 100 fits, the error represents the mean of the fit errors. The points are fitted with a line (dashed), the resulting parameters are presented in the plots. The dotted line indicates the nominal response ($y = x$) line.

decay mode	scaled off-peak data	scaled M.C.
DchI	940^{+100}_{-93}	1068^{+27}_{-26}
DchII	198^{+48}_{-41}	429^{+17}_{-16}
DstI	69^{+30}_{-23}	112^{+9}_{-8}
DstII	40^{+23}_{-17}	107^{+9}_{-8}
DstIII	79^{+31}_{-25}	78^{+7}_{-7}
DstIV	69^{+30}_{-23}	30^{+5}_{-4}

Table 6.2: Fitted number of $q\overline{q}$ events and asymmetrical error, both scaled to the full on-peak data sample size, for the off-peak data and full Monte Carlo simulated data samples. The scaling factor for the off-peak data is 9.9 and for the Monte Carlo data is 0.66.

6.2 Validation studies performed on data

Several tests have been performed on data to validate the selection and likelihood fit setup.

First, we review the likelihood-fit results on data as performed in Sect. 5.6. Second, we compare the selection and fits on off-resonant data with continuum background full Monte Carlo simulated data. Next, we present a test to validate the data selection, using the D_s^+ resonance in the $\eta\pi$-invariant mass distribution. And finally we test the response of the fit setup using a signal Monte Carlo enriched data sample.

6.2.1 Continuum background description

The continuum $q\overline{q}$ ($q = u, d, s, c$) background that is formed in the e^-e^- collisions in the PEP-II beam interactions is described by the $q\overline{q}$ p.d.f. where the p.d.f. shape parameters are fixed on the $q\overline{q}$ generated full Monte Carlo events. The agreement between the generated $q\overline{q}$ events and the $q\overline{q}$ background in the data is verified by studying the fit performance on the off-peak data set. The off-peak data are taken at a center-of-mass energy 40 MeV lower than the on-resonance data, *i.e.* below the $b\overline{b}$ production threshold. We correct the data for the energy scale difference in $m_{\rm ES}$ and ΔE.

The full Monte Carlo simulated data are shown in Fig. 6.4. The simulated data are projected in $m_{\rm ES}$, ΔE and $m_{\eta\pi}$ and are shown for each reconstructed decay mode separately. The likelihood fit of the $q\overline{q}$ p.d.f. is projected as a line on top of the data points. The $q\overline{q}$ p.d.f. parameters are fixed on the shown samples.

The (energy-scaled) data, projected in $m_{\rm ES}$, ΔE and $m_{\eta\pi}$, are presented in Fig. 6.5 for each reconstructed decay mode separately. The fitted $q\overline{q}$ p.d.f. is projected on top of the data. The off-peak data sample are about ten times smaller than the on-peak sample (21 fb^{-1} versus 208 fb^{-1}) and is therefore limited in statistics. We conclude that the $q\overline{q}$ p.d.f. shape describes the energy-scaled off-peak data points adequately within the statistics that are available.

Table 6.2 shows the fitted number of$q\overline{q}$ events that are scaled to the full on-peak dataset of 208 fb^{-1}. The prediction from the Monte Carlo simulation does not fully

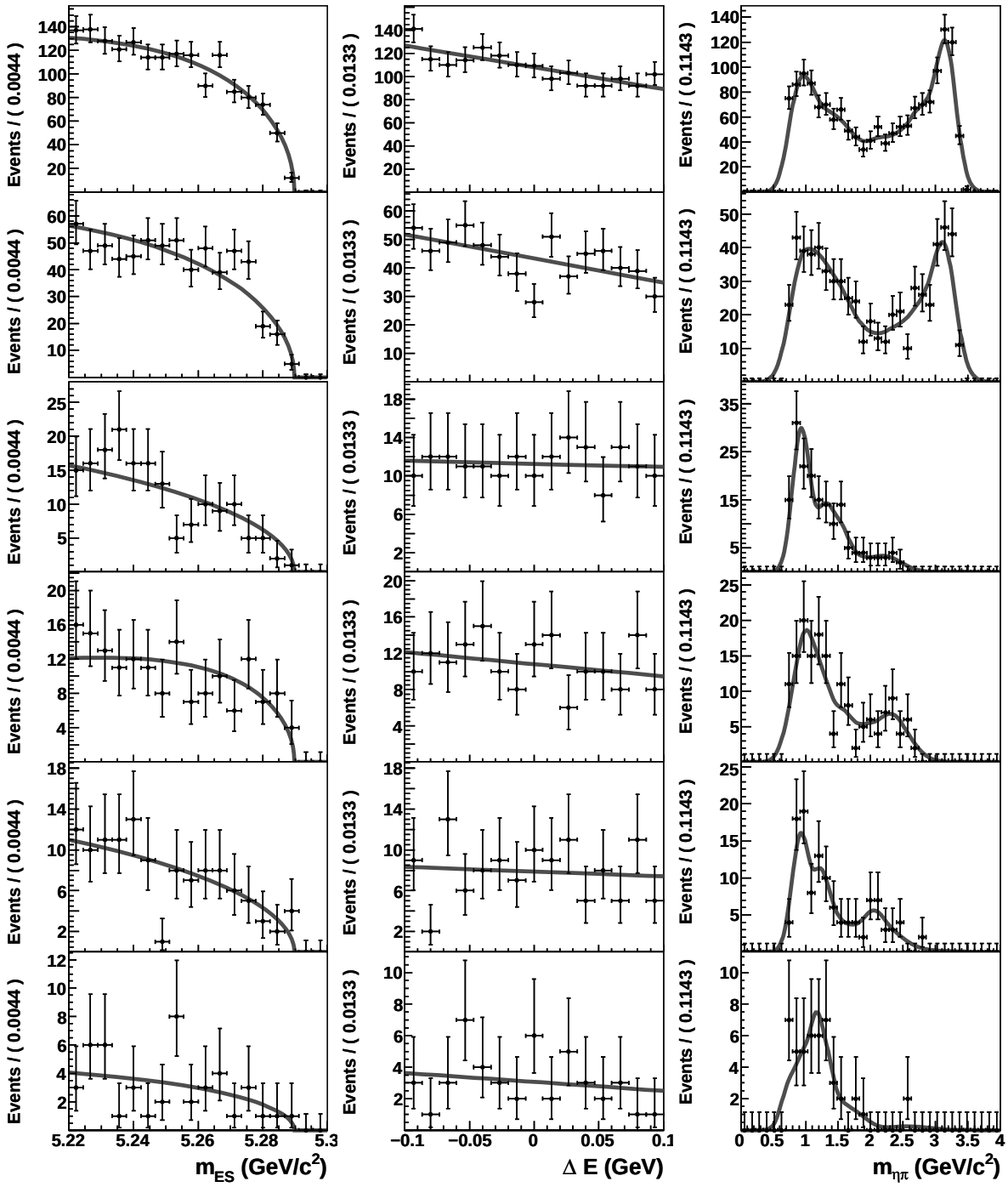

Figure 6.4: Off-peak Monte Carlo data projected on $m_{\rm ES}$, ΔE and $m_{\eta\pi}$ (from left to right) for the DchI, DchII, DstI, DstII, DstIII and DstIV from top to bottom. The likelihood fit of the continuum background p.d.f. is projected on the data as a solid line.

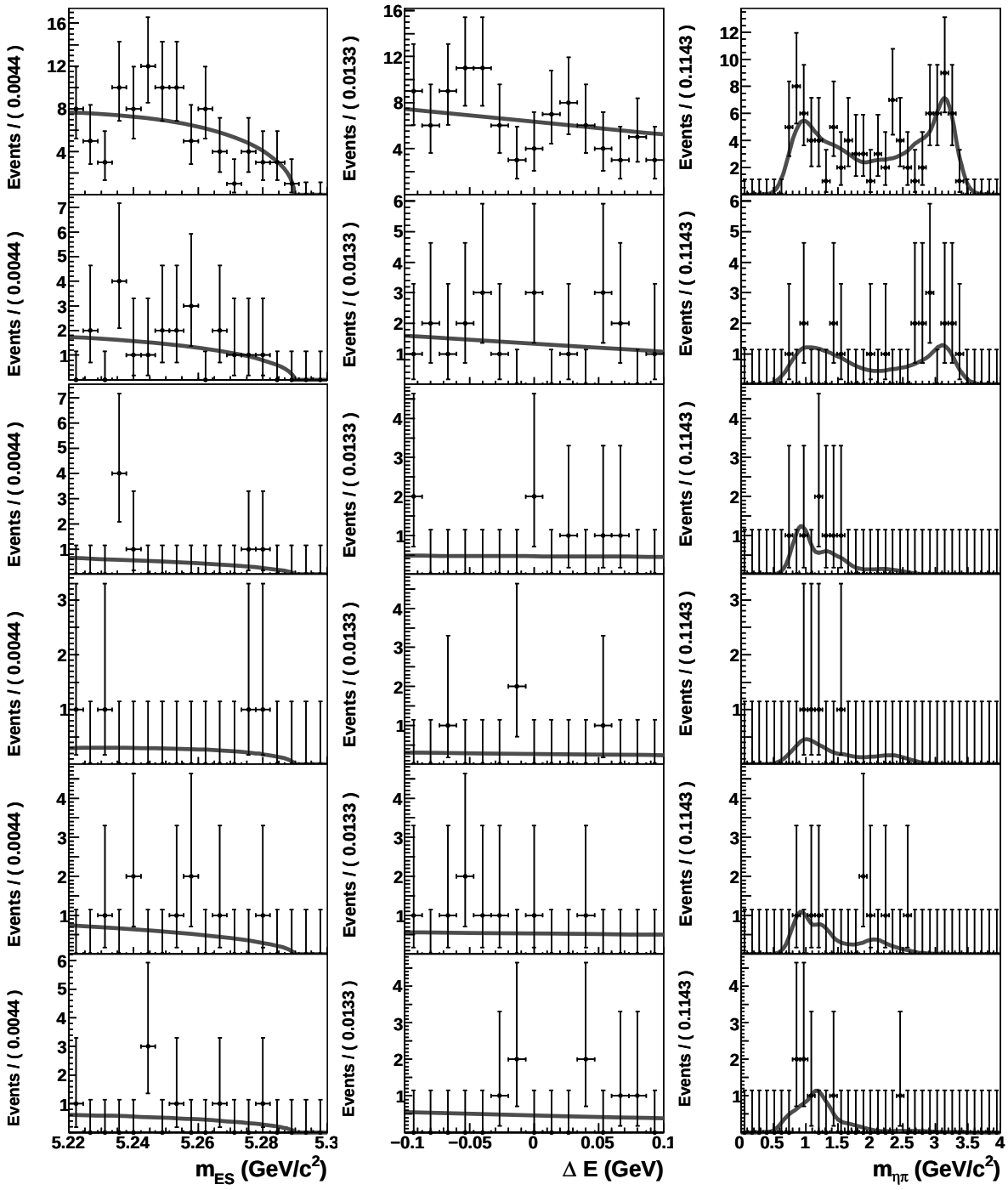

Figure 6.5: Off-peak data projected on $m_{\rm ES}$, ΔE and $m_{\eta\pi}$ (from left to right) for the DchI, DchII, DstI, DstII, DstIII and DstIV from top to bottom. The likelihood fit of the continuum background p.d.f. is projected on the data as a solid line.

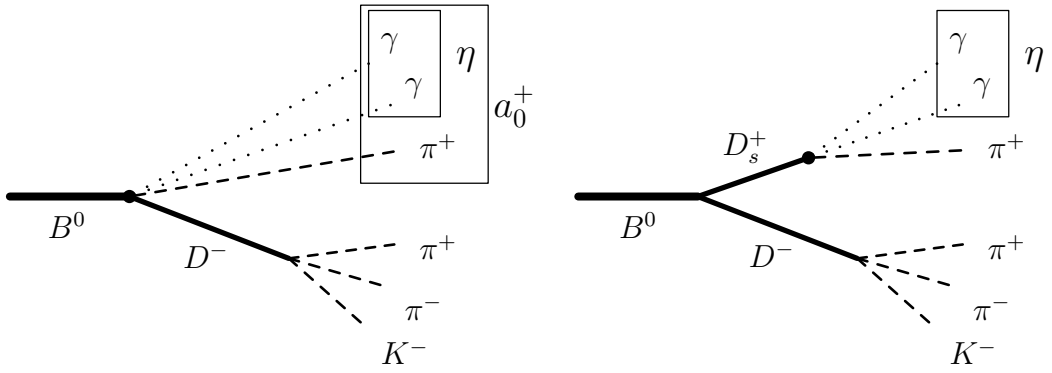

Figure 6.6: Schematic drawing of the $B^0 \to D^{(*)-}a_0^+$ (*left*) and $B^0 \to D^{(*)-}D_s^+$ decays (*right*) time of flight.

overlap with the observed number of events in the off-peak data sample. This does not influence the results of the fitted number of (non-)resonant events or $B^0 \to D^{(*)-}D_s^+$ events.

As we have concluded earlier, `Jetset` does not implement several suppression mechanisms that are present. Only a naive prognosis of decay channels is produced. The chances of a $q\overline{q}$ event to pass the selection are not uniform over all produced channels and, as such, the Monte Carlo sample produced by `Jetset` may well lead to a wrong prediction of the size of the background in the data sample. Although the likelihood fit, as it has been setup, is not very sensitive to fitting the precise ratio between $q\overline{q}$ and $B\overline{B}$ background, it *is* for distinguishing signal from background. As a result, since the shapes are well described, no errors are expected from the difference between the measured and predicted sample sizes.

6.2.2 Validation of reconstruction and selection criteria using the D_s resonance

The $B^0 \to D^{(*)-}D_s^+$, $D_s^+ \to \eta\pi^+$, decay is an excellent decay mode to validate the reconstruction and selection criteria. The decay has the same final state ($D^{(*)-}\eta\pi^+$) as the $B^0 \to D^{(*)-}a_0^+$ and $B^0 \to D^{(*)-}\eta\pi^+$ analysis and has a relatively large branching ratio, $\mathcal{B}(B^0 \to D^-D_s^+) = (7.4 \pm 0.7) \cdot 10^{-3}$ and $\mathcal{B}(B^0 \to D^{*-}D_s^+) = (8.3 \pm 1.1) \cdot 10^{-3}$.

Although the exact same reconstruction of the B meson and selection criteria are used, the reconstruction efficiency of this decay is lower for the $B^0 \to D^{(*)-}D_s^+$ reconstruction than that of $B^0 \to D^{(*)-}\eta\pi^+$ and $B^0 \to D^{(*)-}a_0^+$. This is because some of the selection variables are sensitive to difference in flight length of the D_s and a_0 mesons; the a_0 decays almost instantaneous while the D_s meson has a short but significant flight length. Figure 6.6 shows a schematic drawing of the flight length difference between the decays. The **TreeFitter** decay chain fit is highly sensitive to this difference. It is configured to fit for no flight length for the a_0 meson in the reconstructed $B^0 \to D^{(*)-}a_0^+$ decay hypothesis. For a produced $B^0 \to D^{(*)-}a_0^+$ or $B^0 \to D^{(*)-}\eta\pi^+$ event it converges five times more often than for a produced $B^0 \to D^{(*)-}D_s^+$ decay.

	DchI		DchII		DstI	
selected	#ev	fitted value	#ev	fitted value	#ev	fitted value
# selected	171		40		54	
$\#D_s$		$48.1^{+7.9}_{-7.2}$		$2.1^{+1.9}_{-1.2}$		$19.1^{+5.2}_{-4.4}$
#Bkg		123^{+12}_{-11}		$37.9^{+6.5}_{-5.8}$		$34.9^{+6.6}_{-5.9}$
slope		$-0.07^{+0.17}_{-0.16}$		$-0.22^{+0.25}_{-0.24}$		$-0.32^{+0.31}_{-0.30}$
	DstII		DstIII		DstIV	
selected	#ev	fitted value	#ev	fitted value	#ev	fitted value
# selected	36		52		8	
$\#D_s$		$15.4^{+4.6}_{-3.9}$		$13.8^{+4.9}_{-4.1}$		$0.0^{+0.6}_{-0.0}$
#Bkg		$20.6^{+5.2}_{-4.5}$		$38.2^{+7.1}_{-6.3}$		$8.0^{+3.2}_{-2.5}$
slope		$-0.54^{+0.34}_{-0.28}$		$-0.30^{+0.26}_{-0.24}$		$0.2^{+0.5}_{-0.6}$

Table 6.3: Results from the likelihood fits (to the data) corresponding to Fig. 6.7-6.12 and the number of selected B candidates for the reconstructed modes.

As a result of this difference, the reconstruction efficiency in the $B^0 \to D^{(*)-}D_s^+$ channels is lower than in the $B^0 \to D^{(*)-}a_0^+$ channel. And hence, we cannot make a direct quantitative comparison between the two analyses. Instead, we compare the expected number of reconstructed $B^0 \to D^{(*)-}D_s^+$ events, as obtained from Monte Carlo simulation studies, with the observed number of $B^0 \to D^{(*)-}D_s^+$ events in the data sample.

For the comparison, a mass window around the D_s resonance of 250 MeV/c^2 in the $\eta\pi$-invariant mass observable is selected. The background in this small mass window, is to a good approximation, flat. The likelihood fit is performed in the three observables $m_{\rm ES}$, ΔE and $m_{\eta\pi}$ and modeled with the generic $B\overline{B}$ and $B^0 \to D^{(*)-}D_s^+$ p.d.f. components, as described in Table 5.1. The $B\overline{B}$ p.d.f. in the $m_{\eta\pi}$ observable has been replaced by a first order polynomial to describe the flat background in the region.

The results of the likelihood fit to the (unscaled) Monte Carlo data are presented in Fig. 6.13-6.18 and summarized in Table 6.4. The results of the likelihood fit to the data are presented in Fig. 6.7-6.12 and the summarized results are found in Table 6.3. For easy comparison Table 6.5 presents the scaled Monte Carlo results next to the results obtained from the data.

From the Figs. 6.7-6.12, a clear difference is seen in the ΔE and $m_{\eta\pi}$ plots between the $m_{\rm ES}$ side and signal region, both in the data distribution and in the projected fitted p.d.f.. The shapes of the $m_{\rm ES}$ Argus function, the ΔE slope of the $B\overline{B}$ p.d.f., as well as the $m_{\rm ES}$ and ΔE Cruijff functions, and the Breit-Wigner lineshape function in the $B^0 \to D^{(*)-}D_s^+$ p.d.f. match the projected data points adequately.

Decays of D_s^{*+} mesons into $D_s^+\gamma$, produced in $B^0 \to D^{(*)-}D_s^{*+}$ decays, can also contribute to the D_s^+ resonance in the $\eta\pi$-invariant mass spectrum. In the reconstruction as $B^0 \to D^{(*)-}\eta\pi^+$ events, the omitted photon will lead to missing energy and momentum and as a result, the events will peak in neither $m_{\rm ES}$ nor ΔE. In Fig. 6.17 we can clearly identify a D_s^+ resonance in the $m_{\rm ES}$ sideband where the events have been iden-

	DchI		DchII		DstI	
p.d.f./MC	#ev	fitted value	#ev	fitted value	#ev	fitted value
# selected	690		187		242	
$\#D_s$		177^{+15}_{-14}		$23.5^{+5.9}_{-5.1}$		113^{+12}_{-11}
#Bkg		513^{+24}_{-23}		163^{+13}_{-13}		129^{+12}_{-12}
slope		$-0.17^{+0.08}_{-0.08}$		$-0.28^{+0.13}_{-0.13}$		$0.03^{+0.17}_{-0.17}$
	DstII		DstIII		DstIV	
p.d.f./MC	#ev	fitted value	#ev	fitted value	#ev	fitted value
# selected	183		200		66	
$\#D_s$		$76.5^{+9.6}_{-8.9}$		$70.4^{+9.6}_{-8.8}$		$22.5^{+5.3}_{-4.7}$
#Bkg		$0.6^{+0.0}_{-0.0}$		130^{+12}_{-12}		$43.5^{+7.1}_{-6.5}$
slope		$-0.10^{+0.18}_{-0.17}$		$-0.09^{+0.16}_{-0.16}$		$-0.26^{+0.25}_{-0.23}$

Table 6.4: Results from the likelihood fits (to the Monte Carlo) corresponding to Fig. 6.13-6.18 and the number of selected B candidates for the reconstructed modes.

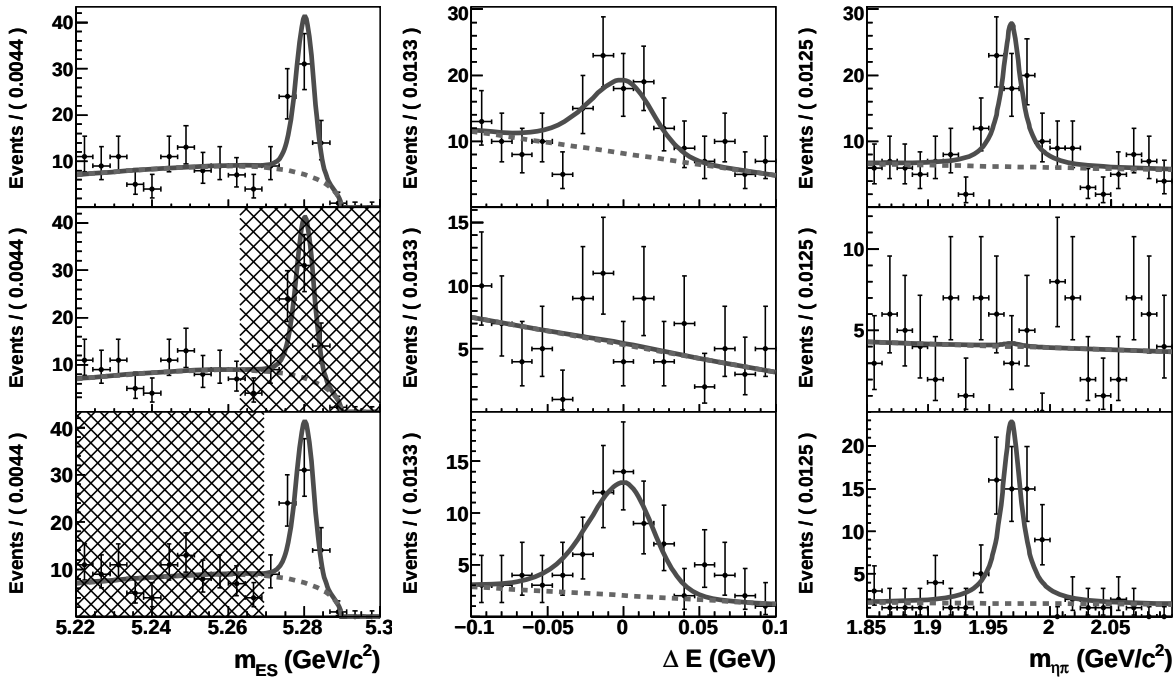

Figure 6.7: Observed distribution of the reconstructed B candidates in the DchI mode projected (from left to right) in $m_{\rm ES}$, ΔE and $m_{\eta\pi}$. The top (middle, *bottom*) row shows the full (sideband, *signal* selected) region. The excluded region is indicated by the hatched area in the $m_{\rm ES}$ projection of the data sample. The component background p.d.f.'s are accumulated in the following order: background (dashed), $B^0 \to D^{(*)-}D_s^+$ (solid) line.

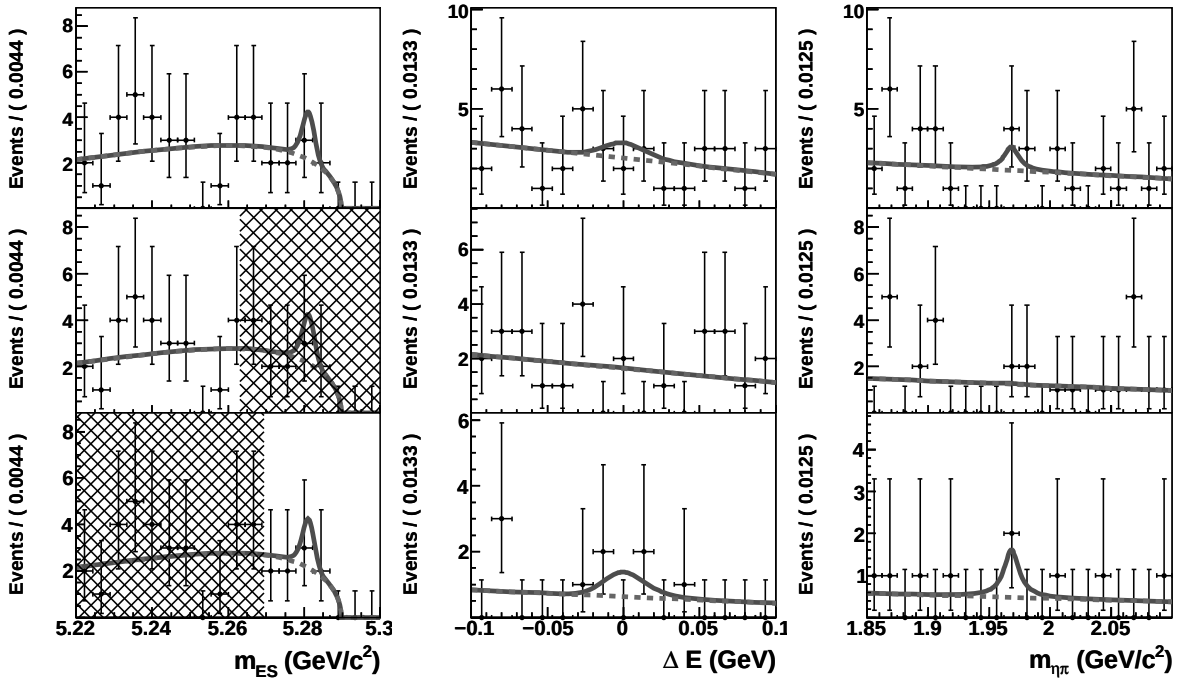

Figure 6.8: Observed distribution of the reconstructed B candidates in the DchII mode, see Fig. 6.7 for a description.

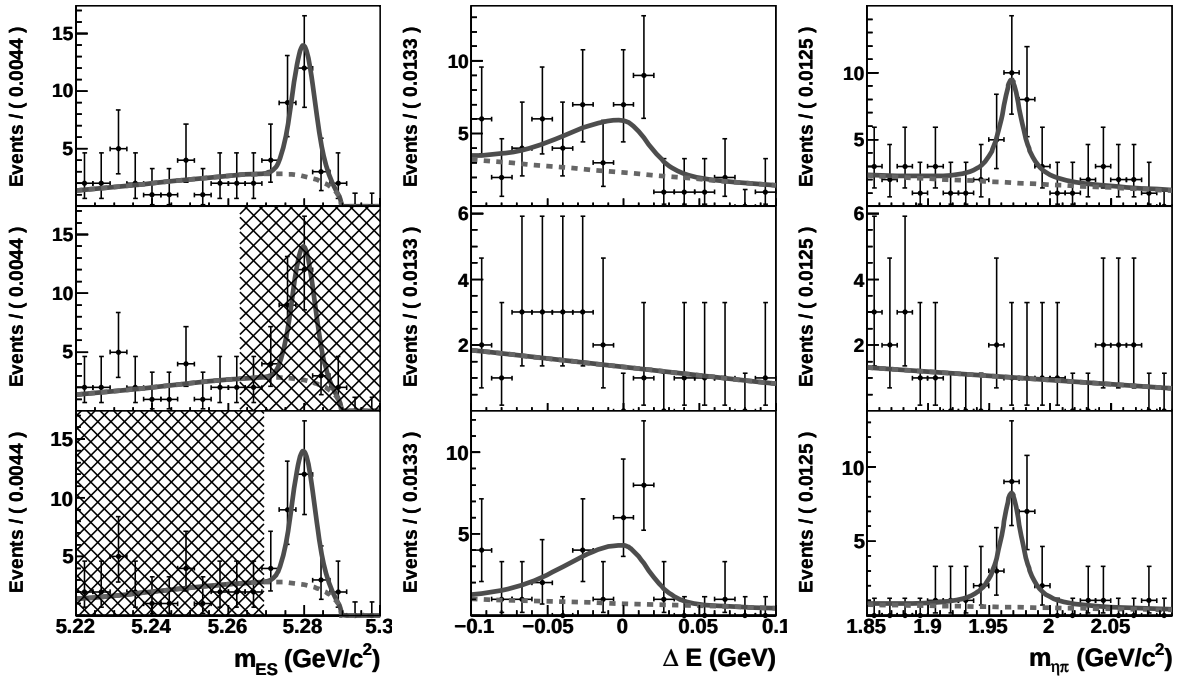

Figure 6.9: Observed distribution of the reconstructed B candidates in the DstI mode, see Fig. 6.7 for a description.

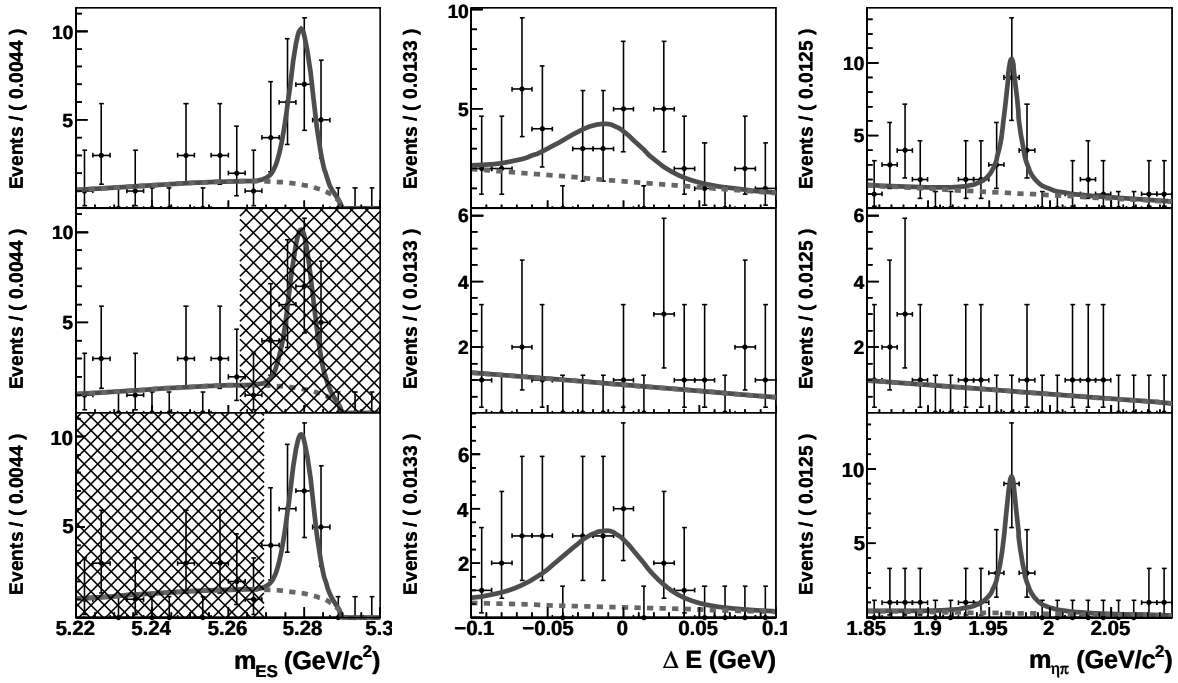

Figure 6.10: Observed distribution of the reconstructed B candidates in the DstII mode, see Fig. 6.7 for a description.

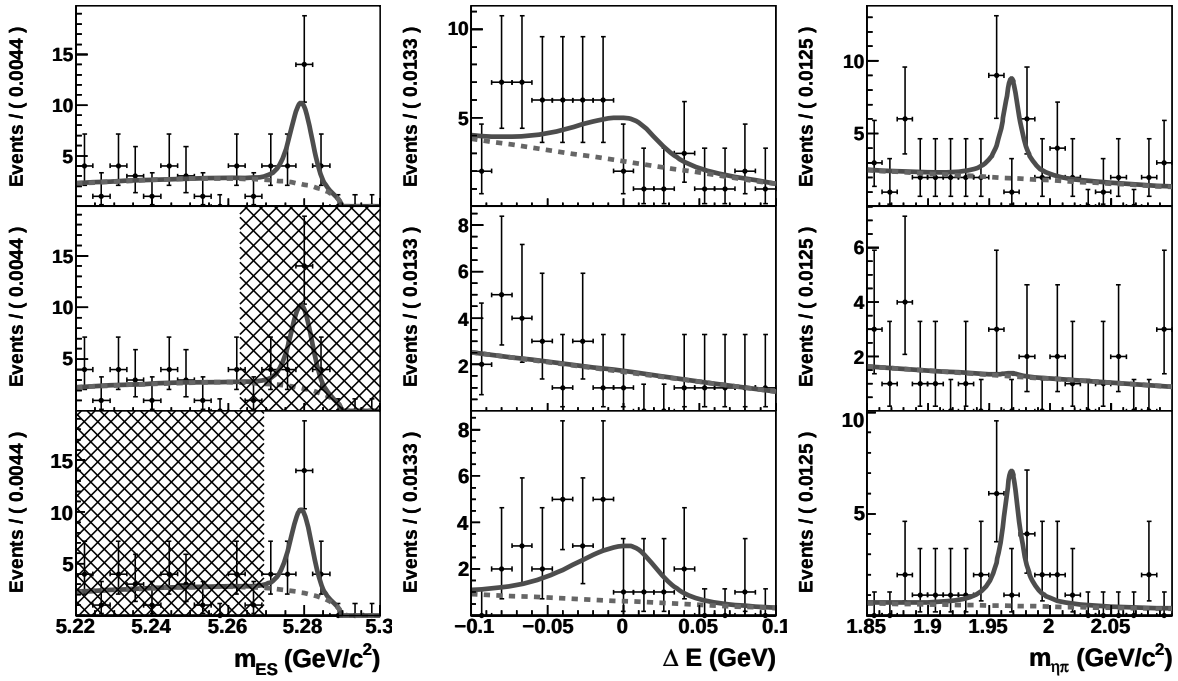

Figure 6.11: Observed distribution of the reconstructed B candidates in the DstIII mode, see Fig. 6.7 for a description.

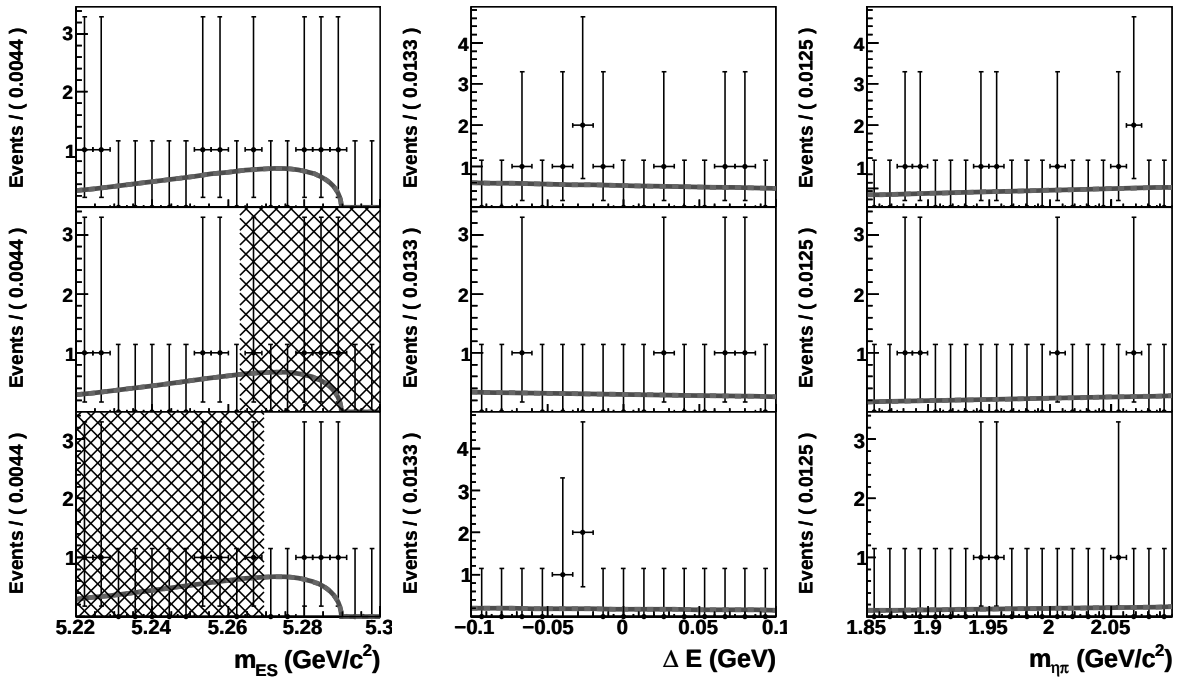

Figure 6.12: Observed distribution of the reconstructed B candidates in the DstIV mode, see Fig. 6.7 for a description.

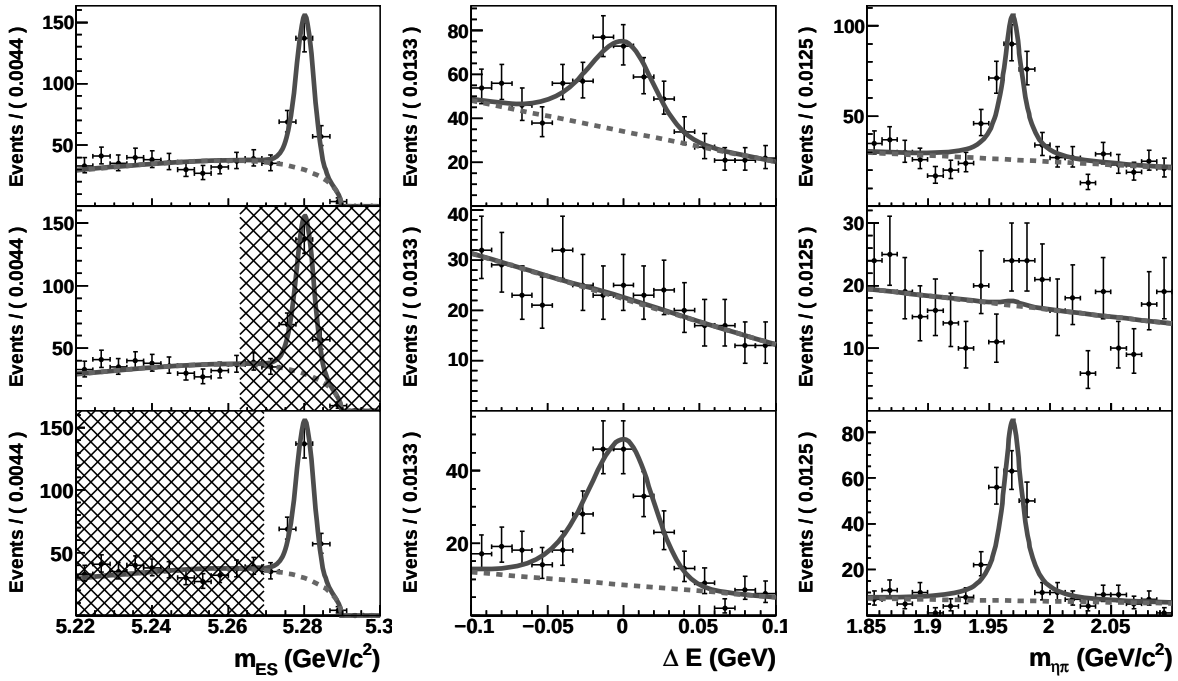

Figure 6.13: Distributions of the Monte Carlo simulated data reconstructed in the DchI mode, see Fig. 6.7 for a description.

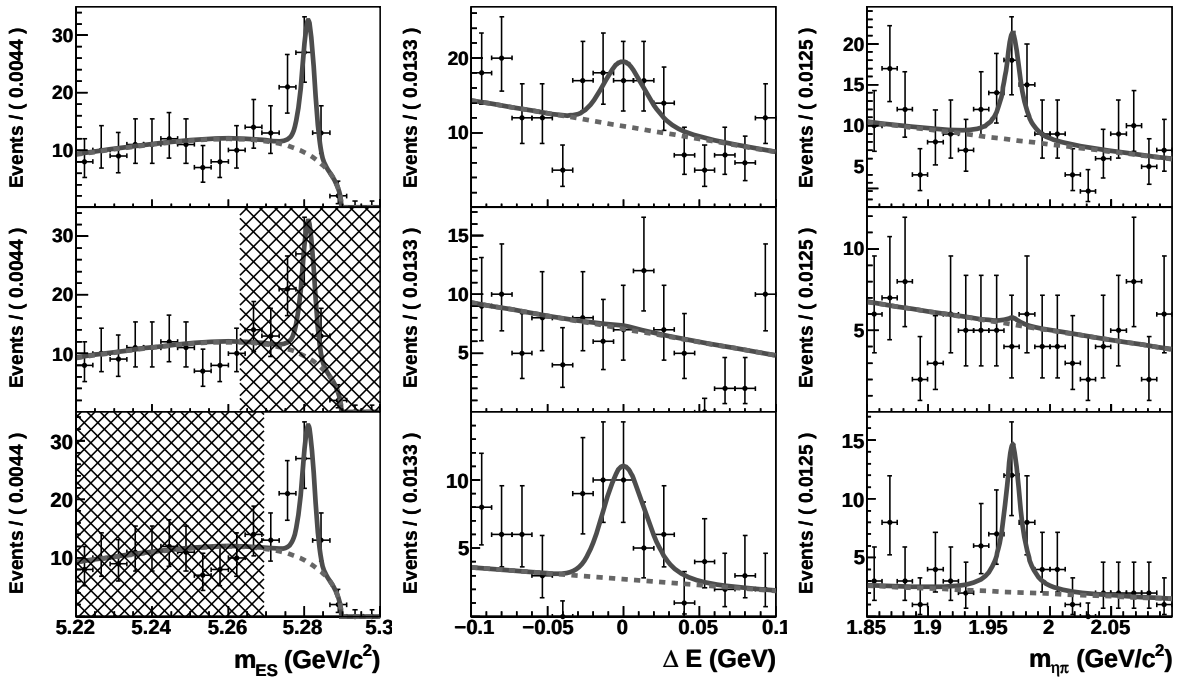

Figure 6.14: Distributions of the Monte Carlo simulated data reconstructed in the DchII mode, see Fig. 6.7 for a description.

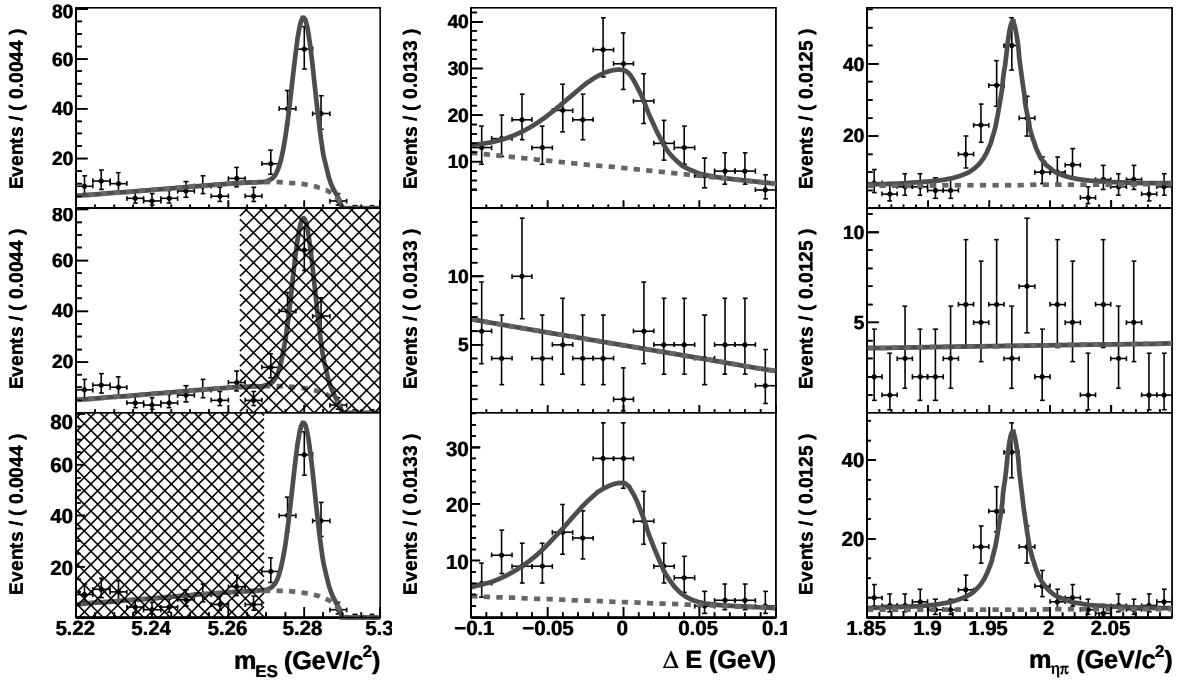

Figure 6.15: Distributions of the Monte Carlo simulated data reconstructed in the DstI mode, see Fig. 6.7 for a description.

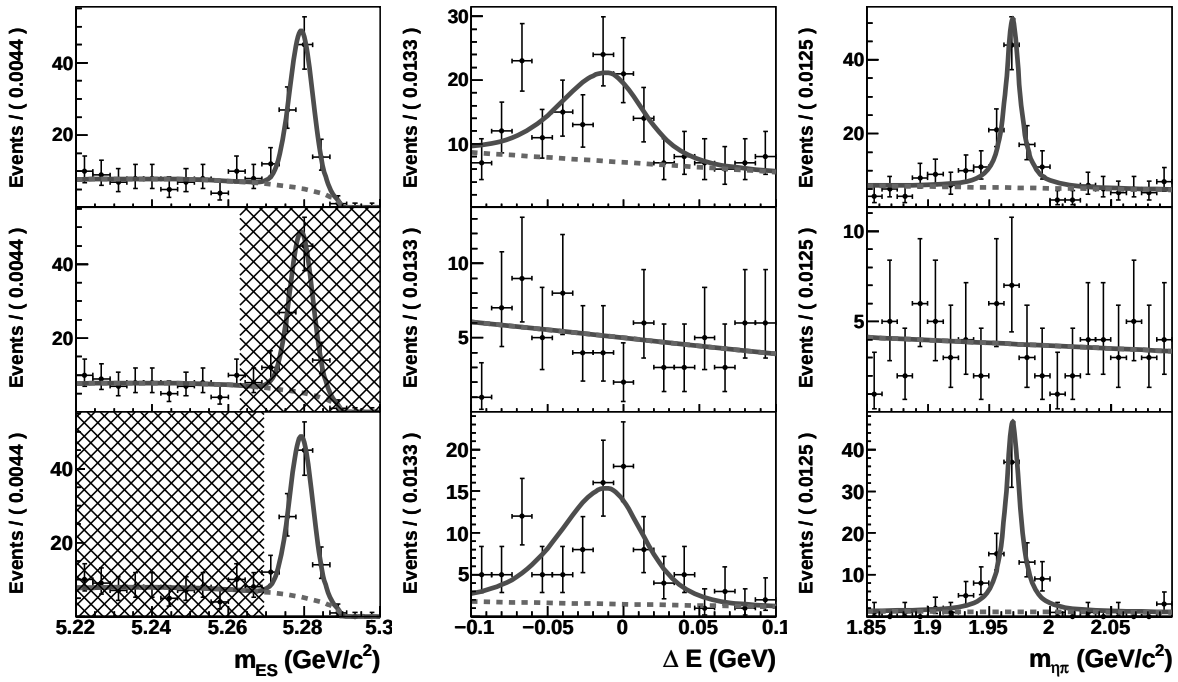

Figure 6.16: Distributions of the Monte Carlo simulated data reconstructed in the DstII mode, see Fig. 6.7 for a description.

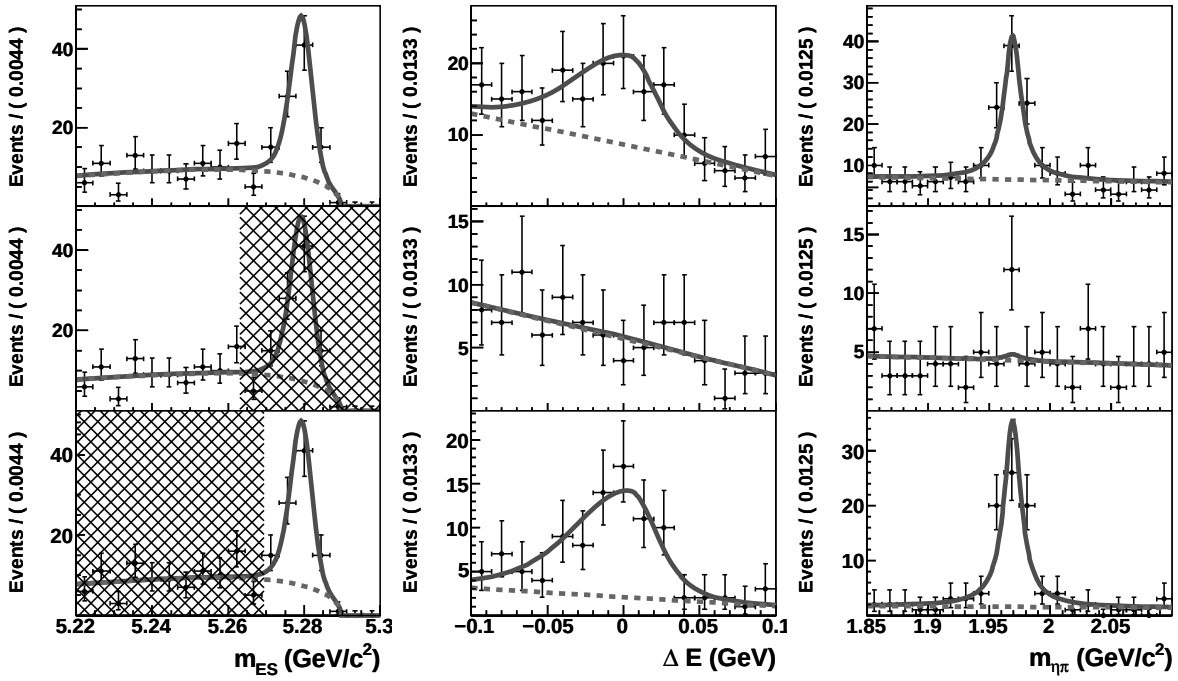

Figure 6.17: Distributions of the Monte Carlo simulated data reconstructed in the DstIII mode, see Fig. 6.7 for a description.

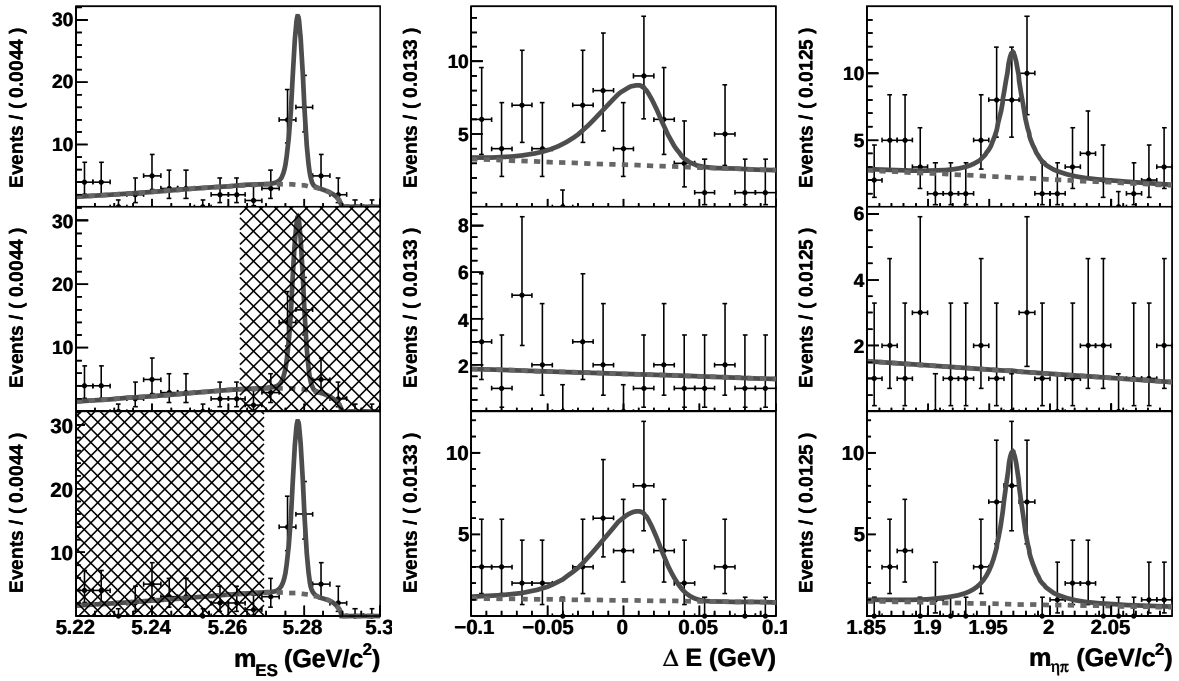

Figure 6.18: Distributions of the Monte Carlo simulated data reconstructed in the DstIV mode, see Fig. 6.7 for a description.

	# reconstructed $B^0 \to D^{(*)-} D_s^+$ events		
decay mode	MC unscaled	MC scaled	data
DchI	177^{+14}_{-14}	$37.9^{+3.1}_{-3.0}$	48^{+7}_{-7}
DchII	$23.5^{+5.9}_{-5.1}$	$5.0^{+1.3}_{-1.1}$	$2.1^{+1.9}_{-1.2}$
DstI	112^{+11}_{-10}	$24.1^{+2.5}_{-2.3}$	19^{+5}_{-4}
DstII	$76.5^{+9.6}_{-8.9}$	$16.4^{+2.1}_{-1.9}$	$15.4^{+4.6}_{-3.9}$
DstIII	$70.4^{+9.6}_{-8.8}$	$15.1^{+2.1}_{-1.9}$	$13.8^{+4.9}_{-4.1}$
DstIV	$22.5^{+5.3}_{-4.7}$	$4.8^{+1.1}_{-1.0}$	$0.0^{+0.6}_{-0.0}$

Table 6.5: Number of reconstructed $B^0 \to D^{(*)-} D_s^+$ events to the Monte Carlo and measured data for each reconstructed decay mode. The Monte Carlo results are presented unscaled and scaled to the measured data.

tified as $B^0 \to D^{(*)-} D_s^{*+}$ events. Some of the D_s^{*+} events may be fitted as D_s^+ events. As the produced branching fraction in Monte Carlo simulations is consistent with the measurements [9], this will not deteriorate the $B^0 \to D^{(*)-} D_s^+$ comparison.

In Table 6.5 the direct comparison is presented between the data and the scaled Monte Carlo simulated data. In general the measured number of $B^0 \to D^{(*)-} D_s^+$ events in data match the predictions from the Monte Carlo simulated data.

It can be argued that the two K_S^0 modes, $B^0 \to D^- a_0^+$ ($D^+ \to K_S^0 \pi^+$) and $B^0 \to D^{*-} a_0^+$ ($D^{*+} \to D^0 \pi^+$, $D^0 \to K_S^0 \pi^+ \pi^-$), do not agree. However, removal of the K_S^0 specific selection variables does not alter the relative difference between the Monte Carlo predictions and

the measurement in data. There is no reason to believe that the difference is caused by selection variables as in all other decays the measurements in data are well predicted by Monte Carlo studies. We would like to point out that uncertainties in the fractional branching ratios in these channels are relatively high. These are presented in Sect. 7.3.

In the next chapter we will calculate the systematic uncertainty for the event shape uncertainties based on the results presented here.

From Monte Carlo studies we expect to see the D_s^+ resonance in the $m_{\eta\pi}$ spectrum in most of the reconstructed decays. This agrees with our observations in data. The distributions that are found in the three observables, $m_{\rm ES}$, ΔE and $m_{\eta\pi}$ in data are adequately described by the $B\overline{B}$ and $B^0 \to D^{(*)-}D_s^+$ p.d.f.'s. The parameters, except for the $m_{\eta\pi}$ slope, of these p.d.f.'s have been determined on the full Monte Carlo simulated data. This leaves us no reason to question the correctness of the description of the event shape variables that are used to select the data.

6.2.3 Fit bias studies with signal enriched data samples

We study the fit response in signal enriched data samples. Samples are created with 2, 5, 10 and 20 added full Monte Carlo signal events, 100 samples each, and subsequently fitted. The distributions of the fitted number of events and the fit errors are fitted with a Gaussian function and the mean of these, central value and error, are plotted versus the added number of signal events, see Fig. 6.19. We correct for the fraction of mis-reconstructed events in the signal Monte Carlo using the fitted ratio, f_S, presented in Table 5.2. The fitted slopes of the signal response are, for all the different decay modes, consistent with one. In other words, for every signal event that is injected to the data set, we fit one extra signal event. The response of the fit is behaving perfectly.

The response test on non-resonant signal is performed using toy Monte Carlo events, as full Monte Carlo events are not available due to the `Jetset` bug. Sets of 2, 5, 10, 20, 30 or 40 events are created and added tot the data sample and fitted. For every set this is repeated 100 times. The distributions of the fitted number of events and errors of the likelihood fit are subsequently fitted using a Gaussian function. The means of the central values and errors are plotted against the added number of events and fitted with a line.

The fitted slopes of the non-resonant signal response are, for all the different decay modes, consistent with one. In other words, for every added non-resonant signal event that is injected to the data set, we fit one extra non-resonant signal event. The response of the fit is behaving perfectly.

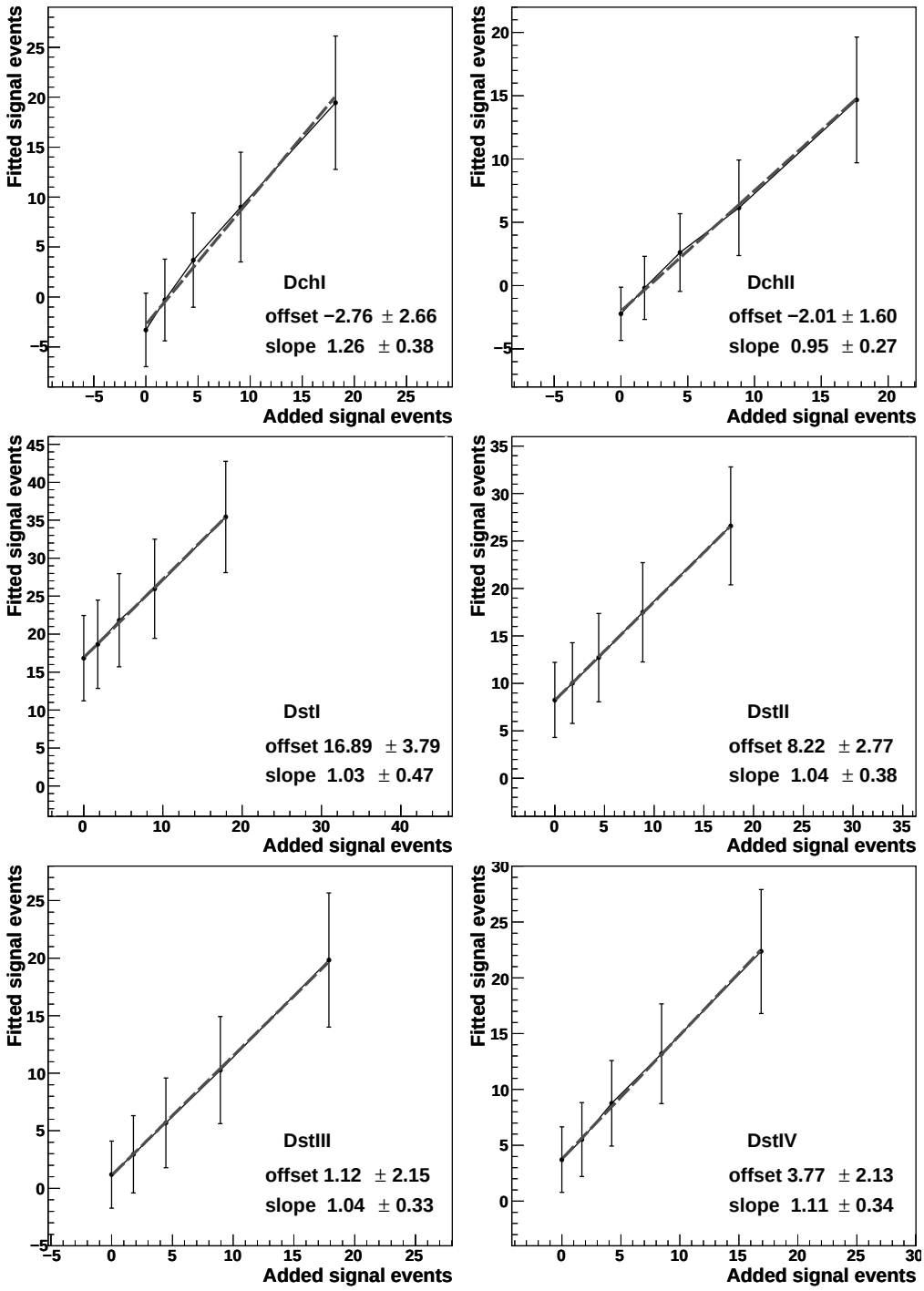

Figure 6.19: Result of bias test on data with added full Monte Carlo signal events. The first point represent the central value and error of the likelihood fit to the data sample. Each following point represents the mean of the central values for 100 fits, the error represents the mean of the fit errors.

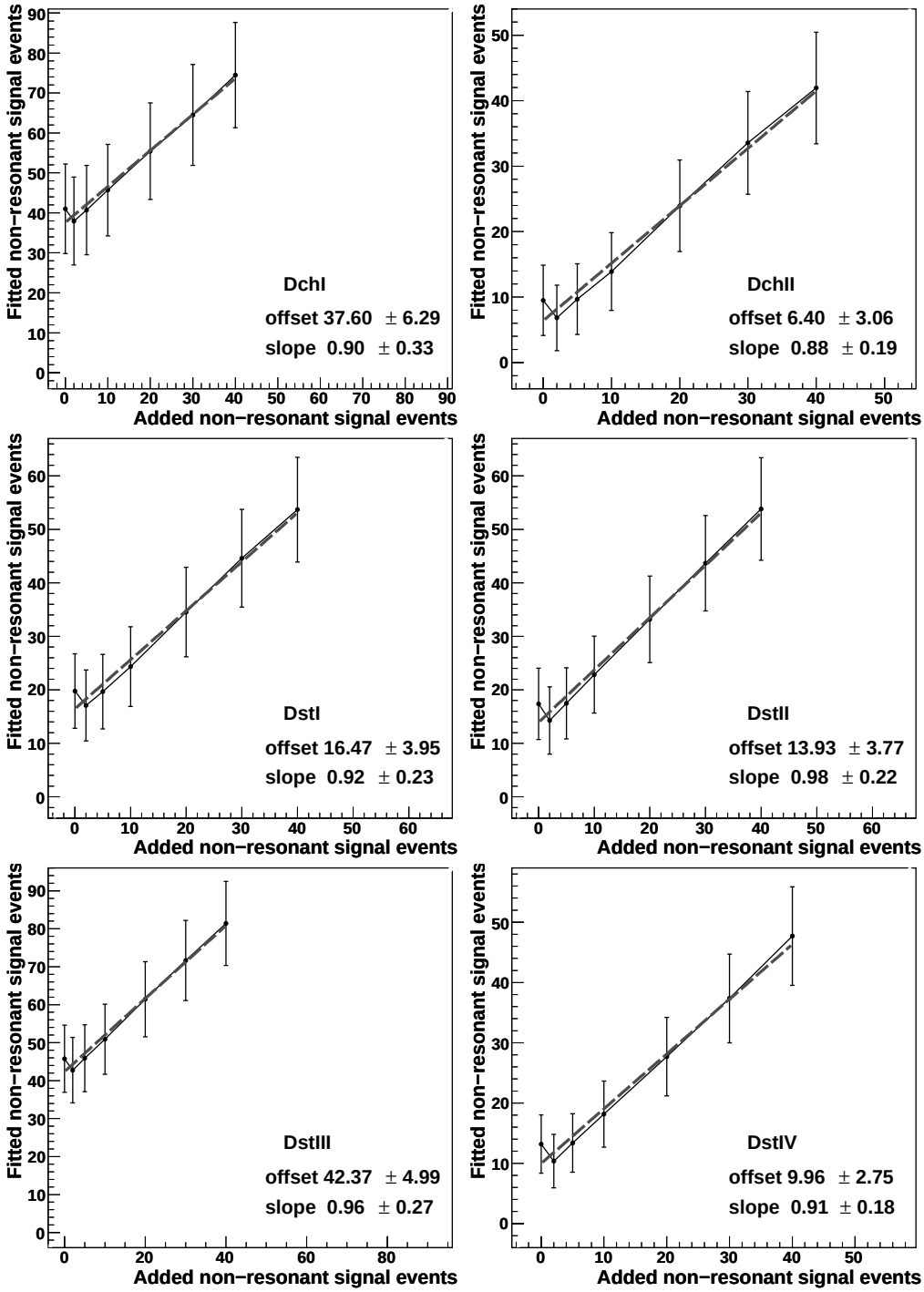

Figure 6.20: Result of bias test on data with added, toy Monte Carlo produced, non-resonant signal events. The first point represent the central value and error of the likelihood fit to the data sample. Each following point represents the mean of the central values for 100 fits, the error represents the mean of the fit errors.

Chapter 7

Evaluation of systematic uncertainties

In this chapter we evaluate the systematic uncertainties that are present in the analysis.

The fitted number of $B^0 \to D^{(*)-}\eta\pi^+$ and $B^0 \to D^{(*)-}a_0^+$ signal events are used to calculate branching ratios using formula Eq. (5.12) on page 98. The sources of systematic errors that we consider are categorized in the four ingredients input to the branching ratio calculation: errors present in N_{obs}, N_B, $\mathcal{B}(D^{(*)\pm})$ and in the efficiency ε. Corrections applied on the observed number of events and to the efficiency are discussed in Sect. 7.1.1 and 7.4 respectively. All results obtained in this chapter are summarized in Sect. 7.5.

7.1 Number of observed events uncertainties

7.1.1 Bias offset

A bias in the fitted number of resonant and non-resonant signal events is determined in a Monte Carlo response test in Sect. 6.1.2. The same test shows that the response is consistent with a linear behavior. All fitted slopes to the plots presented in Fig. 6.2 and Fig. 6.3 are consistent with one. The number of observed signal events is corrected with the observed bias offset determined for the number of observed events. A systematic error that is equal to the size of the correction is assigned to this procedure. Table 7.1 presents the correction values.

7.1.2 Non-resonant $m_{\eta\pi}$ shape description

The p.d.f. that describes the non-resonant invariant $\eta\pi$-mass distribution is the product of the theoretical shape and the selection efficiency as a function of $m_{\eta\pi}$. The selection efficiency function is determined using the generated and selected event distributions, see Sect. 4.5. The two distributions, which are in our case statistically independent, are divided and fitted with a Chebychev polynomial.

decay	resonant signal	non-resonant signal
DchI	+2.7	+8.3
DchII	+1.8	−8.2
DstI	+1.3	+3.7
DstII	+0.5	+2.5
DstIII	−0.9	+4.6
DstIV	−0.5	−3.0

Table 7.1: Correction values to N_{obs}.

The systematic error associated to the statistical uncertainties that are present in the determination of the shape of the final p.d.f., is determined using simulation studies. We produce toy Monte Carlo sets that are Poisson variations of the two original distributions, and repeat the division and fitting process for each of the generated sets. The newly fitted Chebychev polynomial replaces the original non-resonant $m_{\eta\pi}$ efficiency function and used as input in a combined fit to the data. This procedure is repeated 100 times, for each decay mode separately. The combined fits, as described in Sect. 5.7, to obtain the branching ratio's for the four decays ($B^0 \to D^- a_0^+$, $B^0 \to D^{*-} a_0^+$, $B^0 \to D^- \eta\pi^+$ and $B^0 \to D^{*-} \eta\pi^+$), are repeated with the new description of the efficiency curve.

The standard deviations on the fitted branching ratio are $3.2 \cdot 10^{-7}$, $3.8 \cdot 10^{-7}$, $5.3 \cdot 10^{-7}$ and $1.4 \cdot 10^{-6}$ for the $B^0 \to D^- a_0^+$, $B^0 \to D^{*-} a_0^+$, $B^0 \to D^- \eta\pi^+$ and $B^0 \to D^{*-} \eta\pi^+$ branching ratio measurements respectively. The systematic error associated to the uncertainties in the $m_{\eta\pi}$ description are taken as these standard deviations.

7.1.3 Lineshape uncertainties

The lineshape width and nominal mass of the a_0 meson are not accurately known. The current PDG [9] summarizes the measurements of the nominal mass and width of the a_0 meson and quotes $(984.7 \pm 1.2)\,\mathrm{MeV}/c^2$ and a range from (50 to 100) MeV/c^2 respectively.

The width of the Breit-Wigner lineshape, used in the resonant signal p.d.f., is fixed on the Monte Carlo simulated data. This data are generated with a nominal mass of 983 MeV/c^2 and a width of 57 MeV/c^2. The nominal mass is fixed at the central value quoted in the PDG.

The induced error on the fitted number of signal events, introduced by an incorrect nominal mass and/or lineshape width, is investigated by refitting the data using the combined branching ratio fit with different values for the lineshape parameters. The nominal mass value is varied within $(-2\sigma, +2\sigma)$ around the central value of $984.7\,\mathrm{MeV}/c^2$. The linewidth is varied between 50 and 100 MeV/c^2. The results for the individual fits are presented in Fig. 7.1.

The systematic errors associated to the uncertainties in the lineshape are taken to be one standard deviation of the spread of the results induced by deviations to the nominal mass or the linewidth. The standard deviations on the fitted branching ratio are $2.7 \cdot 10^{-7}$, $4.0 \cdot 10^{-6}$, $8.4 \cdot 10^{-7}$ and $6.7 \cdot 10^{-7}$ for the different linewidths and $5.3 \cdot 10^{-8}$, $4.5 \cdot 10^{-8}$, $5.6 \cdot 10^{-8}$ and $5.4 \cdot 10^{-8}$ for the variation of the nominal mass for the branching

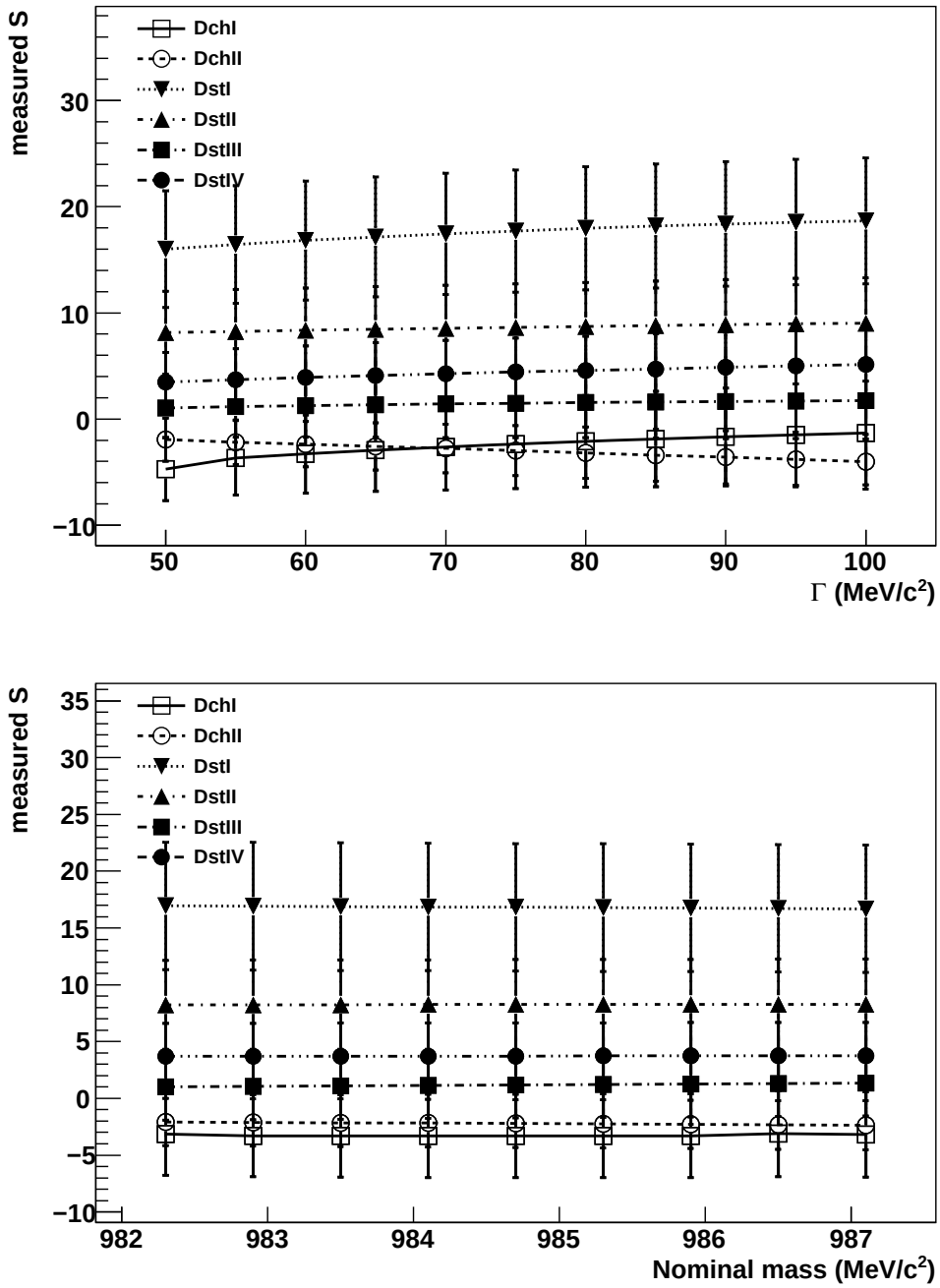

Figure 7.1: Fitted number of signal events for different lineshape parameter values for the six individual decay mode likelihood fits. In the top plot the linewidth is varied, in the bottom plot the nominal mass value.

ratios of $B^0 \to D^- a_0^+$, $B^0 \to D^{*-} a_0^+$, $B^0 \to D^- \eta\pi^+$ and $B^0 \to D^{*-} \eta\pi^+$ respectively.

7.1.4 Cross feed between decay modes

Cross feed between the six reconstructed $D^{(*)\pm}$ decay modes is studied using the full Monte Carlo samples. No significant cross feed is found.

Only one event from the signal Monte Carlo sample that is produced in $B^0 \to D^- a_0^+$ ($D^+ \to K_S^0 \pi^+$) mode is selected in the $B^0 \to D^- a_0^+$ ($D^+ \to K^- \pi^+ \pi^+$) mode, no events were selected in the vice versa way. The cross feed between the two $D^\pm$ modes is smaller than 0.04%. Under the assumption that the branching ratios of the $B^0 \to D^{*-} a_0^+$ and $B^0 \to D^- a_0^+$ are the same, less than 0.5% of the selected events in the reconstructed $B^0 \to D^- a_0^+$ mode originates from $B^0 \to D^{*-} a_0^+$ decays.

For the four analyzed $D^{*\pm}$ modes at most 1% of the selected events were produced in different decay modes. Most of these events lie in the side band and do not change the number of fitted signal events. The number of cross feed events that are fitted as signal is smaller 0.6%. No events are picked up from the generated $D^\pm$ modes.

All numbers quoted are corrected with a 1σ deviation to obtain an upper limit on the associated error. The effects of the cross-feeds are ignored because of the very small error that is introduced by doing so.

7.1.5 P.d.f. shape uncertainties

The p.d.f. shapes depend on the p.d.f. parameters. The error that is associated with the uncertainties in the p.d.f. parameters is studied.

The data are refit varying important shape parameters, one at a time, using the errors $(-\sigma, +\sigma)$ associated to the fitted shape parameter. The following parameters are varied for the $B^0 \to D^{(*)-} D_s^+$ and signal p.d.f.'s: the m_B, σ and α_L for the $m_{\rm ES}$ Cruijff, and all five parameters of the ΔE Cruijff. For the $q\overline{q}$ and $B\overline{B}$ p.d.f.'s the $m_{\rm ES}$ Argus slope and the ΔE slope are varied, and for the peaking $B\overline{B}$ p.d.f. also the $m_{\rm ES}$ Cruijff m_B, σ and α_L. Furthermore the ratio between the peaking and non-peaking $B\overline{B}$ p.d.f. is changed.

The systematic error associated to the p.d.f. shape uncertainties is taken to be one standard deviation of the fitted branching ratios. The standard deviation for the $B^0 \to D^- a_0^+$, $B^0 \to D^{*-} a_0^+$, $B^0 \to D^- \eta\pi^+$ and $B^0 \to D^{*-} \eta\pi^+$ branching ratios is $2.9 \cdot 10^{-7}$, $3.7 \cdot 10^{-7}$, $7.2 \cdot 10^{-7}$ and $8.0 \cdot 10^{-7}$.

7.2 Uncertainties in the number of B events

7.2.1 Luminosity and B counting

The number of B mesons in the data set is calculated by using the increase in the hadronic event rate, compared to direct muon pair production, between the off resonant

decay	branching fraction (%)
$\mathcal{B}(\eta \to \gamma\gamma)$	39.39±0.24
$\mathcal{B}(D^{*+} \to D^0\pi^+)$	67.7±0.5
$\mathcal{B}(D^+ \to K^-\pi^+\pi^+)$	9.51±0.34
$\mathcal{B}(D^+ \to K^0_S\pi^+)$	1.47±0.06
$\mathcal{B}(D^0 \to K^-\pi^+)$	3.82±0.07
$\mathcal{B}(D^0 \to K^-\pi^+\pi^0)$	13.5±0.6
$\mathcal{B}(D^0 \to K^-\pi^+\pi^+\pi^-)$	7.7±0.25
$\mathcal{B}(D^0 \to K^0_S\pi^+\pi^-)$	2.88±0.19
$\mathcal{B}(K^0_S \to \pi^+\pi^-)$	69.20±0.05
$\mathcal{B}(\pi^0 \to \gamma\gamma)$	98.798±0.032

Table 7.2: Branching fractions of sub-decays used to calculate the intermediate branching fractions for the $B^0 \to D^{(*)-}a_0^+$ and $B^0 \to D^{(*)-}\eta\pi^+$ decays [80].

decay mode	branching fraction (%)	rel. error (%)
DchI	3.75±0.14	3.6
DchII	0.401±0.017	4.1
Total D^+ modes	4.15±0.14	3.3
DstI	1.019±0.021	2.1
DstII	3.56±0.16	4.6
DstIII	2.05±0.07	3.4
DstIV	0.53±0.14	25.8
Total $D^{*\pm}$ modes	7.16±0.22	3.1

Table 7.3: Intermediate branching fractions and relative errors for the different decay modes.

and on resonant data. The increase is attributed to $\Upsilon(4S)$ decays. The systematic uncertainty in the B counting is 1.1% and is dominated by differences between the data and Monte Carlo tracking efficiency. The statistical uncertainty is negligible [79].

7.3 Fractional branching ratio uncertainties

The uncertainties on the fractional branching fraction of the $D^{(*)\pm}$ decay are calculated using the values and errors taken from [9], and are summarized in Table 7.2. The resulting intermediate branching fractions for each decay mode, and the relative errors are presented in Table 7.3.

7.4 Uncertainties and corrections in the selection efficiency

7.4.1 Statistical errors on the determined selection efficiency

The statistical errors on the calculated selection efficiencies, presented in Table 5.8 on page 98, are taken into account.

7.4.2 Reconstruction and selection criteria uncertainties

The systematic error associated to the reconstruction and selection criteria uncertainties is estimated using the $B^0 \to D^{(*)-} D_s^+$ decay. In Sect. 6.2.2 we have used this decay for validation studies and compared the Monte Carlo predictions with the observations. The resulting number of predicted and observed $B^0 \to D^{(*)-} D_s^+$ events are summarized in Table 6.5.

From these results we test the hypothesis that the measurement matches the prediction with no bias or scaling factor. We define a normalized χ^2 by

$$\chi^2_{norm} = \sum_i^N \frac{1}{N} \cdot \frac{(N_m - N_p)_i^2}{(\sigma_m + \sigma_p)_i}, \tag{7.1}$$

where the summation sums over all decay modes, N_m is the number of measured $B^0 \to D^{(*)-} D_s^+$ events, N_p is the predicted number of events, and σ_m and σ_p are the associated errors. The error associated to the prediction, σ_p, contains the error from the likelihood fit and the associated error of the fractional branching ratio of the $D^{(*)\pm}$ decay chain. The error σ_m is taken to be the square root of the predicted number of events, to reduce the impact of statistical fluctuations in the errors observed in data at the current low statistics.

The calculated normalized χ^2 is 1.24 which corresponds to a systematic error of 10% using the following equation

$$\sigma_{sys} = 1 - \sqrt{\frac{1}{\chi^2_{norm}}}. \tag{7.2}$$

7.4.3 Track finding efficiency

The track finding efficiency for the different tracking lists are determined by a dedicated working group in *BABAR*, using the information of the SVT and DCH [81]. The GoodTracksVeryLoose efficiencies in the Monte Carlo are assigned a 1.4% systematic error per track, the GoodTracksLoose 1.3% per track and the KsDefault 1.5% per reconstructed K_S^0. The uncertainties are added linearly. The resulting systematic errors are given in Table 7.5.

	$D^{\pm}$ modes		$D^{*\pm}$ modes			
Source	DchI	DchII	DstI	DstII	DstIII	DstIV
η eff. (%)	-3.0	-3.0	-3.0	-3.0	-3.0	-3.0
K_S^0 eff. (%)	–	-2.0	–	–	–	-2.0
π^0 eff. (%)	–	–	–	-0.5	–	–
tracking (%)	-2.6	-1.3	-2.3	-2.3	-3.6	-1.8

Table 7.4: Efficiency correction factors.

7.4.4 Neutral particle identification

A dedicated working group determines the systematic bias and error in the neutral particle identification using τ decays [82]. We use the results of the performed studies and apply a systematic error of 3% per reconstructed π^0 and η meson. The η meson, which is composed of the same lists (GoodPhotonLoose) as the π^0 meson, is treated in the same way.

7.4.5 Summary of efficiency corrections

Efficiency corrections are performed for differences between the Monte Carlo and data in the reconstruction of charged tracks and neutral particle identification [81, 82]. A -0.5% correction is applied to compensate for the differences between Monte Carlo and data due to a different description of the π^0 reconstruction. The efficiency is corrected with -0.8% per GoodTrackLoose track and -0.5% per GoodTrackVeryLoose track.

7.5 Systematic errors summary tables

All systematic uncertainties that are quoted in this chapter are summarized in Table 7.5. The largest common error is induced by the uncertainty of the Monte Carlo description of the selection variables. All values are used in the next chapter to determine the systematic errors on the determined branching ratios.

source	$D^{\pm}$ modes		$D^{*\pm}$ modes			
	DchI	DchII	DstI	DstII	DstIII	DstIV
Resonant signal specific errors						
observed number of events						
bias offset (a.v.)	2.7	1.8	1.3	0.5	0.9	0.5
observed branching ratio						
Γ_{a_0} (a.v)	$2.7 \cdot 10^{-7}$		$4.0 \cdot 10^{-6}$			
m_{a_0} (a.v.)	$5.3 \cdot 10^{-8}$		$4.5 \cdot 10^{-8}$			
$m_{\eta\pi}$ eff. (a.v.)	$3.2 \cdot 10^{-7}$		$3.8 \cdot 10^{-7}$			
p.d.f. shape (a.v)	$2.9 \cdot 10^{-7}$		$3.7 \cdot 10^{-7}$			
Non-resonant signal specific errors						
observed number of events						
bias offset (a.v.)	8.3	8.2	3.7	2.5	4.6	3.0
observed branching ratio						
Γ_{a_0} (a.v)	$8.4 \cdot 10^{-7}$		$6.7 \cdot 10^{-7}$			
m_{a_0} (a.v.)	$5.6 \cdot 10^{-8}$		$5.4 \cdot 10^{-8}$			
$m_{\eta\pi}$ eff. (a.v.)	$5.3 \cdot 10^{-7}$		$1.4 \cdot 10^{-6}$			
p.d.f. shape (a.v)	$7.2 \cdot 10^{-7}$		$8.0 \cdot 10^{-7}$			
Common errors						
number of B events						
B counting (%)	1.1		1.1			
fractional D decay						
$D^{(*)\pm}$ decay (%)	3.6	4.1	2.1	4.6	3.4	25.8
efficiency						
π^0 ID (%)	–	–	–	3.5	–	–
K_S^0 ID (%)	–	0.5	–	–	–	0.5
η ID (%)	3		3			
tracking (%)	5.4	4.2	5.5	5.4	8.2	5.6
selection (%)	10		10			

Table 7.5: Summarized systematic errors.

Chapter 8

Determination of the branching ratios

The setup and results of the combined likelihood fit to the $B^0 \to D^- a_0^+$, $B^0 \to D^{*-} a_0^+$, $B^+ \to D^0 \eta\pi^+$ and $B^0 \to D^{*-} \eta\pi^+$ branching ratios are presented in this chapter.

Section 8.1 discusses the method used to combine the separate decay modes in two final likelihood fits. The results of the combined fits are given in Sect. 8.2. In Sect. 8.3 the significance levels and exclusion limits are derived from the results.

8.1 Combined branching ratio fit

The number of signal events are corrected for the bias offset, obtained in Sect. 6.1.2, and multiplied with a scaling factor to derive the corresponding branching ratio. The following equation is used

$$\mathcal{B}(B^0 \to D^{(*)-} a_0^+)_i \times \mathcal{B}(a_0^+ \to \eta\pi^+) = (N_{obs,i} - N_{bias,i}) \times \underbrace{\frac{1}{N_B \times \mathcal{B}(D^{(*)\pm})_i \times \varepsilon_{eff,i}}}_{scaling\,factor}, \quad (8.1)$$

where N_{obs}, is the number of signal events (S) fitted in decay mode i, N_{bias} is the bias correction determined on Monte Carlo samples, N_B is the number of B events, $\mathcal{B}(D^{(*)\pm})$ is the branching ratio of the $D^\pm$ or $D^{*\pm}$ decay chain and ε_{eff} is the efficiency corrected for the factors given in Sect. 7.4. The equation that gives the branching ratio for the non-resonant signal can be found by substituting $\mathcal{B}(B^0 \to D^{(*)-} a_0^+)_i \times \mathcal{B}(a_0^+ \to \eta\pi^+)$ by $\mathcal{B}(B^0 \to D^{(*)-} \eta\pi^+)_i$ and the observed number of signal events, S, by the observed number of non-resonant signal events (NR) as N_{obs}. The scaling factor is different for each of the different decay modes. All numbers used to calculate the scaling factor are summarized in Table 8.1.

Combined likelihood fits are setup for the two $D^\pm$ and the four $D^{*\pm}$ decay modes. In the combined fits both the branching ratio of the resonant and non-resonant signal are fitted simultaneously. All other parameters, the number and constitution of background

Quantity		Value					
		DchI	DchII	DstI	DstII	DstIII	DstIV
N_{bias}	res.	$+2.7$	$+1.8$	$+1.3$	$+0.5$	-0.9	-0.5
	non-res.	$+8.3$	-8.2	$+3.7$	$+2.5$	$+4.6$	-3.0
N_B				$229.4 \cdot 10^6$			
$\mathcal{B}(D^{(*)\pm})(\%)$		3.8	0.4	1.0	3.6	2.1	0.5
$\varepsilon_{eff}(\%)$	res.	5.0	8.7	7.7	2.0	2.8	3.8
	non-res.	3.36	5.8	3.9	0.9	1.2	1.8

Table 8.1: Summary table for numbers used in the scaling factor.

events and the number of $B^0 \to D^{(*)-} D_s^+$ events, are fitted for every decay mode separately. In a single likelihood fit in total 8 parameters are fitted for the $D^{\pm}$ and 14 for the $D^{*\pm}$ analysis at the same time.

8.2 Combined fit results

8.2.1 Analysis of reconstructed $B^0 \to D^- \eta\pi^+$ events

In this section we present the results of the simultaneous likelihood fit on the $B^0 \to D^- a_0^+$, where $D^+ \to K^-\pi^+\pi^+$or $D^+ \to K_S^0\pi^+$, reconstructed events. All fitted parameters, eight in total, are summarized in Table 8.2. The data and likelihood-fit results are presented in Fig. 8.1. The figure shows nine projections of the same data set on the $m_{\rm ES}$, ΔE and $m_{\eta\pi}$ observables. The second and third rows show the side- and signal region in $m_{\rm ES}$ respectively as is indicated in the corresponding $m_{\rm ES}$ plot. The fitted p.d.f. is projected on the data in the plots. Note that all nine plots are projections of the same data set and the same fit result.

The $B^0 \to D^- a_0^+$ branching ratio is fitted at $(-0.11^{+0.93}_{-0.67}) \cdot 10^{-5}$ and we conclude from this result that no significant signal has been found. Propagation of the systematic error, on the scaling factor and the bias offset correction gives a final result of

$$\mathcal{B}(B^0 \to D^- a_0^+) \times \mathcal{B}(a_0^+ \to \eta\pi^+) = (-0.11^{+0.93}_{-0.67}(\text{stat})^{+0.29}_{-0.76}(\text{sys})) \cdot 10^{-5}. \tag{8.2}$$

An upper limit on the exclusion of signal is determined in Sect. 8.3.2.

The non-resonant $B^0 \to D^- \eta\pi^+$ branching ratio is fitted at $(13.41^{+3.54}_{-3.25}) \cdot 10^{-5}$. This corresponds to about 46 non-resonant fitted $B^0 \to D^- \eta\pi^+$ events in the sample. Propagation of the systematic error, on the scaling factor and the correction for the bias offset, gives

$$\mathcal{B}(B^0 \to D^- \eta\pi^+) = (13.41^{+3.54}_{-3.25}(\text{stat})^{+2.42}_{-1.94}(\text{sys})) \cdot 10^{-5}. \tag{8.3}$$

The significance of this result is determined in Sect. 8.3.1.

In Figs. 8.2 and 8.3 projections of the selected data sample are shown with cuts to select the resonant signal region in the $m_{\eta\pi}$ observable and combined ΔE and $m_{\rm ES}$ and observables respectively. Both figures show no indication of $B^0 \to D^- a_0^+$ signal events present in the data sample.

Quantity		Value
resonant signal BF		$(-0.11^{+0.93}_{-0.67}) \cdot 10^{-5}$
corresponding signal events	DchI	-3.2
	DchII	-1.9
non-resonant signal BF		$(13.41^{+3.54}_{-3.25}) \cdot 10^{-5}$
corresponding non-resonant signal events	DchI	30.5
	DchII	15.4
number of $B^0 \to DD_s$ events	DchI	$50.1^{+8.4}_{-7.7}$
	DchII	$2.1^{+1.9}_{-1.2}$
number of background events	DchI	$1488.0^{+39.9}_{-39.2}$
	DchII	$478.6^{+22.3}_{--0.0}$
background ratio	DchI	$0.50^{+0.04}_{-0.04}$
	DchII	$0.37^{+0.07}_{-0.06}$

Table 8.2: Fitted parameters.

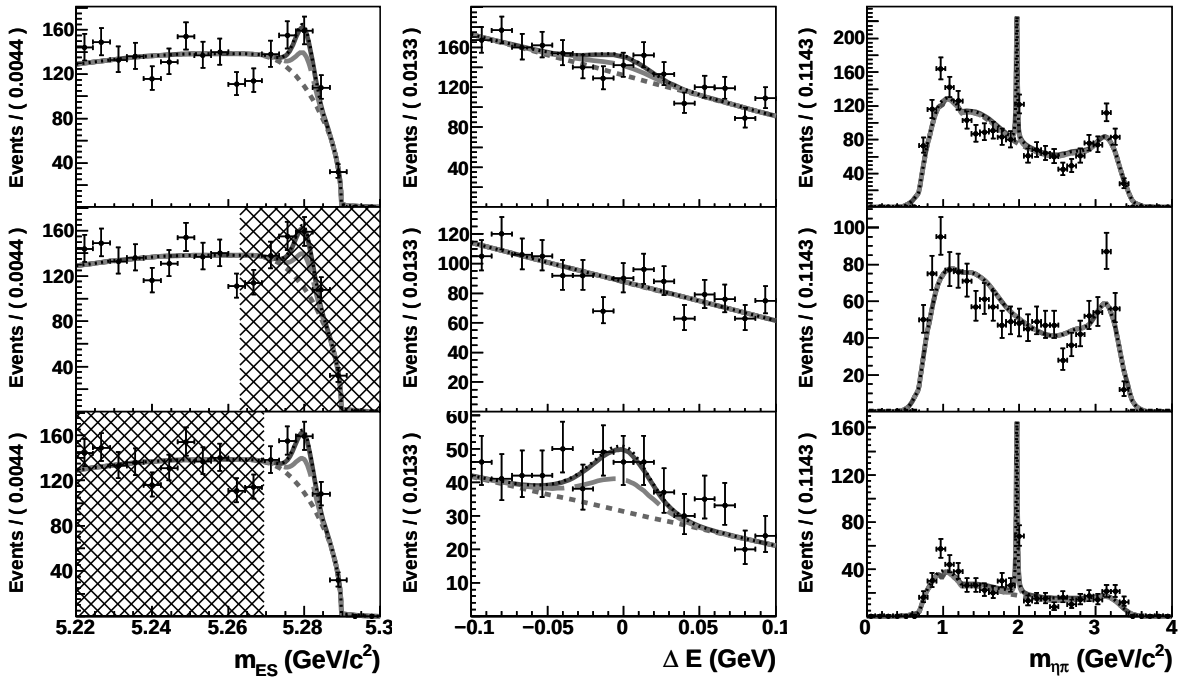

Figure 8.1: Observed distributions of the reconstructed $B^0 \to D^-\eta\pi^+$ candidates projected in, from left to right, $m_{\rm ES}$, ΔE and $m_{\eta\pi}$. The top (middle, *bottom*) row shows the full (sideband, *signal* selected) region. The exclusion region per row is indicated by the hatched area in the $m_{\rm ES}$ projection of the data sample. The component background p.d.f.'s are accumulated in the following order: background (short dashed), $B^0 \to D^{(*)-}D_s^+$ (long dashed), non-resonant $B^0 \to D^-\eta\pi^+$ signal (dotted), $B^0 \to D^- a_0^+$ signal (solid) curve.

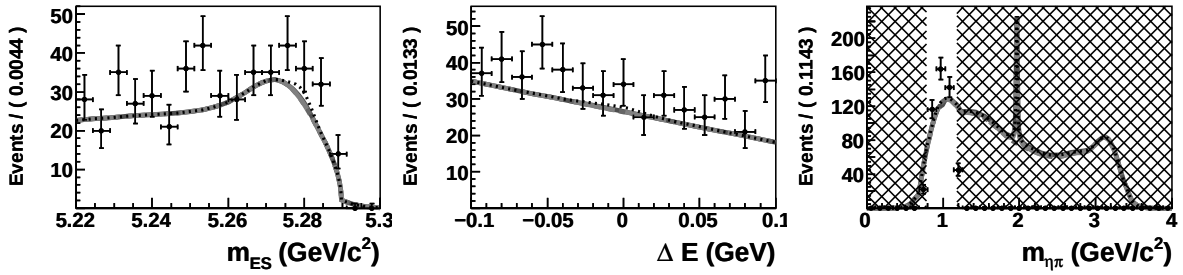

Figure 8.2: Observed distributions of the reconstructed $B^0 \to D^-\eta\pi^+$ candidates projected in, from left to right, $m_{\rm ES}$, ΔE and $m_{\eta\pi}$. The plots only show the data that lie in a selected area in the $m_{\eta\pi}$ observable between 780 and 1180 MeV/c^2 around the a_0 mass peak. The excluded regions are indicated with the hatched area. The component background p.d.f.'s are accumulated in the following order: background (short dashed), $B^0 \to D^{(*)-}D_s^+$ (long dashed), non-resonant $B^0 \to D^-\eta\pi^+$ signal (dotted), $B^0 \to D^- a_0^+$ signal (solid) curve. In the $m_{\rm ES}$ and ΔE plots, no significant indication of resonant $B^0 \to D^- a_0^+$ signal is recognized.

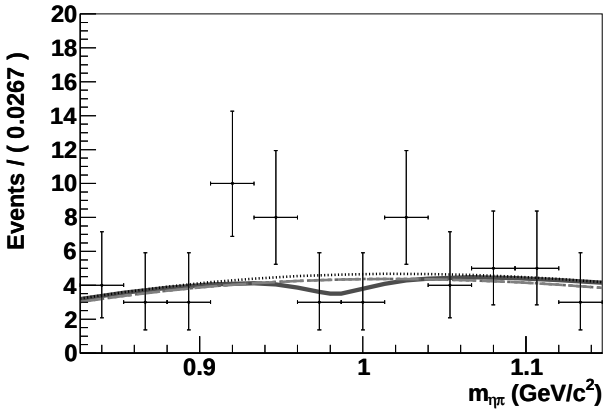

Figure 8.3: Observed distribution in the reconstructed $B^0 \to D^-\eta\pi^+$ candidates projected in the $m_{\eta\pi}$ observable where the data has been selected above 5.27 GeV/c^2 in $m_{\rm ES}$ and between -50 and +50 MeV in ΔE. The component background p.d.f.'s are accumulated in the following order: background (short dashed), $B^0 \to D^{(*)-}D_s^+$ (long dashed), non-resonant $B^0 \to D^-\eta\pi^+$ signal (dotted), $B^0 \to D^- a_0^+$ signal (solid) curve. No significant indication of resonant $B^0 \to D^- a_0^+$ signal is recognized.

Quantity		Value
resonant signal BF		$(5.93^{+1.64}_{-1.48}) \cdot 10^{-5}$
corresponding signal events	DstI	9.4
	DstII	9.0
	DstIII	8.6
	DstIV	3.2
non-resonant signal BF		$(33.91^{+5.47}_{-5.11}) \cdot 10^{-5}$
corresponding non-resonant signal events	DstI	27.6
	DstII	23.3
	DstIII	14.2
	DstIV	10.4
number of $B^0 \to DD_s$ events	DstI	$19.5^{+5.4}_{-4.7}$
	DstII	$14.9^{+4.6}_{-3.9}$
	DstIII	$15.8^{+5.3}_{-4.5}$
	DstIV	$0.0^{+0.5}_{--0.0}$
number of background events	DstI	$272.1^{+17.5}_{-16.8}$
	DstII	$214.9^{+15.6}_{-14.9}$
	DstIII	$254.6^{+17.0}_{-16.3}$
	DstIV	$110.3^{+11.1}_{-10.4}$
background ratio	DstI	$0.56^{+0.08}_{-0.08}$
	DstII	$0.60^{+0.13}_{-0.14}$
	DstIII	$0.81^{+0.09}_{-0.10}$
	DstIV	$0.71^{+0.11}_{-0.12}$

Table 8.3: Fitted parameters.

8.2.2 Analysis of reconstructed $B^0 \to D^{*-}\eta\pi^+$ events

This section summarizes the results of the simultaneous likelihood fit on the $B^0 \to D^{*-}a_0^+$, where $D^{*+} \to D^0\pi^+$ and $D^0 \to K^-\pi^+$, $K^-\pi^+\pi^0$, $K^-\pi^+\pi^+\pi^-$, $K^0_S\pi^+\pi^-$, reconstructed events. All fitted parameters, fourteen in total, are summarized in Table 8.3. The data and likelihood fit results are presented in Fig. 8.4 and show nine projections of the same data set in the $m_{\rm ES}$, ΔE and $m_{\eta\pi}$ observables. The second and third rows show the data in the side- and signal region in $m_{\rm ES}$, respectively, as is indicated in the corresponding $m_{\rm ES}$ plot. The fitted p.d.f. is projected on the data point in the plots. All nine plots are projections of the same data set and likelihood fit.

The $B^0 \to D^{*-}a_0^+$ branching ratio is fitted at $(5.93^{+1.64}_{-1.48}) \cdot 10^{-5}$ which corresponds to about 30 events in the selected data sample. Propagation of the systematic errors that are present in the scaling factor and the bias offset correction gives the final result of

$$\mathcal{B}(B^0 \to D^{*-}a_0^+) \times \mathcal{B}(a_0^+ \to \eta\pi^+) = (5.93^{+1.64}_{-1.48}(\text{stat})^{+2.22}_{-1.52}(\text{sys})) \cdot 10^{-5}. \qquad (8.4)$$

The significance of this result is determined in Sect. 8.3.1.

The non-resonant $B^0 \to D^{*-}\eta\pi^+$ branching ratio is fitted at $(33.91^{+5.47}_{-5.11}) \cdot 10^{-5}$, corresponding to about 76 non-resonant $B^0 \to D^{*-}\eta\pi^+$ events in the data sample. Prop-

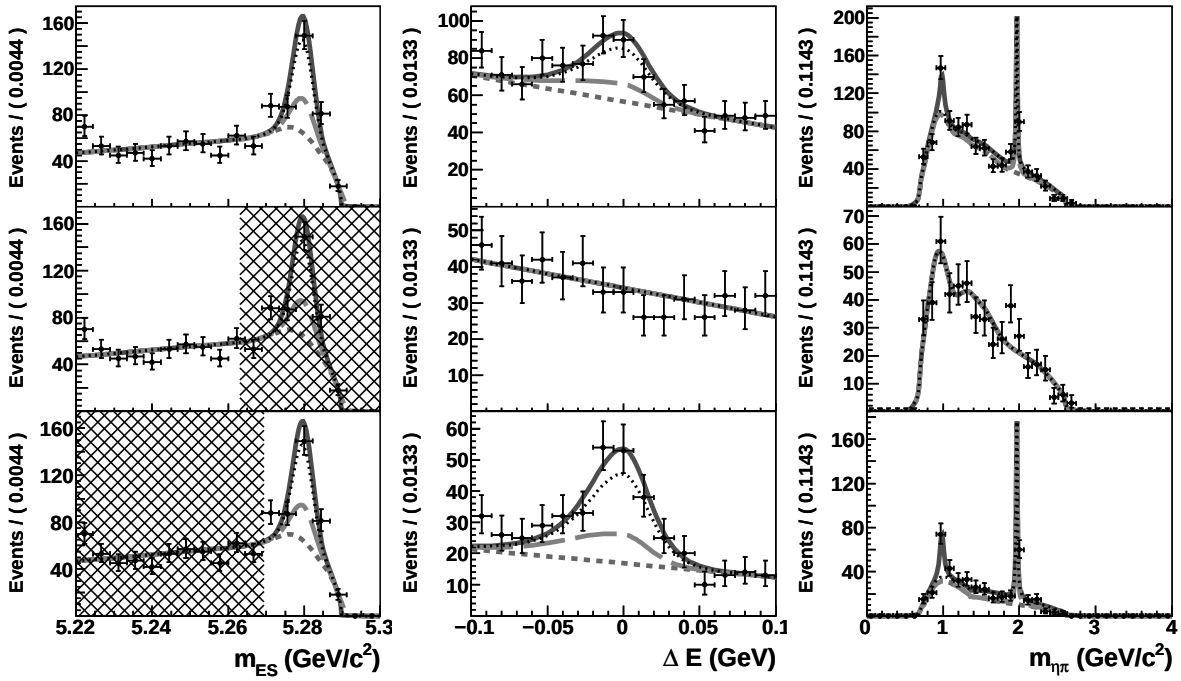

Figure 8.4: Observed distributions of the reconstructed $B^0 \to D^{*-}\eta\pi^+$ candidates projected in, from left to right, $m_{\rm ES}$, ΔE and $m_{\eta\pi}$. The top (middle, *bottom*) row shows the full (sideband, *signal* selected) region. The exclusion region per row is indicated by the hatched area in the $m_{\rm ES}$ projection of the data sample. The component background p.d.f.'s are accumulated in the following order: background (short dashed), $B^0 \to D^{(*)-}D_s^+$ (long dashed), non-resonant $B^0 \to D^{*-}\eta\pi^+$ signal (dotted), $B^0 \to D^{*-}a_0^+$ signal (solid) curve.

agation of the systematic error present in the scaling factor and bias offset corrections gives

$$\mathcal{B}(B^0 \to D^{*-}\eta\pi^+) = (33.91^{+5.47}_{-5.11}(\text{stat})^{6.86}_{5.14}(\text{sys})) \cdot 10^{-5}. \tag{8.5}$$

The significance of this result is determined in Sect. 8.3.1.

Figure 8.5 show the projection of the data sample and likelihood fit in the $m_{\rm ES}$ and ΔE observables where a region in $m_{\eta\pi}$, around the a_0 mass peak, is selected. The rejected area is indicated with the hatched boxes. Selecting this signal region in the $m_{\eta\pi}$ observable, the signal area in ΔE, around zero GeV, and in $m_{\rm ES}$, around the B^0 mass at 5.280 GeV/c^2, clearly show an excess of events above the expected background levels indicating the presence of signal events.

In Fig. 8.6 the data points are projected in the $m_{\eta\pi}$ observable that lie in the signal areas in both $m_{\rm ES}$ and ΔE. The fitted p.d.f. is projected on top of the data points. The Breit-Wigner lineshape is visible on top of the projected background and non-resonant $B^0 \to D^{*-}\eta\pi^+$ p.d.f.'s. The total p.d.f. describes the data points well.

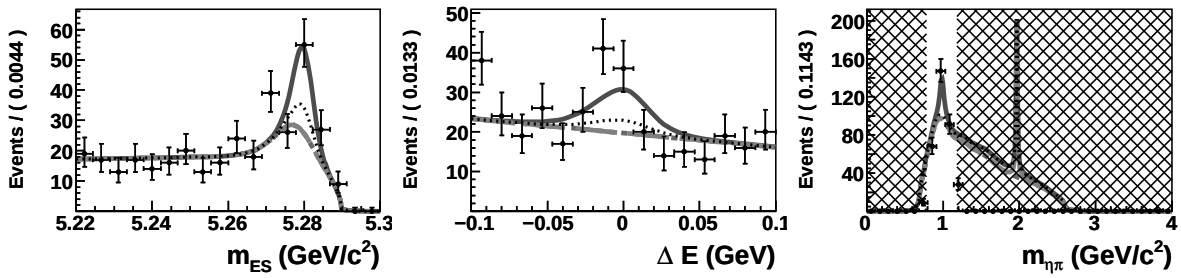

Figure 8.5: Observed distribution in the reconstructed $B^0 \to D^{*-}\eta\pi^+$ candidates projected in, from left to right, $m_{\rm ES}$, ΔE and $m_{\eta\pi}$. The plots only show the data where $780 < m_{\eta\pi} < 1180\,{\rm MeV}/c^2$ around the a_0 mass peak. The excluded regions are indicated in the left plot with the hatched area. The component background p.d.f.'s are accumulated in the following order: background (short dashed), $B^0 \to D^{(*)-}D_s^+$ (long dashed), non-resonant $B^0 \to D^-\eta\pi^+$ signal (dotted), $B^0 \to D^- a_0^+$ signal (solid) curve. A clear indication for the $B^0 \to D^{*-} a_0^+$ signal is present in the $m_{\rm ES}$ and ΔE projections.

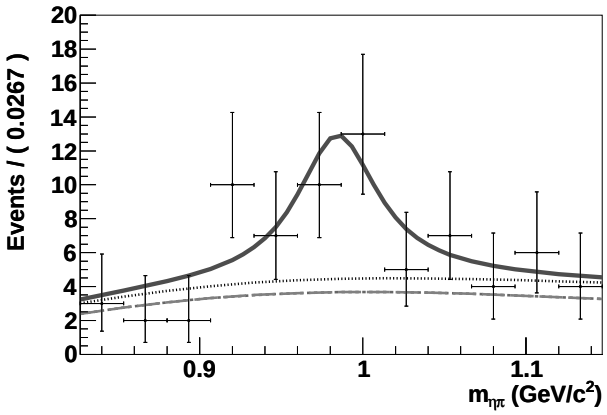

Figure 8.6: Observed distribution in the reconstructed $B^0 \to D^{*-}\eta\pi^+$ candidates projected in the $m_{\eta\pi}$ observable where the data has been selected above 5.27 GeV/c^2 in $m_{\rm ES}$ and between -50 and +50 MeV in ΔE. The component background p.d.f.'s are accumulated in the following order: background (short dashed), $B^0 \to D^{(*)-}D_s^+$ (long dashed), non-resonant $B^0 \to D^-\eta\pi^+$ signal (dotted), $B^0 \to D^- a_0^+$ signal (solid) curve.

8.3 Significance of the results

In this section we determine the significance of the fitted branching ratios for the non-resonant $B^0 \to D^-\eta\pi^+$ analysis and the resonant and non-resonant $B^0 \to D^{*-}\eta\pi^+$ analysis. The resonant $B^0 \to D^-\eta\pi^+$ analysis did not result in a positive fitted branching ratio. For this analysis we determine an upper limit for the signal exclusion.

8.3.1 Significance levels

The significance levels of the obtained results are determined using profile likelihoods. A profile shows the difference with the global minimum of the likelihood fit for different values of the observable. The significance can then be calculated using the difference between the minimized likelihood and the likelihood for the absence of signal, at a branching ratio of zero.

The significance is defined is

$$\sigma = \sqrt{2 \cdot \Delta ll}, \tag{8.6}$$

where Δll is the difference in likelihood between the zero signal and the minimized branching ratio.

The effects of the systematic errors on the significance are propagated by recalculating the profile while varying the scaling factor and bias offset corrections. Also the width and central mass in the a_0 lineshape function are varied. The lowest significance that is obtained is quoted.

The systematic error on the scaling factor does not influence the significance of the result. The likelihood profile is squeezed or stretched by the scaling factor and it does change the minimized value of the branching ratio, however the difference in the likelihood between the minimized point and the null hypothesis is unaltered.

Figures 8.7, 8.8 and 8.9 present the results of the profile likelihood fits for the non-resonant $B^0 \to D^-\eta\pi^+$, resonant and non-resonant $B^0 \to D^{*-}\eta\pi^+$ branching ratios respectively. The significance of the branching ratio measurements are: 4.4σ for the non-resonant $B^0 \to D^-\eta\pi^+$ signal, 5.3σ for the $B^0 \to D^{*-}a_0^+$ signal and 8.2σ for the non-resonant $B^0 \to D^{*-}\eta\pi^+$ signal.

8.3.2 Upper limit for the $B^0 \to D^- a_0^+$ signal exclusion

The profile of the $B^0 \to D^- a_0^+$ branching ratio is presented in Fig. 8.10. For the determination of the upper limit of the branching ratio we calculate the probability distribution using the following formula

$$P = e^{-\Delta ll}, \tag{8.7}$$

using the profile likelihood, Δll. The integral ratio

$$A_R = \frac{\int_0^x P d\mathcal{B}}{\int_0^\infty P d\mathcal{B}}, \tag{8.8}$$

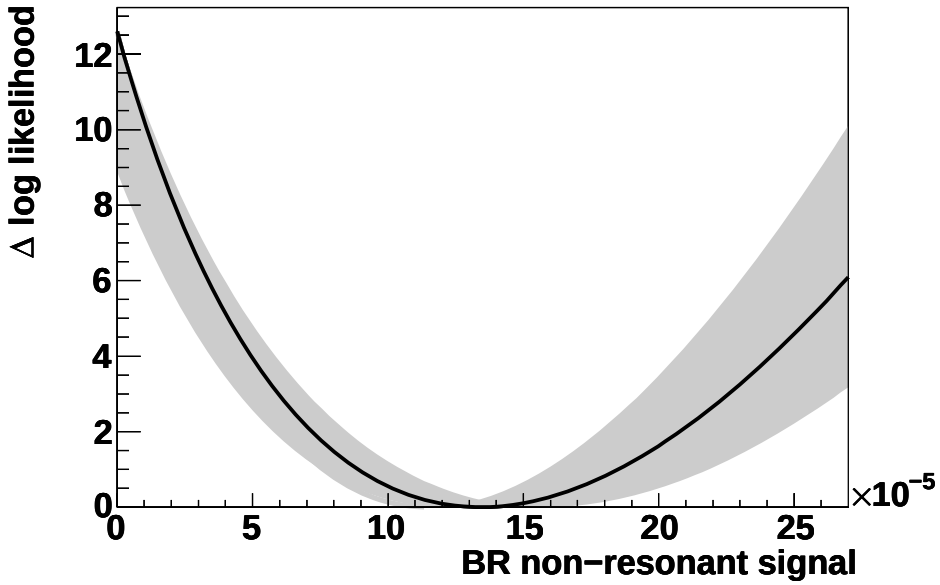

Figure 8.7: Profile likelihood fit to the $B^0 \to D^- \eta \pi^+$ data sample projected on the non-resonant signal branching ratio. The black curve indicates the profile obtained by the nominal scaling factor and bias offset correction. The gray area indicates the effect of the different systematic errors.

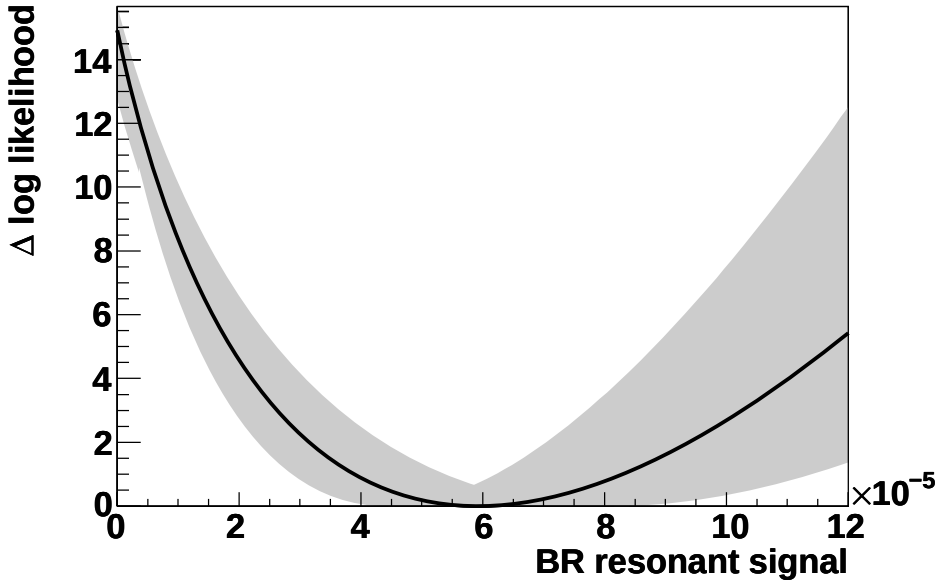

Figure 8.8: Profile likelihood fit to the $B^0 \to D^{*-} \eta \pi^+$ data sample projected on the resonant signal branching ratio. The black curve indicates the profile obtained by the nominal scaling factor and bias offset correction. The gray area indicates the effect of the different systematic errors.

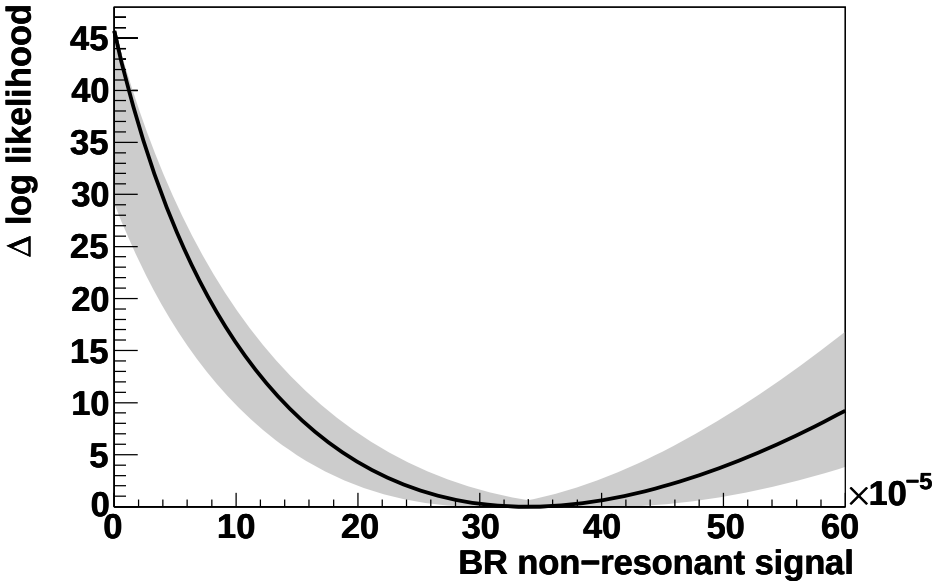

Figure 8.9: Profile likelihood fit to the $B^0 \to D^{*-}\eta\pi^+$ data sample projected on the non-resonant signal branching ratio. The black curve indicates the profile obtained by the nominal scaling factor and bias offset correction. The gray area indicates the effect of the different systematic errors.

gives the relative area, A_R, in the physical range (for positive values of the branching ratio) up till a branching ratio of $\mathcal{B} = x$. The 90% confidence limit (CL) is set at $\mathcal{B} = x$ when the relative area is 90%, $A_R = 0.9$, of the total physical area.

In Fig. 8.10 the distribution of the profile likelihoods is presented. The black curve indicates the profile likelihood using the nominal scaling factor and lineshape settings. The gray area indicates the propagation of the varies systematic errors in the function. The dominant error is produced by the linewidth uncertainty of the Breit-Wigner a_0 lineshape. A broad lineshape gives a higher probability to find a larger branching ratio of the $B^0 \to D^- a_0^+$ signal.

The profile likelihood that produces the largest probabilities to find signal in the data sample, indicated with the dashed curve in Fig. 8.10, is used to calculate the probability distribution to set the upper limit at 90% CL. The resulting probability distribution is shown in Fig. 8.11.

The upper limit for the exclusion of $B^0 \to D_s^{(*)+} a_0^-$ signal, determined with the method described in this section, is found at

$$\mathcal{B}(B^0 \to D^- a_0^+) < 2.3 \cdot 10^{-5} @ 90\% \text{CL}. \tag{8.9}$$

8.4 Summary of obtained results

We have performed unbinned likelihood fits to the selected events in the selected B decays reconstructed in the $B^0 \to D^-\eta\pi^+$ and $B^0 \to D^{*-}\eta\pi^+$ decay modes.

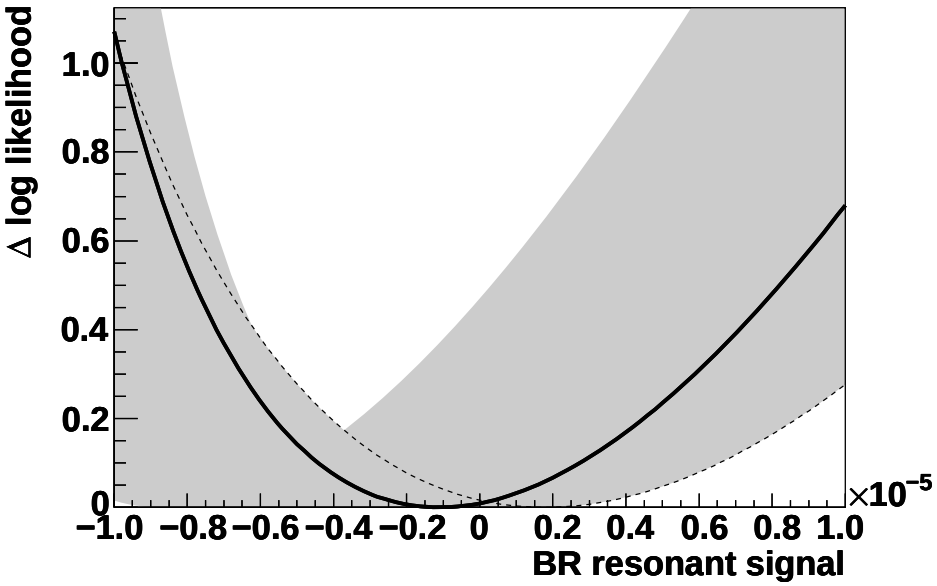

Figure 8.10: Profile likelihood fit to the $B^0 \to D^-\eta\pi^+$ data sample projected on the $B^0 \to D^- a_0^+$ branching ratio. The black curve indicates the profile obtained by the nominal scaling factor and bias offset correction. The gray area indicates the effect of the different systematic errors. The dashed curve corresponds to the profile likelihood that is used to calculated the probability function presented in Fig. 8.11.

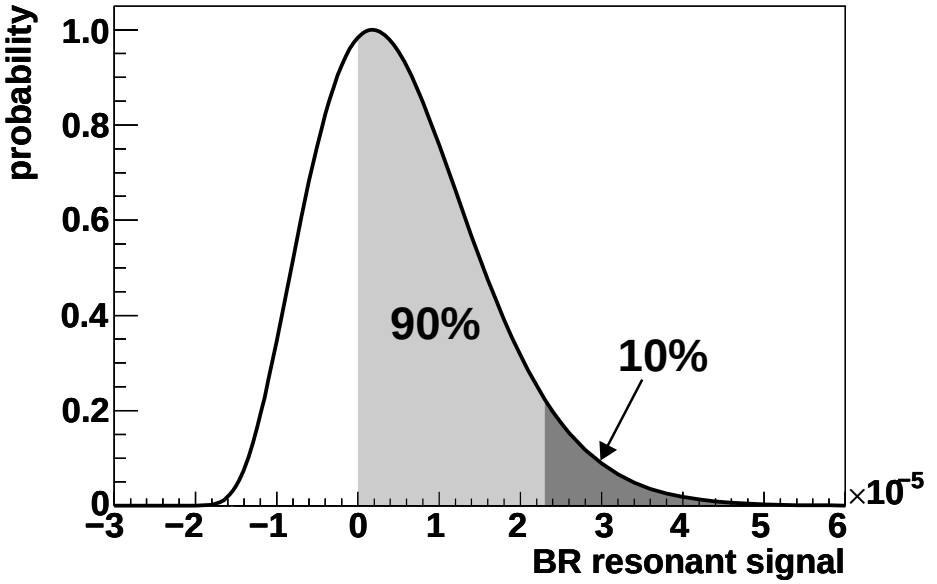

Figure 8.11: Probability distribution for the resonant $B^0 \to D^- a_0^+$ signal.

The $\mathcal{B}(B^0 \to D^- a_0^+) \times \mathcal{B}(a_0^+ \to \eta\pi^+)$ and the non-resonant $\mathcal{B}(B^0 \to D^- \eta\pi^+)$ branching ratios where fitted with a combined unbinned likelihood fit to the $B^0 \to D^- a_0^+$, where $D^+ \to K^-\pi^+\pi^+$or $D^+ \to K_S^0\pi^+$, reconstructed events. In total eight parameters where fitted simultaneously.

The $B^0 \to D^- a_0^+$ branching ratio is fitted at

$$\mathcal{B}(B^0 \to D^- a_0^+) \times \mathcal{B}(a_0^+ \to \eta\pi^+) = (-0.11^{+0.93}_{-0.67}(\text{stat})^{+0.29}_{-0.76}(\text{sys})) \cdot 10^{-5}, \tag{8.10}$$

and is consistent with the null-hypothesis. An upper limit was set at

$$\mathcal{B}(B^0 \to D^- a_0^+) < 2.3 \cdot 10^{-5} @ 90\%\text{CL}. \tag{8.11}$$

The $B^0 \to D^- \eta\pi^+$ branching ratio fit result gives

$$\mathcal{B}(B^0 \to D^- \eta\pi^+) = (13.41^{+3.54}_{-3.25}(\text{stat})^{+2.42}_{-1.94}(\text{sys})) \cdot 10^{-5}, \tag{8.12}$$

and excludes the null-hypothesis with 4.4σ.

The $\mathcal{B}(B^0 \to D^{*-} a_0^+) \times \mathcal{B}(a_0^+ \to \eta\pi^+)$ and the non-resonant $\mathcal{B}(B^0 \to D^{*-} \eta\pi^+)$ branching ratios where fitted with a combined unbinned likelihood fit to the $B^0 \to D^{*-} a_0^+$, where $D^{*+} \to D^0\pi^+$ and $D^0 \to K^-\pi^+$, $K^-\pi^+\pi^0$, $K^-\pi^+\pi^+\pi^-$, $K_S^0\pi^+\pi^-$ reconstructed events. In total fourteen parameters where fitted simultaneously.

The $B^0 \to D^{*-} a_0^+$ branching ratio is fitted at

$$\mathcal{B}(B^0 \to D^{*-} a_0^+) \times \mathcal{B}(a_0^+ \to \eta\pi^+) = (5.93^{+1.64}_{-1.48}(\text{stat})^{+2.22}_{-1.52}(\text{sys})) \cdot 10^{-5}. \tag{8.13}$$

The significance of this result is determined to be 5.3σ. The branching ratio of the non-resonant $B^0 \to D^{*-} \eta\pi^+$ events results in

$$\mathcal{B}(B^0 \to D^{*-} \eta\pi^+) = (33.91^{+5.47}_{-5.11}(\text{stat})^{+6.86}_{-5.14}(\text{sys})) \cdot 10^{-5}, \tag{8.14}$$

this measurement excludes the null-hypothesis with 8.2σ.

Chapter 9

Conclusions

In this chapter we summarize our measurements and review the theoretical implication the measurements have. First we recapitulate the important conclusions that are drawn in Chapter 1 in Sect. 9.1. A brief summary of the results of the branching ratio is presented in Sect. 9.2, which are interpreted in Sect. 9.3. An outlook is given in Sect. 9.4.

9.1 Theory recap

The $B^0 \to D^{(*)-}a_0^+$ decays have two important contributing diagrams, presented in Fig. 9.1. The decay amplitudes of the $B^0 \to D^{(*)-}a_0^+$ decay modes are calculated for each diagram individually. The combination of both amplitudes results in the predicted branching ratio of the $B^0 \to D^{(*)-}a_0^+$ decay mode.

The decay amplitudes are calculated using factorization principles that divide the calculation in two parts. For the CKM allowed and CKM suppressed decays presented in Fig. 9.1 this is expressed as

$$\langle D^{-(*)}a_0^+|\mathcal{H}_{eff}|B^0\rangle = \langle D^{-(*)}|\mathcal{H}_W|B^0\rangle\langle a_0^+|\mathcal{H}_W|0\rangle, \quad \text{and} \tag{9.1}$$

$$\langle D^{-(*)}a_0^+|\mathcal{H}_{eff}|\overline{B}^0\rangle = \langle a_0^+|\mathcal{H}_W|\overline{B}^0\rangle\langle D^{-(*)}|\mathcal{H}_W|0\rangle, \tag{9.2}$$

respectively. In the naive factorization principle the quarks produced in the W decay hadronize independently from the rest of the B decay. Corrections on this principle are made using QCD hard-scattering correction terms.

CKM allowed decay

The branching ratio of the CKM allowed decay, the left diagram in Fig. 9.1, is calculated using QCD correction terms to the naive factorization principles. The correction terms apply to the a_0 production process.

The coupling of the a_0 meson with the weak interaction is G-parity violating, which causes a heavy suppression of the decay amplitude. Strong limits on the breaking of G parity have been set in different experiments using nuclear and leptonic decays [83, 39].

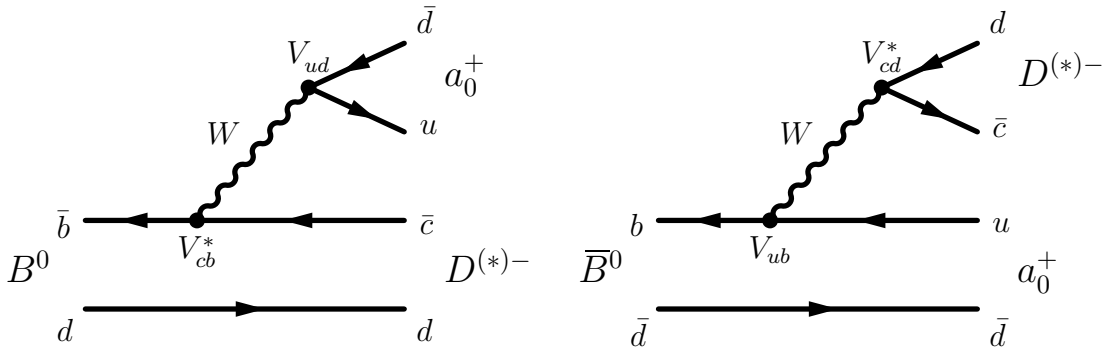

Figure 9.1: The CKM allowed B^0 decay (*left*) and the CKM suppressed $\overline{B}^0$ decay (*right*) to the final state $D^{(*)-}a^+$.

The branching ratio for the $B^0 \to D^- a_0^+$ CKM-allowed decay is calculated to be $1.1 \cdot 10^{-6}$ implementing the naive factorization approach and between $2.0 \cdot 10^{-6}$ and $4.0 \cdot 10^{-6}$ using QCD factorization. For the $B^0 \to D^{*-} a_0^+$ CKM-allowed decay the naive factorization approach predicts a branching ratio of $1.0 \cdot 10^{-6}$ and the QCD factorization predicts branching ratios between $1.8 \cdot 10^{-6}$ and $3.7 \cdot 10^{-6}$ [24].

The calculations depend on the quark structure of the a_0 meson. In these prediction it is assumed that the a_0 meson consists of two quarks, a u and a d quark. A possible four-quark structure of the a_0 meson would result in an even smaller decay rate [24, 48].

CKM suppressed decay

The branching ratio of the CKM suppressed decay, the right diagram in Fig. 9.1, is calculated using naive factorization models. The decay is very similar to the CKM suppressed $B^0 \to D^{*-}\pi^+$ decays and no large theoretical uncertainty due to the factorization model is expected.

Large uncertainties however do arise from the $F_1(0)^{B \to a_0(980)}$ form factor that is present in the B decay amplitude. Estimates of this form factor, that are calculated using light-cone sum rules, are used in the calculations.

The branching ratio of the CKM suppressed $B^0 \to D^{(*)-} a_0^+$ decays are calculated to be $\mathcal{B}(B^0 \to D^+ a_0^-) = 2.1 \cdot 10^{-6}$ and $\mathcal{B}(B^0 \to D^{*+} a_0^-) = 1.9 \cdot 10^{-6}$ [24].

The factorization approach and the form-factor assumption is validated by a measurement of the branching ratio of the SU(3) conjugated decay modes $B^0 \to D_s^{(*)+} a_0^-$. These decay can only occur via a single tree diagram presented in Fig. 9.2. The upper limits that are set by the *BABAR* collaboration at 90% CL are $\mathcal{B}(B^0 \to D_s^+ a_0^-) < 1.9 \cdot 10^{-5}$ and $\mathcal{B}(B^0 \to D_s^{*+} a_0^-) < 3.6 \cdot 10^{-5}$[49]. These limits are lower than the predicted $\sim 8 \cdot 10^{-5}$ that is calculated by substituting the CKM element V_{cd} by V_{sd} and form factor f_D by f_{D_s} in the $B^0 \to D^{(*)-} a_0^+$ branching ratio calculations. These results imply that the predictions made for the branching ratio of the CKM suppressed $B^0 \to D^{(*)-} a_0^+$ decay are too large.

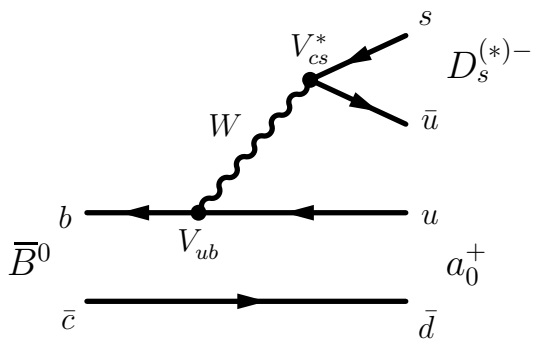

Figure 9.2: Feynman diagram for the $\overline{B}^0 \to D_s^{(*)-} a_0+$ decay.

Combined $B^0 \to D^{(*)-} a_0^+$ factorized branching ratio predictions

The decay amplitudes from both the CKM allowed as well as the CKM suppressed diagrams are predicted in the order of 10^{-6} for the $B^0 \to D^- a_0^+$ and $B^0 \to D^{*-} a_0^+$ decay modes.

The predicted total branching ratio of the $B^0 \to D^- a_0^+$ decay mode is $3.2 \cdot 10^{-6}$ for naive factorization, and in the range $(4.1 - 6.1) \cdot 10^{-6}$ using QCD correction terms in the CKM-allowed amplitude calculations.

For the $B^0 \to D^{*-} a_0^+$ decay mode this summarizes to $2.9 \cdot 10^{-6}$ for the naive factorization approach and in the range $(3.7 - 5.6) \cdot 10^{-6}$ using the QCD correction terms in the CKM-allowed diagram.

Rescattering effects

Rescattering effects can contribute to the $B^0 \to D^- a_0^+$ and $B^0 \to D^{*-} a_0^+$ decay amplitudes. Reliable methods to compute the size of the contribution to the amplitudes are not available at present. Results from $D\rho \leftrightarrow D^*\pi$ rescattering [50] are used to estimate the size of the inelastic rescattering effects in $B^0 \to Da_1 \to D^* a_0$ to be in the order of a branching fraction of 10^{-6}.

Three qualitative arguments to why the inelastic rescattering effects should in fact be larger than this result are made. (A factor ten enhancement of the rescattering amplitude would lead to a contribution to the branching fraction of order 10^{-4}.) The first is the larger mass of the a_0 and a_1 mesons, compared to the π and ρ mesons, allowing more time for the rescattering process to occur; The second is the smaller energy transfer that is needed between the D^*/D mesons and the a_0/a_1 compared to π/ρ meson system; And the third is the fact that the a_0/a_1 mesons are from the same quark spin triplet, and thus are expected to alter the internal angular momentum more easily.

Inelastic rescattering effects to the $D^+ a_0^-$ final state are even more complicated to estimate. Contributions could come from $B^0 \to D^* a_1 \to D a_0$, similar to rescattering in $K^*\rho \leftrightarrow K\pi$ described by Wirbel [25]. The branching ratio of the decay $B^0 \to D^* a_1$ is of the same order as $B^0 \to Da_1$, $(1.30 \pm 0.27) \cdot 10^{-2}$ versus $(6.0 \pm 3.3) \cdot 10^{-3}$. But the inelastic soft rescattering between $D^* a_1 \leftrightarrow D a_0$ is probably smaller than $Da_1 \leftrightarrow D^* a_0$. This is because only the zero angular momentum projection of the $D^* a_1$-meson pair can contribute to form a Da_0 meson pair. The contribution to the amplitude in the

$B^0 \to D^- a_0^+$ decay arising from soft inelastic rescattering is expected to be smaller than the rescattering contribution in the $B^0 \to D^{*-} a_0^+$ decay amplitude.

Non-resonant $B^0 \to D^{(*)-}\eta\pi^+$ branching ratio

Non-resonant $B^0 \to D^{(*)-}\eta\pi^+$ events had so far not been observed. Theoretical predication on the branching ratio are not available either.

As for the $B^0 \to D^{(*)-} a_0^+$ decay, the diagram where the B decays into a $D^{(*)\pm}$ meson and the weak current couples to an $\eta\pi$ state is not allowed due to G-parity violation, as follows from arguments made in Sect. 1.6.2. Other diagrams can contribute. One example is a diagram where a pion is formed from the weak current and a $D^{(*)\pm}\eta$ meson is produced in the B^0 decay. Two other diagrams exist where the $D^{(*)\pm}$ meson is produced in the weak decay and creates an $\eta\pi^\pm$ meson pair in the B^0 decay. These contributions are expected to be suppressed compared to the $B^0 \to D^{(*)-} a_0^+$ decay, because they require an additional quark pair created from the vacuum. Additionally, there are no known excited D^+ mesons that decay to a $D^{(*)+}\eta$ pair.

Experimental measurements from the similar non-resonant $B^0 \to D^{*-}\pi^+\pi^0$ decay also suggest this suppression. The branching ratio of the non-resonant $B^0 \to D^{*-}\pi^+\pi^0$ decay is suppressed compared to the resonant $B^0 \to D^{*-}\rho^+$ decay amplitude [53].

Measurement of CKM angle γ

The interference of the two diagrams in Fig. 9.1, contributing to the $B^0 \to D^{(*)-} a_0^+$ decay, gives access to a measurement of the CKM angle γ. The interference is similar to the current studies that have been performed on $B^0 \to D^{*-}\pi^+$, $B^0 \to D^{*-}\rho^+$ and $B^0 \to D^{*-} a_1(1260)^+$.

The sensitivity to the *CP* asymmetry, and thus to the angle γ can be much larger in the $B^0 \to D^- a_0^+$ and $B^0 \to D^{*-} a_0^+$ decays compared to the current available studies. This is because the contributions from two interfering diagrams are predicted to be, more or less, at the same size.

However, if the predicted branching ratios of the $B^0 \to D^{(*)-} a_0^+$ decays are *too* small, the extraction of γ in a time-dependent analysis will be impossible due to a lack of events.

9.2 Summary of branching ratio measurements

The $B^0 \to D^- a_0^+$ branching ratio is fitted at

$$\mathcal{B}(B^0 \to D^- a_0^+) \times \mathcal{B}(a_0^+ \to \eta\pi^+) = (-0.11^{+0.93}_{-0.67}(\text{stat})^{+0.29}_{-0.76}(\text{sys})) \cdot 10^{-5}, \tag{9.3}$$

and is consistent with the null-hypothesis. An upper limit was set at

$$\mathcal{B}(B^0 \to D^- a_0^+) < 2.3 \cdot 10^{-5} @ 90\%\text{CL}. \tag{9.4}$$

The $B^0 \to D^{*-} a_0^+$ branching ratio is fitted at

$$\mathcal{B}(B^0 \to D^{*-} a_0^+) \times \mathcal{B}(a_0^+ \to \eta\pi^+) = (5.93^{+1.64}_{-1.48}(\text{stat})^{+2.22}_{-1.52}(\text{sys})) \cdot 10^{-5}. \tag{9.5}$$

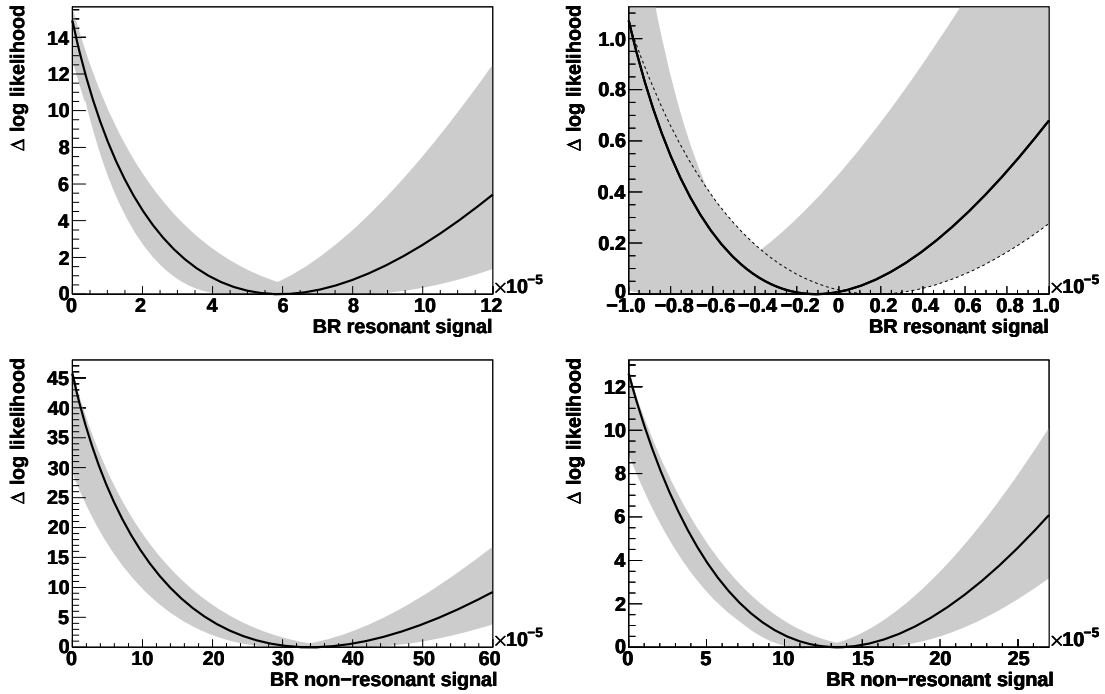

Figure 9.3: Profile likelihood fits where the delta log likelihood is fitted versus the branching ratio of the $B^0 \to D^{*-} a_0^+$ (*top-left*), the $B^0 \to D^- a_0^+$ (*top-right*) and the non-resonant $B^0 \to D^{*-}\eta\pi^+$ (*bottom-left*) and $B^0 \to D^-\eta\pi^+$ (*bottom-right*) decay modes. The black curve indicates the profile obtained by the nominal scaling factor and bias offset correction. The gray area indicates the effect of the different systematic errors.

The significance of this result is determined to be 5.3σ. The $B^0 \to D^-\eta\pi^+$ branching ratio fit result gives

$$\mathcal{B}(B^0 \to D^-\eta\pi^+) = (13.41^{+3.54}_{-3.25}(\text{stat})^{+2.42}_{-1.94}(\text{sys})) \cdot 10^{-5}, \tag{9.6}$$

and excludes the null-hypothesis with 4.4σ. The branching ratio of the non-resonant $B^0 \to D^{*-}\eta\pi^+$ events results in

$$\mathcal{B}(B^0 \to D^{*-}\eta\pi^+) = (33.91^{+5.47}_{-5.11}(\text{stat})^{+6.86}_{-5.14}(\text{sys})) \cdot 10^{-5}, \tag{9.7}$$

this measurement excludes the null-hypothesis with 8.2σ.

The profile likelihoods of these measurements are presented Fig. 9.3. The a_0 mass peak in the reconstructed $B^0 \to D^{*-} a_0^+$ events is presented in Fig. 9.4.

This is the first observation of the $B^0 \to D^{*-} a_0^+$ and $B^0 \to D^{*-}\eta\pi^+$ decays and the first evidence for the $B^0 \to D^-\eta\pi^+$ decay.

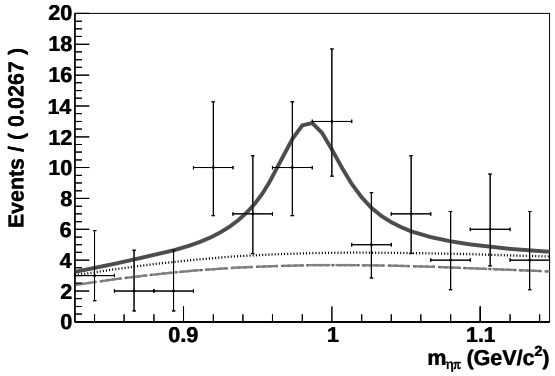

Figure 9.4: Observed distribution in the reconstructed $B^0 \to D^{*-}\eta\pi^+$ candidates projected in the $m_{\eta\pi}$ observable where the data has been selected above 5.27 GeV/c^2 in $m_{\rm ES}$ and between -50 and $+50$ MeV in ΔE. The component background p.d.f.'s are accumulated in the following order: background (short dashed), $B^0 \to D^{(*)-}D_s^+$ (long dashed), non-resonant $B^0 \to D^-\eta\pi^+$ signal (dotted), $B^0 \to D^- a_0^+$ signal (solid) curve.

9.3 Interpretation of the results

The measured branching ratio for the $B^0 \to D^{*-} a_0^+$ decay mode is a factor ten times larger then expected from theoretical prediction using QCD factorization models. The branching ratio of the $B^0 \to D^- a_0^+$ decay mode, on the other hand, is in full agreement. Both measured non-resonant signal branching ratios, of $B^0 \to D^-\eta\pi^+$ and $B^0 \to D^{*-}\eta\pi^+$, are much larger than expected. We will now discuss the implications of these results.

The resonant signal

First, let us look at possible explanations for a larger $B^0 \to D^{*-} a_0^+$ branching ratio, within the QCD factorization model.

In the CKM allowed diagram there are two possible sources. The first is a larger form factor for the $B \to D$ decay. This form factor, however, is accurately known from many other charmed B decays [20]. The second possibility would arise from a higher coupling between the weak interaction and the a_0 meson. Again, this is unlikely. The decay is G-parity suppressed and G-parity violating processes have been excluded to a high level [83, 39]. Also, recent searches for other B decays involving a_0 mesons have not been observed [84], which is in agreement with the suggested suppression mechanisms.

The CKM suppressed diagram also leaves no room for a larger contribution than expected. The $D^{(*)\pm}$ weak decay constant in the CKM suppressed diagram is again very well known from other charmed B decays. The uncertainty in the $B \to a_0$ form factor is large, but is excluded to be larger than expected by the measurement in the SU(3) conjugated $B^0 \to D_s^{(*)+} a_0^-$ decay modes [49].

In conclusion, there is no room within the QCD factorization approach for a large $B^0 \to D^{*-} a_0^+$ branching.

The most likely hypothesis that remains is that the $D^{*\pm}a_0^{\mp}$ final state is produced via rescattering processes. We have already shown that this is possible via the $B^0 \to Da_1 \to D^*a_0$ decay. Differences between the $B^0 \to D^{*-}a_0^+$ and $B^0 \to D^-a_0^+$ branching ratios can be explained. The rescattering process that leads to the $D^{\pm}a_0^{\mp}$ final state, $B^0 \to D^*a_1 \to Da_0$, is suppressed since only the zero angular momentum projection of the D^*a_1-meson pair can contribute to form a Da_0 meson pair.

The possible four-quark meson state of the a_0 becomes highly unlikely with the high measured branching ratio in $B^0 \to D^{*-}a_0^+$. There is no scenario that would accommodate a four-quark state a_0 and the size of the measured branching ratio in $B^0 \to D^{*-}a_0^+$.

The non-resonant signal

The measured branching ratios of both $B^0 \to D^-\eta\pi^+$ and $B^0 \to D^{*-}\eta\pi^+$ are larger than naively expected. At current, no likely scenario is present that could explain this, other than the presence of an excited $D^{\pm}$ meson state that decays into $D^{(*)\pm}\eta$.

9.4 Outlook

The measured branching ratio of the $B^0 \to D^{*-}a_0^+$ decay is larger than was theoretically expected. The question now is if we can use this decay to measure $\sin(2\beta+\gamma)$ in a time-dependent analysis.

First let us compute the number of $B^0 \to D^{(*)-}a_0^+$ events that would currently be available for a time dependent analysis. We have observed 30 events in the used data set. The *BABAR* data sample that is currently available is twice as large as the data set that is used in this thesis. Extrapolating to the larger data sample would give us 60 events. For a time-dependent analysis we would need B tagging which reduces the selection efficiency by a factor three. In total, this would leave us about 20 events to perform the time-dependent fit. The data selection is optimized for an observation of the branching ratio. Optimizing for a measurement of the *CP* asymmetry could loosen some restrictions and increase the signal selection efficiency. However, more than a factor two is not expected to be gained. At most 40 events are expected to be available in the present data sample. This is not enough to perform a full time-dependent analysis.

The amplitude ratio between the interfering diagrams was expected to be around one from the theoretical predictions derived with the factorization approach. If the high branching ratio in the $B^0 \to D^{*-}a_0^+$ decay mode indeed originates from rescattering via the $B^0 \to Da_1 \to D^*a_0$ decay, this ratio is altered. The produced $B^0 \to Da_1$ events are predominantly produced in the CKM favored decay. Let us assume that the difference between the measured and predicted $B^0 \to D^{*-}a_0^+$ branching ratio is caused by rescattering via the CKM favored $B^0 \to Da_1$ decay mode. In this case the amplitude ratio between the interfering diagrams is one in ten, still five times larger than the sensitivity in $B^0 \to D^{*-}\pi^+$, $B^0 \to D^{*-}\rho^+$ or $B^0 \to D^{*-}a_1(1260)^+$ decays.

The number of events present in the currently available *BABAR* data set is not expected to be enough. However, the advantage of the high sensitivity to the CKM angle

γ, compared to other less sensitive decays, remains. And as such, the attempt for a full time-dependent analysis should be made.

Summary

This thesis describes the measurement of the branching fractions of the suppressed charmed $B^0 \to D^{(*)-}a_0^+$ decays and the non-resonant $B^0 \to D^{(*)-}\eta\pi^+$ decays in approximately 230 million $\Upsilon(4S) \to B\overline{B}$ events. The data have been collected with the *BABAR* detector at the PEP-II B factory at the Stanford Linear Accelerator Center in California.

Theoretical predictions of the branching fraction of the $B^0 \to D^{(*)-}a_0^+$ decays show large QCD model dependent uncertainties. Non-factorizing terms, in the naive factorization model, that can be calculated by QCD factorizing models have a large impact on the branching fraction of these decay modes. The predictions of the branching fractions are of the order of 10^{-6}. The measurement of the branching fraction gives more insight into the theoretical models. In general a better understanding of QCD models will be necessary to conduct weak interaction physics at the next level.

The presence of *CP* violation in electroweak interactions allows the differentiation between matter and antimatter in the laws of physics. In the Standard Model, *CP* violation is incorporated in the CKM matrix that describes the weak interaction between quarks. Relations amongst the CKM matrix elements are used to present the two relevant parameters as the apex of a triangle (Unitarity Triangle) in a complex plane. The overconstraining of the CKM triangle by experimental measurements is an important test of the Standard Model. At this moment no stringent direct measurements of the CKM angle γ, one of the interior angles of the Unitarity Triangle, are available.

The measurement of the angle γ can be performed using the decays of neutral B mesons. The $B^0 \to D^{(*)-}a_0^+$ decay is sensitive to the angle γ and, in comparison to the current decays that are being employed, could significantly enhance the measurement of this angle. However, the low expected branching fraction for the $B^0 \to D^{(*)-}a_0^+$ decay channels could severely impact the measurement. A prerequisite of the measurement of the CKM angle is the observation of the $B^0 \to D^{(*)-}a_0^+$ decay on which this thesis reports.

The *BABAR* experiment consists of the *BABAR* detector and the PEP-II e^+e^- collider. The design of the experiment has been optimized for the study of *CP* violation in the decays of neutral B mesons but is also highly suitable for the search for rare B decays such as the $B^0 \to D^{(*)-}a_0^+$ decay. The PEP-II collider operates at the $\Upsilon(4S)$ resonance and is a clean source of $B\overline{B}$ meson pairs.

The B mesons are fully reconstructed in the desired final state $B^0 \to D^{(*)-}a_0^+$ where $a_0^+ \to \eta\pi^+$. No restrictions on the a_0 meson mass are applied in the reconstruction and during the first stages the analysis is set up to select $B^0 \to D^{(*)-}\eta\pi^+$ decays. About

thirty variables are used to distinguish the signal decays from background decays. The optimization of the rectangular box cuts on the selection variables is performed simultaneously using a dedicated optimization program. After the selection is performed, three observables are employed in an unbinned maximum likelihood fit to further separate the signal events from the background and to distinguish the resonant $B^0 \to D^{(*)-}a_0^+$ events from non-resonant $B^0 \to D^{(*)-}\eta\pi^+$ events. Background $B^0 \to D^{(*)-}D_s^+$ events, where $D_s^+ \to \eta\pi^+$, have the same final state and are described with a separate p.d.f. in the fit. These events are utilized as a control sample and are used to test the validity of the analysis setup.

From the unbinned maximum likelihood fit, the following branching fractions follow:

$$\begin{aligned}
\mathcal{B}(B^0 \to D^- a_0^+) \times \mathcal{B}(a_0^+ \to \eta\pi^+) &= (-0.11^{+0.93+0.29}_{-0.67-0.76}) \cdot 10^{-5}, \\
\mathcal{B}(B^0 \to D^{*-} a_0^+) \times \mathcal{B}(a_0^+ \to \eta\pi^+) &= (5.93^{+1.64+2.22}_{-1.48-1.52}) \cdot 10^{-5}, \\
\mathcal{B}(B^0 \to D^- \eta\pi^+) &= (13.41^{+3.54+2.42}_{-3.25-1.94}) \cdot 10^{-5}, \\
\mathcal{B}(B^0 \to D^{*-} \eta\pi^+) &= (33.91^{+5.47+6.86}_{-5.11-5.14}) \cdot 10^{-5},
\end{aligned}$$

where the first error is the statistical and the second represents the systematic uncertainty. An upper limit is determined for the branching fraction of $\mathcal{B}(B^0 \to D^- a_0^+)$ at $\mathcal{B}(B^0 \to D^- a_0^+) < 2.3 \cdot 10^{-5}$@90%CL. The significance of the observations, including systematic uncertainties, for the measured branching fractions are 5.3, 4.4 and 8.2σ respectively and were determined using a profile likelihood.

This is the first reported observation of the $B^0 \to D^{*-} a_0^+$ and $B^0 \to D^{*-}\eta\pi^+$ decays and the first evidence for the $B^0 \to D^-\eta\pi^+$ decay. The observed branching fraction for the $B^0 \to D^{*-} a_0^+$ signal is a factor ten larger than the theoretical predictions. At present no scenario using naive factorization or QCD factorization models can explain the large observed decay amplitude. A possible scenario is rescattering via the $B^0 \to D^- a_1^+ \to D^{*-} a_0^+$ decay channel.

It is unlikely that the number of $B^0 \to D^{*-} a_0^+$ events present in the currently available *BABAR* dataset is enough for a measurement of the CKM angle γ. However, the advantage of the potential high sensitivity remains, as such, the attempt for a full time-dependent analysis should be made.

Populaire samenvatting

Onderdrukte betoverde B-meson vervallen

In de komende pagina's zal ik proberen om enige uitleg te geven over dit proefschrift. Allereerst begin ik met het opzetten van het raamwerk van de elementaire deeltjesfysica. Hierna zal ik een korte introductie geven van het *BABAR* experiment. Tenslotte volgen een samenvatting van de onderzoeksvraag en het onderzoek dat beschreven wordt in dit proefschrift.

Elementaire deeltjesfysica

Het zal velen bekend zijn dat de wereld om ons heen bestaat uit kleine deeltjes. Op moleculair niveau wordt bepaald wat voor eigenschappen verschillende stoffen hebben. De moleculen zelf zijn weer opgebouwd uit atomen, waarvan er op dit moment 112 bekend zijn. Die atomen bestaan op hun beurt uit een kern en elektronen die daaromheen draaien. Een elektron is een elementair deeltje, dat wil zeggen we kunnen het niet langer opsplitsen. De atoomkern kan echter nog wel verder worden opgesplitst in zogeheten protonen en soms ook neutronen. Zowel de protonen als neutronen zijn opgebouwd uit quarks. Van quarks denken we dat ze elementair zijn, dat we ze niet meer kunnen opdelen.

Protonen en neutronen zijn allebei opgebouwd uit twee verschillende soorten quarks, uit 'op' en 'neer' quarks (up en down in het Engels). Eigenlijk bestaat alles wat we op aarde hebben uit elektronen en op en neer quarks. We kennen nog vier andere quarks: tover, vreemd, top en bodem (charm, strange, top, bottom). Deze deeltjes kunnen we maken in deeltjesversnellers. Deeltjes die een toverquark bevatten noemen we betoverd, vandaar het woord in de titel.

Een positron is een anti-elektron. Het heeft alle eigenschappen van een elektron, zoals de massa, maar het deeltje heeft precies de omgekeerde lading. Een elektron heeft een negatieve lading ($-1e$) en een positron dus een positieve lading ($+1e$). Positronen zijn voor het eerst ontdekt in straling die uit de ruimte komt. We kunnen de lading van deeltjes bepalen door ze in een magnetisch veld af te buigen. Als we elektronen materie noemen, dan zijn positronen antimaterie. Positronen zijn geen lang leven beschoren op aarde, zodra ze in contact komen met materie gaan ze een reactie aan en komt er warmte en licht vrij.

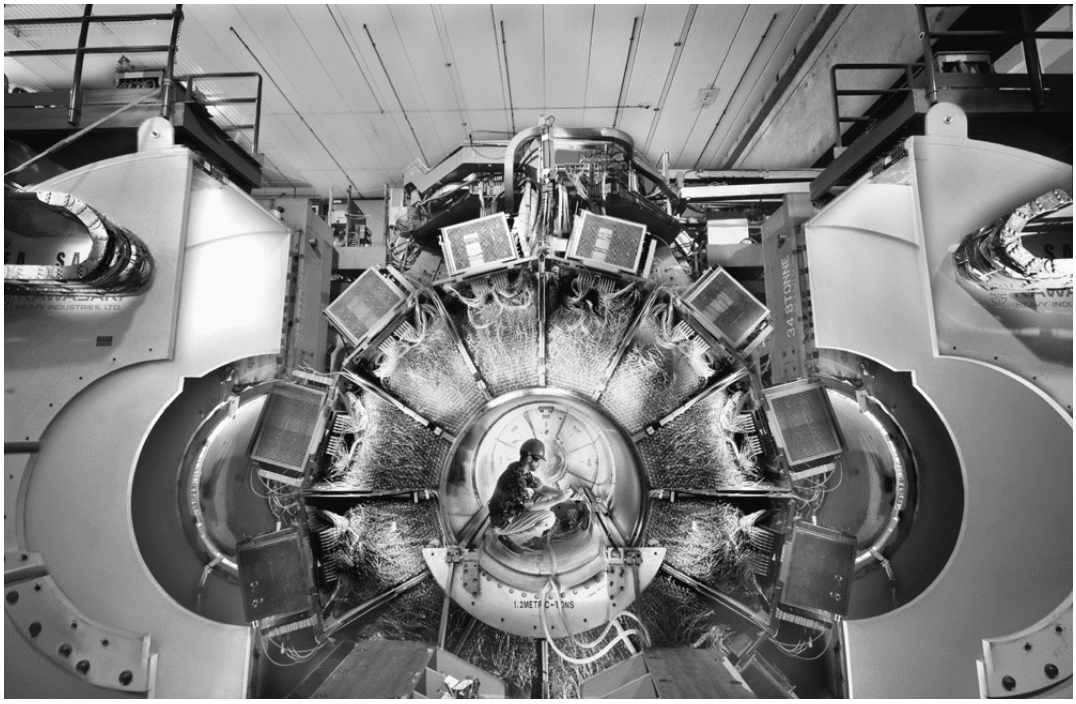

Figuur 1: De *BABAR* detector tijdens de opbouwfase.

Er bestaan ook antiquarks. Elk van de 6 soorten quarks heeft een eigen antitype. Dus we hebben ook een anti-op en een anti-neer quark. Een proton bestaat uit 2 op quarks en 1 neer quark. Samen geeft dat een positieve lading van $+1e$. Als we nu elk van de quarks vervangen door antiquarks krijgen we een deeltje dat veel lijkt op een proton, maar met precies de omgekeerde lading van $-1e$. Een antiproton dus! Het grappige is dat we dit ook kunnen doen met een neutron, ondanks dat deze geen lading draagt. Een neutron bestaat uit 1 op quark en 2 neer quarks. Als we deze vervangen door antiquarks worden het antineutronen. Op het eerste gezicht zijn er geen verschillen te zien tussen het neutron en zijn antideeltje. Maar het is toch mogelijk om ze te onderscheiden.

In het leven van de quarks spelen verschillende krachten een rol. Er is de sterke kracht, die quarks bij elkaar houdt en ze tot bijvoorbeeld protonen en neutronen vormt. Dan is er de elektrische kracht die er voor zorgt dat geladen deeltjes elkaar afstoten of juist aantrekken. De zwaartekracht speelt voor de kleine quarks nauwelijks een rol. Maar er is ook nog de zwakke kracht. De zwakke kracht kan ervoor zorgen dat quarks om worden gezet in andere quarks, dus bijvoorbeeld een op quark kan veranderen in een neer quark. Er wordt dan nog een elementair (geladen) deeltje uitgezonden: een zogeheten W-boson. Dit boson is niet stabiel en vervalt naar bijvoorbeeld een elektron met een antineutrino deeltje.

Ook een vrij neutron is instabiel. Het vervalt door de zwakke kracht. Eén van de twee neer quarks veranderd hierdoor in een op quark. Het neutron verandert dan in een proton! Bij dit verval wordt vaak een elektron en een antineutrino deeltje uitgezonden.

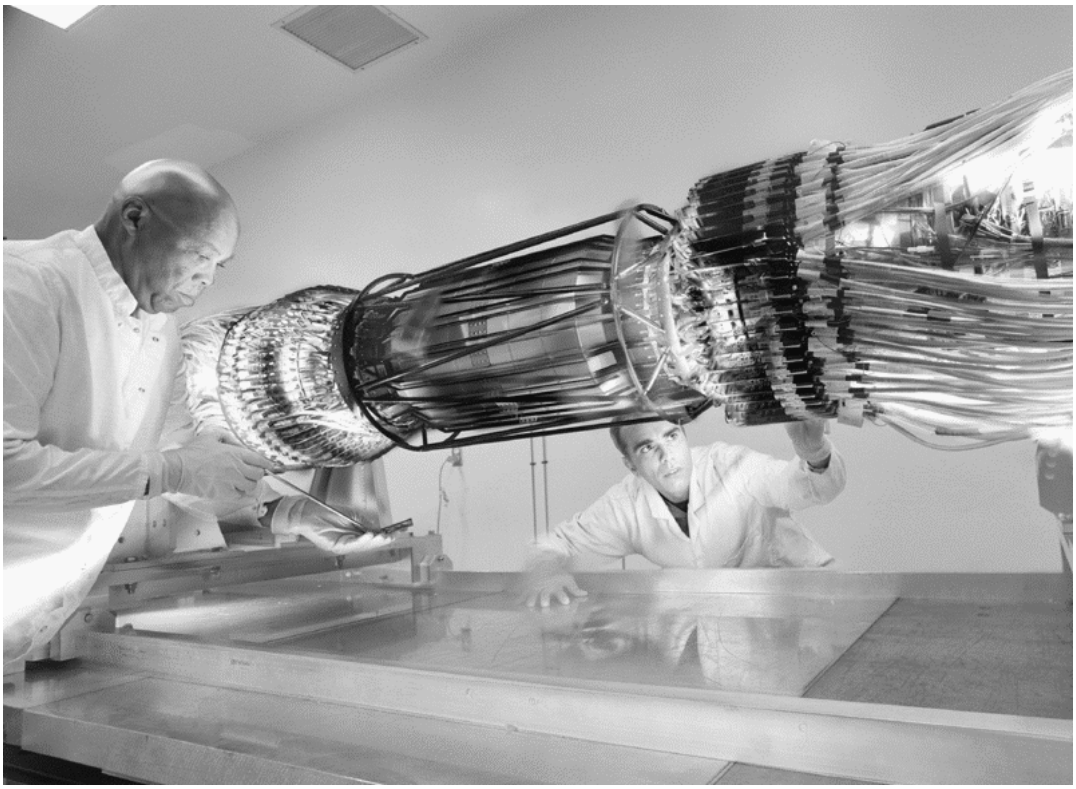

Figuur 2: De binnenste detectorlaag van de *BABAR* detector vlak voordat deze werd geplaatst. De botsingen vinden plaats binnenin deze detector.

Neutrino's en hun antideeltjes zijn nogal moeilijk te zien, maar elektronen en positronen zijn door hun lading en massa gemakkelijk waar te nemen. Het verval kunnen we opschrijven als $n \rightarrow p^+ e^- \overline{v}_e$. Door dit verval kunnen we onderscheid maken tussen neutronen en antineutronen. In een antineutron zou namelijk het antineer quark zijn veranderd in een anti-op quark en zou het antineutron dus naar een antiproton zijn vervallen. In het proces was dan niet een elektron maar een positron ontstaan!

Het *BABAR* experiment

Het *BABAR* experiment bestaat uit twee onderdelen, de PEPII versneller en de *BABAR* detector, zie ook figuur 1. Het gehele experiment staat bij de Stanford Universiteit in Menlo Park in de staat Californië van de Verenigde Staten van Amerika. In de PEPII versneller worden elektronen en positronen met grote snelheid in botsing gebracht. De energie die hierbij vrijkomt wordt heel precies afgeregeld op de resonantie van het $\Upsilon(4S)$ deeltje en bij sommige botsingen wordt er een dergelijk deeltje gemaakt. Het deeltje bestaat uit een bodem en een antibodem quark. Een deeltje dat uit een quark en antiquark bestaat noemen we een meson.

Het $\Upsilon(4S)$ deeltje is niet stabiel en vervalt naar twee B mesonen. Er bestaan geladen B mesonen (combinatie van antibodem en op) en neutrale B mesonen (antibodem en neer). Van beide type bestaan ook weer antimesonen. In elk verval wordt precies een van elk type gemaakt, dus voor elk geproduceerd B meson is er ook een geproduceerd anti-B-meson. De PEPII versneller is dus eigenlijk een grote B-meson fabriek. Het experiment heeft meetgegevens verzameld van oktober 1999 tot en met april 2008 en in die tijd zijn er ongeveer 1 miljard B mesonen gemaakt.

Op de plek waar de botsingen van de versneller plaatsvinden is de *BABAR* detector gebouwd. Met de detector kunnen we de botsingen onderzoeken. Het apparaat bestaat uit verschillende onderdelen. Een van de onderdelen van de detector is afgebeeld in figuur 2. Allereerst hebben we een grote magneet die ervoor zorgt dat we de negatieve van de positieve deeltjes kunnen onderscheiden. Dan zijn er detectoren waarin de deeltjes sporen achterlaten als ze er doorheen vliegen. Vervolgens zijn er apparaten die de energie van de deeltjes meten. Alles bij elkaar kunnen we dan precies bepalen wat voor lading, massa en energie de deeltjes hebben die door de detector vliegen. Genoeg om precies te weten wat voor soort deeltjes het zijn.

De onderzoeksvraag

Nu we weten wat voor soort deeltjes er worden gemaakt en hoe we die waarnemen zal ik vertellen wat we nu eigenlijk precies te weten willen komen.

De geproduceerde B mesonen zijn op hun beurt ook weer instabiel en vervallen onder invloed van de zwakke kracht weer in andere deeltjes. Met behulp van de B mesonen proberen we meer te weten te komen van de werking van de zwakke kracht. In de natuur lijkt de zwakke kracht onderscheid te maken tussen materie en antimaterie. Dat wil zeggen dat materie deeltjes iets anders reageren op de zwakke kracht dan antimaterie deeltjes doen. Tot nu toe is dit de enige plek in de natuurwetten die we kennen waar er verschillen zijn tussen materie en antimaterie. De andere krachten, zoals de zwaartekracht en de elektrische kracht, maken bijvoorbeeld geen onderscheid tussen de geaardheid van materie.

Een B meson kan vervallen naar verschillende combinaties van deeltjes. We kunnen niet voorspellen naar welke combinatie een enkel B meson zal vervallen. Net als dat we niet kunnen voorspellen hoeveel ogen je gooit bij een enkele worp van een dobbelsteen. Dit betekent niet dat de Natuurkunde geen exacte wetenschap meer is. Met behulp van de kwantummechanica kunnen we wel uitrekenen wat de kans is dat het B meson naar een bepaalde combinatie vervalt. Bij het uitrekenen van deze kans komt onze kennis over zowel de sterke als de zwakke kracht kijken.

Zoals ik eerder schreef willen we in het *BABAR* experiment meer te weten komen over de zwakke kracht. Maar bij de vervalsprocessen spelen ook sterke krachten een rol. Dit proefschrift gaat over een meting van een specifiek B-meson verval. Bij dit verval komen de onderzekerheden die er bestaan over de werking van de sterke kracht extra naar boven. Je kunt deze meting zien als een test van onze kennis van de rekenmethodes die we gebruiken om de kansprocessen te voorspellen.

Het soort B-meson verval dat ik onderzoek in dit proefschrift is nog niet eerder

waargenomen. Onder de werking van de zwakke kracht vervalt het B meson naar twee andere mesonen. De ene is een D meson, die bestaat uit een tover en een anti-neer quark, en de andere een a_0 meson, die bestaat weer uit een op en anti-neer quark. We schrijven dit dan als $B^0 \to D^{(*)\pm} a_0^{\mp}$. Eigenlijk zijn dit twee vervallen, de haakjes geven aan dat we ook zoeken naar een D^* meson. Het sterretje geeft aan dat de twee quarks in dit meson op een bijzondere manier om elkaar heen draaien.

Het verval, $B^0 \to D^{(*)\pm} a_0^{\mp}$, is sterk onderdrukt, wat betekent dat de kans op het proces erg klein is. De uitgerekende kans is in de orde van één op een miljoen. Door precies te meten hoe vaak het verval voorkomt testen we de rekenmethodes. Op hetzelfde moment is het interessant of we het B-meson verval vaak genoeg zien. Als dit namelijk het geval is kan er in de toekomst wellicht een erg precieze meting van een eigenschap van de zwakke wisselwerking mee worden verricht. Andere pogingen om die precieze eigenschap te meten zijn tot nog toe niet goed gelukt.

Het onderzoek

De B mesonen zelf nemen we niet waar in de detector, wel de deeltjes waar ze naartoe vervallen. We nemen dus eigenlijk de brokstukken waar. Om te zien wat voor brokstukken we over houden in ons verval moeten we kijken naar de gevormde D en a_0 mesonen. Het a_0 meson vervalt naar een zogeheten pion en een eta meson, beide bestaan uit op en neer quarks. Het pion kunnen we direct waarnemen in de detector. Het eta meson vervalt naar twee fotonen (lichtdeeltjes). Het D meson kan naar allerlei toestanden vervallen. We reconstrueren in dit proefschrift 6 verschillende eindtoestanden. Een voorbeeld is een kaon-pion-pion combinatie (een kaon bestaat uit een antivreemd en een op quark). De uiteindelijke combinatie van deeltjes die in mijn B-meson verval ontstaan zijn dus: 1 kaon, 2 fotonen en 3 pionen. Dat zijn de deeltjes die we uiteindelijk in de detector waarnemen. Het lastige is nu dat deze eindtoestand ook kan worden gemaakt door andere B-meson vervallen die veel vaker voorkomen.

Om ons $B^0 \to D^{(*)\pm} a_0^{\mp}$ verval ('signaal') te onderscheiden van de andere vervallen, die misschien wel duizend keer vaker voorkomen, kijken we naar verschillende eigenschappen. We bedenken allerlei criteria waar de signalen in de detector aan zouden moeten voldoen. Eerst kijken we of we kaonen, pionen en fotonen zien in de botsing. Vervolgens of we van de brokstukken de originele deeltjes kunnen reconstrueren. Bijvoorbeeld of het kaon en twee van de pionen wel van één plek in de detector afkomen. En zo bedenken we nog veel meer criteria. Door het toepassen hiervan proberen we zoveel mogelijk botsingen weg te gooien waar we niet in geïnteresseerd zijn. Maar we verliezen soms toch ook wat van onze signaalvervallen.

Om nu precies te bepalen hoe de set van criteria werkt, maken we gebruik van door de computer gesimuleerde botsingen. Zo kunnen we precies zien hoeveel van de achtergrond botsingen we kwijt raken en hoeveel signaal we overhouden. Een van de achtergrondvervallen bleek lastig te onderscheiden van de signaalvervallen met behulp van alleen de set van opgestelde criteria. Het verval heeft exact dezelfde eindtoestand als het signaalverval. In plaats van dat een pion en twee fotonen van een a_0 meson afkwamen, zijn deze direct ontstaan in het verval: $B^0 \to D^{(*)\pm} \eta \pi^{\mp}$. Dit probleem hebben we opgelost

door tegelijkertijd een meting te doen van beide processen, zowel van $B^0 \to D^{(*)\pm} a_0^{\mp}$ als van $B^0 \to D^{(*)\pm} \eta\pi^{\mp}$.

Uiteindelijk hebben we de volgende kansen gemeten:

$$\begin{aligned}
\mathcal{K}(B^0 \to D^- a_0^+) \times \mathcal{K}(a_0^+ \to \eta\pi^+) &= (-0.11^{+0.93+0.29}_{-0.67-0.76}) \cdot 10^{-5}, \\
\mathcal{K}(B^0 \to D^{*-} a_0^+) \times \mathcal{K}(a_0^+ \to \eta\pi^+) &= (5.93^{+1.64+2.22}_{-1.48-1.52}) \cdot 10^{-5}, \\
\mathcal{K}(B^0 \to D^- \eta\pi^+) &= (13.41^{+3.54+2.42}_{-3.25-1.94}) \cdot 10^{-5}, \\
\mathcal{K}(B^0 \to D^{*-} \eta\pi^+) &= (33.91^{+5.47+6.86}_{-5.11-5.14}) \cdot 10^{-5},
\end{aligned}$$

waarbij $\mathcal{K}$ voor kans staat. Zoals je ziet is er voor het verval $B^0 \to D^- a_0^+$ geen positieve kans bepaald. Dit is misschien wat lastig te interpreteren maar het betekent dat we het verval niet hebben waargenomen. We hebben doorom een bovenlimiet bepaald, met 90% waarschijnlijkheid, dat de kans op het proces kleiner is dan $2.3 \cdot 10^{-5}$. Voor de andere vervallen, $B^0 \to D^{*-} a_0^+$, $B^0 \to D^- \eta\pi^+$ en $B^0 \to D^{*-} \eta\pi^+$, is dit de eerste keer dat ze zijn waargenomen.

We hebben uiteindelijk 30 botsingen gevonden waarin we het $B^0 \to D^{*-} a_0^+$ verval kunnen reconstrueren. Dit zijn er waarschijnlijk niet genoeg om de interessante meting te doen van de zwakke kracht. Toch zou dit in de toekomst moeten worden geprobeerd. Als het wel lukt zou het een belangrijke bijdrage kunenn leveren aan de kennis van de zwakke kracht.

De gemeten kans in het $B^0 \to D^{*-} a_0^+$ verval is tien maal hoger dan de voorspelde kans. Dit is een erg bijzonder resultaat, er zijn op dit moment geen rekenmodellen die dit kunnen verklaren. Wel zijn er processen te bedenken, waarvan we altijd dachten dat ze zeer klein waren, die kunnen bijdragen aan de kans. Helaas zijn er op dit moment geen manieren om precies te berekenen hoe groot deze bijdragen aan de kans zijn.

Appendix A

Selection variable tables

This appendix summarizes the selection power of the variables used to select the final data set as is described in Chapter 4.

	SigMC		NonRes		GenB		$q\overline{q}$	
variable	R(%)	U	R(%)	U	R(%)	U	R(%)	U
m_{ES}	14.47	93	19.87	233	35.26	1836	37.32	1197
ΔE	36.94	540	40.58	1157	51.21	4694	50.42	1658
χ^2	59.56	523	68.21	1226	91.05	2333	92.53	1369
$\cos\theta_T$	13.70	29	14.00	55	16.49	51	47.21	28
$\cos\theta_B$	3.00	15	3.33	39	4.22	61	4.45	27
$\cos\theta_S$	17.48	41	17.52	64	20.03	62	55.32	38
T	0.14	3	0.16	6	0.16	5	1.19	16
$ln(DOCA)$	0.41	0	0.25	0	0.15	0	0.24	1
$\mathcal{F}$	48.71	1348	50.61	2874	58.16	2667	87.56	2765
$m_{D^{\pm}}$	36.08	197	45.79	392	75.74	722	79.79	566
dls_D	27.64	847	29.29	1874	42.63	2144	47.44	1507
p^*_K	6.28	200	3.88	259	6.17	202	12.52	113
$p^*_{\pi 2}$	0.58	6	0.59	14	1.50	14	1.29	5
m_η	41.67	460	47.52	852	67.67	1196	66.56	388
p^*_η	5.28	42	18.86	55	37.90	350	27.62	62
$m^{VETO}_{\pi^0}$	22.90	840	29.39	1542	49.18	2692	43.88	826
$\cos\theta_\eta$	36.42	32	34.43	87	41.40	75	48.08	27
$E_{\pi B}$	3.64	22	14.80	151	29.08	183	19.04	79
$p^*_{\pi B}$	5.02	18	28.06	441	55.39	1488	38.78	492
θ_π	1.54	34	2.10	141	2.07	83	2.49	43
E_γ	42.56	290	43.73	449	56.16	593	59.99	170
$\mathcal{L}_2/\mathcal{L}_0$	12.29	8	12.19	11	12.43	4	55.59	5
fit status	4.06	-	4.73	-	8.14	-	11.43	-
$\#cand < 30$	0.05	-	0.02	-	0.02	-	0.01	-

Table A.1: Rejected candidates, R, for the DchI selection (in %) and the number of uniquely rejected candidates, U, for different event types. The quoted number for the variable ($\#cand < 30$) is the percentage of rejected events.

	SigMC		NonRes		GenB		$q\overline{q}$	
variable	R(%)	U	R(%)	U	R(%)	U	R(%)	U
$m_{\rm ES}$	17.28	37	25.68	57	36.76	516	36.78	454
ΔE	39.45	199	43.95	252	51.83	1380	50.63	655
χ^2	69.23	324	78.56	490	93.44	2338	93.75	2374
$\cos\theta_T$	6.45	6	7.01	8	8.28	16	24.46	5
$\cos\theta_B$	2.41	4	2.56	5	3.27	22	3.38	16
$\cos\theta_S$	20.30	48	20.79	57	23.97	84	57.45	55
T	2.50	3	1.66	3	2.05	5	29.30	79
$ln(DOCA)$	7.83	6	6.56	11	6.09	10	8.94	4
$\mathcal{F}$	26.10	82	27.62	104	31.75	163	71.60	267
$m_{D^\pm}$	18.64	5	24.50	14	35.27	18	36.03	33
dls_D	34.22	289	35.19	431	44.22	662	47.70	678
$m_{K^0_S}$	19.74	5	28.39	3	42.54	21	43.60	27
$dls_{K^0_S}$	22.10	63	33.43	117	56.08	966	54.13	1212
$p^*_{\pi 1}$	4.65	49	2.76	39	3.02	63	11.75	67
m_η	35.37	29	42.23	36	60.63	143	59.59	50
p^*_η	5.06	19	18.68	23	35.00	111	28.65	22
E_η	1.35	1	7.23	4	14.68	19	12.39	8
$m^{VETO}_{\pi^0}$	0.83	3	1.03	5	1.87	24	1.66	12
$\cos\theta_\eta$	32.64	3	31.47	14	38.80	27	43.70	16
$E_{\pi B}$	3.97	3	12.76	18	23.33	27	21.00	11
$p^*_{\pi B}$	7.86	4	28.37	67	49.25	420	42.80	205
E_γ	36.85	66	37.09	65	47.53	139	51.34	72
$\mathcal{L}_2/\mathcal{L}_0$	13.57	11	13.59	15	14.53	6	55.16	22
fit status	10.62	-	14.16	-	20.30	-	21.23	-
$\#cand < 30$	0.01	-	0.00	-	0.01	-	0.00	-

Table A.2: Rejected candidates, R, for the DchII selection (in %) and the number of uniquely rejected candidates, U, for different event types. The quoted number for the variable ($\#cand < 30$) is the percentage of rejected events.

	SigMC		NonRes		GenB		$q\overline{q}$	
variable	R(%)	U	R(%)	U	R(%)	U	R(%)	U
m_{ES}	11.13	49	15.11	74	29.62	370	37.12	125
ΔE	33.93	242	37.39	380	51.20	1384	51.48	166
χ^2	57.25	500	64.56	801	83.55	795	95.21	258
$\cos\theta_T$	0.68	2	0.68	2	0.83	0	3.18	0
$\cos\theta_B$	6.74	35	7.43	64	9.95	93	10.36	9
$\cos\theta_S$	9.60	54	10.56	63	12.85	43	43.43	12
R2	1.08	1	0.95	2	1.35	1	19.28	0
T	1.53	2	1.32	7	1.88	1	24.74	1
$ln(DOCA)$	4.26	5	3.49	9	2.77	4	5.93	0
$\mathcal{F}$	19.23	120	21.34	223	24.89	161	74.40	143
$m_{D^{*\pm}}$	17.72	27	22.67	46	45.47	33	65.58	12
$\cos\theta_{D^*}$	4.59	12	19.74	588	16.92	177	18.51	47
$\cos\theta_{a_0}$	0.45	4	0.50	9	1.04	2	1.34	1
m_{D^0}	0.08	0	0.05	0	0.11	1	0.16	0
θ_{D^0}	0.93	4	1.31	14	2.18	13	3.25	5
dls_D	20.89	60	25.97	77	38.35	66	55.89	7
ϕ_K	0.49	5	0.33	8	0.38	7	0.38	1
$p^*_{\pi 1}$	0.84	5	0.42	3	1.57	2	6.21	7
$p_{S\pi}$	3.16	23	4.41	32	8.69	24	10.73	1
$\phi_{S\pi}$	0.98	15	1.02	23	0.98	10	1.03	1
m_η	28.88	44	34.43	73	53.31	162	52.23	24
p^*_η	7.03	31	22.75	37	49.59	201	36.24	16
E_η	2.83	2	11.09	14	25.91	27	18.73	2
$m^{VETO}_{\pi^0}$	32.09	499	38.64	739	64.04	1848	59.67	181
$\cos\theta_\eta$	38.66	79	37.22	109	42.74	164	48.45	14
$E_{\pi B}$	0.56	0	7.60	2	18.15	12	12.87	1
$p^*_{\pi B}$	1.60	1	22.94	66	48.90	212	32.14	6
θ_π	0.11	0	0.28	6	0.20	4	0.21	1
E_γ	35.43	6	34.68	11	42.74	26	47.54	5
$\mathcal{L}_2/\mathcal{L}_0$	4.78	3	5.73	10	5.86	4	39.51	0
fit status	11.79	-	14.94	-	28.40	-	40.45	-
$\#cand < 30$	0.00	-	0.01	-	0.01	-	0.00	-

Table A.3: Rejected candidates, R, for the DstI selection (in %) and the number of uniquely rejected candidates, U, for different event types. The quoted number for the variable ($\#cand < 30$) is the percentage of rejected events.

	SigMC		NonRes		GenB		$q\overline{q}$	
variable	R(%)	U	R(%)	U	R(%)	U	R(%)	U
$m_{\rm ES}$	16.36	35	23.14	66	34.33	384	37.78	142
ΔE	44.11	269	48.71	343	53.48	993	52.61	197
χ^2	86.20	1223	92.49	1669	96.91	1811	98.13	606
$\cos\theta_T$	36.00	223	37.99	222	41.62	201	83.12	80
$\cos\theta_B$	17.55	189	19.70	188	21.03	192	21.32	51
$\cos\theta_S$	18.83	12	20.39	24	22.72	21	62.52	6
R2	4.90	12	4.56	13	5.23	6	44.79	8
$ln(DOCA)$	5.97	14	4.61	6	3.90	6	7.60	6
$\mathcal{F}$	13.66	2	15.30	4	16.66	7	64.39	6
$m_{D^{*\pm}}$	41.58	40	53.72	53	66.31	173	71.65	38
$\cos\theta_{D^*}$	13.18	67	31.37	739	28.28	221	28.04	68
$\cos\theta_{a_0}$	7.98	57	12.11	110	20.83	45	23.58	18
m_{D^0}	33.18	279	42.96	741	43.71	348	43.48	64
dls_D	35.27	73	39.11	92	41.59	65	46.50	18
$p^*_{\pi 1}$	0.25	0	0.11	0	0.38	3	0.82	0
$p^*_{\pi 2}$	5.10	13	4.28	25	4.12	21	3.34	1
$p_{S\pi}$	3.95	30	6.35	33	10.98	53	10.89	8
m_η	33.63	60	42.51	65	59.20	154	58.25	15
p^*_η	8.25	15	27.82	11	51.19	61	38.88	14
$m^{VETO}_{\pi^0}$	42.30	660	53.05	719	74.68	1698	70.96	246
$\cos\theta_\eta$	35.36	19	33.66	30	38.33	37	44.77	4
$E_{\pi B}$	1.82	0	13.99	4	27.33	4	19.19	2
$p^*_{\pi B}$	4.89	6	33.28	66	57.41	195	39.82	19
E_γ	38.26	39	39.25	34	47.81	72	52.41	16
$\mathcal{L}_2/\mathcal{L}_0$	19.35	7	20.70	8	21.99	4	72.26	6
fit status	34.25	-	44.89	-	54.77	-	57.32	-
$\#cand < 30$	1.78	-	1.53	-	1.09	-	0.49	-

Table A.4: Rejected candidates, R, for the DstII selection (in %) and the number of uniquely rejected candidates, U, for different event types. The quoted number for the variable ($\#cand < 30$) is the percentage of rejected events.

	SigMC		NonRes		GenB		$q\overline{q}$	
variable	R(%)	U	R(%)	U	R(%)	U	R(%)	U
m_{ES}	22.50	23	27.51	76	36.64	418	38.40	103
ΔE	46.77	192	50.40	360	53.57	1290	53.41	156
χ^2	91.32	957	96.20	2084	98.57	3494	99.09	689
$\cos\theta_T$	5.53	5	5.81	1	6.34	9	21.22	0
$\cos\theta_B$	8.83	21	10.13	44	10.35	50	10.45	2
$\cos\theta_S$	17.39	8	17.37	22	18.73	23	52.27	2
T	4.07	14	2.73	13	2.59	3	27.77	4
$ln(DOCA)$	0.91	0	0.64	1	0.41	0	0.83	0
$\mathcal{F}$	49.20	335	52.31	580	55.76	641	89.74	331
$m_{D^{*\pm}}$	49.84	73	56.23	104	65.50	193	68.00	37
$\cos\theta_{D^*}$	16.41	42	29.32	725	26.42	245	26.41	57
$\cos\theta_{a_0}$	0.85	6	1.39	11	2.50	7	3.26	1
θ_{D^0}	2.43	4	3.10	13	4.19	13	5.98	4
dls_D	63.67	76	70.13	119	72.62	148	74.61	15
p^*_K	4.71	18	5.74	32	6.46	48	6.69	6
$p^*_{\pi 1}$	3.45	5	1.37	7	1.69	6	2.90	3
$p^*_{\pi 3}$	1.07	1	0.94	3	1.04	3	1.13	0
$p_{S\pi}$	5.15	9	8.43	14	14.02	21	14.26	2
m_η	36.54	109	45.47	146	62.38	319	61.60	27
p^*_η	5.74	7	23.58	4	44.71	47	34.92	8
$m^{VETO}_{\pi^0}$	28.33	278	38.60	408	57.54	1048	53.33	115
$\cos\theta_\eta$	40.28	364	39.21	591	44.12	2214	50.34	202
$p^*_{\pi B}$	7.61	36	36.47	190	60.86	800	43.65	48
$\mathcal{L}_2/\mathcal{L}_0$	8.74	0	8.29	0	7.84	0	46.82	3
fit status	39.59	-	48.30	-	56.00	-	59.09	-
$\#cand < 30$	2.97	-	2.35	-	1.34	-	0.85	-

Table A.5: Rejected candidates, R, for the DstIII selection (in %) and the number of uniquely rejected candidates, U, for different event types. The quoted number for the variable ($\#cand < 30$) is the percentage of rejected events.

variable	SigMC		NonRes		GenB		$q\overline{q}$	
	R(%)	U	R(%)	U	R(%)	U	R(%)	U
$m_{\rm ES}$	21.11	8	26.66	22	35.18	123	37.49	48
ΔE	47.28	76	50.17	80	53.04	437	52.66	47
χ^2	91.06	153	95.25	231	98.07	279	98.84	76
$\cos\theta_T$	4.36	3	4.07	1	4.63	2	15.88	1
$\cos\theta_B$	15.65	29	17.17	34	17.74	71	17.84	7
$\cos\theta_S$	18.63	24	18.71	24	20.57	29	55.57	11
R2	1.07	4	1.16	3	1.19	1	15.74	0
$ln(DOCA)$	5.14	2	3.80	4	2.96	4	5.85	0
$\mathcal{F}$	14.42	7	15.31	16	16.16	12	61.22	9
$m_{D^{*\pm}}$	52.66	11	59.38	11	68.67	22	71.77	3
$\cos\theta_{D^*}$	10.44	6	20.95	136	19.00	52	19.09	18
m_{D^0}	59.99	15	64.97	32	67.86	18	69.03	1
dls_D	56.29	17	61.18	30	63.24	34	66.75	10
$m_{K^0_S}$	39.76	0	43.66	0	46.06	0	47.88	1
$dls_{K^0_S}$	44.74	32	49.69	121	51.60	135	48.71	39
m_η	38.94	50	47.59	67	65.14	197	64.38	31
$m_{\pi^0}^{VETO}$	32.86	130	41.71	164	62.79	540	58.27	68
$\cos\theta_\eta$	31.11	72	29.42	117	33.29	400	39.47	54
$p^*_{\pi B}$	3.26	8	29.28	99	53.05	739	37.18	29
E_γ	2.76	0	2.27	0	2.36	0	3.84	0
$\mathcal{L}_2/\mathcal{L}_0$	9.50	4	9.31	10	9.79	6	50.92	3
fit status	44.32	-	50.17	-	56.82	-	59.28	-
$\#cand < 30$	0.37	-	0.30	-	0.17	-	0.09	-

Table A.6: Rejected candidates, R, for the DstIV selection (in %) and the number of uniquely rejected candidates, U, for different event types. The quoted number for the variable ($\#cand < 30$) is the percentage of rejected events.

Bibliography

[1] G. Lueders. Proof of the TCP theorem. *Annals Phys.*, 2:1–15, 1957.

[2] J. S. Schwinger. Spin, statistics, and the TCP theorem. *Proc. Nat. Acad. Sci.*, 44:223–228, 1958.

[3] C. S. Wu, E. Ambler, R. W. Hayward, D. D. Hoppes, and R. P. Hudson. Experimental test of parity conservation in beta decay. *Phys. Rev.*, 105:1413–1414, 1957.

[4] J. H. Christenson, J. W. Cronin, V. L. Fitch, and R. Turlay. Evidence for the 2π decay of the K_2^0 meson. *Phys. Rev. Lett.*, 13:138–140, 1964.

[5] M. Kobayashi and T. Maskawa. CP violation in the renormalizable theory of weak interaction. *Prog. Theor. Phys.*, 49:652–657, 1973.

[6] N. Cabibbo. Unitary symmetry and leptonic decays. *Phys. Rev. Lett.*, 10:531–532, 1963.

[7] L. Wolfenstein. Parametrization of the Kobayashi-Maskawa Matrix. *Phys. Rev. Lett.*, 51:1945, 1983.

[8] C. Jarlskog. Commutator of the quark mass matrices in the standard electroweak model and a measure of maximal CP violation. *Phys. Rev. Lett.*, 55:1039, 1985.

[9] W. M. Yao et al. Review of particle physics. *J. Phys.*, G33:1–1232, 2006.

[10] I. I. Y. Bigi and A. I. Sanda. Notes on the observability of *CP* violations in B decays. *Nucl. Phys.*, B193:85, 1981.

[11] H. Albrecht et al. Observation of B^0- $\overline{B}^0$ mixing. *Phys. Lett.*, B192:245, 1987.

[12] C. Albajar et al. Search for $B^0\overline{B}^0$ oscillations at the CERN proton - anti-proton collider. 2. *Phys. Lett.*, B186:247, 1987.

[13] P. F. Harrison and H. R. Quinn. The *BABAR* physics book: Physics at an asymmetric B factory. *SLAC report*, 504, 1998.

[14] E. Barberio et al. Averages of b-hadron properties at the end of 2006. 2007, 0704.3575.

[15] B. Aubert et al. Observation of direct CP violation in $B^0 \to K^+\pi^-$ decays. *Phys. Rev. Lett.*, 93:131801, 2004, hep-ex/0407057.

[16] R. Fleischer. New strategies to obtain insights into *CP* violation through $B_s \to D_s^{\pm}K^{\pm}$, $D_s^{*\pm}K^{\mp}$, and $B_d \to D^{\pm}\pi^{\mp}$, $D^{*\pm}\pi^{\mp}$ decays. *Nucl. Phys.*, B671:459–482, 2003, hep-ph/0304027.

[17] K. Maltman. The $a_0(980)$, $a_0(1450)$ and $K^{*0}(1430)$ scalar decay constants and the isovector scalar spectrum. *Phys. Lett.*, B462:14–22, 1999, hep-ph/9906267.

[18] S. Narison. QCD tests of the puzzling scalar mesons. *Phys. Rev.*, D73:114024, 2006, hep-ph/0512256.

[19] M. S. Bhagwat and P. Maris. Vector meson form factors and their quark-mass dependence. *Phys. Rev.*, C77:025203, 2008, nucl-th/0612069.

[20] C. K. Chua, W. S. Hou, and K.C. Yang. Final state rescattering and color-suppressed $\overline{B}^0 \to D^{(*)0}h^0$ decays. *Phys. Rev.*, D65:096007, 2002, hep-ph/0112148.

[21] T. K. Pedlar et al. Precision measurements of the timelike electromagnetic form factors of pion, kaon, and proton. *Phys. Rev. Lett.*, 95:261803, 2005, hep-ex/0510005.

[22] H.Y. Cheng and K.C. Yang. Hadronic charmless B decays $B \to AP$. *Phys. Rev.*, D76:114020, 2007, 0709.0137.

[23] V. Chernyak. Estimates of flavoured scalar production in B decays. *Phys. Lett.*, B509:273–276, 2001, hep-ph/0102217.

[24] M. Diehl and G. Hiller. New ways to explore factorization in B decays. *JHEP*, 06:067, 2001, hep-ph/0105194.

[25] M. Wirbel, B. Stech, and M. Bauer. Exclusive semileptonic decays of heavy mesons. *Z. Phys.*, C29:637, 1985.

[26] S. Laplace and V. Shelkov. CP violation and the absence of second class currents in charmless B decays. *Eur. Phys. J.*, C22:431–438, 2001, hep-ph/0105252.

[27] N. C. Mukhopadhyay. Weak form factors of the nucleon. 1998, nucl-th/9810039.

[28] T. D. Lee and C.N. Yang. Charge conjugation, a new quantum number G, and selection rules concerning a nucleon anti-nucleon system. *Nuovo Cim.*, 10:749–753, 1956.

[29] S. Weinberg. Charge symmetry of weak interactions. *Phys. Rev.*, 112:1375–1379, 1958.

[30] R. P. Feynman and M. Gell-Mann. Theory of the Fermi interaction. *Phys. Rev.*, 109:193–198, 1958.

[31] E. C. G. Sudarshan and R. E. Marshak. Chirality invariance and the universal Fermi interaction. *Phys. Rev.*, 109:1860–1862, 1958.

[32] M. Derrick et al. Evidence for the decay $\tau^+ \to \pi^+\eta\bar{\nu}_\tau$. *Phys. Lett.*, B189:260, 1987.

[33] P. Singer. Weak interaction decays of η meson. *Phys. Rev.*, 139:B483–B486, 1965.

[34] H. J. Behrend et al. Upper limit for the decay $\tau \to \eta\pi$ neutrino. *Phys. Lett.*, B200:226, 1988.

[35] D. Coffman et al. An upper limit on B($\tau \to \eta\pi\nu_\tau$). *Phys. Rev.*, D36:2185, 1987.

[36] P. Kooijman. Private communications.

[37] B. Aubert et al. Measurement of the $\tau^- \to \eta\pi^-\pi^+\pi^-\nu_\tau$ branching fraction and a search for a second-class current in the $\tau^- \to \eta'(958)\pi^-\nu_\tau$ decay. *Phys. Rev.*, D77:112002, 2008, 0803.0772.

[38] N. Severijns, M. Beck, and O. Naviliat-Cuncic. Tests of the standard electroweak model in beta decay. *Rev. Mod. Phys.*, 78:991–1040, 2006, nucl-ex/0605029.

[39] D. H. Wilkinson. Limits to second-class nucleonic and mesonic currents. *Eur. Phys. J.*, A7:307–315, 2000.

[40] K. G. Wilson and W. Zimmermann. Operator product expansions and composite field operators in the general framework of quantum field theory. *Commun. Math. Phys.*, 24:87–106, 1972.

[41] E. Witten. Short distance analysis of weak interactions. *Nucl. Phys.*, B122:109, 1977.

[42] H.R. Quinn. Heavy flavor physics. *SLAC PUB*, 9551, 2002.

[43] G. Buchalla, A. J. Buras, and M. E. Lautenbacher. Weak decays beyond leading logarithms. *Rev. Mod. Phys.*, 68:1125–1144, 1996, hep-ph/9512380.

[44] M. Beneke, G. Buchalla, M. Neubert, and C. T. Sachrajda. QCD factorization for $B \to \pi\pi$ decays: Strong phases and CP violation in the heavy quark limit. *Phys. Rev. Lett.*, 83:1914–1917, 1999, hep-ph/9905312.

[45] M. Diehl. Designer mesons for exploring factorization in B decays. 2001, hep-ph/0111009.

[46] M. Beneke, G. Buchalla, M. Neubert, and C. T. Sachrajda. QCD factorization for exclusive, non-leptonic B meson decays: General arguments and the case of heavy-light final states. *Nucl. Phys.*, B591:313–418, 2000, hep-ph/0006124.

[47] R. L. Jaffe. Multi-quark hadrons. The phenomenology of $Q^2\overline{Q^2}$ mesons. *Phys. Rev.*, D15:267, 1977.

[48] H.Y. Cheng, C.K. Chua, and K.C. Yang. Charmless B decays to a scalar meson and a vector meson. *Phys. Rev.*, D77:014034, 2008, 0705.3079.

[49] B. Aubert et al. Search for the rare decays $B^0 \to D_s^{(*)+} a_{0(2)}^-$. *Phys. Rev.*, D73:071103, 2006, hep-ex/0512031.

[50] G. Nardulli and T. N. Pham. Final state interactions in $B \to D\rho$ and $B \to D^*\pi$ decays. *Phys. Lett.*, B391:165–171, 1997, hep-ph/9610525.

[51] K. M. Watson. The effect of final state interactions on reaction cross- sections. *Phys. Rev.*, 88:1163–1171, 1952.

[52] H. Y. Cheng. Nonfactorizable contributions to nonleptonic weak decays of heavy mesons. *Phys. Lett.*, B335:428–435, 1994, hep-ph/9406262.

[53] M. Baak, G. Raven, and L. Wilden. *BABAR Anal. Doc.*, 1101, 2005.

[54] W. Kozanecki. The PEP-II B factory: Status and prospects. *Nucl. Instrum. Meth.*, A446:59–64, 2000.

[55] B. Aubert et al. The *BABAR* detector. *Nucl. Instrum. Meth.*, A479:1–116, 2002, hep-ex/0105044.

[56] V. Re et al. New effects observed in the *BABAR* silicon vertex tracker: Interpretation and estimate of their impact on the future performance of the detector. *IEEE Nucl. Sci. Symp. Conf. Rec.*, 1:73–77, 2006.

[57] A. J. Edwards et al. Radiation monitoring with CVD diamonds in *BABAR*. *Nucl. Instrum. Meth.*, A552:176–182, 2005.

[58] V. Re et al. *BABAR* Silicon Vertex Tracker: Status and Prospects. *Nucl. Instrum. Meth.*, A569:1–4, 2006.

[59] V. Re et al. Status and prospects of the *BABAR* SVT. *Nucl. Instrum. Meth.*, A560:5–8, 2006.

[60] V. Re et al. What can be learned from the *BABAR* Silicon Vertex Tracker running experience. *Nucl. Instrum. Meth.*, A552:224–231, 2005.

[61] V. Re et al. Lessons learned from *BABAR* silicon vertex tracker, limits, and future perspectives of the detector. *IEEE Trans. Nucl. Sci.*, 52:787–792, 2005.

[62] D. J. Lange. The EvtGen particle decay simulation package. *Nucl. Instrum. Meth.*, A462:152–155, 2001.

[63] S. Agostinelli et al. GEANT4: A simulation toolkit. *Nucl. Instrum. Meth.*, A506:250–303, 2003.

[64] P. Billoir. Track fitting with multiple scattering: A new method. *Nucl. Instrum. Meth.*, A225:352–366, 1984.

[65] A. Drescher et al. Calibration and monitoring of the ARGUS shower counters. *Nucl. Instrum. Meth.*, A249:277, 1986.

[66] G. Mancinelli and S. Spanier. Kaon selection at the *BABAR* experiment. *BABAR Anal. Doc.*, 116, 2001.

[67] G. Mancinelli and S. Yellin. An event likelihood algorithm for DIRC-based particle identification. *BABAR Anal. Doc.*, 165, 2001.

[68] W. D. Hulsbergen. Decay chain fitting with a kalman filter. *Nucl. Instrum. Meth.*, A552:566–575, 2005, physics/0503191.

[69] G. Punzi. Sensitivity of searches for new signals and its optimization. *ECONF*, C030908:MODT002, 2003, physics/0308063.

[70] S. Brandt, C. Peyrou, R. Sosnowski, and A. Wroblewski. The principal axis of jets. an attempt to analyze high- energy collisions as two-body processes. *Phys. Lett.*, 12:57–61, 1964.

[71] J. D. Bjorken and S. J. Brodsky. Statistical model for electron - positron annihilation into hadrons. *Phys. Rev.*, D1:1416–1420, 1970.

[72] G. C. Fox and S. Wolfram. Observables for the analysis of event shapes in e^+e^- annihilation and other processes. *Phys. Rev. Lett.*, 41:1581, 1978.

[73] R. A. Fisher. The use of multiple measurements in taxonomic problems. *Annals Eugen.*, 7:179–188, 1936.

[74] C. Dallapiccola. Analysis of neutral B decays to $\pi^+\pi^-$, $K^+\pi^-$ and K^+K^-. *BABAR Anal. Doc.*, 160, 2001.

[75] H. Albrecht et al. Search for hadronic $b \to u$ decays. *Phys. Lett.*, B241:278–282, 1990.

[76] W. Verkerke and D. Kirkby. The RooFit toolkit for data modeling. 2003, physics/0306116.

[77] W. Hulsbergen et al. Measurement of the branching ratio and time-dependent *CP* asymmetries for $B^0 \to K^0_S\pi^0$ decays on run 1-4 data. *BABAR Anal. Doc.*, 904, 2005.

[78] K. S. Cranmer. Kernel estimation in high-energy physics. *Comput. Phys. Commun.*, 136:198–207, 2001, hep-ex/0011057.

[79] B. Aubert et al. Study of inclusive production of charmonium mesons in B decay. *Phys. Rev.*, D67:032002, 2003, hep-ex/0207097.

[80] C. Amsler et al. Review of particle physics. *Phys. Lett.*, B667:1, 2008.

[81] M. Bona et al. Report of the tracking efficiency task force. *BABAR Anal. Doc.*, 324.

[82] M. T. Allen, M. T. Naisbit, and A. Roodman. A Study of π^0 efficiency. *BABAR Anal. Doc.*, 870, 2001.

[83] K. K. Gan. New results on the τ lepton. Invited talk presented at the SLAC Summer Institute on Particle Physics, Stanford, Calif., Aug 10-21, 1987.

[84] B. Aubert et al. Search for neutral B-meson decays to $a_0\pi$, a_0K, $\eta\rho^0$, and ηf_0. *Phys. Rev.*, D75:111102, 2007, hep-ex/0703038.

Acknowledgements

It is really a pleasure to write this very final part of my thesis. Many people have contributed in past years to this little booklet and unfortunately I will only be able to thank a small selection. So here it goes.

I would like to thank Jo van den Brand for being my promotor and for giving me the opportunity to graduate. Then my copromotor, Gerhard, your enthusiasm is catching. Our relation has grown over the years. I hope somewhere in the future we will work together again.

The time that I spent at SLAC were simply great. I enjoyed working as a part of the SVT group, for this I would like to specially thank Amedeo Perazzo, Giovanni Calderini and Gabriele Simi. Also, I would like to thank Sören Prell, Vitaly Eyges and Leif Wilden for starting up this analysis.

Other people at SLAC that I want to thank for making my time there so enjoyable are: Haleh (you were a great office mate!), Amir, David, Sylvie, Owen, Carsten, Donna, Chiara, Niels, Lideke, Mark, Tulay, Wouter V., Paola, Olya, Wouter H., Ed and Maarten.

Back in Amsterdam I was very happy to join the bfys group at Nikhef again. Marcel, you are an excellent group leader, many thanks for everything you have done for me in the past years. Nikhef is a very special place to work, and there is simply too many people to list every valuable colleague here.

Aart, many thanks for reading parts of this thesis and for the mental support in the last year. Gabriël, we studied at the VU together and now have spend the last year sweating in the same office. I hope to read your thesis soon!

Then my family. I would like to thank my parents and my brother. You have encouraged me through every step of my education and things weren't always easy along the way. Arjan and Surya: thank you both for being my paranimfen! Max, I don't know where to start. Most certainly you made the past years a lot more pleasant! Thanks for all your support and help and I hope we will start a lot more campfires in the years to come.

Index

A

analysis framework, 45
  selection, 59
  skim, 45, 50
Argus, *see* function
asymmetry amplitude, 2, 5, 10, 17, 18, 19, 22, 29, 148
AToM readout chip, 37, 39
axial vector current, 20, 21
a_0 box, 61
a_0 meson
  decay constant, 18
  form factor, 18
  four-quark structure, 26

B

B counting, 128
B factory, 1, 13, 33
B mixing, 9, 10, 13
B oscillation, 10, 14, 15
B tagging, 13, 151
BABAR, 33
beam energy substituted mass ($m_{\rm ES}$), 70, 84
Breit-Wigner, *see* function

C

Cabibbo, 6; *see also* suppression
calorimeter, *see* electromagnetic calorimeter
Čerenkov detector, *see* detector of internally reflected Čerenkov light
CKM
  allowed diagram, 17, 25, 29, 30, 145
  angle α, 7
  angle β, 7, 16, 151
  angle γ, 1, 5, 7, 16, 17, 19, 148, 151, 153
  mixing matrix, 6
  orthogonality relations, 7
  orthonormality relations, 7
  suppressed diagram, 17, 18, 26, 27, 30, 145, 146, 150
  unitarity condition, 7
  Unitarity Triangle, 1, 5, 7, 153
  Wolfenstein parameters, 6
coherent B decays, 12, 33
color suppression, 24, 48
composite particle, 50, 54
  a_0, 54
  B^0, 57
  D^+, 56
  D^{*+}, 57
  D^0, 56
  η, 56
  K^0_S, 56
  π^0, 55
conserved vector current (CVC), 18, 20, 21
continuum background, 46, 47, 64, 65, 66, 68, 69, 71, 74, 75, 83, 87, 89, 93, 106, 110, 112, 113, 128; *see also* Monte Carlo

CP asymmetry, 2, 10, 13, 14, 15, 16, 17, 19, 29, 148, 151
CP violation, 1, 3, 5, 6, 7, 9, 10, 13, 33, 153
  direct, 13, 14
  indirect, 14
  mixing and decay, 14
  through mixing, 14
Cruijff, *see* function
crystal, *see* electromagnetic calorimeter
  bumps, 52
  seeding, 52

D

data
  off-peak, 46, 110, 113
  on-peak, 46
data acquisition (DAQ), 42, 44
ΔE, 69, 85
ΔE sideband, 61
decay chain fit, 57, 65, 75, 113
decay length significance, *see* selection variable
detector of internally reflected Čerenkov light (DIRC), 34, 40, 41, 53, 84
distance of closest approach, *see* selection variable
drift chamber (DCH), 34, 36, 37, 39, 40, 43, 50, 53
DchI, DchII, DstI, DstII, DstIII, DstIV, 59

E

efficiency
  after fit, 83, 94
  after selection, 80
  after skim, 58
  corrections, 131
  kaon identification, 54
  reconstruction, 50, 114
  signal selection, 45, 58, 87, 98, 125
  tracking, 128, 130
electromagnetic calorimeter (EMC), 34, 41, 42, 43, 51, 52, 53, 84
energy difference (ΔE), 69, 85
EvtGen, *see* Monte Carlo generators
EvtGen lineshape bug, 47, 86

F

factorization, 2, 3, 5, 18, 19, 22, 23, 25, 26, 27, 30, 145, 146, 150, 151, 153, 154
  naive, 18
  QCD, 24
factorization scale μ, 23
Fierz transformation, 23
final-state interactions, *see* rescattering
first-class currents (FCC), 21
Fisher discriminant, *see* selection variable
four-quark structure, 146
function
  Argus, 70, 84, 85, 88, 89, 114, 128
  Blatt-Weisskopf, 86
  Breit-Wigner, 2, 47, 81, 85, 86, 87, 88, 114, 126, 138, 142
  Chebychev polynomial, 80, 85, 87, 89, 125
  Cruijff, 84, 85, 89, 114, 128
  error function, 80, 87
  Gauss, 85, 105, 107, 122
  keys, 87, 88, 89

G

G parity, 18, 21, 22, 31, 145, 148, 150
geant4, 47

global decay chain fit, *see* decay chain fit
gluon exchange, 27

H

helicity angle, *see* selection variable

I

instrumented flux return (IFR), 34, 42, 43
interaction point (IP), 34, 37, 50
isotropic decay, 65, 66, 67, 68

J

Jarlskog invariant, 7
Jetset, *see* Monte Carlo generators
Jetset bug, 48, 87, 89, 107, 122

K

Kalman filter, 50
Kobayashi, 6

L

light-cone calculation, 25
lineshape, *see* Breit-Wigner
luminosity, 34, 35, 37, 41, 43

M

magnet, 34, 50
  superconducting solenoid, 42
Maskawa, 6
$m_{\rm ES}$, 70, 84
$m_{\rm ES}$ sideband, 61
mixing, 6, 9, 10, 14
Monte Carlo, 46, 63, 70
  B^+B^-, 47
  $B^0\overline{B}^0$, 47
  $c\bar{c}$, 47
  full, 105
  generic samples, 47
  single mode, 47
  toy, 105
  type I/II, 47
  uds, 47
Monte Carlo generators
  EvtGen, 47, 86
  Jetset, 47, 48, 80, 87, 113

N

natural spin-parity state, 20
Nobel Prize, 1, 6
non-resonant signal, 30

O

off resonance, *see* data, off-peak
on resonance, *see* data, on-peak
online computing system, 42
operator
  C, 5
  CP, 6, 9, 14
  CPT, 6
  G, 21
  P, 5
  T, 6

P

partially conserved axial current (PCAC), 20

particle candidate list, 50
CalorNeutral, 53
ChargedTracks, 52
GoodNeutralLooseAcc, 53
GoodPhotonLoose, 53
GoodTracksLoose, 52
GoodTracksVeryLoose, 52
KMicroNotPionGTL, 54, 55
KsDefault, 56
NotAPion, 54, 55
Pi0AllDefault, 55
peaking background, 70
penguin diagram, 23
PEP-II, 33, 34, 46, 110, 153
pion-kaon separation, 40, 53
probability density function, *see* function
combined, 87
component, 83, 84, 87
parameters, 83, 89
parts, 89

R

rescattering, 3, 19, 27, 28, 29, 30, 147, 151, 154
resonant signal, 30

S

second-class currents (SCC), 21
selection variable
angle, 75
χ^2, 75
ΔE, 69
decay length significance, 72, 76
DOCA, 75
Fisher discriminant, 65, 68, 69
Fox-Wolfram moment, 67
helicity angle, 72, 73, 74
mass, 75
$m_{\rm ES}$, 70
momentum, 75
momentum flow, 68
overlapping photon veto, 72
second Legendre moment, 67
sphericity, 66
sphericity angle, 66
thrust, 65
thrust angle, 65
thrust axis, 65
sideband estimation, 61
signal region, 61
significance level, 59, 60, 63
silicon vertex tracker (SVT), 35, 36, 37, 39, 40, 50, 53, 54, 130
skim, *see* analysis framework
spin-parity state
natural, 20
unnatural, 20
strong phase, 9, 10
suppression
Cabibbo, 7, 48
CKM, 7
color, 24, 48
CVC, 18, 20
G parity, 18

T

time dependent evolution, 13, 17, 29, 33
TreeFitter, *see* decay chain fit
trigger, 42, 43, 44
calorimeter trigger, 43
drift chamber, 43
efficiency, 43
global, 43
level 1, 43, 47
level 2, 43
level 3, 43, 47

U

unitarity matrix, *see*
CKM
Unitarity Triangle, 7
unnatural spin-parity state, 20

V

vector current, 18, 20, 21
vertex detector, *see*
silicon vertex tracker
V_{CKM}, 6

W

weak phase, 9, 10
Wolfenstein parametrization, 6